ALMA MATER STUDIORUM – Università di Bologna

FACOLTÀ DI CHIMICA INDUSTRIALE
Dipartimento di Chimica Industriale e dei Materiali

NEW CATALYST FOR THE H_2 PRODUCTION BY WATER-GAS SHIFT REACTION PROCESSES

Tesi di dottorato di ricerca in
CHIMICA INDUSTRIALE (Settore CHIM/04)

Presentata da
Dr. **Giuseppe BRENNA**

Relatore
Prof. **Angelo VACCARI**

Coordinatore
Prof. **Fabrizio CAVANI**

Correlatori
Prof. **Giuseppe FORNASARI**
Dr. **Francesco BASILE**

ciclo XXIII

Anno 2010

A me stesso

Key words

Copper and Iron as active phase
Hydrogen
Hydrotalcite
Perovskite
Water-gas shift reaction

Abbreviations

WGS – Water-Gas shift
HDS – Hydrodesulphuration
FT – Fischer-tropsch
ATR – Auto-thermal reforming
POX – Partial oxidation
CPO – Catalytic partial oxidation
SR – Steam reforming
CO-PROX – CO preferential oxidation
LTS – Low temperature shift
MTS – Medium temperature shift
HTS – High temperature shift
GHSV - gas hourly space velocity
DG – Dry gas
PVK – Perovskite
HT – Hydrotalcite

SUMMARY

1 INTRODUCTION

The total primary energy supply (TPES) is dominated by fossil fuels as energy sources and it amounted to about 87 % in 2008, with an oil contribution of 33 % (Fig. 1.1) (***1***). Moreover, oil is the most versatile of the fossil fuels, with high energy density and ease of transportation. However, in view of the limited reserves, a number of alternative fuels are being considered, such as LPG (liquefied petroleum gas), natural gas, methanol, DME (dimethyl ether), ethanol, bio-diesel, Fischer-Tropsch synthetic fuels and hydrogen.

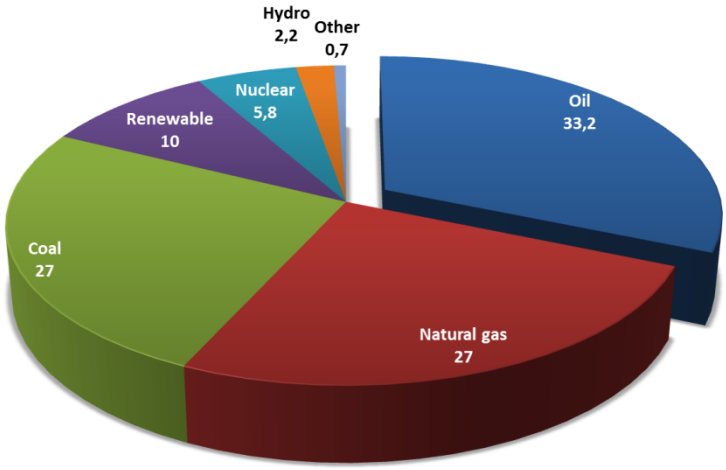

Fig. 1.1 Total primary energy supply by sources in 2008 (**1**).

The synthesis gas (syngas) is a mixture of hydrogen and carbon monoxide. It may contain carbon dioxide together with some inert gases, depending on the used source and the production process. Syngas may be manufactured by coke and biomass gasification as well as steam reforming or partial oxidation of hydrocarbons, usually natural gas.

Today, "hydrogen economy" is a priority in the political and research strategies. Hydrogen is a "building block" product of remarkable industrial interest and is claimed to replace hydrocarbons and provide a clean fuel without carbon emissions to be used in stationary and mobile applications as well (Fig. 1.2). Fuel cells will play a key role for both applications. However, hydrogen is an energy carrier of increasing relevance, not a fuel (***2***), because it cannot be extracted like natural gas or oil, but needs to be released by applying energy. This is a drawback because the process requires the input of primary energy carriers like coal, natural gas or biomass.

The advantage is that different feedstocks and energy sources can be used for its production, for example fossil fuels, biofuels, etc. by thermochemical way or water by electrolytic way (***3***).

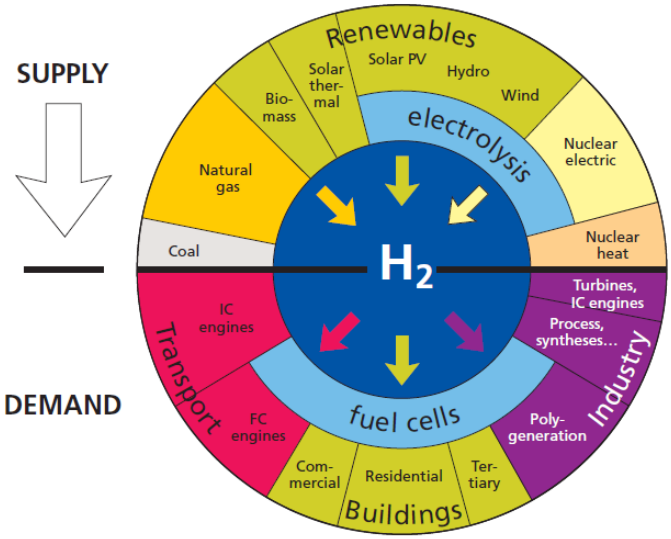

Fig. 1.2 Hydrogen: primary energy sources, energy converters and applications (size of "sectors" has no connection with current or expected markets) (***4***).

1.1 HYDROGEN

Hydrogen is the most abundant element in the universe and the third most abundant element on the earth, after oxygen and silicon; considering all the compounds that form, it is present in 15.4 % in the earth's crust (***5***). In recent years, the fuel market and environmental policies (such as the Kyoto Protocol in 1997) have reinforced the key role of this element, increasing the demand and studies focused on achieving a gradual reduction of pollutant emissions (CO_x, NO_x) and an energy independence from fossil fuels. For this reason, it is particularly interesting to consider that the hydrogen combustion does not give rise to pollutant emissions (only a small amount of NO_x in the combustion by air), it is renewable (you can produce hydrogen from water, which is also the only product of its combustion) and it has high efficiency. Since hydrogen is not an energy source, but an energy carrier, it must be produced and this requires the use of energy (***6***).

Currently, worldwide production of hydrogen exceeds 55×10^{10} Nm^3/y in 2010, of which about 60 % by reforming of light fractions of hydrocarbons, 30 % by cracking of heavy oil, 7 % by gasification of coal and 3 % by electrolysis of water. Steam reforming of natural gas is the main hydrogen production technology (large-scale and low cost), while other are still in the laboratory phase, with small-scale productions by steam reforming (SR) and/or gasification of biomasses, possibly in combination with electrolysis (***7***).

Regarding to the chemical, petrochemical and refining industry, hydrogen plays a crucial role (Fig. 1.3): the chemical industry uses approximately 50 % of hydrogen produced in the world for the ammonia synthesis, while the demand of the refinery (hydrotreating and hydrocracking) is continuously increasing to respect the stringent regulations (Fig. 1.4), reaching approximately 37 % of the hydrogen production (***8***,***9***). Further uses are the methanol and liquid hydrocarbons syntheses (8 %), the production of plastics and reduced metals.

Fuel cells use the electrolytic conversion of hydrogen to produce electricity and heat, being able to achieve efficiencies in the order of 60 % compared to 33-35 % of electricity generation plants by combustion. Their characteristics allow a modulating of power supply, crucial for future widespread production. Some high-pressure fuel cells have also achieved efficiencies to 85 % (***5***).

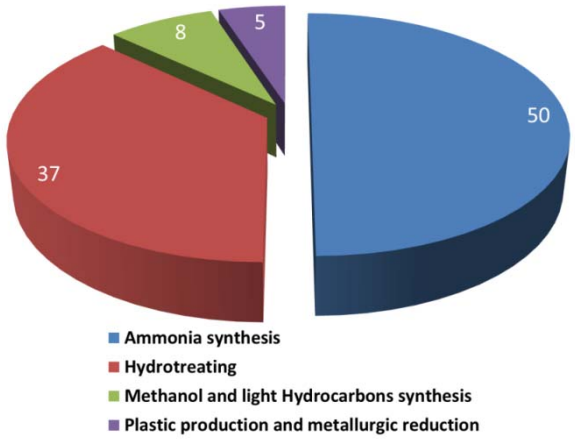

Fig. 1.3 Hydrogen role in the chemical industry.

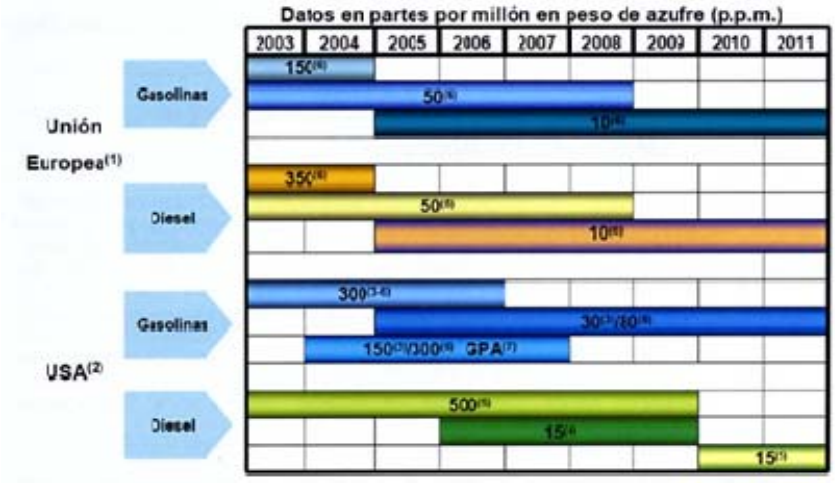

(1) Specifications approved January 31, 2003 (Directive 2003/17/EC) by the European Parliament and the Council of Ministers.
(2) EPA is proposing the residual content of sulphur in diesel fuel to ensure clean operation of trucks and cars, Environmental News, May 17, 2000.
(3) of the U.S. National average.
(4) maximum sulphur content of 15 ppm in '80% of the U.S. domestic market.
(5) maximum sulphur content of 15 ppm in 100% of the U.S. domestic market and the availability of diesel fuel with a sulphur content of 10 ppm in the market.
(6) Maximum concentration.
(7) Geographical Area Phase-in (Alaska, New Mexico, Colorado, Idaho, Montana, North Dakota, Utah, and Indian reservations in neighbouring states).

Fig. 1.4 Regulations related to S-content in gasoline and diesel for EU and USA (***8***).

1.1.1 INDUSTRIAL APPLICATIONS

The development of hydrogen production technologies requires the identification of the potential markets and the constraints associated with them. Existing and potential hydrogen markets may be identified as follows (***10***):

- *Industrial*. The main industrial markets for hydrogen are fertilizer production (ammonia), steel, methanol and H_2 for cracking and hydrodesulphurization.
- *Vehicles*. Transportation requirements can be met with different fuels (methanol, dimethyl ether, Fischer-Tropsch fuels or gasoline, diesel, jet fuel and, in the future, H_2 itself).
- *Power*. Hydrogen is a candidate for power production, particularly as a vector for storage and use to produce when necessary.
- *Commercial*. Hydrogen is being considered for commercial applications in the buildings with the co-generation of power and heat.

The hydro-processes are widely used because the hydrogen presence during a thermal process avoids the formation of coal, increasing the yield in distillates such as diesel, kerosene and jet fuel (***11***). These processes on oil fractions can be classified as non-destructive (hydrotreating) or destructive (hydrocracking) and they are different for the operating conditions, drastic for the first and less stringent for the latter (Table 1.1). The hydrogen consumption is very sensitive to the quality and the composition of the feed: those with a high content of contaminants, as well as those with high concentrations of unsaturated compounds, lead to a higher hydrogen consumption (***9***,***11***).

PROCESS	Main aim of treatment	Consumption ($Kg_{H2}/tonn_{feed}$)
HYDROTREATING		
Hydrotreating of gasoline	Elimination of poisons (mainly sulphur and nitrogen) for the reforming catalyst and isomerization. Compliance with the specifications related to sulphur content in gasolines	0.5-10.0
Hydrodesulphurization of kerosene	Compliance with specifications related to sulphur content in middle distillates	1.0-3.0
Hydrodesulphurization of diesel	Compliance with specifications related to sulphur content in middle distillates	3.0-12.0
Hydrotreating of middle distillates	Pre-treatment of feedstock for the upgrading processes, such as FCC (Fluid Catalytic Cracking) and hydrocracking	5.0-15.0
Dearomatization	Compliance with the specifications related to aromatic content in various fractions (for example in middle distillates)	3.0-15.0
HYDROCRACKING		
Conversion of middle distillates	Conversion of heavy vacuum fractions into lighter products such as LPG, virgin naphtha, kerosene, diesel (upgrading of the feed)	15.0-25.0
Hydrotreating and conversion of fuel oils	Reduction of content of undesired elements (metals, sulphur, nitrogen, etc.) to improve the quality of fuel oil. Partial upgrading of the residue to be fed	10.0-25.0

Table 1.1 H_2 consumption in the principal hydrotreating and hydrocracking processes (***9***).

1.1.1.1 HYDROTREATING

Hydrotreating processes are conducted in mild operating conditions and may be defined as stages of removal of compounds containing nitrogen, sulphur or oxygen. The most important process is the hydrodesulphurization (HDS) for selective hydrogenation of sulphur-containing compounds with Co-Mo or Ni-Mo catalysts (in the form of sulphides) supported on alumina (Table 1.2). At the operating conditions, 370 °C and from 7.0 to 14.0 MPa of H2, the desulphurization is accompanied to a small extent also by the reactions of hydrogenation and hydrocracking (***11***).

It should be noted, however, such as HDS, represents only one of the methods for the removal of sulphur (Fig. 1.5). The desulphurization has not a unified classification, so it may be classified according to the type of transformation of sulphur-containing compounds, or the role of hydrogen in the chemical and physical nature of the process (***12***). The HDS, both conventional and advanced, may be considered as a catalytic process with breakage of organic compounds, producing hydrogen sulphide and causing no significant changes to the boiling point of feed (***11***).

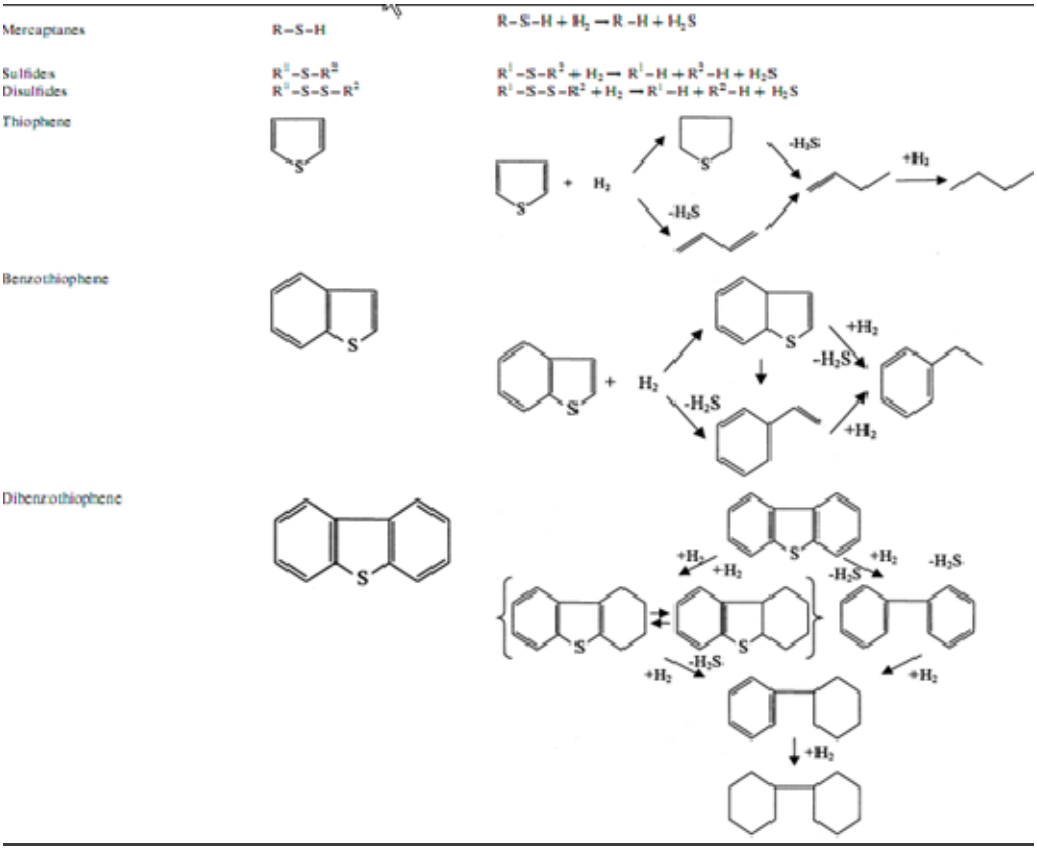

Table 1.2 Organic sulphides and hydrotreating mechanisms (***12***).

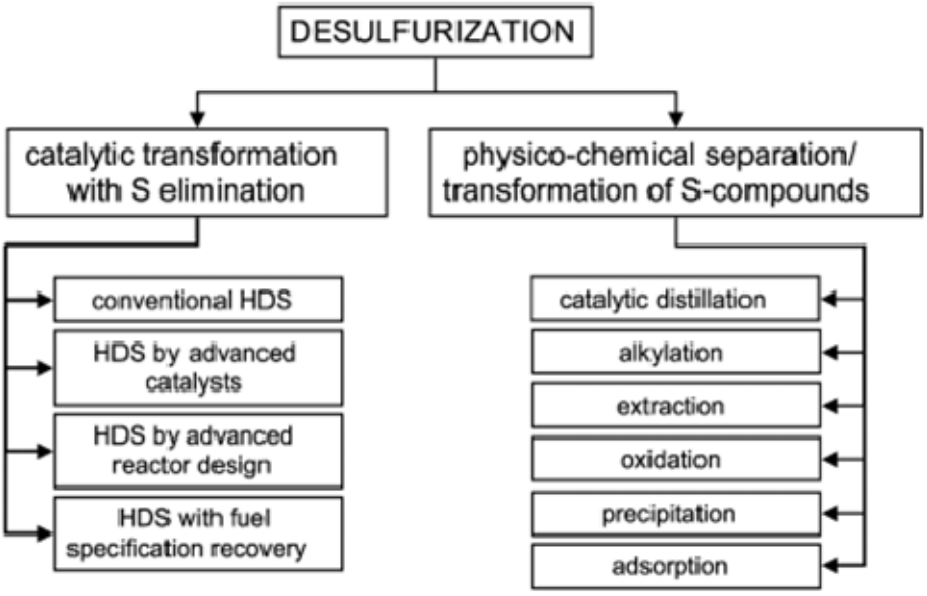

Fig. 1.5 Technologies of desulphurization (***12***).

1.1.1.2 HYDROCRACKING

The hydrocracking is a process similar to catalytic cracking, with subsequent hydrogenation and/or simultaneous reaction of cracking. Modern hydrocracking processes, initially developed for the conversion of heavy residual fuel oil and jet fuel, were successively optimized for the conversion to middle distillates and gas topping vacuum residues. These charges are difficult to handle for both reforming and for catalytic cracking as generally characterized by a high content of aromatic hydrocarbons and a high concentration of compounds containing sulphur or nitrogen, the main poisons for catalysts (***9***).

1.1.1.3 AMMONIA SYNTHESIS

The ammonia is used for the fertilizer production, the synthesis of explosives, propellants, polymers and nitriding steels (***13***). The importance of this synthesis can be derived from the global production of ammonia, 110 Mtonn, expressed as nitrogen, distributed in more than 600 facilities around the world. Ammonia production consumes about half of the hydrogen produced today and is the primary chemical industry use of hydrogen (as previously shown in Fig. 1.3). In 1911, at BASF, more than 2,500 formulations were studied for the catalyst, enabling the development of the basic principles of the catalysis (***14***).

At the beginning of the 20th century, the use of nitrogenous fertilizers was already well established. Haber and Bosch developed the direct synthesis of ammonia from hydrogen and nitrogen (reaction 1.1) (***14***). It is a clean reaction without by-products formation and the

thermodynamic is seemingly straightforward. The ammonia synthesis reaction is composed of several steps, proceeding along a well-defined Langmuir-Hinshelwood reaction path: dissociation of N_2, dissociation of H_2, and formation of N–H bonds. The main role of the ammonia catalyst is to dissociate the N_2 bond (***14***).

$$1/2\ N_2 + 3/2\ H_2 \leftrightarrows NH_3 \qquad \Delta H^0_{298} = -\ 92.4\ kJ\ mol^{-1} \qquad \textbf{reaction 1.1}$$

The reaction is exothermic and accompanied by a decrease in volume at constant pressure. Therefore, the value of the equilibrium constant (K_p) increases as the temperature is lowered and ammonia concentration at the equilibrium increases by increasing the pressure. The optimum pressure for economic operation is 15.0-35.0 MPa. Thermodynamically, low temperature is advantageous, but for kinetic reasons high temperatures have to be used (Fig. 1.6).

All commercial ammonia synthesis catalysts are currently based on metallic iron promoted by alkali (K) and various metal oxides, as aluminium, calcium or magnesium oxides. The principal material used to make these catalysts is usually magnetite (Fe_3O_4) and approximately 0,8 % K_2O, 2.0 % CaO, 0.3 % MgO, 2.5 % Al_2O_3 and 0.4 % SiO_2, as well as traces of TiO_2, ZrO_2 and V_2O_5.

However, Ru-based catalysts are known to be active for NH3 synthesis at atmospheric pressure and low temperature (***15***,***16***,***17***,***18***); in fact, they exhibit a 10-fold increase in activity over the conventional iron-based catalysts under similar conditions. In 1992, the introduction of the KAAP process (Kellogg Advanced Ammonia Process) reduced the costs proposing a Ru-based catalyst, active in less severe operating conditions (4.0 instead of 10.0-25.0 MPa) and can provide higher yields (Fig. 1.7) (***19***,***20***,***21***,***22***). Therefore, Ru-based catalysts could become the 2nd-generation catalysts for ammonia synthesis, but it is not widely employed in industrial ammonia synthesis, because they are expensive (***23***).

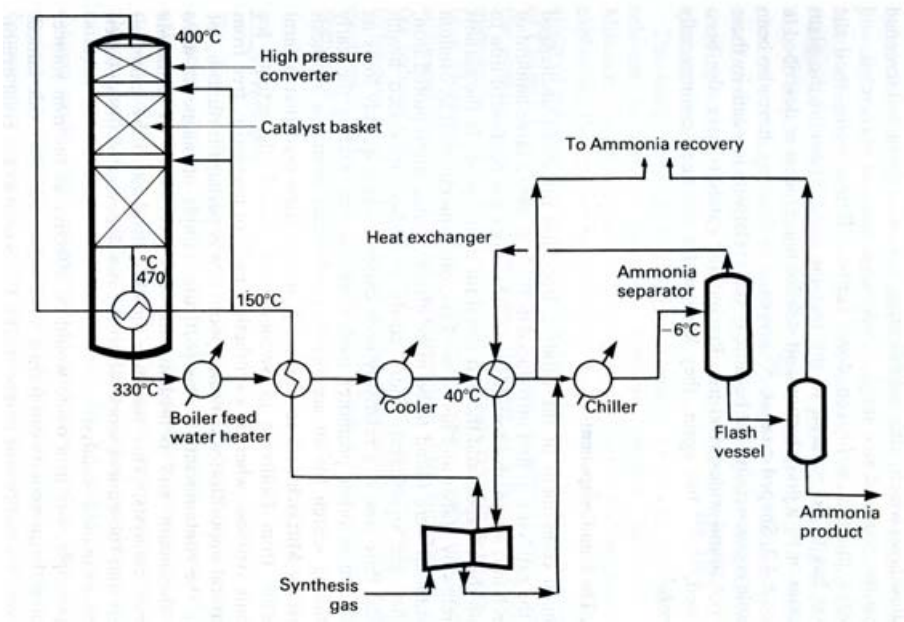

Fig. 1.6 Flow-sheet of typical ammonia synthesis (1,000 t/d) (***14***).

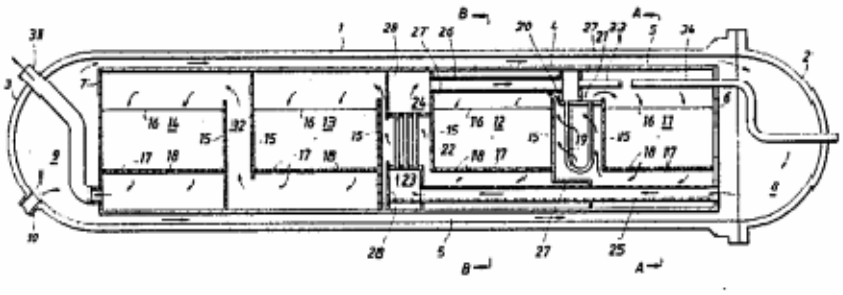

Fig. 1.7 Reactor scheme assigned to Kellog M W Co. for ammonia synthesis (*22*).

1.1.1.4 DIRECT REDUCTION OF IRON ORES (DRI)

Direct reduction of iron ores is today a major process for generating metallic iron, necessary in the iron and steel industry. World production of direct reduce iron (DRI) grew from near zero (1970) to 45.1 Mtonn (2002) (***24***,***10***). In 1998, about 4 % of the primary iron in the world was produced by the DRI process with a rapid growth in iron production, using syngas (a mixture of H2 and CO made from natural gas) to reduce iron ores to iron. The major chemical reactions are the followings:

$Fe_3O_4 + CO \leftrightarrows 3\ FeO + CO_2$	$\Delta H^0_{298} = -22.6$ kJ mol^{-1}	reaction 1.2
$Fe_3O_4 + H_2 \leftrightarrows 3\ FeO + H_2O$	$\Delta H^0_{298} = -63.8$ kJ mol^{-1}	reaction 1.3
$FeO + CO \leftrightarrows Fe + CO_2$	$\Delta H^0_{298} = +12.6$ kJ mol^{-1}	reaction 1.4
$FeO + H_2 \leftrightarrows Fe + H_2O$	$\Delta H^0_{298} = -24.5$ kJ mol^{-1}	reaction 1.5

The DRI process has lower capital costs than alternative methods used to produce iron, but requires a low-cost source of hydrogen. The primary market for DRI is to provide a purified iron feed for electric arc furnaces (EAF's) that produce various steel products. EAF's have lower capital costs than traditional steel mills and are environmentally cleaner operations than blast furnaces. Over a third of the world's steel production uses this process, reaching. the 45 %.

Iron production is potentially a significant existing market for hydrogen and, if low-cost hydrogen is available, the DRI process would replace the other ones. The economics of DRI relative to other processes (and the potential demand for hydrogen) depend upon three factors:

- *Technological developments*. The continuing improvements in EAF technology in terms of reduced production costs and increased capabilities to produce higher-quality steel have expanded the market share of this technology.
- *Environmental protection*. Traditional steel processes use coal and generate large quantities of pollutants, so clean air requirements strongly affect the economics of these processes.

- *Hydrogen costs*. The process is used where there is low-cost natural gas for hydrogen production near iron deposits.

1.1.1.5 METHANOL SYNTHESIS

Methanol is inside the top 10 produced molecules and is a common chemical feedstock for several important chemicals such as acetic acid, methyl ter-butyl ether (MTBE), methyl methacrylate (MMA), formaldehyde and chloromethane. The annual world demand is currently about 32 Mt/y. Moreover, being a clean liquid fuel, methanol could provide convenient storage of energy for fuel cell applications, particularly in transportation and mobile devices (***25***,***26***,***27***,***28***).

The process to synthesize methanol from carbon monoxide and hydrogen was introduced by BASF in 1923 and it was the second large-scale application of catalysis (after ammonia synthesis) and high-pressure technology (10.0-30.0 bar) to the chemical industry (***14***). Some researchers indicate that the main reaction is the hydrogenation of CO (reaction 1.6), while others stages include the reaction of CO_2 hydrogenation (reaction 1.7) and the reverse WGS reaction (reaction 1.8) (***29***). Reactions 1.7 and 1.8 combined together are equivalent to the reaction 1.6, so that either, or both, the carbon oxides can be the starting point for methanol synthesis. All reactions involved in the methanol synthesis are exothermic; reactions 1.6 and 1.7 are accompanied by a decrease in volume. Hence, high conversions to methanol, with a sufficiently active catalyst, are obtained at high pressures and low temperatures.

$CO + 2\ H_2 \leftrightarrows CH_3OH$	$\Delta H^0_{298} = -90.6$ kJ mol^{-1}	reaction 1.6
$CO_2 + 3\ H_2 \leftrightarrows CH_3OH + H_2O$	$\Delta H^0_{298} = -49.5$ kJ mol^{-1}	reaction 1.7
$CO + H_2O \leftrightarrows CO_2 + H_2$	$\Delta H^0_{298} = -41.2$ kJ mol^{-1}	reaction 1.8

For the future environmental developments, it is important to consider how to produce H_2 through the dry reforming of natural gas, identifying a process to use the CO_2 produced, for example by a sustainable and economical synthesis of methanol from CO_2 (***29***). In addition to the synthesis of methanol, both carbon monoxide and carbon dioxide can take part in other hydrogenation reactions, producing by-products such as hydrocarbons, ethers and higher alcohols (reaction 1.9-1.11).

$CO + 3\ H_2 \leftrightarrows CH_4 + H_2O$	$\Delta H^0_{298} = -206.2$ kJ mol^{-1}	reaction 1.9
$2\ CO + 4\ H_2 \leftrightarrows CH_3OCH_3 + H_2O$	$\Delta H^0_{298} = -204.8$ kJ mol^{-1}	reaction 1.10
$2\ CO + 4\ H_2 \leftrightarrows C_2H_5OH + H_2O$	$\Delta H^0_{298} = -255.6$ kJ mol^{-1}	reaction 1.11

These reactions are much more exothermic than the previous ones and methanol is thermodynamically less stable and less likely to be formed from carbon monoxide and hydrogen than the other possible products, such as methane. The large exothermic heat of reaction in addition to the low heat capacity of the vapour increases the potential for thermal run-away and

damage of the catalyst in the vapour phase, thus limiting the maximum operable reaction temperature (***30***).

There are two classes of catalysts studied and used for methanol synthesis (***30***):

(i) *High-pressure catalysts.* They contain zinc oxide and chromia and are used at high pressure and temperature above 350 °C. The zinc oxide/chromia catalysts are tolerant to impure synthesis gases, and may have a life in the plant of several years. They are not very selective and depending on synthesis conditions, as much as 2 % of the inlet carbon oxide could be converted to methane, with a similar proportion to dimethyl ether. Because these side reactions are very exothermic, careful control of catalyst temperature is necessary.

(ii) *Low-pressure catalysts*. In the copper/zinc oxide/alumina catalysts, high activity and stability are obtained by optimizing the compositions and producing very small particles of the components (***31***,***25***)**Errore. Il segnalibro non è definito.**. Although chromia had been shown effective as a stabilizer in the high pressure catalyst, alumina is superior to it as the third component in the low pressure catalyst. The alumina, present as a high surface area and poorly crystalline phase, is more effective than zinc oxide to prevent the sintering of copper crystallites, but zinc oxide is much more effective than alumina in picking up and holding typical poisons, such as sulphur and chlorine compounds (***32***).

The predominant processes operate at low pressure (<10.0 MPa) with Cu/Zn catalysts. The methanol synthesis reaction has been the subject of many mechanistic studies since the process was at first introduced; CO_2 adsorption is the starting point, but there are also evidences of methanol synthesized directly from CO_2 (***33***,***30***). A surface formate is the pivotal intermediate over both catalysts; surface formate is made by the hydrogenation of adsorbed carbon dioxide, and the rate determining step in methanol synthesis appears to be hydrogenolysis of the formate intermediate first to methoxy and then to methanol. The remaining adsorbed oxygen is removed by carbon monoxide or hydrogen, depending on the reaction conditions, to give CO_2 or H_2O.

The crude methanol is distilled to separate the methanol from water and impurities in low concentrations, such as higher alcohols, ethers, etc..

1.1.1.6 DIMHETYL ETHER SYNTHESIS

Dimethyl ether (DME) is an alternative fuel that could potentially replace petroleum-based fuels (***34***). DME is the simplest ether (CH_3OCH_3) with physical properties similar to those of liquefied petroleum gases (propane and butane). It burns with a visible blue flame and is non-peroxide forming in the pure state or in aerosol formulations. Unlike methane, DME does not require an odorant because it has a sweet ether-like odor. It is a volatile organic compound, but is non-carcinogenic, non-teratogenic, non-mutagenic and non-toxic (***35***).

Currently, the major usage of DME is as a propellant in the aerosols industry, but it can also be used as a clean-burning fuel in diesel engines, as a household fuel (LPG alternative) for heating

and cooking, as a fuel for gas turbines in power generation, as a fuel for fuel cells and, finally, as a chemical feedstock for higher ethers and oxygenates (***36***,***30***).

Traditionally, DME has been produced in a two steps processes where syngas is first converted to methanol (reaction 1.6), followed by methanol dehydration to dimethyl ether ().

$CO + 2\ H_2 \leftrightarrows CH_3OH$		reaction 1.6
$2\ CH_3OH \leftrightarrows CH_3OCH_3 + H_2O$	$\Delta H^0_{298} = -23.4\ kJ\ mol^{-1}$	reaction 1.12
$H_2O + CO \leftrightarrows H_2 + CO_2$		reaction 1.8
$3\ CO + 3\ H_2 \leftrightarrows CH_3OCH_3 + CO_2$	$\Delta H^0_{298} = -258.6\ kJ\ mol^{-1}$	reaction 1.13

Coal and biomass can also be used to generate syngas, not only natural gas. Hence, DME production is not limited to one feedstock and its synthesis process price is directly related to the price of the feedstock. New processes are being commercialized to produce DME in a single step via autothermal reactors and slurry phase reactors. DME can be introduced and exploited with existing technologies, and enable the eventual implementation of advanced technologies, such as fuel cells. The prominent advantages of DME as a fuel and energy carrier are (***35***,***37***,***34***):

- DME, due to its high cetane number, may be used in the most efficient engine technology currently produced, with lower NO_x and SO_x emission than conventional diesel.
- Using exiting engine technology, DME produces the least amount of well-to-wheel greenhouse gas emissions compared to FT diesel, FT naphtha, bio-diesel, bio-naphtha, methanol, methane and ethanol.
- Excluding natural gas, DME has the highest well-to-wheel efficiency of all non-petroleum based fuels using conventional, hybrid and fuel-cell-vehicle technologies.
- DME can be used as a residential fuel for heating and cooking.
- On-board automotive fuel processors using methanol and DME exhibit the lowest start-up energies and the lowest fuel processor volumes – correlating to higher overall efficiencies as compared to ethanol, methane and gasoline fuel processor fuel-cell vehicles.
- The infrastructures of DME are less cost intensive than those for hydrogen, because DME can use the existing LPG and natural gas infrastructures for transport and storage.

Synthesis of DME from syngas in a single step is more favourable in thermodynamic and economical aspects (***35***,***36***). Single-stage DME synthesis in the vapour phase suffers from low per pass conversions due, in part, to the effects of high temperature on the catalysts. Gas-phase DME synthesis processes, in general, suffer from the drawbacks of low hydrogen and CO conversions per pass, along with low yield and selectivity in DME, coupled with a high yield in carbon dioxide. These processes are typically expensive due to high capital costs for reactors and heat exchangers, and high operating costs due to inefficient CO utilization and high recycle rates. Using an inert liquid as a heat sink for highly exothermic reactions offers a number opportunities in syngas processing. Heat generated by the exothermic reactions is readily accommodated by the inert liquid medium; this enables the reaction to be run isothermally; minimizing catalyst deactivation commonly associated with the more adiabatic gas phase technologies (***30***).

The single stage, liquid phase, DME synthesis processes are based on dual-catalytic synthesis in a single slurry reactor system, and based on a combination of an equilibrium limited reaction (methanol synthesis) and an equilibrium unlimited reaction (methanol dehydration).

The methanol synthesis and the water gas shift reaction take place over the co-precipitated $Cu/Zn/Al_2O_3$ catalyst and the methanol dehydration takes place over γ-Al_2O_3 or zeolite catalysts (***36***,***35***,***37***). Moreover, by varying the mass ratios of methanol synthesis catalyst, it is possible to co-produce DME and methanol in any fixed proportion, from 5 % to 95 % DME (***30***).

1.1.1.7 FISCHER-TROPSCH SYNTHESIS (FTS)

The Fischer-Tropsch (FT) process, i.e. the synthesis of liquid hydrocarbons rich in oxygenated compounds (paraffins, olefins, alcohols) through the hydrogenation of CO (reaction), is able to process coal, waste, natural gas, sludge waste, biomass, etc. (***10***). Initially developed and optimized for the production of gasoline and jet fuel (C_5-C_{11}), the FT processes have recently been addressed in response to emerging market demands, the production of diesel (C_9-C_{25}) and wax (C_{35}-C_{120}) , the latter to be subjected to hydrogenolysis to increase the yield of diesel (Fig. 1.8) (***38***) (***39***). A number of synthesis reactions can occur and the whole are quite exothermic, ΔH = -170 kJ (C atom^{-1}).

$CO + 3\ H_2 \leftrightarrows CH_4 + H_2O$		reaction 1.9
$n\ CO + (2n + 1)\ H_2 \leftrightarrows C_nH_{2n+2} + n\ H_2O$	ΔH^0_{298} = - 40.0 kJ mol^{-1}	reaction 1.14
$n\ CO + 2n\ H_2 \leftrightarrows C_nH_{2n} + n\ H_2O$	ΔH^0_{298} = - 35.0 kJ mol^{-1}	reaction 1.15
$n\ CO + 2n\ H_2 \leftrightarrows C_nH_{2n+1}OH + (n-1)\ H_2O$	ΔH^0_{298} = - 35.0 kJ mol^{-1}	reaction 1.16

Some other reactions, as the WGS (reaction 1.6) and the Boudouard (reaction 1.17) reactions, also occur.

$CO + H_2O \leftrightarrows CO_2 + H_2$	reaction 1.6
$2\ CO \rightarrow C_{(s)} + CO_2$	reaction 1.17

The hydrocarbon synthesis is normally favoured in the range of 200-400°C (***40***). Thermodynamically, the favoured formation is:

Methane > hydrocarbons > olefins > alcohols

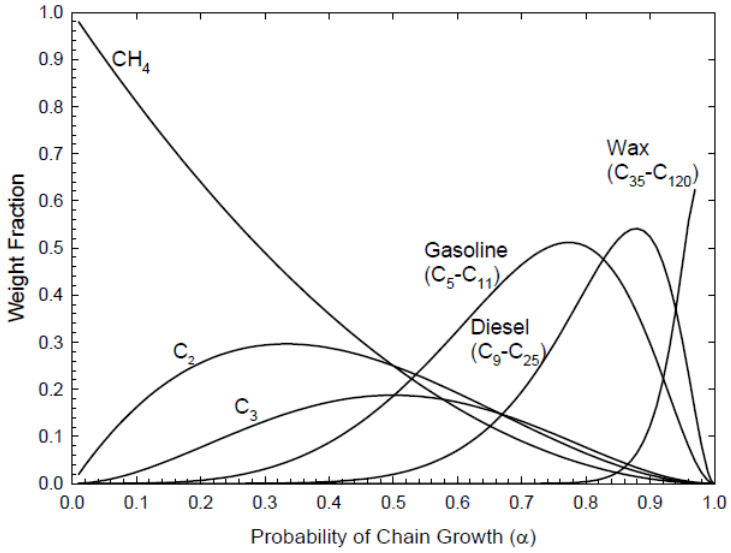

Fig. 1.8 FT products depending on probably of chain growth (Anderson-Schultz-Flory distribution) (***41***).

The production of hydrocarbons using traditional FT catalysts is governed by chain growth or polymerization kinetics. The so-called "surface carbide" mechanism is a plausible one for the interaction of CO and H_2 with the catalytic surface and the subsequent synthesis of hydrocarbons (***40***,***36***).

Processes are classified as high and low temperature, using catalysts based on Fe (HTFT) or Co/Fe (LTFT) (***41***). At low temperatures, the main primary products are linear alkanes, alcohols and aldehydes; the linearity of the product is important for many of their applications. It gives the waxes with high melting point and low viscosity. The C_9 to C_{15} olefins are ideal for the manufacture of biodegradable detergents. The C_{10} to C_{18} cut is an excellent diesel fuel (with the high cetane number of 75 and zero aromatics). At higher synthesis temperatures, side reactions occur, i.e. branched hydrocarbons and aromatics are formed. In that way, the diesel cetane number decreases, while the gasoline octane number increases (***40***).

Sabatier was the first to react carbon monoxide and hydrogen over a nickel catalyst in 1902. The result was the production of methane and water. Then, in 1923 Franz Fischer and Hans Tropsch of the Kaiser Wilhelm Institute (Germany) developed the Fischer-Tropsch process (i.e. Synthol process), in which a carbon monoxide and hydrogen flow, in the presence of iron, cobalt or nickel catalyst at 180-250 °C and at low pressures (preferentially atmospheric), produced a mixture of straight hydrocarbons and smaller amounts of oxygenates.

In recent years, the FT process have had a new interest to produce liquid hydrocarbons (Fig. 1.9). In the first step, natural gas is converted to synthesis gas (syngas) through the commercially known methods (steam-reforming, partial oxidation, or autothermal reforming). The syngas in the second step is converted to hydrocarbons via the F-T synthesis process. In the third step, the primary hydrocarbons in the form of syncrude are worked up to final products consisting mainly of naphtha, diesel fuel and kerosene (middle distillates).

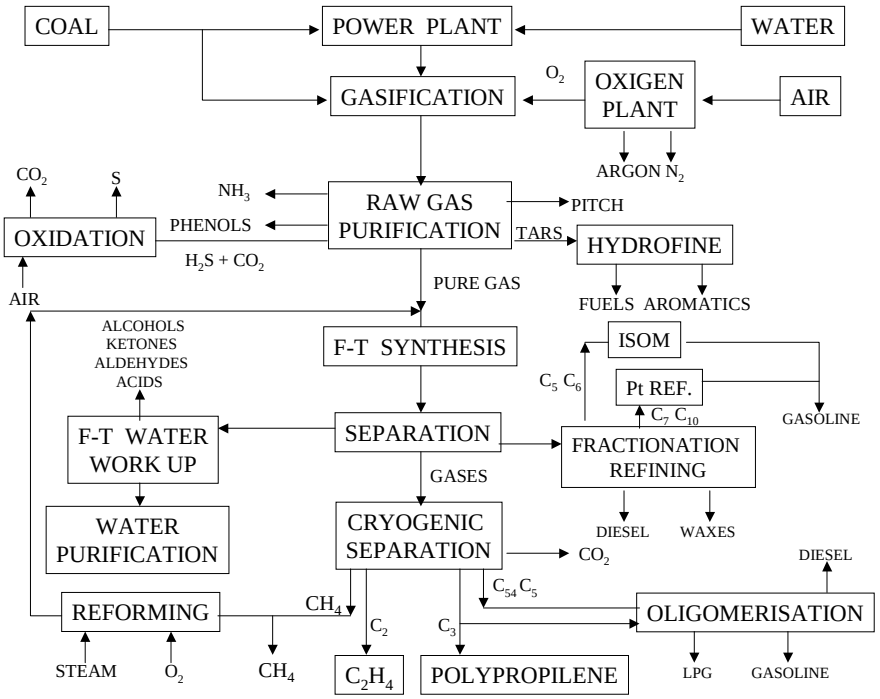

Fig. 1.9 Scheme of the overall FT process.

Sasol is the largest producer of synfuels and chemicals made by coal gasification (Lurgi's technology is employed). The commercial catalyst used is an iron-based catalyst but, in recent years, the advantages of cobalt-based catalyst for use in slurry phase reactor have been recognized (***42***,***43***).Iron catalysts are commonly used because of their low costs, have a high selectivity to olefins and a high water-gas shift activity (***44***,***45***). A disadvantage of Fe-based catalysts is that they deactivate faster due to oxidation and coke deposition. Instead, Co-supported catalysts do not oxidize or carburize under normal FT conditions, so they should deactivate less rapidly than iron catalysts. They can give high yields of liquid hydrocarbons and waxes, but with a higher methane and olefin yields than iron catalysts. The yields of oxygenated compounds are lower for cobalt catalysts and this can be an advantage if they are not desired.

1.1.2 ENERGY CARRIER

The increasingly stringent regulations in terms of emissions can be met through technological interventions on the engines, when they relate to the emission of NO_x and hydrocarbons, but it cannot get beyond a certain limit on CO_2 emissions. In fact, with conventional fuels, a certain amount of energy is necessarily associated with a fixed quantity of CO_2 (***46***). Fuel cells have rather high efficiency without polluting emissions, no moving parts and, in some cases, operate at low temperature and with a start-up fast. Fig. 1.10 shows a vehicle powered by fuel cells, which performs the electrochemical conversion of hydrogen producing electricity, that powers an

electric motor. The efficiency of the entire system, stage and level of electrochemical power supply, is higher than that of the only stadium in the conventional internal combustion engines. Furthermore, the development of prototypes powered by fuel cells has been focused to direct use of pure hydrogen, preferred in high pressure gaseous form rather than in the liquid (***46***).

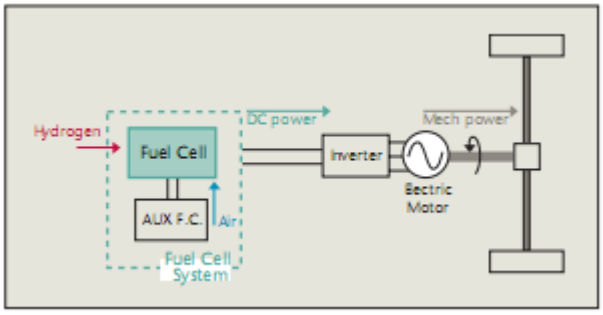

Fig. 1.10 Vehicle with fuel cell traction (***46***).

1.1.2.1 FUEL CELLS

A fuel cell is an electrochemical device in which the chemical energy stored in a fuel is converted directly into electricity (Fig. 1.14) (***47***). Fuel cells operate without combusting fuel and with few moving parts, so they are very attractive from both energy and environmental standpoint (***48***). A fuel cell can be two or three times more efficient than an internal combustion engine in converting fuel to electricity. Because a fuel cell transforms chemical energy directly into electrical energy, its theoretical efficiency is not limited by the Carnot inefficiency problem for heat-to-work conversion, unlike conventional power generation plants or the internal combustion engines (***40***). Therefore, a fuel cell system can exhibit a higher fuel-to-electricity efficiency than almost all the other energy conversion systems.

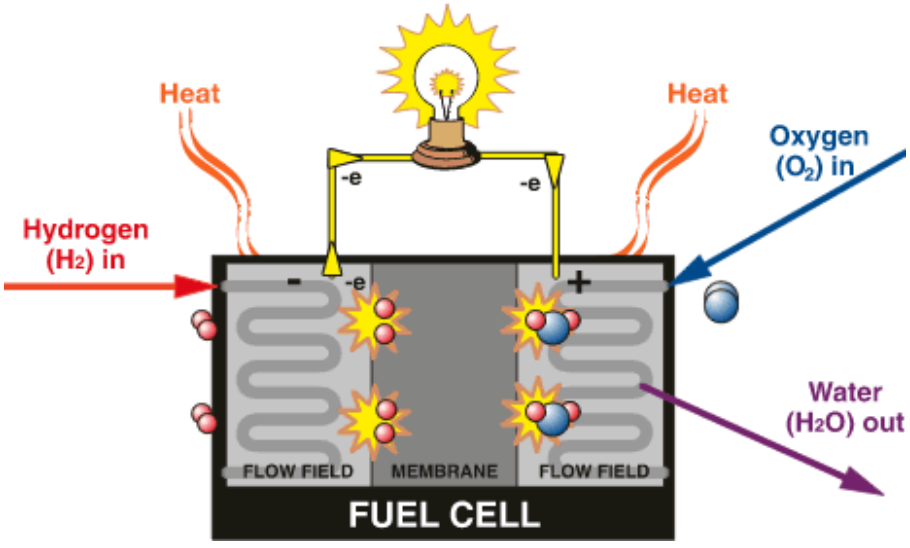

Fig. 1.11 Fuel cell system (***49***).

Specifically, a fuel cell consists of an anode – to which a fuel, commonly hydrogen, is supplied – and a cathode – to which an oxidant, commonly oxygen, is supplied. The oxygen needed by a fuel cell is generally supplied by feeding air. The two electrodes are separated by an ion-conducting electrolyte. The input fuel passes over the anode, where it catalytically splits into electrons and ions, and oxygen passes over the cathode. The electrons go through en external circuit to serve an electric load, while the ions move through the electrolyte toward the oppositely charged electrode. At the electrode, ions combine to create by-products, primarily heat, water in the form of steam or liquid water, and CO_2 in the case of hydrocarbon fuels (***48***,***47***).

Most individual fuel cells are small in size and produce between 0.5 and 0.9 V of DC electricity. Combination of many individual cells in a "stack" configuration is necessary to produce high voltages (***48***). On the basis of the electrolyte employed, there are five types of fuel cells (Table 1.3):

1) PEMFC (proton exchange membrane fuel cells)
2) AFC (alkaline fuel cells)
3) PAFC (phosphoric acid fuel cells)
4) MCFC (molten carbonate fuel cells)
5) SOFC (solid oxide fuel cells)

FUEL CELL	PEMFC	AFC	PAFC	MCFC	SOFC
Electrolyte	Ion-exchange membrane	$KOH_{(aq)}$ in solid asbestos	H_3PO_4	Li_2CO_3/K_2CO_3	ZrO_2-Y_2O_3
Temperature [°C]	70-90	120-250	180-230	650-700	800-1000
Transmitted charge	H^+	OH^-	H^+	CO_3^{2-}	O^{2-}
Anode catalyst	Pt	non-noble metals (i.e. Ni)	Pt	Ni	Ni
Fuel	H_2	H_2	H_2	Reformate, CO/H_2	Reformate, CH_4, CO/H_2

Table 1.3 Summary of fuel cell types (***47***).

The general advantages of fuel cells are reflected by the following desirable characteristic:

(i) High energy conversion efficiency.
(ii) Extremely low emissions of pollutants.
(iii) Extremely low noise or acoustical pollutions.
(iv) Effective reduction of greenhouse gas (CO_2) formation at the source compared to low-efficiency devices.
(v) Process simplicity for conversion of chemical energy to electrical energy.

Depending on the specific types of fuel cells, other advantages may include fuel flexibility and existing infrastructure of hydrocarbon fuel supplies, co-generation capability, modular design for mass production and relatively rapid load response. Therefore, fuel cells have great potential to penetrate into markets for both stationary power plants (i.e. industrial, commercial and residential home applications) and mobile power plants for transportation by cars, buses, trucks, trains and

ship, as well as man-portable micro-generators (Fig. 1.15) (***48***). Fuel cells plants can be built in a wide range of sizes – from 200 kW units suitable for powering commercial buildings, to 100 MW plants that can add base-load capacity to utility power plants. The disadvantages include the costs of fuel cells and that of the "on-board" H2 production via reforming, if required (***48***).

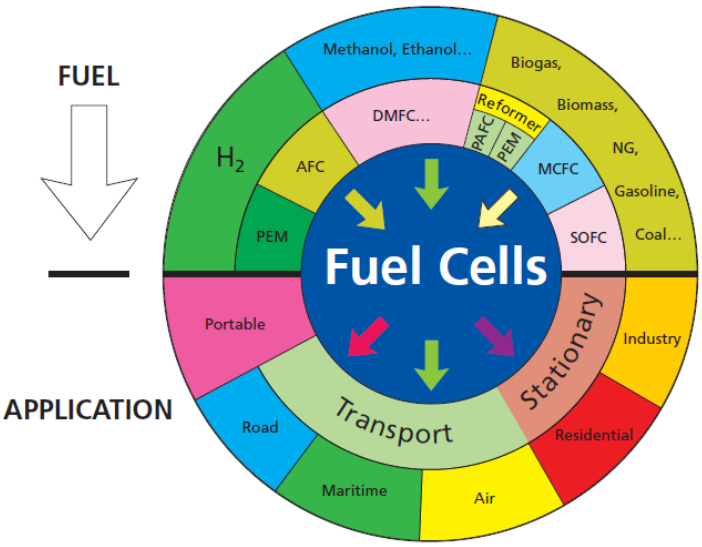

Fig. 1.12 Fuel cell technologies, possible fuels and applications (size of "sectors" has no connection with current or expected markets) (***4***).

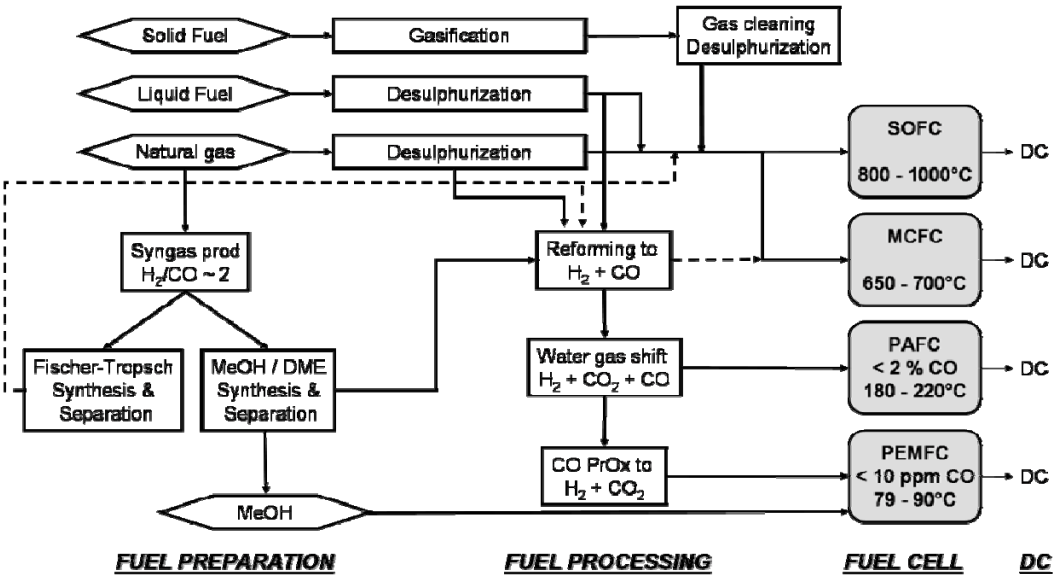

Fig. 1.13 The concept and the steps for fuel processing of gaseous, liquid and solid fuels for high and low temperature fuel cell applications (***48***).

Hydrogen, reformate (rich in H2) and methanol are the primary fuels available for current fuel cells (Fig. 1.13). The S-containing compounds, present in the hydrocarbon fuels, poison the catalysts in the fuel processor and fuel cells, thus they have to be removed. Syngas can be generated from reforming and reformate gas may be used as fuel for high-temperature fuel cells, such as SOCF and MCFC. Hydrogen is the real fuel for low-temperature fuel cells, such as PEMFC and PAFC. When natural gas or other hydrocarbon fuels is used in a PAFC system, the reformate must be processed by water-gas shift reaction, in order to have only 1-2 % of CO. If used in a PEMFC, the product gas from WGS must be further processed to reduce CO to < 10 ppm. Synthetic ultra-clean fuels can be made by FT or methanol synthesis using the synthesis gas produced from natural gas or from coal gasification, but the synthetic cleanness is obtained at the expense of extra cost for the extra conversion and processing steps (***48***).

1.1.2.1.1 PROTON-EXCHANGE MEMBRANE FUEL CELL (PEMFC)

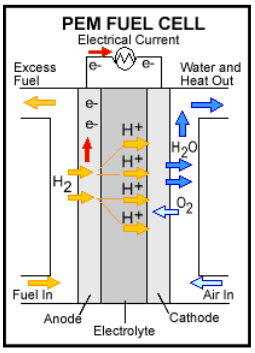

ANODE

$$2H_2 \rightarrow 4H^+ + 4e^-$$

CATODE

$$O_2 + 4H^+ + 4e^- \rightarrow 2H_2O$$

Fig. 1.14 Proton exchange membrane fuel cell (***50***).

The electrolyte used in PEMFC is a polymer membrane with characteristics of electronic insulator and conductor of protons (Fig. 1.14). The ion-exchange membrane used is fluorinated sulfonic acid polymer (Nafion). The acid molecules are fixed to the polymer and cannot leak out, but the protons on these acid groups are free to migrate through the membrane. The solid electrolyte exhibits excellent resistance to gas crossover (***48***). The electrodes are made of porous carbon and noble metal (Pt) as catalyst. The PEM operating at low temperature (70-90 °C) ensures a rapid start-up of the system, as well as less stress for the materials involved (***47***). The PEMFC technology is primarily suited for residential/commercial (business) and transportation applications. The use of a solid polymer electrolyte eliminates the corrosion and safety concerns associated with liquid electrolyte fuel cells (***48***). On the other hand, the need to use Pt as a catalyst involves high concern of poisoning by the CO (for amounts > 10 ppm), with the impossibility of reforming systems to adapt to "on-board". Therefore, research is directed particularly to the study of alternative catalysts, such as Pt/Ru, more tolerant to higher amounts of CO (***47***).

1.1.2.1.2 ALKALINE FUEL CELL (AFC)

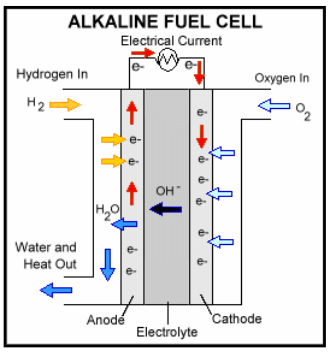

ANODE

$$2H_2 + 4OH^- \rightarrow 4H_2O + 4e^-$$

CATODE

$$O_2 + 2H_2O + 4e^- \rightarrow 4OH^-$$

Fig. 1.15 Alkaline fuel cell (***50***).

AFC used as electrolyte, an aqueous solution of KOH in a solid matrix of asbestos (Fig. 1.15). The catalysts used may be Ni, spinel, metal oxides or noble metals. The concentration of the electrolyte determines the operating range of cell temperature: 85 % KOH for cells operating at high temperature (250 °C) or 35-50 % for cells operating at low temperature (< 120 °C) (***47***). The presence of CO in the fuel causes the poisoning of the electrodes, while the CO_2 reacts with the electrolyte to form K_2CO_3, thus changing the chemical nature. For this reasons, it is required as fuel H_2 with high purity (***47***).

1.1.2.1.3 PHOSPHORIC ACID FUEL CELL (PAFC)

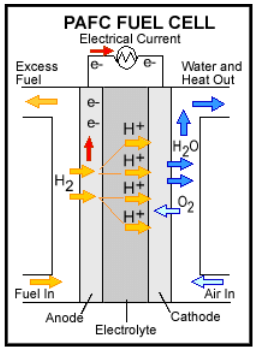

ANODE

$$2H_2 \rightarrow 4H^+ + 4e^-$$

CATODE

$$O_2 + 4H^+ + 4e^- \rightarrow 2H_2O$$

Fig. 1.16 Phosphoric acid fuel cell (***50***).

PAFC uses liquid, concentrated phosphoric acid as the electrolyte (Fig. 1.16). The phosphoric acid is usually contained in a Teflon-bonded SiC matrix (***48***). The small pore structure of this matrix preferentially keeps the acid in place through capillary action. Some acid may be entrained in the fuel or oxidant streams and addition of acid may be required after many hours of operation. Pt supported on porous carbon is used on both anode and cathode sides of the electrolyte. The low operating temperature, typically around 200 °C, associated with a high speed start-up and a certain tolerance to contaminants coming from the reforming of hydrocarbons, have encouraged

the application of these cells in the short term (***47***). PAFC plant also produces heat for domestic hot water and space heating (***48***).

1.1.2.1.4 MOLTEN CARBONATE FUEL CELL (MCFC)

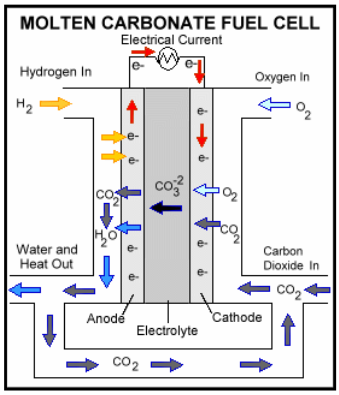

ANODE

$$CO_3^{2-} + H_2 \rightarrow H_2O + CO_2 + 2e^-$$

CATODE

$$CO_2 + \tfrac{1}{2}O_2 + 2e^- \rightarrow CO_3^{2-}$$

Fig. 1.17 Molten carbonate fuel cell (***50***).

The electrolyte used in MCFC is composed by a solution of molten alkali carbonates (Li_2CO_3-K_2CO_3) (Fig. 1.17). At the operating temperature of about 650 °C, the salt mixture is liquid and a good ionic conductor. The electrolyte is suspended in a porous, insulating and chemically inert ceramic ($LiAl_2O$) matrix. High temperatures can reduce operational costs by using non-noble metals (i.e. Ni) as catalysts. Developed especially for use in plants for the production of electricity from natural gas or coal, it has very high efficiency: from 60 % to 85 % by recovering heat (***47***). The cell performance is sensitive to operating temperature; a change in cell temperature from 650 to 600 °C results in a drop in cell voltage of almost 15 %. It does not suffer poisoning by CO and a source of CO_2 is required to the cathode to reform carbonates (***47***). The disadvantages of MCFC are that the electrolytes is corrosive and mobile, and a source of CO_2 is requires at the cathode to form the carbonate anions (***48***).

1.1.2.1.5 SOLID OXIDE FUEL CELL (SOFC)

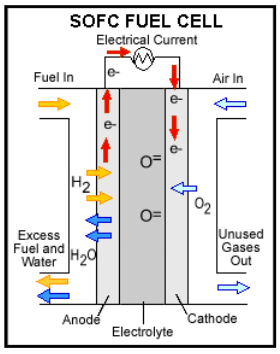

ANODE

$$2H_2 + 2O^{2-} \rightarrow 2H_2O + 4e^-$$

$$2CO + 2O^{2-} \rightarrow 2CO_2 + 4e^-$$

CATODE

$$O_2 + 4e^- \rightarrow 2O^{2-}$$

Fig. 1.18 Solid oxide fuel cell (***50***).

The SOFC uses a ceramic solid electrolyte that reduces corrosion problems and eliminates those related to the use of liquid electrolyte (Y-stabilized zirconia) (Fig. 1.18). The anode is a porous ceramic material Ni/ZrO_2 or Co/ZrO_2, while the cathode is $LaMnO_3$ doped with Mg or Sr (***47***,***48***). They have an efficiency of 50-60 % in converting fuel into electricity, which reaches 85 % recovered heat (***34***). The operating temperatures of 800-1000 °C allows use of non-noble metals as catalysts reducing the costs;, additional savings can come from the ability to operate a SOFC internal reforming of hydrocarbons. Fuel cells are more resistant to poisoning by sulphur, and can also be used as fuel CO (***47***). The necessity of using thermal insulation, compared with the high operating temperatures, has directed research related to the SOFC to the development of cheaper resistant materials and, in addition, to tests SOFC with lower operating temperatures, but at the expense of electric efficiency (***47***).

1.1.3 PRODUCTION PROCESSES

The indirect production of hydrogen, resulting from the catalytic reforming process, is not sufficient, taking into account its increasing demand. For this reason, it is necessary to use auxiliary plants to obtain an additional hydrogen production (Table 1.4) (***9***,***51***). Currently, steam reforming of hydrocarbons (SR) especially steam methane reforming (SMR) is the largest and generally the most economical way to make H_2. Alternative non-catalytic, industrial chemical approaches include partial oxidation (POX) of heavy oil or coal (***52***,***53***). Biomass can be also used to produce H_2 by thermochemical or biological processes, thus an interesting alternative for the treatment of wastes. Some other approaches are in development: solar photodecomposition of water still has many technical hurdles, remaining that suggest it is decades away from large scale, cost-effective implementation (***54***). When electricity is available and relatively inexpensive, electrolysis of water offers an alternative commercial approach (***55***,***52***).

1	Catalytic Reforming
2	Dry Reforming
3	Steam reforming (SR, WGS, CO-Prox)
4	Auto-thermal reforming (ATR)
5	Partial Oxidation (POX, CPO)
6	Biomass and electrolysis

Table 1.4 Processes for hydrogen production.

The choice of the process for additional hydrogen production is generally governed by economic considerations, such as capital and operating costs, the market trend in raw material costs, etc. (Fig. 1.19) (***9***,***53***). The choice of technology for manufacture of syngas depends on the scale of operation (***53***).

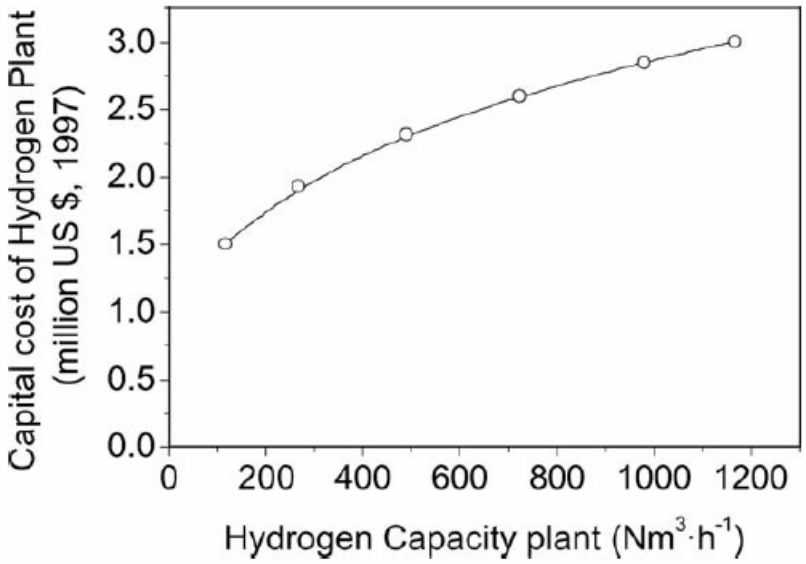

Fig. 1.19 Capital cost of a hydrogen plant as a function of capacity (***54***).

Depending on the technology used and the feed processed, the hydrogen yield widely changes, as shown in Table 1.5 (***9***). In all cases syngas is obtained as an intermediate product. Catalytic reforming shows lower yields than the other processes, but it is important to point out that its main purpose is the production of high-octane gasoline and that hydrogen is only a by-product (***9***). Generally, the SR process is preferred to the gasification of residues, because it has markedly lower capital and operating costs, so greater hydrogen yields may be achieved. Refineries can also use the following strategies to meet the hydrogen demand (***9***):

- Optimization of the management of the hydrogen available in the refinery through careful analysis of the distribution network (hydrogen management).
- Revamping of the existing plant based on the reforming process (modernization).
- External acquisition of hydrogen from industrial gas suppliers (hydrogen over-the-fence).

Process	H_2 Yield (% of the feed)
Semi-regenerative catalytic reforming	1.2-1.7 %
Continuous catalytic reforming	2.3-2.6 %
Steam reforming	30-40 %
Partial oxidation of methane	≈ 30 %
Gasification of the residue (in the case of complete conversion of the hydrogen contained in the syngas and in the presence of the conversion section for CO)	15-20 %

Table 1.5 Yields from the various processes for hydrogen production (***9***).

1.1.3.1 CATALYTIC REFORMING

Hydrogen is traditionally obtained as a by-product from the catalytic reforming of gasoline and the main reactions which lead to the hydrogen formation are the dehydrocyclization of paraffins and the dehydrogenation of naphthenes (***9***):

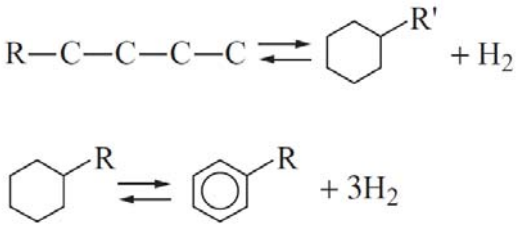

Fig. 1.20 The paraffins dehydrocyclization and the naphthenes dehydrogenation (***9***).

The process of catalytic reforming is mainly based on two types of catalytic reactors: a fixed-bed and a mobile-bed (circulating) reactor. Therefore, the process may be a fixed-bed semi-regenerative reforming (traditional plant), a cyclic reforming and a continuous regeneration reforming (***9***).

The continuous development of the reforming process has enabled a reduction in the severity of operating conditions and the formation of coke (with a consequent increase of the catalyst life-time), thus allowing gasoline with a higher octane number and greater hydrogen yields obtained. In the continuous regeneration processes, the higher hydrogen yield is ensured by lower pressures, in order to have a more complete aromatization and a limited hydrocracking reactions. The catalyst deactivation is faster with low pressure, due to the increase in the coke formation, but the continuous regeneration of the catalyst minimizes this phenomenon (***9***).

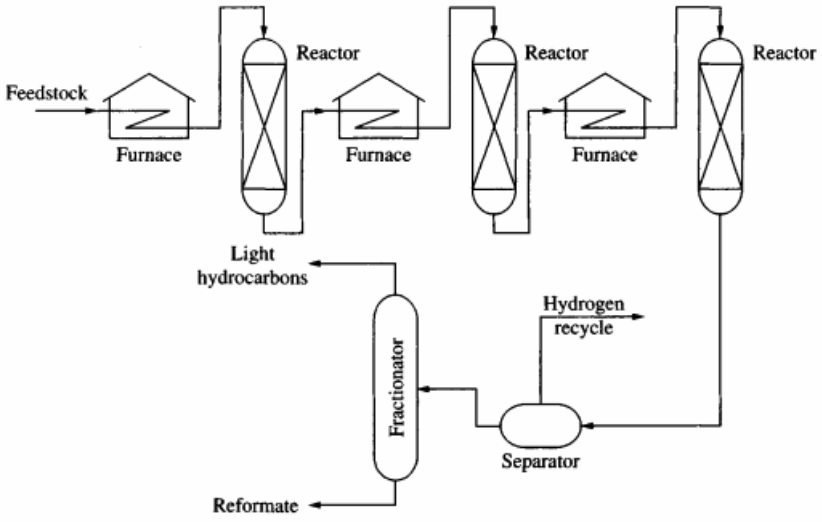

Fig. 1.21 Flow-sheet of catalytic reforming plant (***11***).

1.1.3.2 DRY REFORMING

Recently, attention has been focused on already known processes, such as the CO_2 reforming of CH_4, named dry reforming (reaction **1.18**). This type of reforming is economically attractive, because it uses two cheap carbon-containing streams to produce a syngas with a H_2/CO ratio close to 1, useful for the synthesis of oxygenates or long-chain hydrocarbons (***29***). From the environmental point of view, the dry reforming may be a useful way to use and reduce CO_2 emissions, but it should be noted that the process is endothermic and carried out at temperatures above 800 °C, thus requiring heat from fossil fuels, with an effect on overall balance of CO_2. The Fig. 1.22 shows the composition at thermodynamic equilibrium as a function of temperature for the dry reforming process (***29***).

$$CO_2 + CH_4 \leftrightarrows 2\ CO + 2\ H_2 \qquad \Delta H^0_{298} = +\ 247.0\ kJ\ mol^{-1} \qquad \text{reaction 1.18}$$

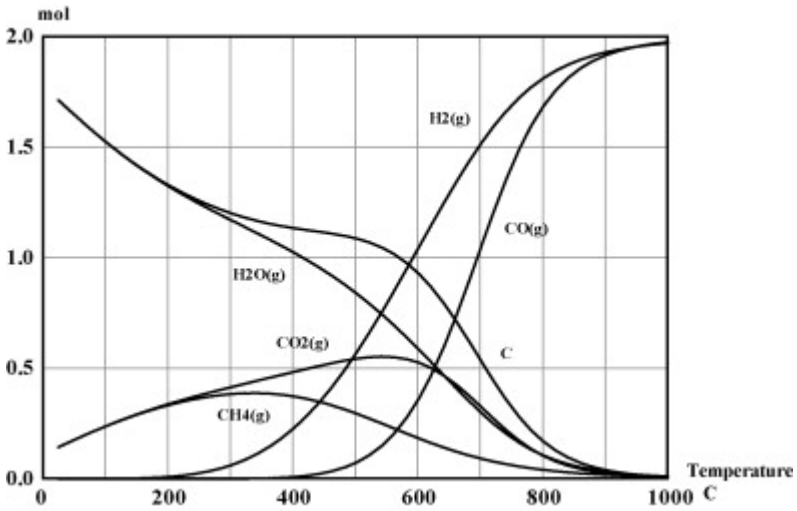

Fig. 1.22 Product composition of dry reforming as a function of temperature at thermodynamic equilibrium calculated by HSC Chemistry (feed: CH4/CO2 = 1, p = 1 atm) (***29***).

1.1.3.3 STEAM REFORMING (SR) AND WATER-GAS SHIFT (WGS)

Steam reforming (SR) is the most commonly process used in refinery to produce additional hydrogen by using natural gas or methane (SMR), as feedstock. Moreover, the gradual technological improvements, such as more selective catalysts, new furnace design and different flow schemes, have contributed to the development of more efficient and flexible SR process (***9***). Steam reforming of hydrocarbons is based on the following catalytic reaction:

$$C_nH_{2n} + 2n\ H_2O \leftrightarrows n\ CO + (2n+1)\ H_2 \qquad \text{reaction 1.19}$$

This reaction is endothermic and, therefore, favoured by high temperatures (750-850 °C), as well as by low pressure. In the case of methane, the above reaction becomes (***9***):

$$CH_4 + H_2O \leftrightarrows CO + 3H_2 \qquad \Delta H^0_{298} = +\ 206.2\ kJ\ mol^{-1} \qquad \text{reaction 1.20}$$

The Ni-based catalyst, used for this process, is very sensitive to minimal quantities of contaminants (such as sulphur, arsenic, phosphorous or lead); therefore, the feed must be pre-treated in order to reduce the quantity of these poisons (***9***). The quantity of unconverted methane, and, therefore, the outlet composition of syngas depend not only on the type of feed used, but above all on the operating conditions (pressure and temperature), on the quantity of steam used (S/C ratio) and on the performance of the catalyst. For a given feed, pressure and temperature, at exit from the steam reforming furnace, the unconverted quantity of methane contained in the syngas decrease with an increase of the S/C ratio, with a consequent increase in hydrogen yield (Fig. 1.23). Clearly, to obtain the same level of methane conversion with heavier hydrocarbon feedstock, under the same temperature and pressure conditions, it is necessary to increase the quantity of steam (***9***).

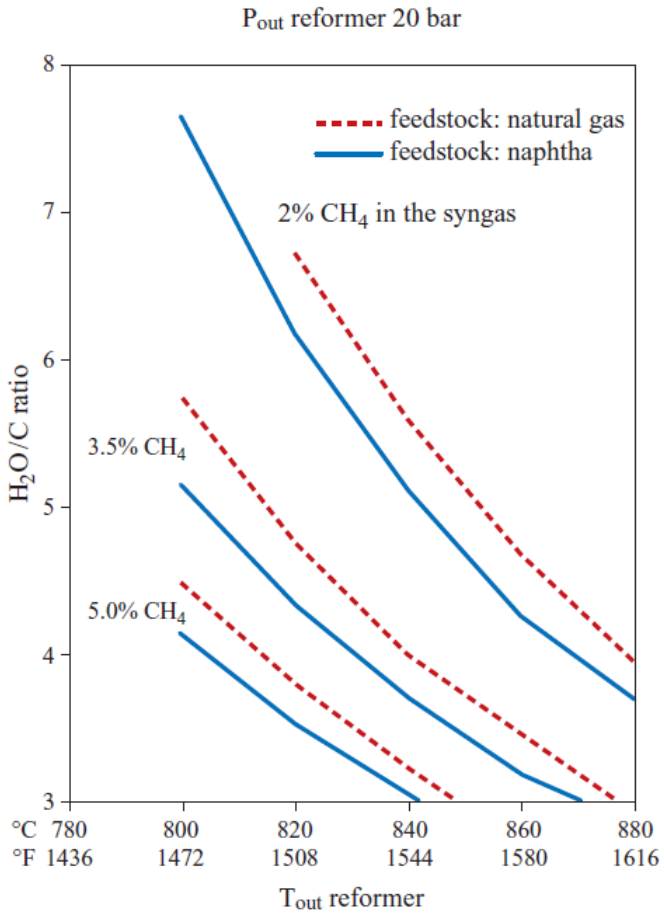

Fig. 1.23 Effect of the operating conditions on hydrogen production from steam reforming (***9***).

Parallel secondary reactions may occurred (reaction), leading to lower hydrogen yields and to the coke formation (***9***).

$CH_4 \rightleftharpoons C + 2\ H_2$	methane pyrolysis	reaction 1.21
$CO + H_2 \rightleftharpoons C + H_2O$	reduction of CO	reaction 1.22
$2\ CO \rightleftharpoons C + CO_2$	Boudouard reaction	reaction 1.17

The pyrolysis reaction is of minor importance under the SR operating conditions, unless heavier hydrocarbons are used as feedstock. It is important to stress that, in the various portions of the tubes in the reforming furnace, the composition of the process gas, the temperature and the catalyst activity influence the rate and the direction to which these secondary reactions proceed and, therefore, the possibility that coke formation takes place (Fig. 1.28) (***9***). In order to avoid the coke deposition on the catalyst active sites, it is necessary to be in the area where carbon does not form, where the operating conditions favour the consequent removal of the coke and, therefore, the reaction 1.17reaction **1.22** from right to left (for example increasing the S/C ratio), with respect to the pyrolysis reaction of the methane. In fact, the carbon removal rate becomes greater than its formation rate. In particular, carbon deposition occurs on the catalyst active sites within the portion of the tube (from the inlet) corresponding to about 30 % of its total length (***9***).

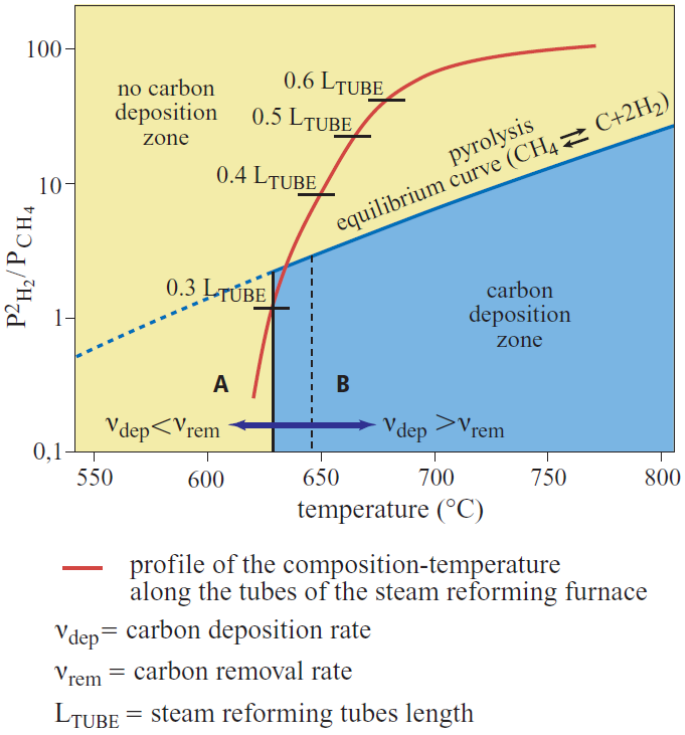

Fig. 1.24 Coke formation in the tubes of the steam reforming furnace as a function of the operating conditions. A and B lines identify the border between the area where carbon does not form and the area where it does (the latter is smaller in B) (***9***).

The subsequent stage of the process, known as water-gas shift (WGS) reaction, consists of the conversion of the carbon monoxide into carbon dioxide by further use of steam (***9***).

$CO + H_2O \leftrightarrows CO_2 + H_2$ $\Delta H^0_{298} = -41.2$ kJ mol^{-1} reaction 1.6

This type of unit allows a 2-5 % increase in hydrogen yield and there are three types of shift conversion employed which differ according to their working temperatures (***9***):

- ✓ High Temperature Shift (HTS), 330-360°C;
- ✓ Medium Temperature Shift (MTS), 220-270°C;
- ✓ Low Temperature Shift (LTS), 190-220°C.

Economic considerations have influenced the choice to use two subsequent converter: a HTS rector and a second LTS reactor, warranting an increase in feed conversion and a reduction of the heat required in the steam reforming furnace. The outlet syngas is sent to the purification and recovery section, where CO_x are eliminated. In conventional schemes, the purification section consisted of a methanator, that allows hydrogen recovery with purity levels of 92-97 % (***9***). Currently, the PSA (Pressure Swing Adsorption) process has replaced that scheme due to many reasons (***9***):

a) Production of very pure hydrogen (99.99 %)
b) Reduced operating complexity, due to the lower number of process units
c) Lower capital and operating costs
d) Easier optimization of the process under operating conditions for reforming

1.1.3.4 AUTO-THERMAL REFORMING (ATR)

The auto-thermal reforming (ATR) is a catalytic steam reforming process, where the reactor temperature is maintained using the partial oxidation of the hydrocarbons feedstock, typically natural gas, with oxygen in a sub-stoichiometric flame (reaction **1.23**) (Fig. 1.26) (***56***). It is the preferred technology for large-scale power plants for the synthesis of methanol or diesel fuel via Fischer-Tropsch reaction (***6***). A H_2/CO ratio close to 2 may be achieved by working with S/C or with a minimum recirculation of CO_2 (***56***).

$CH_4 + 3/2\ O_2 \rightarrow CO + 2H_2O$ $\Delta H^0_{298} = -520.0$ kJ mol^{-1} reaction 1.23

$CH_4 + H_2O \leftrightarrows CO + 3\ H_2$ $\Delta H^0_{298} = +206.2$ kJ mol^{-1}

$CO + H_2O \leftrightarrows CO_2 + H_2$ $\Delta H^0_{298} = -41.2$ kJ mol^{-1}

This process was developed by H. Topsoe AS with the aim to perform the POX and the SR in a single reactor. The preheated streams ($CH_4 + H_2O$ and $H_2O + O_2$) are mixed in a burner placed at the top where the POX reactions take place. The final steam reforming and equilibration take

place in the catalyst bed below the burner. Typically, the ATR operates at high temperatures, 1200-1300 °C in the combustion zone and 950-1200 °C in the catalytic zone; this results in a lower oxygen consumption (O_2/CH_4 = 0.55-0.60), although a certain amount of steam is added to the feedstock to eliminate carbon formation. C-formation in the combustion zone is an undesired reaction deposition that causes equipment damage, pressures losses and heat transfer problems (***56***).

Fig. 1.25 Auto-thermal reforming (ATR) reactor (***56***).

1.1.3.5 PARTIAL OXIDATION (POX AND CPO)

The partial oxidation is another route to hydrogen production and may be non-catalytic (POX) or catalytic (CPO).

The POX process converts heavy hydrocarbons of various kinds (fuel oil, biomass or coal) into syngas for the H_2 production (reaction **1.24**) (***46***). The process produces syngas with H_2/CO ratio of about 1.7-1.8 (***6***), because part of the H_2 and CO formed in these conditions are combusted with O_2. Coal gasification could become particularly attractive in the near future, because of market availability and price significantly and permanently lower than that of other commodities. The reduction in demand for high S-containing fuel, linked to the new specifications, has made available large quantities of waste that can be treated by this process, whose efficiency can reach values of 50-80 % (***56***).

The CPO is performed in a fixed bed reactor without a burner, by using, in particular, the natural gas. The CPO is the ideal solution for the partial oxidation of methane (reaction **1.25**), because it is possible to obtain the correct ratio of H_2 and CO for the methanol synthesis (***56***). It has a low heat of reaction and the contact times used (order of milliseconds) can get H_2 and CO selectivity of 90 %. The minimum improvements in the process do not justify the use, dangerous, of high-pressure of oxygen, which had hitherto industrial applications (***56***).

1.1.3.5.1 PARTIAL OXIDATION OF FOSSIL FUELS (POX)

The POX is the non-catalytic partial oxidation of fossil fuels (reaction **1.24**), where the thermal oxidation is run at 3.0-10.0 MPa with pure O_2 using a special burner inside a refractory lined vessel at ≈ 1300 °C.

$$C_nH_m + n/2\ O_2 \leftrightarrows n\ CO + m/2\ H_2 \qquad \text{reaction 1.24}$$

In the non-catalytic process, a mixture of oxygen and natural gas is pre-heated, mixed and ignited in a burner. The actual use requires O_2/CH_4 ratio of about 0.7. Combustion products, like CO_2 and H_2O, are also formed to a certain extent. Subsequently, endothermic reaction, as SR, occurs and determine the outlet temperature of 1000-1200 °C. At this stage, the gas composition is near thermodynamic equilibrium.

It appears that although the reactor in principle is simple, the cost of an oxygen plant is considerable. A process advantage is that it can work at high pressures, thereby saving costly compressors. Some carbon is formed by the thermal cracking of methane and has to be removed by washing. Texaco and Shell commercialize this conversion process (***51***).

In the POX process, steam is not used as a feed, but due to a lot of coke formation as by-product by using higher hydrocarbon feeds. Net reducing conditions avoid NO_x or SO_x production but, if the feed contains any sulphur compounds, H_2S and COS are by-products which must be scrubbed. A clear disadvantage is the need to have huge quantities of O_2 available continuously, thus requiring the substantial investment in an adjoining O_2 plant. Additional unit operations are required for gas purification (largely to remove H_2S) and to remove soot from the waste water (***51***).

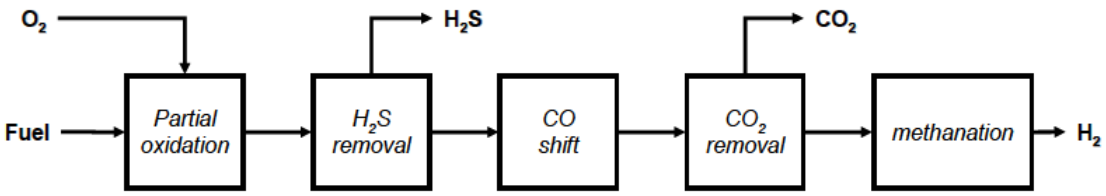

Fig. 1.26 Block diagram of the whole non catalytic partial-oxidation of methane.

Moreover, CO is also a co-product, a HTS converter is therefore needed to convert CO with steam to H_2. In addition, the CO_2 can be removed by adsorption and final traces of CO destroyed by follow-up methanation (***55***,***51***). The thermal efficiency of a POX plant feed with heavy hydrocarbons is estimated to be ≈ 70 % versus 81 % with SMR (***55***).

1.1.3.5.2 CATALYTIC PARTIAL OXIDATION OF METHANE (CPO)

A new interesting process for conversion of methane into syngas is the catalytic partial oxidation (CPO) (reaction **1.25**), that uses Ni-containing catalysts. In contrast to steam reforming

of methane (SMR), methane partial oxidation is exothermic. However, the partial oxidation requires pure oxygen, which is produced in expensive air separation units that are responsible for up to 40 % of the cost of a synthesis gas plant (in contrast, the steam reforming process does not require pure oxygen) (***57***).

$CH_4 + 1/2\ O_2 \leftrightarrows CO + 2\ H_2$ $\Delta H^0_{298} = -38.0$ kJ mol^{-1} reaction 1.25

From thermodynamic simulations, it is clear that the reaction is favoured at temperatures higher than 850 °C in excess of CH_4, although both CO and H_2 selectivity are modified by the formation of CO_2 and H_2O in combustion reactions, which are much more exothermic (reaction **1.26** and 1.27).

$CH_4 + 3/2\ O_2 \rightarrow CO + 2\ H_2O$ $\Delta H^0_{298} = -519.0$ kJ mol^{-1} reaction 1.26

$CH_4 + 2\ O_2 \rightarrow CO_2 + 2\ H_2O$ $\Delta H^0_{298} = -803.0$ kJ mol^{-1} reaction 1.27

For methane partial oxidation to syngas, the thermodynamic calculation results suggest a high temperature is advantageous for high CH_4 conversion and selectivity to CO and H_2 (Fig. 1.27) (***58***). However, an increasing of the pressure in the reactor is unfavourable (***59***). Since CPO reaction is slightly exothermic, a process based on this reaction would be much more energy efficient than the energy intensive SMR process. In addition, the partial oxidation reaction is also much faster than the reforming reactions, suggesting that a single stage process for syngas production would be an attractive alternative to SMR and also results in smaller reactors and higher productivity.

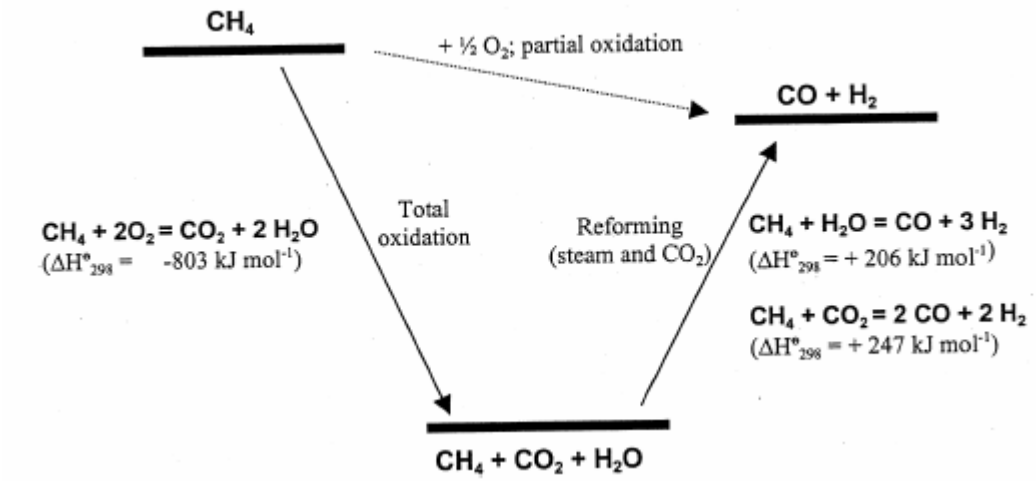

Fig. 1.27 Thermodynamic representation of the partial oxidation of methane (***59***).

The direct oxidation has not been developed at industrial scale, and it is difficult to study because it involves co-feeding CH_4/O_2 mixtures and reaction close flammable or even explosive conditions. Local hot spot are usually formed which can irreversible damage the active catalyst. Moreover, the gas phase reactions in a high reducing atmosphere can led to carbon and soot deposition over the catalyst surface.

Choudhary et al. (***60***,***61***,***62***,***63***,***64***) reported a high conversion of CH_4 and high selectivity to CO and H_2 with Ni- and Co-based catalysts. Compared with non-noble metal catalysts, the noble metal catalysts exhibit high stability, with excellent activity and selectivity. The major drawback of noble metal catalysts is their high cost, which restrict the potential use in industrial process. However, the major problem encountered with these non-noble metal catalysts is their relatively low stability. The main causes of the catalyst deactivation are carbon deposition and metal sintering (***57***).

This process is likely to become more important in the future of methane conversion due to the thermodynamic advantages that this process has over steam reforming.

- Partial oxidation is mildly exothermic, while steam reforming is highly endothermic. Thus, a partial oxidation reactor would be more economical to heat. In addition, it can be combined with endothermic reactions, such as steam or dry reforming with CO_2 to make these processes more energy efficient.
- The H_2/CO ratio produced in stoichiometric partial oxidation is around 2, and this ratio is ideal for downstream processes, in particular methanol and FT synthesis. This avoids the need to reverse shift hydrogen, which is produced in excess in the steam reforming.
- The product gases from methane partial oxidation can be extremely low in CO_2content, which must often be removed before synthesis gas may be used downstream.
- Partial oxidation technology avoids the need for large amounts of expensive super-heated steam. However, an oxygen separation plant, which is also costly, may be required in cases where N_2 (from air) is undesirable in high pressure downstream processes.

1.1.3.6 BIOMASS AND ELECTROLYSIS

The use of biomass and fuels derived from a renewable resource is of considerable interest for the hydrogen production, taking into account that many regions of the world have access to large amounts of biomass, as industrial waste. Currently, these processes are not yet available on the market and not yet economically competitive compared to the SR of natural gas (***6***).

Electrolysis, known for over 200 years, is the only way to produce hydrogen from water, but it is not a direct production. In fact, it requires electrical current as energy carrier and the cheapness of the latter determines the feasibility (***6***). The conventional process of electrolysis uses an alkaline solution as electrolyte and may reach order of efficiencies of 65 %. To avoid the mixing of the gases, microporous barrier are used between the anode and cathode.

An alternative is to use solid conductors as electrolyte, such as Nafion in PEMFC, which plays the role of both electrolyte and barrier. Particularly promising is the high-pressure electrolysis process: the main advantages are the production of hydrogen under pressure and greater efficiency due to internal power resistance (***6***).

REFERENCES

1. IEA. *Key World Energy Statics;* International Energy Agency, 2010.
2. Rostrup-Nielsen, J. R. *Catal. Rev.* **2004,** *46,* 247.
3. Wietschel, M.; Hasenauer, U.; De Groot, A. *Energy Policy* **2006,** *34,* 1284.
4. Community research. *Hydrogen Energy and Fuel Cells;* Final report; European Commission, 2003.
5. Greenwood, N. N.; Earnshaw, A. *Chemistry of the Elements,* 2nd ed.; Butterworth-Heinemann: Oxford (UK), 1998.
6. Mogensen, M.; Jensen, E. S.; Sehested, J.; Aasberg-Petersen, K. *Technologies for producing hydrogen;* Risø Energy Report 3: Hydrogen and its competitors; Risø National Laboratory, 2004.
7. van Ruijven, B.; van Vuuren, D. P.; de Vries, B. *Int. J. Hydrogen Energy* **2007,** *32* (12), 1655.
8. Molina, A. I. *Catalizadores de cobalto soportados sobre sòlidos mesoporosos para reacciones de hidrotratamiento;* PhD thesis; Malaga University, 2006.
9. di Luozzo, M. The hydrogen cycle. In *Encyclopaedia of hydrocarbons;* Treccani: Milano (I), 2006; Vol. II, p 59.
10. Forsberg, C. W. *Int. J. Hydrog. Energy* **2007,** *32,* 431.
11. Alì, M. F.; Alì, B. M. E.; Speight, J. G. *Handbook of Industrial Chemistry;* McGraw-Hill: New York (US), 2005.
12. Babich, I. V.; Moulijn, J. A. *Fuel* **2003,** *82,* 607.
13. Hellman, A.; Honkala, K.; Remediakis, I. N.; Logadóttir, Á.; Carlsson, Á.; Dahl, S.; Christensen, C. H.; Nørskov, J. K. *Surf. Sci.* **2006,** *600,* 4264.
14. Twigg, M. V. *Catalyst Handbook,* 2nd ed.; Wolfe: London (UK), 1996.
15. Liang, C.; Wei, Z.; Xin, Q.; Lin, C. *Appl. Catal. A* **2001,** *208,* 193.
16. Yunusov, S. M.; Kalyuzhnaya, E. S.; Moroz, B. L.; Ivanova, A. S.; Reshetenko, T. V.; Avdeeva, L. B.; Likholobov, V. A.; Shur, V. B. *J. Molec. Catal. A* **2004,** *219,* 149.
17. Xu, Q.; Lin, J.; Li, J.; Fu, X.; Yang, Z.; Guo, W.; Liao, D. *J. Molec. Catal. A* **2006,** *259,* 218.
18. Seetharamulu, P.; Kumar, V. S.; Padmasri, A. H.; Raju, B. D.; Rao, K. S. R. *J. Molec Catal. A* **2006,** *263,* 253.
19. Kowalczyk, Z.; Jodzis, S.; Sentek, J. *Appl. Catal. A* **1996,** *138,* 83.
20. Noe, S. A. to Kellogg M W (US). US Patent 4,735,780, 1998.
21. Shires, P. J.; Cassata, J. R.; Mandelik, B. G. to Kellogg M W (US). US Patent 4,479,925, 1990.
22. Noe, S. A. to Kellogg M W (US). US Patent 4,696,799, 1992.
23. Yang, Z.; Guo, W.; Lin, J.; Liao, D. *Chin. J. Catal.* **2006,** *27,* 378.
24. Parisi, D. R.; Laborde, M. A. *Chem. Eng. J.* **2004,** *104,* 35.
25. Liu, X.; Lu, G. Q.; Z.Yan; Beltramini, J. *Ind. Eng. Chem. Res.* **2003,** *42,* 6518.
26. Choudary, T. V.; Goodman, D. W. *J. Molec. Catal. A* **2000,** *163,* 9.
27. Keil, F. J. *Microporous and Mesoporous Mater.* **1999,** *29,* 49.
28. Stöcker, M. *Microporous and Mesoporous Mater.* **1999,** *29,* 3.
29. Raudaskoski, R.; Tuepeinen, E.; Lenkkeri, R.; Pongràcz, E.; Keiski, R. L. *Catal. Today* **2009,** *144* (3-4), 318.
30. Lee, S.; Sardesai, A. *Top. Catal.* **2005,** *32,* 197.

31. Guo, Y.; Meyer-Zaika, W.; Muhler, M.; Vukojevic, S.; Epple, M. *Eur. J. Inorg. Chem.* **2006,** 4774.
32. Nakamura, I.; Fujitani, T.; Uchijima, T.; Nakamura, J. *Surf. Sci.* **1998,** *400,* 387.
33. Saito, M.; Murata, K. *Catal. Surv. Asia* **2004,** *8,* 285.
34. Semelsberger, T. A.; Borup, R. L.; Greene, H. L. *J. Power Sources* **2006,** *156,* 497.
35. Fei, J.; Tang, X.; Huo, Z.; Lou, H.; Zheng, X. *Catal. Comm.* **2006,** *7,* 827.
36. Moradi, G. R.; Nosrati, S.; Yaripor, F. *Catal. Comm.* **2007,** *8,* 598.
37. Sun, K.; Lu, W.; Qiu, F.; Liu, S.; Xu, X. *Appl. Catal. A* **2003,** *252,* 243.
38. Klerk, A. D. to Sasol Tech (PTY). WO Patent 2008,144,782, 2008.
39. Berge, J. v.; Loosdrecht, J. v. d.; Barradas, S. to Sasol Tech (PTY). WO Patent 2003,012,008, 2007.
40. Krumpelt, M.; Krause, T. R.; Carter, J. D.; Kopasz, J. P.; Ahmed, S. *Catal. Today* **2002,** *77,* 3.
41. Spath, P. L.; Dayton, D. C. *Preliminary Screening - Technical and Economic Assessment of Synthesis Gas to Fuels and Chemicals with Emphasis on the Potential for Biomass-Derived Syngas;* Technical report; National Renewable Energy Laboratory, 2003.
42. Dry, M. E. The Fischer-Tropsch Process-Commercial aspects. Elsevier: Amsterdam (NL), 1990; p 183.
43. Espinoza, R. L.; Steynberg, A. P.; Jager, P.; Voslao, A. C. *Appl. Catal. A* **1999,** *186,* 13.
44. Schulz, H. *Appl. Catal. A* **1999,** *186,* 3.
45. Bartholomew, C. H. New Trends in CO Activation. Elsevier: Amsterdam (NL), 1991; Vol. 64, p 158.
46. Fuganti, A.; Bellerate, E.; Pedersen, A. S. *Technologies for producing hydrogen;* Risø Energy Report 3rd: Hydrogen for transport; Risø National Laboratory, 2004.
47. Hirschenhofer, J. H.; Stauffer, D. B.; Engleman, R. R.; Klett, M. G. *Fuel Cell Handbook,* 4th ed.; US Department of Energy, FETC, 1998.
48. Song, C. *Catal. Today* **2002,** *77,* 17.
49. http://carid.unife.it/com_online/articolionline/piem/approf1.html.
50. http://www1.eere.energy.gov/hydrogenandfuelcells/fuelcells/fc_types.html.
51. Peña, M. A.; Gómez, J. P.; Fierro, J. L. G. *Appl. Catal. A* **1996,** *144,* 7.
52. Armor, J. N. *Catal. Lett.* **2005,** *101,* 131.
53. Rustrup-Nielsen, J. R. *Catal. Today* **2000,** *63,* 159.
54. Ferreira-Aparicio, P.; Benito, M. J.; Sanz, J. L. *Catal. Rev.* **2005,** *47,* 491.
55. Armor, J. N. *Appl. Catal. A* **1999,** *176,* 159.
56. Aasberg-Petersen, K.; Hansen, J. H. B.; Christensen, T. S.; Dybkjaer, I.; Christensen, P. S.; Nielsen, C. S.; Madsen, S. E. L. W.; Rostrup-Nielsen, J. R. *Appl. Catal. A* **2001,** *221,* 379.
57. Hu, Y. H.; Ruckenstein, E. *Adv. Catal.* **2004,** *48,* 297.
58. Reyniers, M.; Smet, C. R. H. d.; Menon, P. G.; Marin, G. B. *Cattech.* **2002,** *6,* 140.
59. York, A. P. E.; Xiao, T.; Green, M. L. H. *Top. Catal.* **2003,** *22,* 345.
60. Choudhary, V. R.; Rajput, A. M.; Prabhakar, B. *Catal. Lett.* **1992,** *15,* 363.
61. Choudhary, V. R.; Rajput, A. M.; Prabhakar, B. *J. Catal.* **1993,** *139,* 326.
62. Choudhary, V. R.; Rajput, A. M.; Rane, V. H. *Catal. Lett.* **1992,** *16,* 269.
63. Choudhary, V. R.; Rajput, A. M.; Rane, V. H. *J. Phys. Chem.* **1992,** *96,* 8686.
64. Choudhary, V. R.; Sansare, S. D.; Mamman, A. S. *Appl. Catal. A* **1992,** *90,* L1.
65. Hu, Y. H.; Ruckenstein, E. *Ind. Eng. Chem. Res.* **1998,** *37,* 2333.
66. Basile, F.; Fornasari, G.; Trifiro, F.; Vaccari, A. *Catal. Today* **2001,** *64,* 21.
67. Gavalas, G. R.; Phichitcul, C.; Voecks, G. E. *J. Catal.* **1984,** *88,* 54.

2 THE WATER-GAS SHIFT (WGS) REACTION

2.1 REACTION

The **water-gas shift (WGS) reaction** is a catalytic process to convert CO and to obtain additional H_2 by reaction with steam (reaction 2.1) (***1***). This reaction is an important H_2 source that, in the classic unit of ammonia production, improves H_2 production of 20 % (***2***). Moreover, CO concentration is reduced to less than 0.3 % before that CO_2 is removed and the process gas is sent to the methanation unit (***1***).

$$CO + H_2O \leftrightarrows CO_2 + H_2 \qquad \Delta H^0_{298} = -41.2\ kJ\ mol^{-1} \qquad \text{reaction 2.1}$$

2.1.1 THERMODYNAMIC

The WGS reaction is moderately exothermic (ΔH^0_{298} = - 41.2 kJ/mol) and hence high conversions are favoured by low temperature (Fig. 2.1) (***1***). From the thermodynamic properties and relations, the equilibrium constant for the shift reaction can be derived in a conventional way (equation a) (***3***). However, a simpler equation for K_{eq} has been proposed by Moe (equation b) (***4***). The position of equilibrium is virtually unaffected by pressure in the industrial conditions (P = 0.1 – 5.0 MPa), being an equimolar reaction (***5***).

$$\ln K_{eq} = \frac{5693.5}{T} + 1.0077 \ln T + 5.44 \times 10^{-4} T - 1.125 \times 10^{-7} T^2 - \frac{49170}{T^2} - 13.148 \qquad \text{(a)}$$

$$K_{eq} = exp\left(\frac{4577.8}{T} - 4.33\right) \qquad \text{(b)}$$

where $K_{eq} \cong \frac{P_{CO_2} P_{H_2}}{P_{H_2O} P_{CO}}$ and T (K) temperature.

As expected, additions of greater than stoichiometric quantities of steam improve conversion. Under adiabatic conditions, conversion in a single bed of catalyst is thermodynamically limited due to the heat of reaction that increases the operating temperature and restricts the possible conversion (***1***). The thermodynamic equilibrium limitations can be reduced by using more beds, with an external inter-bed cooling and removal of CO_2 steps between the catalyst beds (***1***) (***2***). A significant improvement in the CO conversion may be obtained by a two-bed operation (Fig. 2.2)

(***1***): a first bed of chromia-supported iron-based catalyst that operates at high inlet temperature (370-400 °C), known as *high temperature shift (HTS) catalyst*, to achieve an exit CO level of 2-4 %; a second bed operating at lowest possible inlet temperature (about 200 °C), by using a copper-based catalyst, known as *low temperature shift (LTS) catalyst*, sufficiently active to have exit CO concentrations as low as 0.1-0.3 %. These shift catalysts are in oxide shape and the reduction is the first operation to use them. This operation is carried out by using the reforming gases (***2***).

The final CO removal stage was generally an absorption in copper liquor (***1***), i.e. an aqueous solution containing Cu^{II} and Cu^{I} compounds of an organic acid salt, such as formate or acetate, in the presence of an ammonia excess. Under these conditions a weak and reversible Cu^{I}-CO complex is formed.

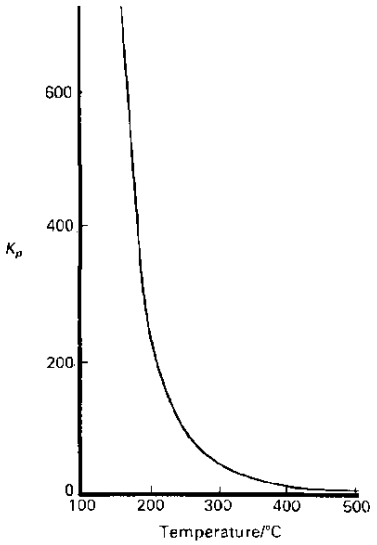

Fig. 2.1 Equilibrium constant (Kp) as a function of the temperature for the WGS reaction (***1***).

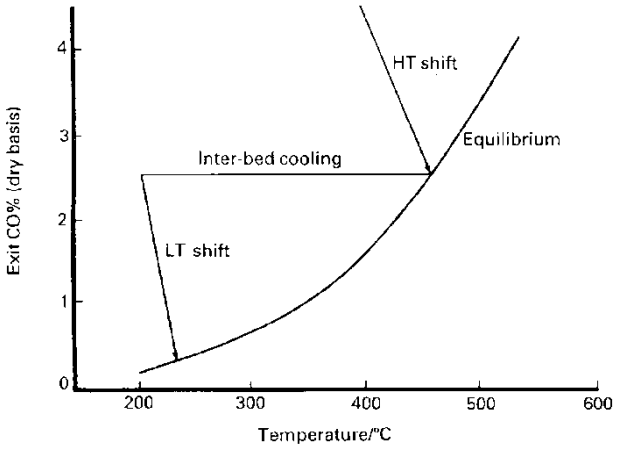

Fig. 2.2 Typical variations of CO levels in HTS and LTS catalyst beds (***1***).

Equilibrium composition at a certain temperature is not affect by pressure until 4.5 MPa, even if the gas contact time is directly proportional to the pressure. Reaction rate is also dependent by

gas diffusion rates over the catalyst surface. At usual pressures (30-45 atm), diffusion rates are notably weaker of the rates observed at the atmospheric pressure (***5***).

For a HTS catalyst (Fig. 2.3) (***5***), the apparent activity at 2.2 MPa is four times that at the atmospheric pressure. After 2.0-2.5 MPa the apparent activity does not change, meaning that, in economical terms, the installation price becomes more expensive at pressures higher than these ones (***5***). For a LTS catalyst (Fig. 2.3 line II), the apparent activity increase proportionally to the pressure, until about 30 atm (***5***).

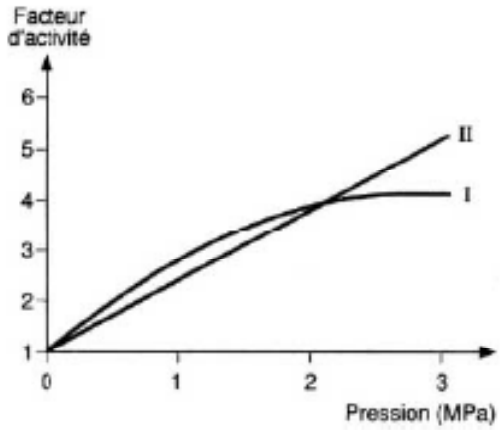

Fig. 2.3 Evolution of apparent activity for HTS (line I) and LTS (line II) catalysts (***5***).

2.1.2 INDUSTRIAL REACTORS

The most simple reactor is the adiabatic reactor with axial continuous flow and a single bed of catalyst based on a grid (***5***). On the other hand, more beds can be disposed in the same reactor, for example trying to minimized the strengths over the grid. For example, industrially there are employed (***5***):

- HTS converters (Fig. 2.4.a) containing subsequently:
  - a catalyst doped (Cu, Rh, V, etc.) to limit side-reactions produced by high CO amount;
  - a classic HTS catalyst (Fe/Cr);
- LTS converters (Fig. 2.4.b) containing subsequently:
  - a guard catalyst to adsorb poisons, such as sulphur and chlorine and to resist to the hydration;
  - a classic LTS catalyst (Cu/Zn/Al) active also at relatively high temperature;
  - eventually, a third catalyst changed less frequently.

The gas conversion obtained by natural gas or light naphtha reforming is enough to dispose subsequently two reactors, a HTS unit and a LTS unit, with thermal exchangers to decrease the temperature between two converters (Fig. 1.5) (***5***). A two-stage WGS reactor with HTS (T = 400 °C) and a LTS stage (T = 280-310 °C) may reduce outlet CO concentration to less than 1 % (***6***).

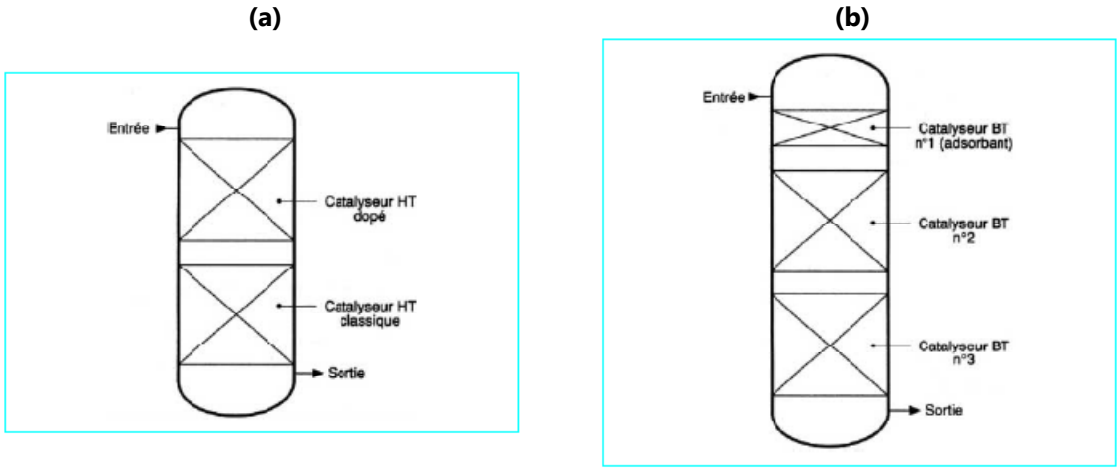

Fig. 2.4 Adiabatic HTS (a) and LTS (b) converters (***5***).

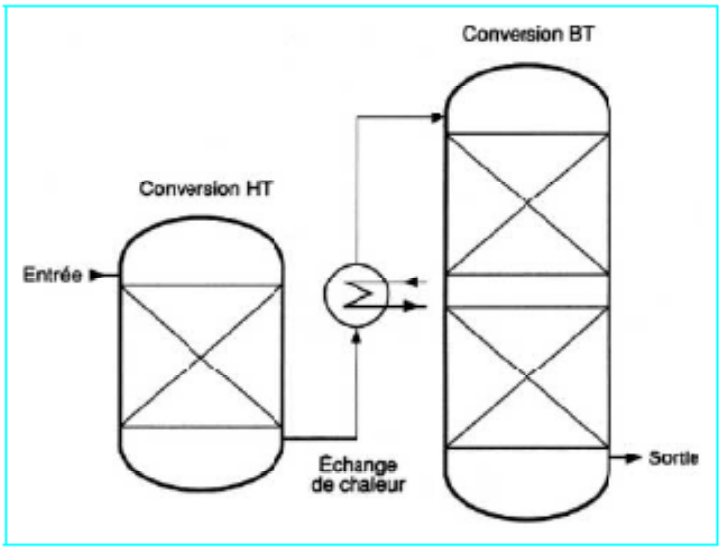

Fig. 2.5 Reactor for gas conversion obtained from natural gas or light naphtha reforming (***5***).

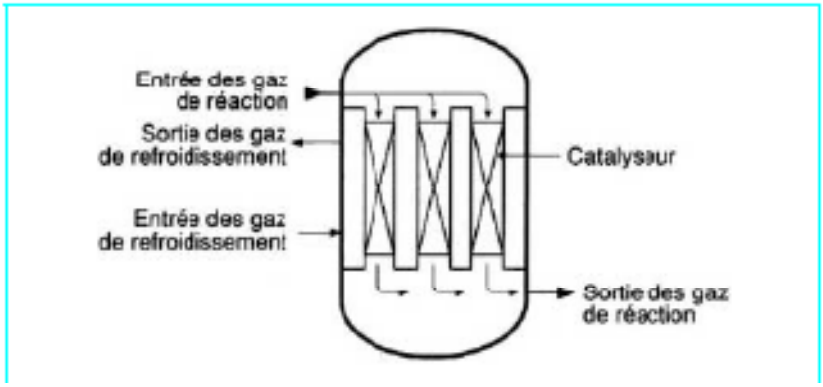

Fig. 2.6 Isothermal reactor (***5***).

A new practice, industrially applied, use an HTS converter with exchanger drowned in the catalyst bed, with an almost isothermal process (Fig. 2.6) (***5***). Pasel *et al.* (***6***) showed a clear advantage of the isothermal operation of WGS reactor over adiabatic mode with the thermodynamic equilibrium reached at lower temperatures (T = 300-310 °C).

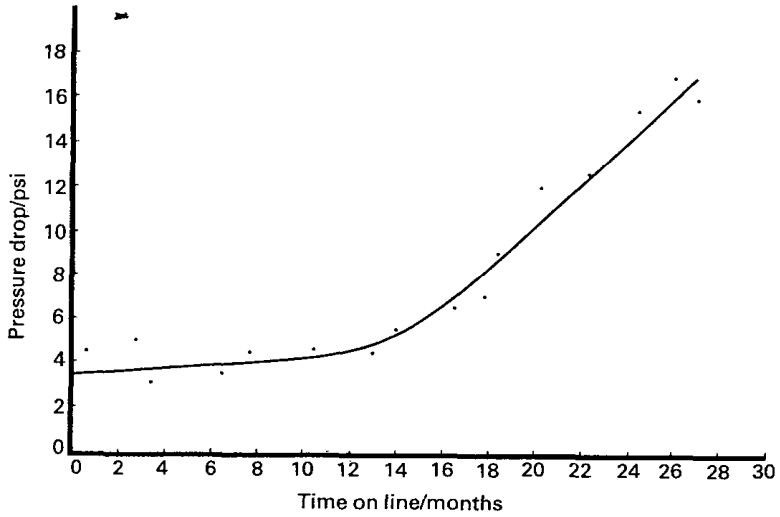

Fig. 2.7 Increase in pressure drop in the HTS converter as a result of a stem leak (***1***).

2.1.3 DIFFUSIONAL EFFECTS AND PELLET SIZE

Good pellet strength is essential to achieve long operating life-time for HTS catalyst (***7***). After the reduction step, the catalyst strength is often inadequate, leading to crushing of the pellets with the formation of fines, which give rise to an unacceptable pressure drop (***4***).

In absence of any mass-transfer limitations on the reaction rate, catalyst activity per unit volume of catalyst bed is directly related to pellet density, although, in the case of HTS catalyst a pore-diffusion limitation becomes significant above 350 °C (***7***). When a reaction is highly pore-diffusion limited, only the outer surface of the catalyst pellet is used by the reactants (***7***). Therefore, it is clear that an advantage from the activity point of view is to use the smaller-sized pellets, which means smaller bed and hence smaller converter. Catalyst volume decreases as the pressure increases. Catalyst strength is also affected by the pellet size that can influence the catalyst life (***7***). Large pellets can withstand bad operation better than smaller ones but, if adequate strength and resistance to attrition may be maintained, there are benefits in using smaller pellets in pore-diffusion limited reactions.

The size and shape of pellets affect the pressure drop which is high for low-pressure operation and becomes less important above about 1.0 MPa (***7***). A cause of pressure drop may be a mechanical failure in the heat exchangers (Fig. 2.7). Hence, condensate or steam leaks go into the

process stream and impinge on the catalyst. This may lead to break-up of the pellets as well as to carry-over of scale which is deposited on the top of the HTS bed.

The shift reaction rate on commercial LTS catalysts is at the borderline, being pore diffusion limited (***1***). Enhanced performances in terms of activity may be achieved using smaller pellets, but practical limits are set by the balance between activity gained and physical properties, such as strength and pressure drop, and manufacturing cost (***1***). It is clear that the poisoning reactions with HCl and H_2S are more strongly diffusion limited than the shift reaction, hence, they are more sensitive to pellet size (***1***). Theoretically, the simplest way to improve the relative poison resistance is to decrease the pellet size (***8***).

2.1.4 REACTION KINETICS

2.1.4.1 MECHANISMS

The mechanism of the WGS reaction has been widely studied, but there are some doubts on the real mechanism occurring in the WGS conditions. Although the reaction appears simple, the catalysts are susceptible to small changes in operating conditions and this complicates the study of this process (***9***). The kinetics of the WGS reaction catalysed by a solid phase has been described in the literature by two main types of mechanisms (***9***), namely *"regenerative (redox) mechanism"* (reactions (a) and (b)) and *"associative (Langmuir-Hinshelwood) mechanism"* (reaction (c)). The WGS reaction involves the H_2O dissociation, that may occur on the metal, the support or both. Similarly, the CO may react with the O-containing species (H_2O, OH or O) of the gas phase, the adsorbed state or the surface lattice.

$$H_2O + [\,]\text{—}Cat \rightarrow H_2 + O\text{—}Cat \qquad (a)$$

$$CO + O\text{—}Cat \rightarrow CO_2 + [\,]\text{—}Cat \qquad (b)$$

where *[ ]—Cat*: reduced site; *O—Cat*: oxidized site.

$$H_2O + CO \rightarrow CO_{(ads)} + H_2O_{(ads)} \rightarrow [int^*] \rightarrow CO_{2(ads)} + H_{2(ads)} \rightarrow CO_2 + H_2 \qquad (c)$$

Both mechanisms have their supporters and, unfortunately, the kinetics of the WGS reaction can well be described by both mechanisms. Even if the redox mechanism is accepted for the HTS catalysts, there is considerable uncertainty about the operative mechanism at low temperatures, over the Cu-based catalysts (***9***). It is possible that both reaction mechanisms occur and that the relative rates of the two pathways are influenced by the experimental conditions.

2.1.4.1.1 REGENERATIVE "REDOX" MECHANISM

The *regenerative* or *"redox" mechanism* consists initially in the H_2O adsorption and dissociation on reduced sites of the catalyst surface to obtain H_2 while oxidizing a site (oxygen atoms adsorbed on the surface) and, after, in the oxidation of CO to CO_2 on this oxidized sites (Table 2.1) (***10***,***11***,***12***). The rate-determining step is dependent, critically, on the composition of the feed gas mixture (***11***): the step 3 is the rate limiting one for a gas with a low S/CO ratio, whereas the step 6 is rate limiting in opposite conditions. In addition, the step 5 is significant in a mixture of CO_2 and H_2.

This model was tested against measurements at 0.1 MPa for an industrial catalyst ($Cu/ZnO/Fe_2O_3$) by Van Herwijnen and de Jong (***13***), showing a good agreement with it (***14***). Physical and chemical measurements showed that catalyst exposed almost exclusively nano-crystallites of Cu(111) facets.

1.	$CO_{(g)} + *$	⇆	$CO*$
2.	$H_2O_{(g)} + *$	⇆	H_2O*
3.	$H_2O* + *$	⇆	$HO* + H*$
4.	$2HO*$	⇆	$H_2O* + O*$
5.	$HO* + *$	⇆	$H* + O*$
6.	$CO* + O*$	⇆	$CO_2* + *$
7.	CO_2*	⇆	$CO_{2(g)} + *$
8.	$2H*$	⇆	$H_{2(g)} + 2*$

(* = adsorption site)

Table 2.1 Steps of the redox mechanism (***11***).

However, when this model was tested under higher pressures, deviation between the calculated and experimental rates appeared (***14***). A redox process is significant at the beginning of the transient reaction period on the activated catalyst, but the main reaction path probably consists in the followin steps: rapid CO and H_2O adsorption, slow H_2O inter-conversion, surface intermediate build-up and decomposition and, finally, H_2 desorption (***15***). So, it is necessary to include the synthesis and hydrogenation of formates to describe the kinetics of the WGSR in industrial conditions (reaction steps 9–11 below) (***14***). The reaction step 9 is in equilibrium under the industrial conditions (high pressure) and step 10 is the possible low step. The formates may be present on the surface, but they are not a species in the catalytic cycle for CO conversion to CO_2 and its effect is mainly to block the active sites (***14***).

9.	$CO_2* + H*$	⇆	$HCOO* + *$
10.	$HCOO* + H*$	⇆	$H_2COO* + *$
11.	$H_2COO* + 4H*$	⇆	$CH_3OH_{(g)} + H_2O_{(g)} + 5*$

This model was further optimized by establishing that the adsorption energies for CO and oxygen (the latter arising from H_2O) may describe the changes in the remaining activation and

adsorption energies through linear correlations (***13***). The model also predicts that the Cu activity may be improved by increasing the strength with which CO and oxygen are bound to the surface, thus suggesting possible directions to improve the LTS catalyst.

2.1.4.1.2 ASSOCIATIVE "LANGMUIR-HINSHELWOOD" MECHANISM

In the *associative (L-H) mechanism*, CO and H_2O adsorb on the catalyst surface and form an intermediate which results in H_2 and CO_2 desorption (Table 2.2). Here, it is a formate intermediate (HCOO∗) formed by the reaction of an adsorbed CO with an adsorbed OH group, but it could be a different one (***16***). The first and most important energy barrier is for the dissociation of H_2O into adsorbed OH and H (step 3). Then, the reaction of OH and CO produces an HCOO (carboxyl or formate species) whose decomposition into CO_2 gas and adsorbed H, which eventually yields the H_2, has the final important energy barrier (***16***,***17***).

1.	$CO_{(g)} + *$	⇆	$CO*$
2.	$H_2O_{(g)} + *$	⇆	H_2O*
3.	$H_2O* + *$	⇆	$HO* + H*$
4.	$HO* + CO*$	⇆	$HCOO*$
5.	$HCOO* + *$	⇆	$H* + CO_2*$
6.	$HCOO* + HO*$	⇆	$CO_2* + H_2O*$
7.	CO_2*	⇆	$CO_{2(g)} + *$
8.	$2H*$	⇆	$H_{2(g)} + 2*$

(∗ = adsorption site)

Table 2.2 Steps of the associative mechanism (***16***).

Van Herwijnen and de Jong (***13***) proposed that surface formate decomposition is the rate-determining step in the WGS reaction on Cu-based catalysts, but the formate decomposition step cannot alone control the shift dynamics on the present catalyst. Campbell (***18***) concluded that on a pure Cu(111) surface the H_2O decomposition step is slow even if it is assumed that the reaction proceeds through surface formates. Several research groups provided consistent spectroscopic information to support a formate mechanism, but the most comprehensive works have been undertaken by Jacobs (***19***,***20***,***21***,***22***,***23***). The key points are as follows:

- IR evidences of the C–H bond formation during the O–H bonds breakage (also replacing H_2O with D_2O or by adsorption of DCOOH and HCOOH), showing that breaking of the D–H or C–H bond is rate-determining as expected for a formate-based mechanism;
- presence of bands consistent with the existence of a formate;
- rapid decomposition of formate species *via* a surface intermediate (unidentate carbonate) due to H_2O addition.

The mechanism involving long-life surface intermediates, like formates or carbonates/carboxylates, is valid only below 350 °C (***19***,***20***). Shido and Iwasawa (***24***,***25***) confirmed

that the WGS reaction on ZnO catalytically proceeds through bidentate formates and unidentate carbonates, as shown in the subsequent scheme (Fig. 2.8). On-top (terminal) hydroxyl groups on Zn ions, which are formed by the first-adsorbed H_2O molecule, react with CO to produce bidentate and bridge formates. The formates are converted to the WGSR products with a second-adsorbed H_2O molecule. In absence of H_2O vapour, adsorbed, CO_2 species exist as unidentate carbonate and carboxylate on ZnO surface. H_2O molecules not only act as a reactant to form the formate, but also active the bidentate formate$_{(ad)}$ to decompose to H_2 and unidentate carbonate$_{(ad)}$ and promote the desorption of the carbonate as CO_2. Therefore, the WGS reaction is an example of a surface catalytic reaction that is assisted by gas phase molecules (***25***,***24***). The behaviour of surface formate intermediates (HCOO) is affected by weakly co-adsorbed H_2O. The decomposition is kinetically controlled, where the steam induces the dehydrogenation path of the surface formates to form CO_2 and H_2.

However, other researchers (***26***) stated that ZnO addition to the industrial catalyst does not modify the rate per unit of surface area of Cu, suggesting that it does not promote the reaction rate.

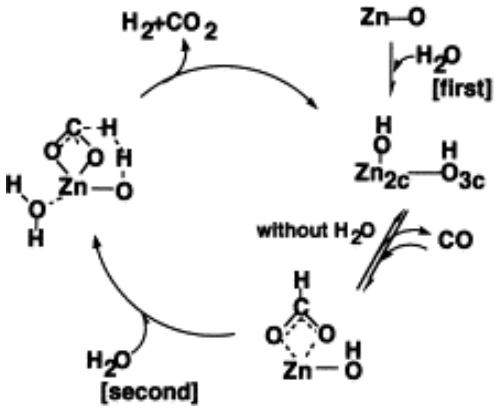

Fig. 2.8 WGS reaction promoted by weakly adsorbed H_2O on ZnO (***24***).

Surface carboxylic species had been observed by spectroscopic techniques on LTS catalysts (***27***,***28***) and considered important, reactive intermediates, which play a central role in the WGSR (***16***,***29***,***30***). DRIFTS analyses combined with the utilization of isotopic tracers had also shown that formates were less reactive than carbonyl and carbonate species under steady state conditions, whereas the reverse trend was observed during the non-steady state, desorption experiments (***31***). On the other hand, Gokhale *et al.* (***16***) suggested that, although it is possible to form the carboxyl group (COOH) in a single, elementary reaction step, it is not possible to form the formate (HCOO) intermediate. Indeed, OH binds to the surface through its O atom and CO through its C atom, whereas the formate binds through its two O atoms, not by its C atom. Therefore, two O atoms of the formate bind to the surface forming a bidentate species, either sequentially (via unidentate formate) or, less likely, simultaneously. Instead, their calculations showed that the formate (HCOO) synthesis by reacting CO_2 with atomic H is the easiest way. Differently, other researchers (***32***) proposed an Eley-Rideal mechanism for the synthesis of formates on the Cu(111), in which a CO_2 molecule directly inserts into a C–H bonds.

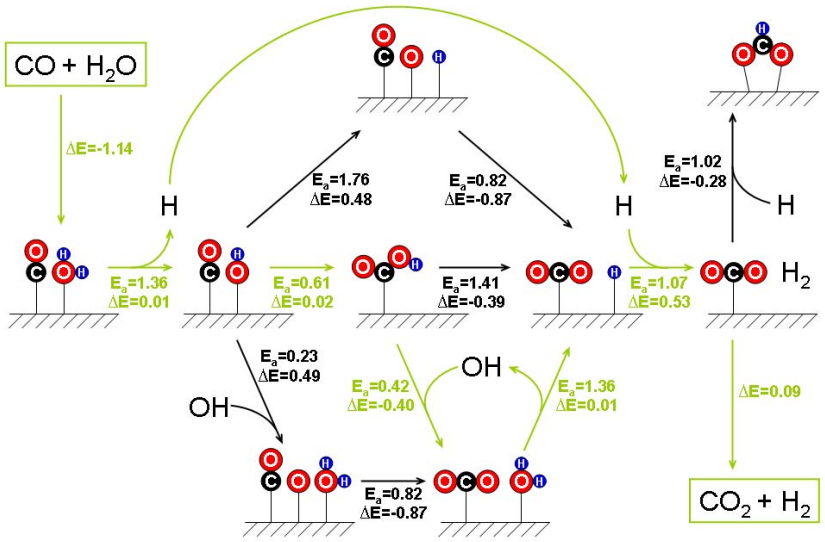

Fig. 2.9 Reaction scheme including both the redox and the associative (carboxyl) mechanism (steps in eV). Minimum energy pathway for the WGS reaction is highlighted with green [analogously to (***16***)].

				E_f	E_r	E_a
1.	$CO_{(g)}$ + *	→	CO*	0	0.51	0.51
2.	H_2 + 2*	→	2H*	0.54	1.07	0.50
3.	$H_2O_{(g)}$ + *	→	H_2O*	0	0.18	0.18
4.	$CO_{2(g)}$ + *	→	CO_2*	0	0.09	0.09
5.	H_2O* + *	→	HO* + H*	1.36	1.35	1.15
6.	HO* + *	→	O* + H*	1.76	1.28	1.19
7.	2HO*	→	O* + H_2O*	0.60	0	0
8.	CO* + O*	→	CO_2* + *	0.82	1.69	0.79
9.	HO* + CO*	→	cis-COOH* + *	0.61	0.59	0.55
10.	*cis*-COOH*	→	*trans*-COOH*	0.52	0.75	0.48
11.	HCOO* + *	→	H* + CO_2*	1.41	1.80	1.18
12.	HCOO* + HO*	→	CO_2* + H_2O*	0.42	0.82	0.38
13.	CO_2* + H*	→	HCOO* + *	1.02	0.74	0.54
14.	HCOO* + *	→	HCOO**	0.10	0.55	0.04
15.	CO_2* + H_2O* +*	→	HCOO** + HO*	1.69	1.83	1.61
16.	CO_2* + HO*	→	HCOO** + O*	2.02	1.75	1.71

Table 2.3 Elementary steps involved in the WGS reaction on Cu(111) Ef and Er represent the forward and reverse activation energy (in eV) with co-adsorbed species at infinite separation from each other (***16***).

Gokhale *et al.* (***16***) developed a mechanistic model of the WGS reaction on Cu(111) in 16 elementary steps (Fig. 2.9 and Table 2.3); in which the step 5 and 9 are rate-controlling under

industrial conditions. In the absence of CO_2 and H_2 in the feed gas mixture, the step 5 has a considerably stronger influence on the overall reaction, while the lowest energy path involves the formation of the carboxyl intermediate (step 9). This barrier is considerably lower than the corresponding barrier for CO∗ oxidation by atomic O∗, suggesting that carboxyl formation is kinetically more accessible, but thermodynamically less favourable than CO_2 formation (***16***). The carboxyl intermediates subsequently decomposed by reaction with OH (step 12); the OH species is regenerated by dissociation of the formed H_2O. When the concentration of the OH groups is limited, the direct decomposition route (step 11) dominates. An excess of H_2O in the feed increases the OH coverage and makes the low energy decomposition path more kinetically accessible, thus enhancing the WGS reaction rate.

Using the DFT-derived parameters as initial estimates for the micro-kinetic model parameters (***16***), they fitted the 16-step model to the experimental WGS reaction rate data published, earlier by Koryabkina *et al.* (***26***), with agreement also by testing the kinetic data of Van Herwijnen and de Jong on a $Cu/ZnO/Al_2O_3$ catalyst (***13***). Based on the good ''fit'' between the calculated and observed data (***16***), they suggested Cu(111) as a dominant active site for the WGS reaction on realistic industrial catalysts. An alternate explanation may be that the WGS reaction on these catalysts is not structure sensitive and, therefore, the reaction rate is comparable on different Cu facets. Finally, to summarize these results on Cu(111) (***23***):

(a) H abstraction from H_2O appears to be the rate-controlling step for the WGS reaction;
(b) carboxyl (COOH) is a very reactive, but short-lived intermediate;
(c) formate (HCOO,) probably formed from CO_2 and H, is a spectator species which tends to block the active sites, and may reach substantial surface coverage, mainly at high pressures. This site-blocking by formates may also explain the observed negative order of the WGS reaction with respect to CO_2.

Addition of bases (alkali ions), which are known to accelerate the formate decomposition, should enhance the WGS reaction rates (***21***) (***22***). An optimal amount of basicity, sufficient to decompose the formates, but not enough to stabilize too much the carbonates, is needed. An improvement in the WGS reaction rate was found by many researchers (***23***,***33***), suggesting that H_2O dissociation was not rate controlling on the alkali-promoted catalysts.

2.1.4.1.3 DOMINANT MECHANISM

The crucial difference between the redox and the associative mechanism is that CO is oxidized to CO_2 by adsorbed O atoms in the conventional redox mechanism, while CO_2 is formed by the decomposition of an intermediate or by the reaction of this last one with a second adsorbed OH group in the associative mechanism (***16***). While there are sufficient experimental evidences to conclude that: (a) formate-like species are present, under WGS reaction conditions, on the surface of Cu/ZnO and precious metal-based; (b) the decomposition of these species leads to the products (CO_2 and H_2), it is not established if CO_2 and H_2 are derived only from the surface formates and, additionally, also from other intermediates, such as carbonates/carboxylates, or by a

completely different mechanism, like the redox mechanism, which does not involve any long-lived and experimentally observable surface intermediate.

Callaghan *et al.* (***34***) extended the study by considering the elementary steps and performing a systematic study to identify the three most dominant pathways on a Cu-based catalysts, namely: the formate, the associative and the modified redox pathways (Table 2.4). The main difference between the last two mechanisms is in the production of adsorbed atomic oxygen and molecular hydrogen (***34***). In the conventional redox mechanism, the dissociation of HO∗ and the production of H_2∗ occur separately (steps 4 and 7). Differently, in the modified redox mechanism, the production of both O∗ and H_2∗ takes place in a single step (step 4). The modified redox mechanism proceeds via a path, that reduces the peaks and valleys encountered in the energy diagram in comparison to the conventional one. It was also shown that adsorbed H_2O does not interact with adsorbed atomic hydrogen or oxygen.

I.	**formate**			**II.**	**associative**		
1.	$CO_{(g)} + *$	⇆	$CO*$	1.	$CO_{(g)} + *$	⇆	$CO*$
2.	$H_2O_{(g)} + *$	⇆	H_2O*	2.	$H_2O_{(g)} + *$	⇆	H_2O*
3.	$H_2O* + *$	⇆	$HO* + H*$	3.	$H_2O* + *$	⇆	$HO* + H*$
4i.	$HO* + CO*$	⇆	$HCOO* + *$	*4.*	$HO* + CO*$	⇆	$CO_2* + H*$
4ii.	$HCOO* + *$	⇆	$H* + CO_2*$				
5.	CO_2*	⇆	$CO_{2(g)} + *$	5.	CO_2*	⇆	$CO_{2(g)} + *$
6.	$2H*$	⇆	$H_2* + *$	6.	$2H*$	⇆	$H_2* + *$
7.	H_2*	⇆	$H_{2(g)} + *$	7.	H_2*	⇆	$H_{2(g)} + *$
III.	**conventional redox**			**IV.**	**modified redox**		
1.	$CO_{(g)} + *$	⇆	$CO*$	1.	$CO_{(g)} + *$	⇆	$CO*$
2.	$H_2O_{(g)} + *$	⇆	H_2O*	2.	$H_2O_{(g)} + *$	⇆	H_2O*
3.	$H_2O* + *$	⇆	$HO* + H*$	3.	$H_2O* + *$	⇆	$HO* + H*$
4.	$HO* + *$	⇆	$H* + O*$	*4.*	$HO* + H*$	⇆	$H_2* + O*$
5.	$CO* + O*$	⇆	$CO_2* + *$	5.	$CO* + O*$	⇆	$CO_2* + *$
6.	CO_2*	⇆	$CO_{2(g)} + *$	6.	CO_2*	⇆	$CO_{2(g)} + *$
7i.	$2H*$	⇆	$H_2* + *$	*7.*	H_2*	⇆	$H_{2(g)} + 2*$
7ii.	H_2*	⇆	$H_{2(g)} + *$				

Table 2.4 Different mechanisms dominant for the WGS reaction on Cu(111) (***34***).

While the redox mechanism is well-established at high temperatures in the case of the HTS catalysts, its applicability to LTS over Cu/ZnO catalysts is uncertain and depends on confirmation of the ability of H_2O to re-oxidize the partially-reduced supported oxide at temperatures below 250 °C, especially in the presence of significant amounts of H_2, as is the case for fuel cell applications (***35***).

Concerning the discussion on the active sites and the reaction mechanism, are noteworthy two important claims of the landmark postulate by Taylor (***36***) on active sites over solid catalysts:

i. particular atoms or groups of atoms on the surface of solids are the active sites responsible for the catalytic activity and selectivity in the present context;
ii. the identity and concentration of the active sites on a catalyst are dependent, not only on the procedures adopted during its preparation, but also on the particular reaction conditions, i.e., the relative reactant concentration, the temperature, the pressure etc.

If these conditions change, the identity and concentration of the active sites also change and, consequently, the path of the reaction mechanism will be different in relation to the particular reaction conditions.

Depending on the raw material (natural gas or coal) or the reforming process used to generate the syngas, the inlet CO concentration changes. Depending on the reformer (SR, POX or ATR) used before the WGS unit, the H_2O and/or CO_2 concentration changes; hence, it is normal to expect that the different concentrations of the inlet mixture influences the nature and, especially, the concentration of chemical species present on the catalyst surface (OH groups, H atoms, anion vacancies etc.). Therefore, it should not be surprising that different mechanisms can be predominant on the same catalyst under different reactant concentration, temperature and pressure, especially in the WGS reaction that is equilibrium-limited at high temperature and kinetically limited at low temperature.

The dominant mechanism depends on the reaction conditions, specifically the temperature and H_2O concentration. It may change from a redox-type process to one dominated by surface intermediate species, including formates, carbonates or carboxylates. It is possible to hypothesize three situations in the reaction mechanism (***35***,***32***,***37***,***38***):

1. at low temperature, especially in presence of a substantial amount of CO_2 (very low S/CO_2 ratio), the carbonate decomposition is the rate-determining step and, hence, the Eley-Rideal processes is less favoured;
2. at intermediate temperature, especially in presence of a large concentration of H_2O (high S/CO_2 ratio), the formate decomposition step is slow and rate-determining;
3. at high temperature, where desorption and/or decomposition of intermediates is very fast, the redox processes is expected to be important to determine the rate of the reaction, mainly in the presence of a high concentration of H_2O (intermediate S/CO_2 ratio), when the surface is covered to a significant extent by OH groups.

Ovesen *et al.* (***14***) had analysed the micro-kinetics of the WGS reaction, on the basis of a previous own study (***12***), considering the surface redox mechanism under industrial conditions and the Cu-based catalyst,; the following conclusions have been achieved:

- at low pressure (0.1 MPa), hydrogen and hydroxide are the dominating intermediates;
- at high pressure (2.0 MPa), hydrogen and formates are the dominating intermediates.

It is interesting to remark that formate coverage increases dramatically with the pressure increase, which has also an immediate consequence for the activation enthalpy (***16***). Differently, the carboxyl intermediates have extremely low coverage at all pressures, implying that they are very reactive intermediates, which might be difficult to identify by spectroscopy. An increase of pressure has practically no effect on CO and H_2O reaction orders (***14***) (***16***). The negative CO_2 and H_2 reaction orders suggest that WGS reaction is inhibited by its products, because progressively more formates are formed on the surface,, blocking the more active sites.

To summarize, it is difficult to determine the mechanism from an empirical kinetic expression alone. Many researchers have used micro-kinetic models, based on the knowledge of elementary steps and their energies. These theoretical approaches enable to deduce reaction orders, activation enthalpies and surface coverages for a given set of elementary steps. For this reason, the applicability of the micro-kinetic models is not restricted to a particular set of parameters, but may be used under various conditions (***14***). In particular, this is important in processes involving very large changes of concentration. Therefore, the advantage of a micro-kinetic model is to explore the chemistry of a given reaction, whereas the advantage of an empirical kinetic model is to provide a very accurate description of the reaction rate, which is essential in reactor design calculations.

Finally, it is possible to conclude that the presence of adsorbed intermediates, like formates, carbonates or carboxylates, is very likely in the MTS conditions (medium temperature, high pressure and Cu-based catalyst).

2.1.4.2 RATE EXPRESSIONS

Different mechanisms, various elementary reaction paths, different rate determining steps and assumptions on the nature of the catalyst active sites create numerous rate expressions (***39***).

For the redox mechanism, some research groups (***40***) derived the equation (c) and reported the validity of this rate expression based on the oxidation–reduction mechanism. Another rate expression (equation (d)) can be derived from the redox mechanism when a single path reaction model is assumed (***41***).

From the adsorptive mechanism, Langmuir–Hinshelwood type rate expressions (equation (e) can be derived. The rate expression is derived from Yang–Hougen Table (***42***) when the surface reaction is assumed to be the rate controlling. This rate expression has been tested using plant and laboratory data by several authors (***43***,***44***) who reported that only the Langmuir–Hinshelwood model can accommodate all the experimental data.

In contrast to those rate expressions derived from detailed reactions, mechanisms and rate determining steps, there is also simple empirical rate expressions (equations (f) and (g)) which do not consider any mechanism. Moe (***4***) used a simple reversible rate expression for carbon monoxide conversion.

Redox

$$r_{CO} = k\frac{P_{CO}P_{H_2O} - P_{CO_2}P_{H_2}/K_p}{P_{CO} + AP_{H_2O}} \quad (c)$$

$$r_{CO} = k\frac{k_1k_2\left(P_{CO}P_{H_2O} - P_{CO_2}P_{H_2}/K_p\right)}{k_1P_{CO} + k_2P_{H_2O} + \left(k_{-1} + k_{-2}\right)P_{CO_2}} \quad (d)$$

Langmuir-Hinshelwood

$$r_{CO} = k\frac{P_{CO}P_{H_2O} - P_{CO_2}P_{H_2}/K_p}{\left(1 + K_{CO}P_{CO} + K_{H_2O}P_{H_2O} + K_{H_2}P_{H_2} + K_{CO_2}P_{CO_2}\right)^2} \quad (e)$$

Power-law

$$r_{CO} = k\left(P_{CO}P_{H_2O} - P_{CO_2}P_{H_2}/K_p\right) = kP_{CO}P_{H_2O}\left(1-\beta\right) \quad (f)$$

$$r_{CO} = kP_{CO}^aP_{H_2O}^bP_{H_2}^cP_{CO_2}^d\left(1-\beta\right) \quad (g)$$

where $\beta = P_{CO_2}P_{H_2}/P_{CO}P_{H_2O}K_p$

Nomenclature

r_{CO}	reaction rate of CO (mol g_{cat}^{-1} h^{-1})	K_{H2O}	adsorption equilibrium constants for H_2O
A	constant	K_{CO}	adsorption equilibrium constants for CO
k	rate constant for the WGSR	K_{CO2}	adsorption equilibrium constants for CO_2
	(mol g_{cat}^{-1} h^{-1} atm^{-2})	K_{H2}	adsorption equilibrium constants for H_2
k_1	rate constant of CO adsorption	P_{CO}	partial pressure of CO (atm)
k_2	rate constant of H_2O adsorption	P_{CO2}	partial pressure of CO_2 (atm)
k_{-1},k_{-2}	rate constant of the reversible	P_{H2}	partial pressure of H_2 (atm)
	shift reaction	P_{H2O}	partial pressure of H_2O (atm)
K_p	equilibrium constant of WGSR	β	factor of reversible reaction

Table 2.5 Model kinetic equations for the WGS reaction **(***39***)**.

In many works (***3***,***43***,***44***,***45***,***46***,***47***,***48***,***10***), the authors used different equations with different apparent activation energies (E_a), adsorption heats (ΔH_i) and pre-exponential factors (A_j); their values were obtained by fitting all the available experimental data.

The Arrhenius equation was used to describe the variation of the rate constant with the temperature and the adsorption equilibrium constants were defined by the van't Hoff equation (***42***,***49***):

$$K_{j,a} = A_j \exp\left(-\Delta H^0_{j,a}/RT\right)$$

where $A_j = \exp\left(\Delta S^0_{j,a}/R\right)$.

The pre-exponential factor (A_j) has to satisfy certain thermodynamic criteria for the mechanisms to be physically meaningful (***50***,***51***); these criteria should be used as constraints for the kinetic study (i) and the adsorption entropy must satisfy the (ii) requirement.

$$\Delta S^0_{j,a} < 0 \quad \text{or} \quad \exp\left(\Delta S^0_{j,a}/R\right) = A_j < 1 \qquad \text{(i)}$$

$$-\Delta S^0_{j,a} < S^0_{j,gas} \qquad \text{(ii)}$$

$S^0_{j,gas}$ (0.1 MPa, 25 °C) values of 198.1, 188.9, 130.8, and 213.9 J/mol·K were found in the literature (***8***) for CO, H_2O, H_2, and CO_2, respectively. Thus, from inequalities (i) and (ii), the following numerical expressions can be formulated:

$$\exp\left(\Delta S^0_{CO,a}/R\right) = A_{CO} > 4.064\times10^{-11}$$

$$\exp\left(\Delta S^0_{H_2O,a}/R\right) = A_{H_2O} > 1.228\times10^{-10}$$

$$\exp\left(\Delta S^0_{H_2,a}/R\right) = A_{H_2} > 1.385\times10^{-7}$$

$$\exp\left(\Delta S^0_{CO_2,a}/R\right) = A_{CO_2} > 6.014\times10^{-12}$$

Ayastuy *et al.* (***49***) identified the Langmuir-Hinshelwood (L-H) rate model (equation 2.15) as the best one describing the kinetics of the low-temperature WGS reaction over commercial $Cu/ZnO/Al_2O_3$ catalyst. This rate equation model had been reported earlier by Amadeo *et al.* (***44***) for the same type of catalyst and similar ranges of operating conditions (T = 180-230 °C and P = 0.2 MPa), as well as by other workers (***52***,***1***) for Fe-based catalysts.

Assuming that the surface reaction was the rate-limiting step, Sun *et al.* (***47***) reduced the number of parameters: reaction orders for CO_2 and H_2O was taken as zero and first order, respectively. The L-H rate expression for this type of surface reaction process (equation (h)) was well documented and postulated only the adsorption of CO and CO_2 (***44***,***47***). The number of fitting parameters or variables had to be minimized before the parameter estimation. To start with a minimal number of fitting parameters, the initial values for the heats of adsorption and their pre-exponential factors for CO and H_2 were obtained from the literature (***47***). Therefore, heat of adsorption and its pre-exponential factors for CO and H_2 were adjusted separately. The differences between the initial and final fitting results were striking (

Parameters	Initial	Final
A **(mol m^{-3} atm^{-2} s^{-1})**	$2x10^7$	$9x10^7$
E **(kJ mol^{-1})**	43	44

A_1 (atm^{-1})	9.4x10^{-11a}	1x10^{-3}
ΔH_1 (kJ mol^{-1})	-100^{a}	−46
A_2 (atm^{-1})	1.1x10^{-10a}	43
ΔH_1 (kJ mol^{-1})	-90^{a}	11

Table 2.6). This approach of isolation of variables minimized the possibility of multiple fitting solutions and greatly improved the accuracy in parameter estimation.

$$r_{CO} = Ae^{-\frac{E}{RT}} \frac{P_{CO}P_{H_2O}}{\left(1 + A_1 e^{-\frac{\Delta H_1}{RT}} P_{CO}\right)\left(1 + A_2 e^{-\frac{\Delta H_2}{RT}} P_{H_2}\right)} \qquad \text{(h)}$$

Parameters	Initial	Final
A (mol m^{-3} atm^{-2} s^{-1})	2x10^{7}	9x10^{7}
E (kJ mol^{-1})	43	44
A_1 (atm^{-1})	9.4x10^{-11a}	1x10^{-3}
ΔH_1 (kJ mol^{-1})	-100^{a}	−46
A_2 (atm^{-1})	1.1x10^{-10a}	43
ΔH_1 (kJ mol^{-1})	-90^{a}	11

Table 2.6 Initial and final parameters fitting results for the L-H rate law; (a) literature data (***47***).

For the redox rate expression (equation (2.16), where r_{CO} is given in s^{-1}, de Molliens (***5***) calculated the values of activity constant (A) and rate constant (k) in T(K) function:

$A = 2.5 \times 10^{9} \exp(-90/RT)$

$k = 6.0 \times 10^{11} \exp(E/RT)$ [s^{-1} atm^{-1}]

where: E=112.2 kJ mol^{-1} and R=8.314 J mol^{-1} K^{-1}.

parameter	mean	standard deviation	95% confidence level interval	|t value|
b	0.53	0.02	±0.03	16.18
c	−0.51	0.03	±0.06	8.69
d	−0.26	0.01	±0.03	8.22
$\ln A_0$	20.32	0.35	±0.71	28.70
E_a (kJ/mol)	81.3	13.6	±2.7	29.88

Table 2.7 Calculated values and squared sum of residuals for the WGS reaction rate models checked by Integral analysis, assuming a = 1 (***49***).

The experimental data were also fitted using the empirical power-law rate (equation 2.18). The reaction orders for all of the reactants and products were quite different from those previously reported by other authors (***14***,***15***,***44***,***49***) over ternary Cu-based catalyst. The results revealed that the sensitivity of the reaction rate to H_2O pressure must be higher than that to CO, as reported by Ayastuy *et al.* (***49***). In the case of the reaction products (***49***), the data reveal that the reaction rate is more sensitive to the H_2 partial pressure than to the CO_2 partial pressure, in agreement with the literature (***14***,***15***). As the CO reaction order is close to 1 over $CuO/ZnO/Al_2O_3$ catalysts, a fitting with this reaction order was also carried out (***14***,***15***,***49***); the parameters calculated with this assumption are listed in Table 2.7.

Other researchers (***48***) reported that the WGS reaction is not a simple order reaction, especially at higher S/C ratios, and determined this rate equation and proper exponent parameter for the high temperatures.

$$r_{CO} = kP_{CO}^{n}P_{H_2O}^{m}\left(1-\beta\right)$$

where $k=k_0 \exp(-E/RT)$

ln k_0=26.1	E=95.0 kJ/mol	n=1.1	m=0.53

The most popular kinetics expression used in the design of the industrial HTS reactor (equation (i)) is that proposed by Moe (***4***,***44***,***53***), which is also given in moles per gram per minutes. This is an empirical expression and no mechanism may be inferred from it. This expression was obtained at atmospheric pressure.

$$r = 1.85\times10^{-5}\exp\left(12.88-\frac{1855.5}{T}\right)p_{CO}\,p_{H_2O}\left(1-\beta\right) \qquad \text{(i)}$$

The MTS is not discussed in the literature, therefore, report rate expressions obtained on LTS catalyst could be valid for a temperature range smaller than the MTS. In addition, they are generally determined at low pressure (0.1 to 0.3 MPa) and supposed without any diffusion limitation.

2.1.4.2.1 PRESSURE EFFECTS

The equilibrium CO concentration is virtually unaffected by the system pressure, that have, however, an impact on the system kinetics due to pore diffusion limitations and partial pressure effects of the reactants. Higher pressures improve overall CO conversion in kinetically-limited applications; however, there is very few information in the literature about the dependency of the WGS reaction on the pressure and some contradictions may be found.

Some authors (***14***,***49***,***54***) introduced a "fudge factor" correcting for the total pressure changes, but this is only necessary in experiments carried out at elevated pressures. The effect of this variable may be considered through the factor (ψ) proposed by Rase (***53***), that also includes the diffusion effects. Therefore the reaction rate expression is given by:

$$\left(-r_{CO}\right)_P = \Psi\left(-r_{CO}\right)_{P\approx 1}$$

where: $\Psi = 0.86 + 0.14P$ for P < 2.48 MPa

On the other hand, Ovesen *et al.* (***14***) corrected a power law, by including a term P_{Total}^{γ} (with γ < 0 and P < 2.0 MPa):

$$r_{CO} = k\ P_{CO}^{a}\ P_{H_2O}^{b}\ P_{CO_2}^{c}\ P_{H_2}^{d}\ P_{Total}^{\gamma}\left(1 - \frac{P_{CO_2}\ P_{H_2}}{K_{eq}\ P_{CO}\ P_{H_2O}}\right)$$

These two approaches are opposite, considering that in the first claim the kinetics increases with pressure, whereas in the second one the contribution of pressure is negative. These discrepancies may derive from the fact that diffusion limitation is potentially pressure dependent.

2.2 COMMERCIAL CATALYSTS

2.2.1 HIGH-TEMPERATURE SHIFT (HTS) [T_{IN} > 300°C]

The high-temperature shift (HTS) processed are performed at 300-450 °C and the fresh unreduced catalysts contain 90-95% of haematite (Fe_2O_3) stabilized with the addition of a small amount of Cr_2O_3 (***1***). The active phase of the catalyst is generally considered to be a spinel with the magnetite structure (Fe_3O_4, or $Fe^{(II)}O\ Fe^{(III)}{}_2O_3$), with part of the iron replaced by a trivalent modifier ion, such as Cr^{3+} (***55***). Chromium substitution in an iron oxide lattice results in an expansion of the tetrahedral sites and the contraction of the octahedral ones, along with the oxidation of some Fe^{2+} to Fe^{3+}. The resulting octahedral cations become more covalent in nature (***56***,***57***,***58***,***59***,***60***). In the presence of significant partial pressures of steam, migration and/or inclusion of chromium oxide into the iron oxide lattice inhibits crystallite growth (***56***).

Cr^{III} oxide is preferably present in amount of 5-15 wt.% because, at these levels, it advantageously confers increased physical strength to the resulting shaped units (***55***). Various HTS catalyst compositions have been tried, and even if 14 wt.% Cr_2O_3 produces the greatest resistance to sintering, a concomitant reduction in activity per unit area evidences that a chromia addition of 8 wt.% is the right compromise (***61***). The surface area of the Cr-containing catalysts remained higher than that of the non-Cr-containing standard after reduction: 8 m^2g^{-1} for the pure Fe_3O_4 sample in comparison to 40 m^2g^{-1} for the Fe_3O_4/8 wt.% Cr_2O_3 catalyst, reduced at 400 °C (***62***).

Inlet temperatures are typically 400-450 °C and pressure is up to 3.5 MPa (***1***). The temperature must be minimum to obtain desired CO conversion, resulting in an increased catalyst life by limiting sintering. In fact, magnetite crystallites are not completely stabilized by the chromium oxide and, during its life-time, the catalyst gradually loses activity as the surface area decreases due to thermal sintering (***1***). Usually, the catalyst is supplied in the form of pellets of a precursor (haematite or Fe_2O_3) and is reduced *in situ* using the process gas (***55***). HTS catalysts are generally robust, but they may be affected by a number of factors other than thermal sintering, like a gradual deposition of stream-volatile components on the top of the bed, which may eventually interfere with the passage of gas into the catalyst particles and cause an increase in pressure drop (***1***). The HTS catalysts operate also with a wide range of S/DG ratios and with moderately high impurity level; in fact, Fe-based catalysts are fortunately not very sensitive to poisoning by sulphur, which is commonly present in feed gas derived from coal or fuel oil (***1***).

The usual life-time of a HTS catalyst is 3-5 y and its end may be indicated by a rise in pressure drop caused by catalyst breakage, an accumulation of deposits or, simply, by a decreased activity.

2.2.1.1 PREPARATION

These HTS catalysts are usually produced by precipitation of an aqueous solution containing iron and modifier (chromium) salts by a base, forming the resultant precipitate into shape catalyst units (***55***). The preferred Fe- and Cr-containing salts are chlorides or sulphates, the latter being preferred as iron source because of their availability and lower cost (***55***,***56***). Preferably the base is an alkali metal aqueous solution, hydroxide or carbonate, to improve the homogeneity of the precipitated composition. The precipitation is carried out at 30-80 °C and a pH of 6-9 and the precipitate is normally filtered, washed and dried (***55***). It is important the washing step to remove traces of residual sulphates which may be converted to H_2S during reduction (***1***); modern catalysts contain less than 0.1 wt.% of residual sulphur. Drying in air should be effected at a temperature below 200 °C, to prevent oxidation of Fe_3O_4 to Fe_2O_3 (***55***). The calcination to convert the basic carbonates to Fe_2O_3 is an important step because it must be carefully controlled to avoid the formation of large quantities of CrO_3 from the air-oxidation of Cr_2O_3 (reaction 2.2) (***1***).

$$2\,Cr_2O_3 + 3\,O_2 \rightarrow 4\,CrO_3 \qquad \text{reaction 2.2}$$

The presence of Cr^{VI} compounds is undesirable not only because of the potential health hazard to the operators, but also because of possible operating problems when the catalyst is reduced

(***1***). Cr^{VI} salts are soluble and, if condensation takes place in the reactor on unreduced catalyst, leaching of Cr^{VI} may occur. In addition, the exothermic conversion of Cr^{VI} to Cr^{III} during the reduction procedure leads to considerable evolution of heat and large increase in bed temperatures (***1***). For this reason, the development of Cr-free catalysts for HTS reaction is a priority in the whole globe. However, these catalysts have problems, such as a complex production process, high costs and introduction of new pollutant, which have to be solved (***63***).

2.2.1.2 FORMULATION IMPROVEMENT

Recently, the Fe/Cr-based catalysts have been improved by adding a small amount of copper, resulting in more active and selective; they have already been used in industrial plants and may work in more severe condition (i.e. lower S/C ratios without being reduced to Fe^0) (***55***,***64***), offering greater operating flexibility than the classic HTS formulations. The highest activity allows to use smaller bed volumes, the protection against Fe^0 formation and, hence, hydrocarbon production saves hydrogen and requires lower temperatures, reducing the sintering rate.

An XRD pattern of Fe_2O_3/Cr_2O_3 commercial (wt.%: 88 Fe, 9 Cr and 3 Cu) shows the peaks at 32° and 35° and those at 21° and 26°, that are characteristic of Fe_2O_3 and Cr_2O_3, respectively (Fig. 2.10) (***65***). The Fe-containing phase is the main active component of the catalyst, while Cu is incorporated to increase the intrinsic activity and Cr acts as a stabilizer (***64***). However, Cu favours sintering, leading to solids with low surface areas. The increase in the catalytic activity and surface area of the solids reflects the synergetic effects required to these dopants.

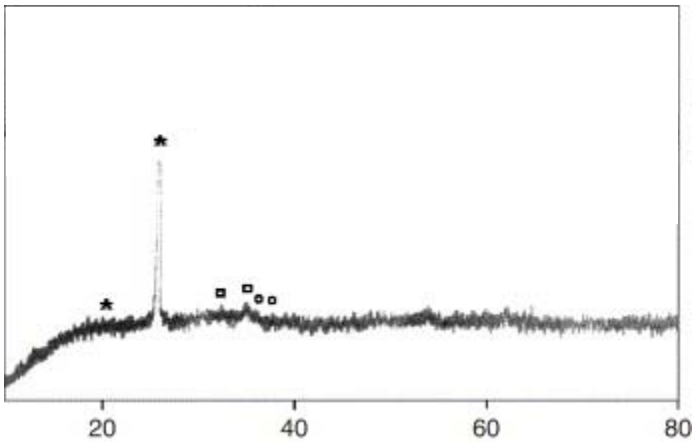

Fig. 2.10 XRD pattern for a Fe_2O_3/Cr_2O_3 catalyst: (□) Fe_2O_3, (∗) Cr_2O_3, (°) CuO (***65***).

It is widely accepted that the Cr^{III} ions have an octahedral preference and substitute the Fe^{II} ions during the spinel formation; as a consequence, Fe^{II} is further oxidized to Fe^{III} increasing the shrinkage (***64***). However, Cu^{II} does not readily substitute Fe^{II}, in spite of its stabilization energy, attributed to its higher electronegativity, leading to Cu–O bonds which are weaker than Fe–O bonds. Copper does not act as a textural promoter, but rather favours a loss of area, although in the presence of chromium this process is delayed. As expected, chromium makes magnetite

sintering more difficult (***58***); while most chromium is inside the solid, copper is distributed non-uniformly along the structure, as proposed by Sidhu *et al.* (***66***). In Cr-free samples, it tends to migrate to the surface, but in the presence of chromium, it goes from the surface. Quadro *et al.* (***64***) concluded that copper acts as a structural promoter in Fe-based catalysts, whereas chromium leads to a decrease in the intrinsic activity.

2.2.1.3 REDUCTION

Before reaction, Fe_2O_3 must be converted to Fe_3O_4 and, if present, CrO_3 to Cr_2O_3 (***1***). The reduction is carried out using process gas and avoiding the further reduction to metallic iron, which promotes methanation and CO disproportionation (Boudouard's reaction) (***1***,***67***). In industrial processes, large amount of steam are used to inhibit the metallic iron formation, implying high operational costs (***64***).

In the H_2-TPR analysis (Fig. 2.11**Errore. L'origine riferimento non è stata trovata.**) (***65***), a Fe_2O_3/Cr_2O_3 catalyst shows a peak at 400 °C, attributed to the reduction of Fe_2O_3 to Fe_3O_4 (390-430 °C) and Cr_2O_3 to CrO (385 °C), with a broad peak at higher temperatures (500-900 °C), related to the subsequent reduction of Fe_3O_4 to Fe, *via* FeO. Therefore, in the HTS process, the active phase is obtained by partial reduction at 400 °C (***65***,***67***).

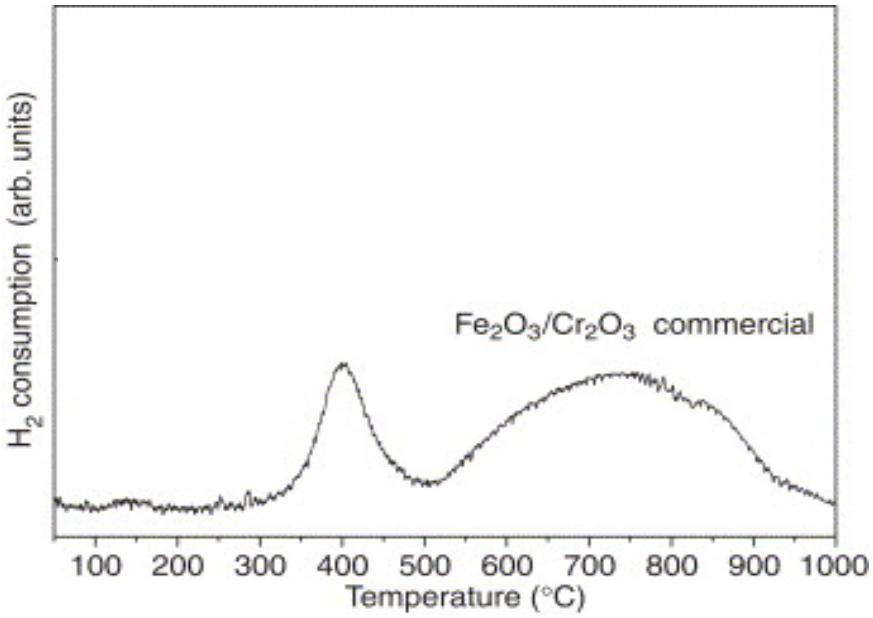

Fig. 2.11 H_2-TPR profiles for a Fe_2O_3/Cr_2O_3 commercial catalyst (***65***).

The actual heat of reduction of a new catalyst varies with the H_2/CO ratio in the reducing gas. In the reduction of Fe_2O_3 (reactions 2.3 and 2.4) the heat evolved is small, while the heat of reduction of CrO_3 (reaction 2.5) is far more significant and varies in proportion of CrO_3 level (***1***). The equilibrium between Fe_2O_3 and Fe_3O_4 phases is determined by the S/H_2 and CO_2/CO ratios

(***68***): at 450 °C, the gas in equilibrium with the two phases contains 96.0 % H_2O and 4.0 % H_2 (reaction 2.3), 99.5% CO_2 and 0.5% CO (reaction 2.4).

$3\,Fe_2O_3 + H_2 \rightarrow 2\,Fe_3O_4 + H_2O$	$\Delta H^0_{298} = -16.3\ kJ\ mol^{-1}$	reaction 2.3
$3\,Fe_2O_3 + CO \rightarrow 2\,Fe_3O_4 + CO_2$	$\Delta H^0_{298} = +24.8\ kJ\ mol^{-1}$	reaction 2.4
$2\,CrO_3 + 3H_2 \rightarrow Cr_2O_3 + 3\,H_2O$	$\Delta H^0_{298} = -684.7\ kJ\ mol^{-1}$	reaction 2.5
$2\,CrO_3 + 3\,CO \rightarrow Cr_2O_3 + 3\,CO_2$	$\Delta H^0_{298} = -808.2\ kJ\ mol^{-1}$	reaction 2.6

Under some conditions, further unwanted reduction of iron active phase may occur (reactions 2.7-2.10). FeO is stable above 565 °C, while in the range 300-565 °C the only stable phases are Fe_3O_4 and Fe^0 (***69***,***70***). At 400 °C, Fe_3O_4 is the stable phase when the S/H_2 ratio exceeds 0.09 or the CO_2/CO ratio exceeds 1.16, while at 550 °C these ratios are 0.28 and 1.00, respectively. The effect of the S/H_2 ratio and temperature on the stable phase composition in the iron/iron oxide system is shown in Fig. 2.12**Errore. L'origine riferimento non è stata trovata.** (***67***).

$Fe_3O_4 + H_2 \rightarrow 3\,FeO + H_2O$	$\Delta H^0_{298} = -63.8\ kJ\ mol^{-1}$	reaction 2.7
$Fe_3O_4 + CO \rightarrow 3\,FeO + CO_2$	$\Delta H^0_{298} = -22.6\ kJ\ mol^{-1}$	reaction 2.8
$FeO + H_2 \rightarrow Fe + H_2O$	$\Delta H^0_{298} = -24.5\ kJ\ mol^{-1}$	reaction 2.9
$FeO + CO \rightarrow Fe + CO_2$	$\Delta H^0_{298} = +12.6\ kJ\ mol^{-1}$	reaction 2.10

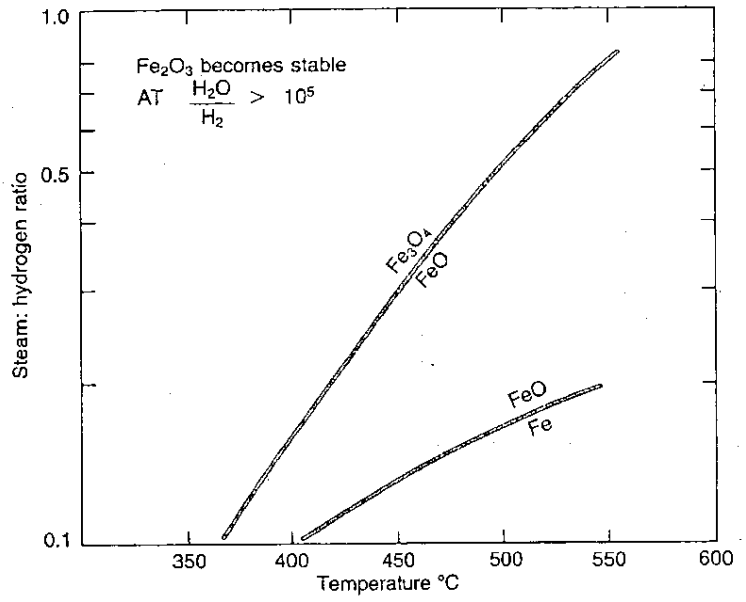

Fig. 2.12 Minimum S/H_2 ratio for the reduction of conventional HTS catalysts (***67***).

It is clear that neither pure H_2 nor rich H_2/N_2 mix have to be used to reduce HTS catalyst to avoid the exothermic reduction to metallic iron (reaction 2.11), which may promote the

methanation of carbon oxides (reaction 2.12), which could give rise to a dangerous temperature runaway, and, probably, also to Boudouard's reaction (reaction 2.13), which carry out to formation of coke hazarding to occlude catalyst pores (***1***,***67***,***5***). When bed temperature is in the range 350-400 °C, residual sulphates in HTS catalyst are reduced in H_2-containing gas to form H_2S (***1***,***67***). With the modern catalyst, desulphurization times have been dramatically reduced and maximum H_2S levels reached are lower than 25 ppm (***1***,***67***). The desulphurization period required is less than 15 h (Fig. 2.13) (***67***).

$Fe_3O_4 + 4\ H_2 \rightarrow 3\ Fe + 4\ H_2O$ $\quad \Delta H^0_{298} = -149.4\ kJ\ mol^{-1}$ reaction 2.11

$CO + 3\ H_2 \rightarrow CH_4 + H_2O$ $\quad \Delta H^0_{298} = -206.2\ kJ\ mol^{-1}$ reaction 2.12

$2\ CO \rightarrow C + CO_2$ $\quad \Delta H^0_{298} = -172.5\ kJ\ mol^{-1}$ reaction 2.13

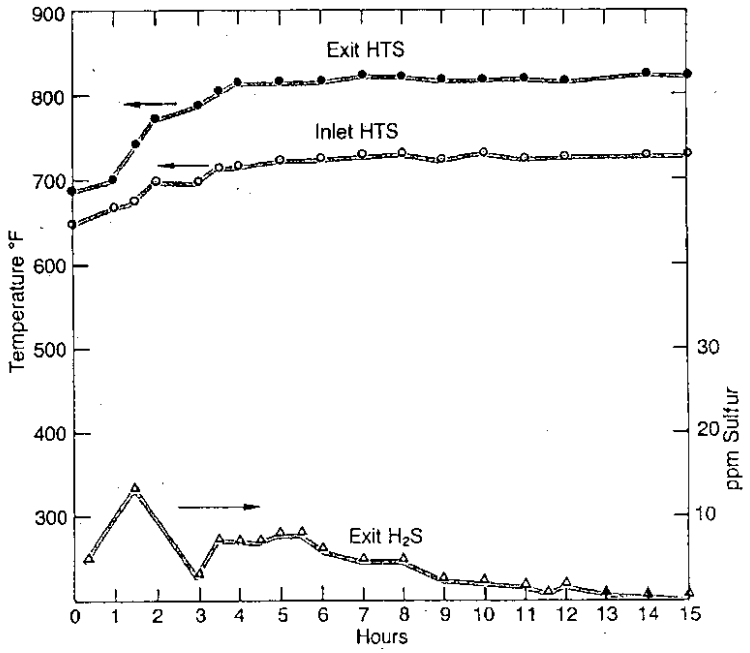

Fig. 2.13 Typical desulphurization of a 40 m^3 charge of a HTS catalyst (***67***).

In the reduced form, HTS catalyst is pyrophoric and the heat released during the oxidation process (reaction 2.14) corresponds to an adiabatic temperature rise of about 450 °C (***1***). Hence, reduced HTS catalyst must not be exposed to oxygen, except under carefully controlled conditions (***1***). Spent catalyst must be removed under N_2 flow and, then, deposited in a safe place where it can slowly oxidize. Alternatively, the converter may be filled with H_2O and the wet catalyst removed (***1***). However, it is important to remember that some H_2 may be formed, according to reaction 2.15 (***1***):

$2\ Fe_3O_4 + ½\ O_2 \rightarrow 3\ Fe_2O_3$ $\quad \Delta H^0_{298} = -464.6\ kJ\ mol^{-1}$ reaction 2.14

$$2\ Fe_3O_4 + H_2O \rightarrow 3\ Fe_2O_3 + H_2$$ reaction 2.15

After partial discharge, it may be desirable to re-use reduced catalyst, by catalyst oxidation *in situ* under controlled conditions, typically cooling the catalyst to 200 °C and passing steam containing 1 % of air through the bed at a space velocity of about 1,000 h^{-1} (***1***).

2.2.1.4 DEACTIVATION AND POISONING

Combined physical characterisation and reactor studies of the Fe_3O_4/Cr_2O_3 catalysts (***71***) have indicated that deactivation is more due to sintering rather than poisoning or coking. Sintering of Fe_3O_4/Cr_2O_3 catalysts leads to lower surface area, reduction in porosity, increase in particle size and decrease of the number of pores smaller than 30 nm which most contribute to the shift reaction (***71***). In addition, it has been demonstrated that deactivation is a multi-step process, with a rapid decrease in activity occurring during the first 150 h of use, followed by a slow decay over extended periods of several years (***72***,***5***). The initial decay has been attributed to particle growth, by two simultaneous but different mechanisms, or to a rapid agglomeration of very small particles.

HTS catalysts do not normally suffer the poisoning but, in coal-based plants, the total amount of sulphur compounds, generally H_2S and COS, can be significant (***1***). Consequently, the Fe_3O_4 may be converted to FeS, according to the reaction 2.16, and any carbonyl sulphide present is converted to hydrogen sulphide (reaction 2.17) (***1***). Sulphide catalyst is active in the WGS reaction, although its activity is only about half of that of catalyst containing Fe_3O_4. Therefore, in circumstances where the catalyst may be sulphided, the volume used has to be doubled compared with that normally employed to obtain satisfactory performance (***1***).

$$Fe_3O_4 + 3\ H_2S + H_2 \rightarrow 3\ FeS + 4\ H_2O \qquad \Delta H^0_{298} = -\ 75.0\ kJ\ mol^{-1}$$ reaction 2.16

$$COS + H_2O \rightarrow CO_2 + H_2S \qquad \Delta H^0_{298} = -\ 34.6\ kJ\ mol^{-1}$$ reaction 2.17

The HTS catalyst can be affected by halides but they are rarely encountered at sufficiently high levels in the feeds to cause major problems (***1***). Arsenic compounds in small concentrations could poison the HTS catalyst, but normally they are unlikely to be present. Phosphorous compounds or silica, which causes deactivation by fouling, may be introduced into the reactor from upstream equipment, or as the result of a boiler failure.

Carbon formed in partial oxidation process, which is carried into the HTS converter, may also block the catalyst pores (***1***). These effects can be mitigated by installing a guard bed, that can be regenerated and, hence, the catalyst is not physically damage by the deposit (***1***). The deactivation of Fe/Cr-based catalyst due to a coke formation seems to be negligible or very small and, therefore, the main cause of deactivation remains the sintering (***71***).

2.2.2 LOW-TEMPERATURE SHIFT (LTS) [$T_{IN} \approx 200$ °C]

The commercial LTS ($CuO/ZnO/Al_2O_3$) catalysts may operate at relatively low temperatures (200-250 °C) and so give equilibrium outlet CO concentrations of less than 0.3 % (***1***). If pure process gas is available and a thermally stable catalyst is used, the CO level at the exit of the LTS converter remains close to the thermodynamic equilibrium value for many years. However, if the poison levels are relatively high, the catalyst life can be appreciably shortened.

The formulation of LTS catalysts is important in terms of selectivity and resistance to poisoning, as well as activity. Selectivity is important because, under LTS conditions, methanation of both CO and CO_2 is thermodynamically very favoured (reactions 2.18 and 2.19) (***1***). Hence, H_2 may be consumed and, being very exothermic, these reactions may cause a dramatic and dangerously destructive rise in temperature (***1***).

$CO + 3\ H_2 \rightarrow CH_4 + H_2O$ $\quad \Delta H^0_{298} = -206.2\ kJ\ mol^{-1}$ reaction 2.18

$CO_2 + 4\ H_2 \rightarrow CH_4 + 2\ H_2O$ $\quad \Delta H^0_{298} = -165.0\ kJ\ mol^{-1}$ reaction 2.19

Cu-based catalysts have good activity for the WGS reaction and have no methanation activity. However, they are particularly prone to easy sintering, then they may be only used in LTS conditions (***1***). The WGS reaction is a structure-sensitive reaction on a $Cu/ZnO/Al_2O_3$ catalysts (***73***). The catalyst prepared by co-precipitation shows higher BET and Cu surface area values and, consequently, as well as higher catalytic activity (***74***,***75***). So, activity depends on inhibiting the sintering tendency of the copper crystallites to form progressively larger crystallites having smaller surface area.

By varying the catalytic reaction conditions, such as S/C ratio or contact time, it is possible to obtain different conversion rates of CO and, thus, operate under conditions of lower steam consumption (***74***,***75***). The CO concentration has an effect on the catalytic activity (Fig. 2.14) (***76***): the maximum CO conversion is reached at 250 °C for every condition, decreasing gradually at higher temperatures where it is also accompanied by the decrease of equilibrium conversion.

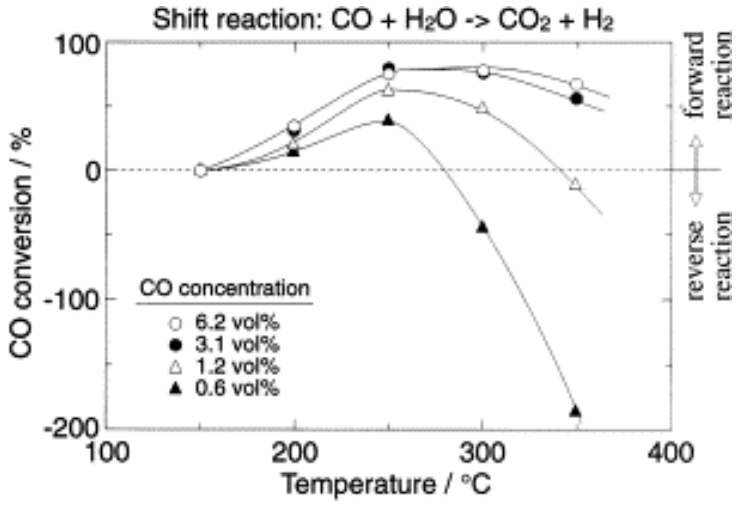

Fig. 2.14 Influence of CO concentration for CO-shift reaction. Reaction conditions: H_2 37.5vol%; H_2O 25vol%; CO_2 12.5vol%; N_2 balance; space velocity equal to $7200h^{-1}$ (***76***).

The WGS process is also affected by the coexisting gas, such as H_2O, H_2, and CO_2 (Fig. 2.15) (***39***,***76***): the CO conversion decreases monotonously with an increase of either CO_2 or H_2 partial pressure because of the reverse WGS reaction. Therefore, a large amount of H_2O is necessary to favour the direct WGS reaction (***39***,***76***). Above S/DG ratio of 0.6, CO conversion remains practically constant, which agrees with the higher copper surface area and dispersion of the Cu-based LTS catalysts (***74***). As expected, the conversion of the WGS reaction decreases slowly also with increase of the space velocity (***39***). Furthermore, the CO conversion changes with the contact time at different S/DG ratios (***74***). At lower values of contact time, the LTS catalyst shows higher CO conversion at higher S/DG ratio. Differently, the CO conversion decreases with the S/DG ratio at higher values of contact time (***74***).

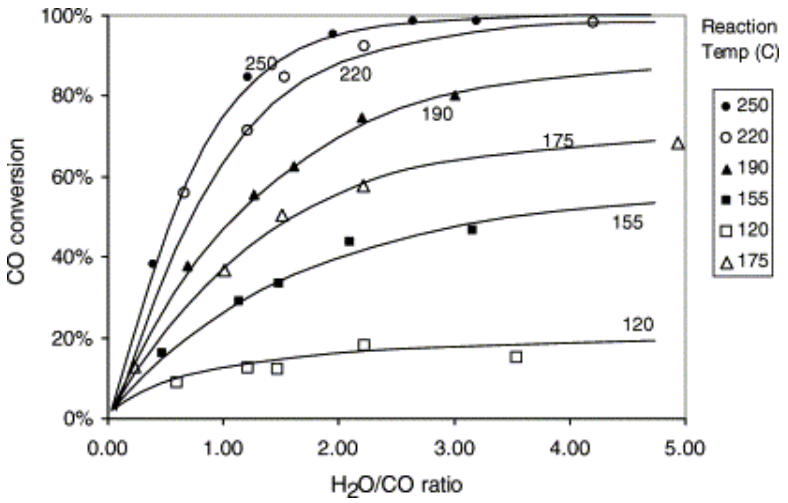

Fig. 2.15 Water gas shift reaction: CO conversion vs. S/CO ratio (reaction temperature 175–250 °C; catalyst loading 1.0 g; pressure 0.1 MPa; gas hourly space velocity 6,100 h^{-1}) (***39***).

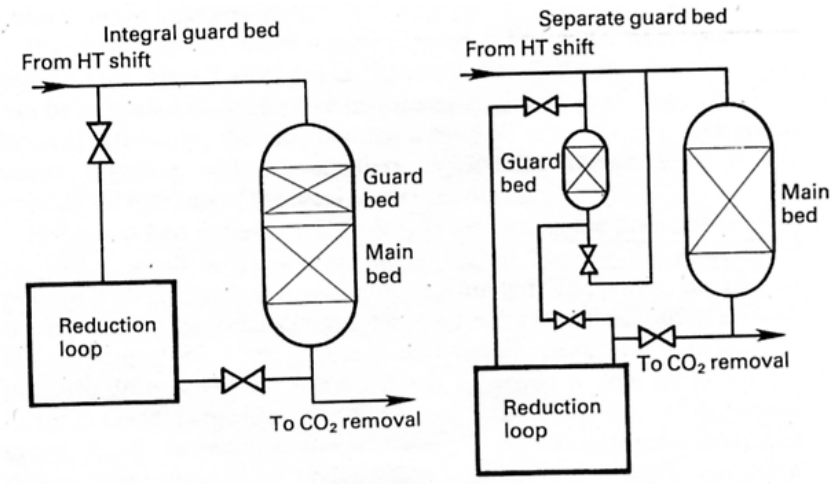

Fig. 2.16 Possible arrangement of guard and main beds of LTS catalyst (***1***).

Usually, the life-time of a well-formulated LTS catalyst, which has a good thermal stability, is only limited by the presence of poisons removed by using a small amount of ZnO as a separate bed in the LTS converter (***1***). Moreover, it may be introduced a small bed of alkalized alumina on the top of the LTS converter to remove HCl from the process gas before it enters the bed of LTS catalyst (***1***). Since the use of a separate guard vessel containing LTS catalyst is the best method to prevent all known poisons entering the main catalyst bed, this arrangement has now been adopted by many operators (Fig. 2.16) (***1***).

The amount of LTS catalyst used in a plant is larger than the design volume needed to achieve the required CO level at the exit, because extra catalyst is included to compensate for the deactivation that inevitably takes place during operations (***1***). Typically, this additional catalyst volume is about 70 % of the total actually charge to operate continuously for 2-3 y. Initially, the reaction takes place in the top part of the bed, and the temperature profile through this region is steep, reflecting the high catalyst activity (***1***). With a well-formulated catalyst with a good thermal

stability these effects are not large, while with less-stable catalysts the activity continues to decrease quite markedly and it becomes necessary to increase the inlet temperature to compensate for the loss of activity (***43***). The poisons contained in the process gas, sufficient to cause gradual deactivation of LTS catalysts, accumulate on the top of the bed and the temperature profile gradually moves downwards (Fig. 2.17) (***1***). As the reaction zone approaches the lower part of the catalyst bed, the CO amount at the exit gradually increases and, therefore, the catalyst must be changed as quickly as possible to avoid loss of overall plant production efficiency (***1***). Excessive condensation of water on LTS catalyst is almost invariably detrimental and, generally, it must be avoided. If condensation occurs, soluble poisons can be washed to the lower parts of the bed and may lead to premature deactivation of the charge (***1***).

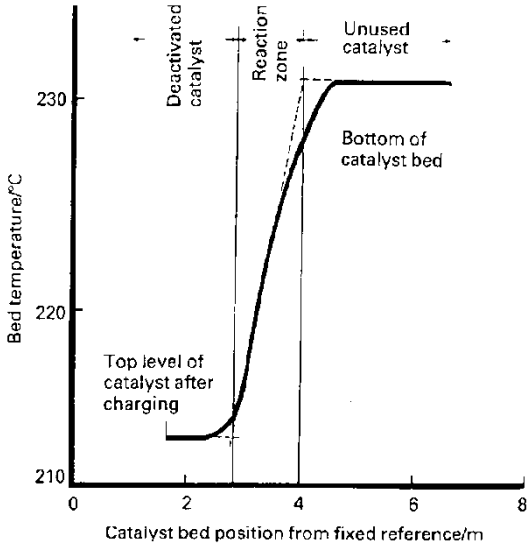

Fig. 2.17 Typical temperature profile through the bed of a LTS catalyst (***1***).

2.2.2.1 PREPARATION

The Cu-based ($CuO/ZnO/Al_2O_3$) catalysts are prepared by co-precipitation from aqueous solutions of element nitrates by a sodium carbonates solution at 30-60 °C and pH of 7-9. The precipitates are filtered, washed with deionized water, dried in air at 100 °C and, then, calcined from 300 to 500 °C (***77***,***78***). The catalytic activity of LTS catalysts for the WGS reaction is related to the residual Na content (***78***). Higher activities are generally observed for the rewashed catalysts, even when they contained comparable residual Na levels (i.e 0.09 wt.% Na) (***78***).

The most important properties of the LTS catalyst (activity, stability, etc.) are likely to be dependent on dispersion of the active phase and on its interaction with the support (***79***). Activity may be related to dispersion and to size of the copper particles. In this case, the method of preparation may have a significant effect on them (***79***). The CuO-crystallite size gradually increases by increasing calcination temperature, but a significant drop in activity is only verified at temperatures higher than 600 °C (Fig. 2.18) (***80***).

Figueiredo *et al.* (***79***) showed that different Cu-surface-area values were obtained for catalysts containing the same Cu amount, solely by varying the sequence of the precursor salt precipitation. Changes in the sequence of co-precipitation of the nitrates lead to changes in the final properties of Cu^0 on the catalyst surface (***79***). Precursors, in which Cu and Zn nitrates were precipitated together, resulted in catalysts with the highest Cu surface area (***79***), that are the most active catalysts.

The phase composition does not depend significantly on the chemical composition of the precursors. In fact, all the classic LTS catalysts contain CuO and ZnO (***77***). A crystalline spinel-like phase ($ZnAl_2O_4$) is detected only if Al_2O_3 amount is higher than about 13 wt.%. On the other hand, CuO and ZnO crystallite sizes are both greatly influenced by the phase composition of the catalytic precursor (***77***): the higher amount of Cu,Zn,Al hydrotalcite-type phase in the precursor results in the lower crystallite sizes in the mixed oxides. The role of aluminium would be not only to act as an alumina or aluminate support, stabilizing the Cu^0 crystallites, but also to form hydrotalcite-type precursors which lead to more active catalysts (***77***).

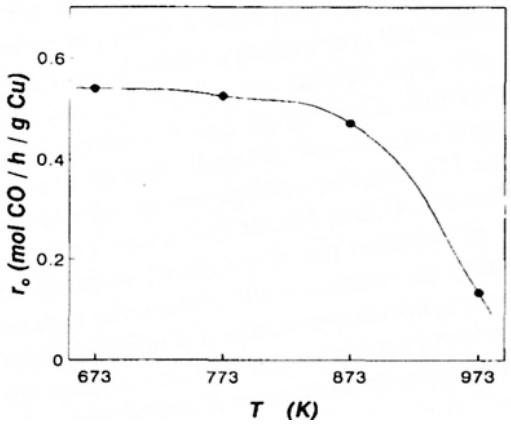

Fig. 2.18 Specific WGS rate (temperature 230 °C, pressure 0.1 MPa, $CO:H_2O:H_2$ = 1:3:3, gas hourly spave velocity 90,000 h^{-1}) as a function of the calcination temperature. Results obtained with samples of set temperatures (***77***).

Sekizawa *et al.* (***76***) investigated some mixed-oxide-based catalysts ($Cu/MO_x/Al_2O_3$ where *M*=Al, Ce, Co, Cr, Fe, Mg, Mn, Sn, Zn, and Zr; *M*/Al=1) for the WGS reaction (Fig. 2.19), showing that all the investigated samples demonstrated an excellent activity at 250 °C, with the following sequence of the catalytic activity:

Zn > Al > Cr > Mn > Mg

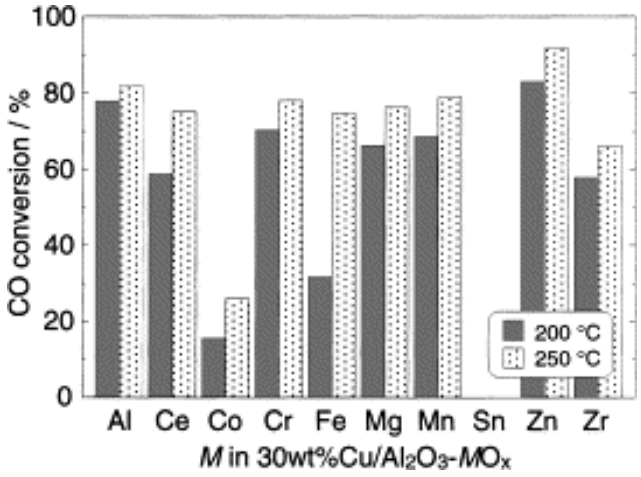

Fig. 2.19 CO-shift reaction over 30 wt.% Cu/Al_2O_3–MOx (M=Ce, Co, Cr, Fe, Mg, Mn, Sn, Zn, or Zr). Reaction conditions: CO 12.5 vol%; H_2O 12.5 vol%; N_2 balance; GHSV = 7,200 h^{-1}; reaction temperature 200 and 250 °C (***76***).

The amount effect of the Cu loading was investigated (Fig. 2.20A) (***76***): the activity increases with high loading of the active species, but heavy Cu loading leads to low dispersion and large agglomerate particles. These results indicate that a 30 wt.% $Cu/ZnO/Al_2O_3$ catalyst possesses the highest activity (***76***). Moreover, the highest activity is observed for the Zn-rich sample (***78***); in particular, for the most active sample (30 wt.% $Cu/ZnO/Al_2O_3$), the relation between activity and ZnO content in the support shows a maximum in CO conversion with the right ZnO content (Fig. 2.20B) (***76***). Several authors postulate that ZnO plays an active role either by stabilizing active Cu^I species in the ZnO matrix or by creating synergetic effects with Cu^0 sites (***81***,***82***); others authors believe that ZnO acts merely as a 'spacer', which helps to disperse the Cu-metallic phase (***83***,***84***).

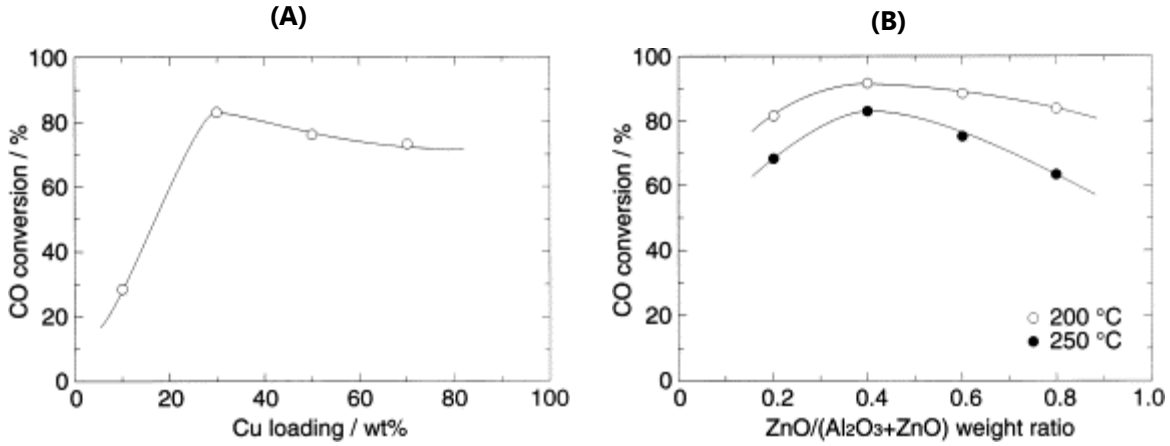

Fig. 2.20 Effect of: (A) Cu loading on CO-shift reaction over Cu/Al_2O_3–ZnO; (B) ZnO content on CO-shift reaction over 30 wt% Cu/*m*Al_2O_3-*n*ZnO. Reaction conditions: CO 12.5 vol%; H_2O 12.5 vol%; N_2 balance; GHSV = 7,200 h^{-1}] (***76***).

Impregnated $Cu/ZnO/Al_2O_3$ catalysts have been also prepared by using γ-Al_2O_3 (***85***): the surface area simply decreased by increasing copper and zinc oxide contents. It may be considered

that a higher Cu-loading leads to more abundant active components and a decrease in surface area. Small pores originally possessed by γ- Al_2O_3 are stuffed by copper and zinc deposits as the reduction of the active surface during the catalytic reaction proceeds (***85***). The effect of calcination temperature is also reported for the impregnated catalyst (***85***): they show a decrease in CO conversion with the increase of temperature, ascribed to the low surface area at high temperature. Optimum content of Cu and ZnO ($Cu/ZnO/Al_2O_3$ as wt.%) for the impregnated catalyst (5/5/90) is far smaller than that for the co-precipitated catalyst (30/30/40) (***85***). For the impregnated catalyst, the active components must be dispersed only on the surface of the alumina support, thus the smaller loading amounts may be favourable. The activity of impregnated catalyst is much lower than the co-precipitated sample only at temperature below 200 °C (***85***). On the other hand, both catalysts demonstrate a CO conversion of about 90 % at 200 °C, continuously for 20 h.

2.2.2.2 FORMULATION IMPROVEMENT

The change in the Cu surface area of the catalyst and of the catalyst activity with the calcination temperature have the same trends, suggesting that the activity may be correlated mainly to the Cu surface area (***86***). The WGS activity of Zr-promoted $Cu/ZnO/Al_2O_3$ catalyst at 250 °C is less affected by the pre-treatments, such as calcination and reduction at high temperature, than that without Zr-promotion (***86***). Therefore, the $Cu/ZnO/ZrO_2/Al_2O_3$ catalyst may be considered more suitable for practical use in the WGS process also at 400 °C.

The addition of a small amount of colloidal silica to a $Cu/ZnO/Al_2O_3$ catalyst greatly improves its long-term stability in the WGS reaction (***87***). The activity of the $Cu/ZnO/Al_2O_3$ catalysts decreases monotonously; on the contrary, the activity of the same catalyst containing 0.8 wt.% of SiO_2 is almost unchanged during 500 h (***87***); this latter may be ascribed to the BET and Cu surface area values, that are about 30 % higher for the SiO_2-containing catalyst, being also confirmed by the XRD profiles for the spent reaction catalysts, where the ZnO and Cu reflections are practically unchanged (***87***).

The Cu-based catalysts are very sensitive also to low concentrations of chloride eventually present in the feed gas (***88***). When improved by adding barium, they show a higher CO conversion (13 times) than that of commercial LTS catalysts.

2.2.2.3 RECENT DEVELOPMENT

A study on ternary Cu/ZnO/*M*O catalysts (*M* = Mg, Ca, Sr and Ba) has shown an increase of activity after the addition of MgO to CuO/ZnO samples. It may be attributed to the increased Cu^0 surface area value, although the BET surface area decreases by the addition of MgO (***89***). MgO addition significantly enhances the formation of Cu^I species, as the active sites. These active sites are located at the surface boundary between Cu^0 particles and ZnO crystals, where MgO assists their formations by stabilizing the cationic species (***89***). The homogeneous precipitation, using urea hydrolysis, affords larger Cu^0 surface area and smaller Cu^0 particle size values, resulting in the higher and more stable activity than the co-precipitation method, although the BET surface area is larger for this latter (***89***). However, the dependency of the CO conversion is more obvious for the

Cu^0 surface area than for the BET surface area (***89***). This homogeneous precipitation method provides also a higher stable activity than that of the commercial $Cu/ZnO/Al_2O_3$ catalyst, suggesting that Al_2O_3 may suppress the formation of Cu^+ species (***90***).

A series of Cu-based spinel-type oxide catalysts (CuM_2O_4, *M*=Al, Cr, Mn and Fe) have been prepared by the co-precipitation method (***91***). High-temperature reduction treatment was not necessary for $CuMn_2O_4$ and it should be avoided to prevent Cu particles from aggregating (***91***). The $CuMn_2O_4$ catalyst, exhibits high WGS activity over 225 °C (≈ 90 %) comparable to that of $Cu/ZnO/Al_2O_3$ and high durability (20 h), whereas $CuFe_2O_4$ shows relatively high WGS activity only at higher temperatures (***91***,***92***). The $CuMn_2O_4$ sample calcined at 900 °C exhibits maximum activity with reduction treatment at 250 °C because Cu-containing species are more highly dispersed on MnO and contribute to high CO conversion at 225-250 °C (***92***). The promoted Cu/Mn/*B* samples (where B is Al, Fe, Zr, Ce, Zn, and Cr) have been prepared by the citric acid method, calcined at 900 °C in air and reduced at 250 °C (***93***). Partial substitution of Mn with Al or Fe improves the catalytic activity of the spinel catalyst to a value comparable with that of a commercial $Cu/ZnO/Al_2O_3$ catalyst above 225 °C, ascribed to a large amount of reducible Cu species (***93***). The best performances are observed with a Cu/Mn/Fe catalyst with a 1/1/1 ratio (***93***).

Li *et al.* (***94***) show that copper deposited on ceria support reaches similar activity to the activated commercial $Cu/ZnO/Al_2O_3$ catalyst at lower temperatures and higher than 90 % of CO conversion at 400 °C (Fig. 2.21).

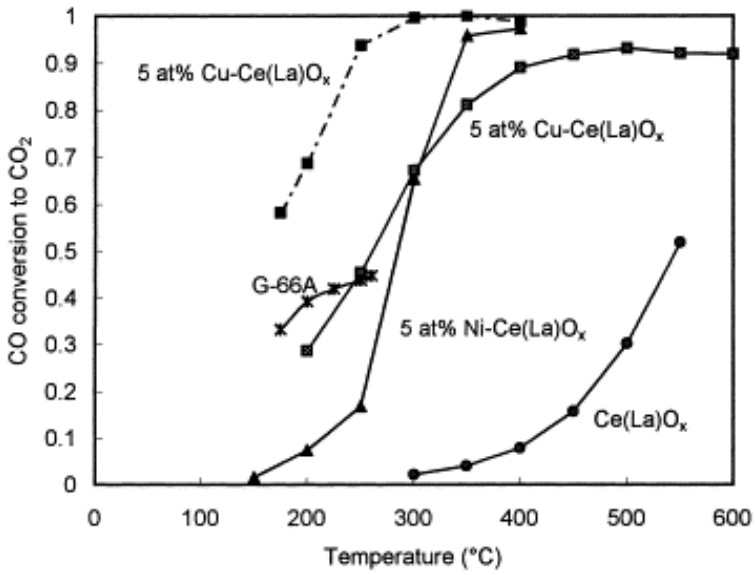

Fig. 2.21 WGS reactivity over several Ce-based catalysts and G-66A (UCI). Reaction conditions: CO 2%; H_2O 10.7%; He balance; solid lines: GHSV = 80,000 h^{-1} (NTP); dashed line: GHSV = 8,000 h^{-1} (NTP) (***94***).

Patt *et al* (***95***), studying the feasibility of high surface area molybdenum carbide for the WGS reaction, reported that Mo_2C is an active LTS formulation with activity comparable or higher than those of $Cu/ZnO/Al_2O_3$ catalysts. These nano-crystalline materials, known as active hydrotreating

catalysts, are sensitive to oxygen and their performances under real fuel processing conditions have not been yet investigated.

2.2.2.4 REDUCTION

The LTS catalysts are supplied in the oxide form and they must be reduced to metallic copper, the real active phase (***1***). The reduction is highly exothermic and sufficient to raise the temperature of the catalyst bed to about 500 °C (reaction 2.20). This is unacceptable, because an heating above 260 °C provokes the catalyst sintering and, consequently, the loss of activity (***1***,***80***). In order to obtain maximum catalyst activity, it is very important to control the reduction carefully, limiting the temperature of catalyst exposition (***1***). The LTS catalysts are activated *in situ* before testing, by using a H_2/N_2 flow and a maximum temperature of 220 °C to completely reduce the Cu-containing species without significant sintering of the metallic crystallites (***28***). When process gas is first introduced, the temperature usually increases rapidly as the catalyst comes to equilibrium with the process conditions (***1***). The catalyst reduction is complete when the inlet and exit H_2 concentrations are the same, or a difference less than 0.5 % for 4 h, and the catalyst bed is at temperature of 225-230 °C (***1***).

$$CuO + H_2 \rightarrow Cu + H_2O \qquad \Delta H^0_{298} = -80.8\ kJ\ mol^{-1}$$ reaction 2.20

The active component is not only Cu^+ but also Cu^0 and the support may play the role to control the Cu^+/Cu^0 ratio, on which the catalytic activity depends (***96***). Burch *et al.* (***97***,***98***) have proposed that the role of ZnO is to act as a reservoir for H_2 and to promote the H_2 spill-over. The reduction is always promoted by ZnO content and is characterized by the presence of two reducible Cu-containing species with lower Cu loading (***99***). Fierro *et al.* (***99***) believe that these copper species, homogeneously dispersed, are more reactive because they are in contact with the surface of the ZnO particles, resulting in a strong interaction with them. Pure ZnO does not reduced under the same experimental conditions. The atomic Cu/Zn ratio increases when the sample is reduced and also when it was re-oxidized, suggesting a re-dispersion of the Cu^0 phase, while the Al/Zn ratio does not show such behaviour (***74***).

The double peak (177 and 200 °C) is replaced by a single and symmetrical reduction peak (215 °C) when the calcination is carried out at higher temperature, consequence of the sintering of the CuO species in a less reducible Cu-containing fraction (***99***). The reduction profile is also characterized by the preparation method (***99***); furthermore, Fleisch and Mieville (***100***) report that the CuO reducibility is higher in the ternary than in binary system. The TPR profile of the $Cu/ZnO/Al_2O_3$ catalyst indicates a superposition of two or three peaks that may represent the reduction of different Cu^{II} species (Fig. 2.22) (***74***): (a) copper in the ZnO lattice, (b) in amorphous Cu oxide phases, (c) in crystalline CuO, and (d) Cu^{2+} in the Al_2O_3 phase. The peak at 160-170 °C, may be assigned to reduction of Cu^{2+} to Cu^{1+} and $Cu^{2+}$and/or Cu^{1+} to Cu^0 species, whereas the shoulder at 210°C may be assigned to copper species interacting with the Al^{2+} phase, which is more difficult to reduce.

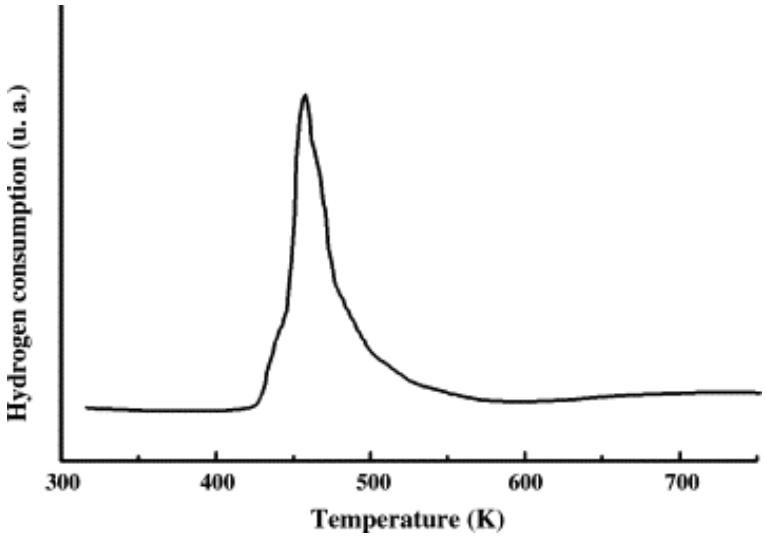

Fig. 2.22 Temperature-programmed reduction (TPR) profile of a calcined $Cu/ZnO/Al_2O_3$ catalysts (measured as H_2 consumption in a thermal conductivity detector) (***74***).

Reduced LTS catalysts are potentially pyrophoric and uncontrolled oxidation in air could result in a temperature raise between 800 and 900 °C (reaction 2.21) (***1***). The usual procedure to discharge the LTS catalyst is to depressurize the reactor, purge the N_2, cool down to less than 50 °C and discharge the catalyst under a N_2 flow (***1***).

$$Cu + ½\ O_2 \rightarrow CuO \qquad \Delta H^0_{298} = -157.2\ kJ\ mol^{-1}$$ reaction 2.21

2.2.2.5 DEACTIVATION AND POISONING

Research provides formulations which are significantly more thermally stable, consisting, before reduction, of alumina in addition to oxides of copper and zinc (***43***). Susceptibility to thermal sintering is, however, an intrinsic property of all dispersed heterogeneous catalysts; in general, Cu-based catalysts are more susceptible than other metallic catalysts (***1***). Early workers always report a rapid deactivation, which is due to both poisoning and a rapid loss of Cu-surface area brought about by sintering (***1***).

Low temperatures favour exothermic adsorption of poisons and result in high surface coverage; as a consequence, LTS catalysts are particularly sensitive to even very low levels of poison, such as sulphide (***1***). Steam may be eliminated as a source of poisons by ensuring that the boiler design prevents carry-over of boiler solids into the process steam system (***1***).

Under LTS conditions, sulphur is a powerful poison for copper and the reaction 2.22 is very favoured (***1***). Therefore, it is important to prevent even very low levels of sulphur contacting the catalyst. With LTS catalyst containing ZnO, sulphur may trap at the top of the bed as zinc sulphide (reaction 2.23), which is more stable than copper sulphide (***1***). There are evidences that, initially, sulphur is preferentially adsorbed from the feed gas onto the more active small copper crystallites (≈ 5 nm) and then transferred to ZnO, where it reacts to form the thermodynamically more stable

zinc sulphide (***1***). For this reason, the catalyst pellets need to be porous to minimize diffusion effects and to have small copper crystallites, as well as maximum surface area of reactive "free ZnO". A catalyst with a significant content of reactive "free ZnO" retain sulphur in a well-defined layer of the bed, so that the rest of the loading remains completely unaffected by sulphur and may continue to operate satisfactorily (***1***).

$2\ Cu + H_2S \rightarrow Cu_2S + H_2$ $\quad \Delta H^0_{298} = -59.4\ kJ\ mol^{-1}$ reaction 2.22

$ZnO + H_2S \rightarrow ZnS + H_2O$ $\quad \Delta H^0_{298} = -76.6\ kJ\ mol^{-1}$ reaction 2.23

Both metal copper and zinc oxide react with HCl. Reaction of bulk metal copper with HCl to form cuprous chloride (reaction 2.24) is thermodynamically much less favoured than the reaction with H_2S (***1***). However, the low melting point of CuCl (430 °C) results in a high mobility under LTS conditions. Consequently, the presence of even extremely small amounts of chloride provides the "catalytic species" necessary for a surface-migration sintering mechanism of the copper crystallites. Because of this, chloride acts as a powerful poison that irreversibly decreases the activity of LTS catalysts (***1***). Zinc chloride species have also high surface mobility and this contributes to a destructive destabilization of the catalytic activity *via* structural changes, that decrease the thermal stability (***1***). Under normal operating conditions, almost all the chlorides present in LTS catalyst are associated with zinc rather than copper species (reactions 2.25) (***1***). The chlorides are strongly retained on the top of the LTS bed in a well-formulated catalyst, usually in the form of zinc hydroxychlorides (***1***). However, these species are soluble in hot water and it is therefore important to avoid the condensation, otherwise condensate could wash chlorides further into the bed (***1***).

$Cu + HCl \rightarrow CuCl + \frac{1}{2} H_2$ $\quad \Delta H^0_{298} = -43.5\ kJ\ mol^{-1}$ reaction 2.24

$ZnO + 2\ HCl \rightarrow ZnCl_2 + H_2O$ $\quad \Delta H^0_{298} = -125.0\ kJ\ mol^{-1}$ reaction 2.25

Silica is frequently found in discharged LTS catalyst and it may be a serious problem because it deposits on the surface and, finally, into the pores of the pellets, where it reacts to form zinc silicate, resulting in a decrease of the CO conversion. Silica reduces the quantity of available "free ZnO" on the top of the bed, which interferes with the normal absorption of poisons (***1***).

Other poisons for copper catalysts include arsenic, which could come from some types of CO_2 removal systems, and trivalent phosphorous, which could originate from boiler water feed, but these are rarely encountered in the process gas (***1***).

2.3 NEW GENERATION (MTS) CATALYSTS

For the shift catalyst, the criticality comes on lower temperature activity (kinetics) and thermal stability (***101***). Advanced medium-temperature shift (MTS) catalysts offer benefits in achieving

incremental H_2 (lower CO-slip) by switching from HTS to MTS with necessary modifications around the existing reactor that may allow additional H_2. This option offers further advantages (***101***):

- a lower S/C ratio in the reformer is possible, without sintering and Fisher-Tropsch reactions from Fe-based (HTS) catalysts;
- no by-pass control on the PG boiler is needed; this controller is prone to metal dusting problems.

Other considerations are similar to LTS process, except that another reactor is needed and an additional exchanger is required to reach MTS process temperatures (***101***).

2.3.1 PRECIOUS METAL-BASED CATALYSTS

Noble-metal-containing formulations have been reported as active and non-pyrophoric, with activity higher than those of conventional WGS catalysts in the MTS range (300-400 °C), thus potential candidates for the WGS process (***102***). The use of supported noble metal catalysts may offer significant advantages, including operation at higher temperatures, where kinetics are more favourable, no need of activation prior to the use, no degradation on exposure to air or temperature cycles and availability of conventional wash-coating technologies (***80***).

These catalysts have been prepared employing the wet impregnation method, using the nitrates, as precursors, and the following commercial metal oxide powders as supports (***80***): CeO_2 (3.3 m^2/g), TiO_2 (42.0 m^2/g), Y-stabilized zirconia (YSZ, 12.0 m^2/g), Al_2O_3 (83.0 m^2/g), MgO (22.0 m^2/g), La_2O_3 (7.0 m^2/g), and SiO_2 (144.0 m^2/g). The effect of the nature of the metallic phase has been investigated over Pt, Rh, Ru, and Pd supported on CeO_2 (***80***,***103***,***104***), Al_2O_3 (***80***,***104***) and TiO_2 (***105***) and the activity follows the same order (Fig. 2.23):

$$\boldsymbol{Pt > Rh \approx Ru > Pd}$$

On the contrary, other researchers (***54***) reported that activity over Al_2O_3, varied with the order:

$$\boldsymbol{Ru > Pt > Pd \approx Rh}$$

while for other authors (***106***) the rates were essentially the same for CeO_2. These differences may be attributed to the different nature of the support used and/or, as will be discussed below, to the effects of the structural and morphological characteristics of the support on catalytic activity (***105***). In fact, Pt/CeO_2 catalysts are 15 times more active than Pt/Al_2O_3 catalysts (***107***). The introduction of the noble metals onto the ceria surface creates surface defects, which promote the decomposition of the surface intermediates (***28***). Ceria-supported precious metals have great potential for use as WGS catalysts (***108***).

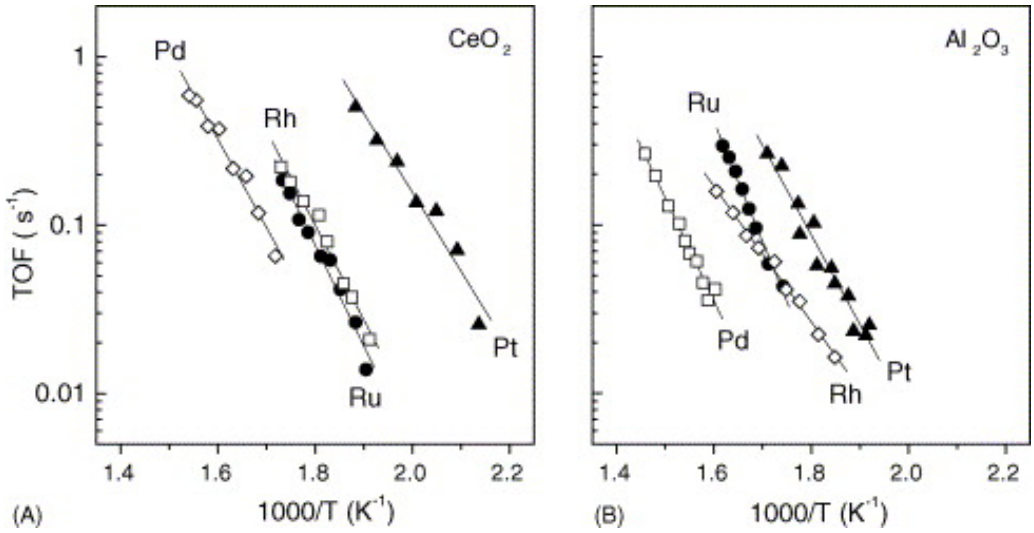

Fig. 2.23 Arrhenius plots of rates (TOF values) of CO conversion obtained for Pt-, Rh-, Ru-, and Pd-containing catalysts (0.5 wt.%) supported on (A) CeO_2 and (B) Al_2O_3 (***80***).

The TOF values of CO conversion do not depend on metal loading, dispersion or crystallite size, but depend strongly on the nature of the metal oxide carrier (***80***,***105***). Therefore, the reducibility of the support plays a crucial role on the catalytic performances of dispersed noble metal catalysts on "reducible" metal oxides (***80***). On the other hand, it is very important to note that Pt –containing catalysts exhibit significantly higher activities when supported on "reducible" (TiO_2, CeO_2, La_2O_3, and YSZ) rather than on "non-reducible" oxides (Al_2O_3, MgO, and SiO_2) (***80***). The activity of the catalysts is related to the kind of support used; however, there is not an identifiable correlation between the activity and surface area of the support for the catalysts (***109***).

Furthermore, Gorte *et al.* (***108***) observed that Pd and Pt dispersion may change rather dramatically under WGS conditions at 400 °C, even after less than 100 min. Additional evidences that ceria-supported Pd and Pt undergo sintering under these mild conditions have been reported by Shen *et al.* (***110***), who found even more dramatic increases in the size of Pd particles supported on CeO_2 when the catalyst was used for methanol synthesis.

The most interesting additive that dramatically affect the WGS rate is Fe: small quantities of Fe (2.2 wt.%) increase the WGS rate of 1 wt.% Pd/CeO_2 catalysts rather dramatically (***108***). Moreover, $Pt/CeO_2/Al_2O_3$ seems to be the best catalyst formulation, especially in MTS conditions (***107***). The activity dependence on the metal precursor, other than the method of support genesis, may be also observed (***109***,***111***,***112***,***113***,***114***).

The deactivation may be explained by many mechanisms, including surface coverage by *in-situ* formed carbonate-like species, and partial loss of the re-oxidizing ability in highly reducing CO/H_2 environment (***102***). Among the various metal-support combinations examined so far, the Pt/CeO_2 catalyst seems to be a promising candidate, characterized by high activity at low-to-medium reaction temperatures (***105***). However, recent studies under conditions typical of a reformer outlet showed a progressive deactivation of ceria-supported noble metals (***115***), that has been attributed to the irreversible reduction of the support (***115***) and/or to structural changes and sintering of the metallic phase (***106***,***116***).

Work performed at Johnson Matthey (UK) on Pt/CeO_2 catalysts indicates that despite the high initial activity obtained in the medium–high temperature range (325-400 °C) (,Fig. 2.24), the catalyst loses activity under synthetic and real reformate tests due to a further gradual decrease in the total BET surface area and to the occlusion by Pt particles of the support (***102***). In addition, methanation takes place on Pt/CeO_2 at temperatures higher than 375 °C (***102***,***117***). A new formulation developed by Johnson Matthey (JM8) consists of non-pyrophoric Pt-containing species, with improved durability and no methanation activity between 200 and 500 °C) (***102***).

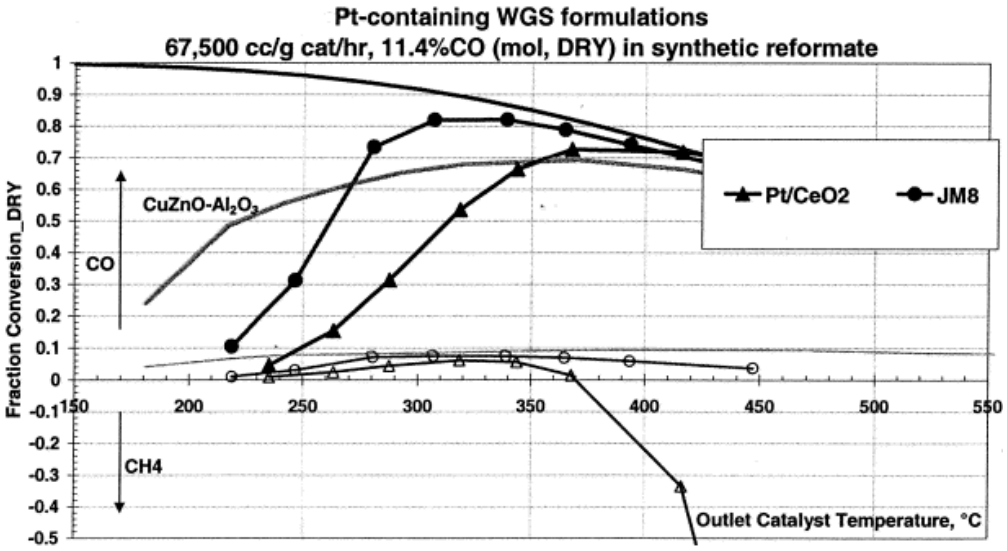

Fig. 2.24 Performance of a new Johnson Matthey Pt-containing WGS catalyst (JM8) compared to a Pt/CeO_2 catalyst at the same metal content (***102***).

2.3.2 GOLD CATALYSTS

Gold catalysts show a rapidly growing interest for WGS processes due to their high activity for CO oxidation at low temperature (***118***,***119***,***120***,***121***,***122***,***123***,***124***,***125***,***126***,***127***). The catalytic activity of the gold/metal oxide catalysts depends strongly not only on the dispersion of the gold particles, but also on the state and structure of the supports (***128***,***129***). The nature of the support exerts a decisive influence on the catalytic activity of Au-containing catalysts (***118***,***130***,***129***).

Generally, the high activity values of Au-containing systems are attributed to the synergism between Au and support, which involves the formation of intermediate species by interaction between CO, adsorbed on the support cations, and OH groups arising from the dissociation of water molecules on ultrafine Au particles (***119***,***120***,***131***). However, it is still uncertain if the catalytically active species are metal Au or oxidized Au species (***132***).

Au-containing catalysts, however, are sensitive to the preparation conditions, the desired properties of the final materials depend on the dispersion, Au-particle size, and intimate metal-support contact. The Au-particle size may easily changes during the reaction and strongly impacts the activity (***128***,***130***,***133***,***134***,***122***). The preferred technique for the preparation of highly

dispersed Au-based catalysts is the deposition-precipitation method (***120***) (***125***) (***121***) (***135***), that involves the deposition of gold hydroxide onto the support through a chemical reaction in aqueous solution between $HAuCl_4 \cdot 3H_2O$ and Na_2CO_3. The deposition-precipitation has the advantage, over co-precipitation, to allow the preparation of catalysts with narrower particle size distribution, where Au is mainly localized on the surface of the supports (***121***,***135***). Haruta *et al* (***125***) reported that catalysts with Au particles smaller than 5 nm were highly active in CO oxidation.

Many investigations (***136***,***137***) showed that the pre-treatment conditions exert decisive effects on the chemical state of gold, and consequently on the ultimate catalytic activity. Lee et al. (***138***) observed the transition of Au_2O_3 through AuO to metallic Au, regardless of the support used. It appears that gold-oxide species are very sensitive to temperature treatments, as they seem to transform into metallic Au below 400 °C (***125***,***138***,***139***,***140***).

Ceria is a very suitable support for WGS catalysts and Andreeva *et al.* (***123***) have recently reported that deposition of Au on ceria leads not only to a high WGS activity; for the first time high stability over a long-term test was recorded for this type of Au-containing catalysts. Ceria is a crucial component in emission control catalysts, mainly on account of its role in oxygen storage (***141***). The ease Ce^{4+}/Ce^{3+} redox reaction ($2\ CeO_2 \leftrightarrows Ce_2O_3 + ½\ O_2$) is believed to be the driving force leading to this behaviour. However, the role of ceria as a support for noble metal-based catalyst is not only related to its high oxygen storage capacity, but also to improved dispersion of the noble metal and promotion of the WGS reaction (***142***,***94***).

Au/Fe_2O_3 catalysts have been reported as good ones in the low temperature WGS reaction, due to a specific interaction between Au and ferric oxide support (***135***,***143***). Therefore, the activity in the low temperature region (150-250 °C) is attributed to the Au-containing species, while the activity in the high temperature region (> 300 °C) attributed to the active magnetite phase (***144***).

The comparison of the low-temperature WGS activity of Au/CeO_2 prepared by modified deposition-precipitation (***130***) and Au/Fe_2O_3 (***121***) shows the importance of the nature of the support and method of preparation on the catalytic activity and selectivity of Au-containing catalysts, mainly during CO removal from the methanol reformate gas in fuel-cell applications (***126***). Moreover, the crystallinity and reductive property of the support appreciably affect the catalytic activity (***131***,***145***).

The catalytic stability tests, however, show that the activity of the Au-containing catalysts decreases during the catalytic operations (***121***). Au particles usually agglomerate into bigger ones after the catalytic tests, and this is usually considered to be the main reason for the deactivation of Au-based catalysts (***123***). Pt/CeO_2, Au/CeO_2 and Au/Fe_2O_3 catalysts, tested for 48 h, show a good stability of the first sample in comparison to the other two catalysts (Fig. 2.25**Errore. L'origine riferimento non è stata trovata.**) (***135***). The stability of the Au/CeO_2 catalyst dramatically decreases, due to the higher average size of the Au particles after reaction.

Whereas CeO_2 is inactive for the WGS reaction, the Au/CeO_2 catalysts are initially very active, with rates that are in some cases superior to those for a commercial Cu/Zn/Al (Süd Chemie) catalyst (***146***).

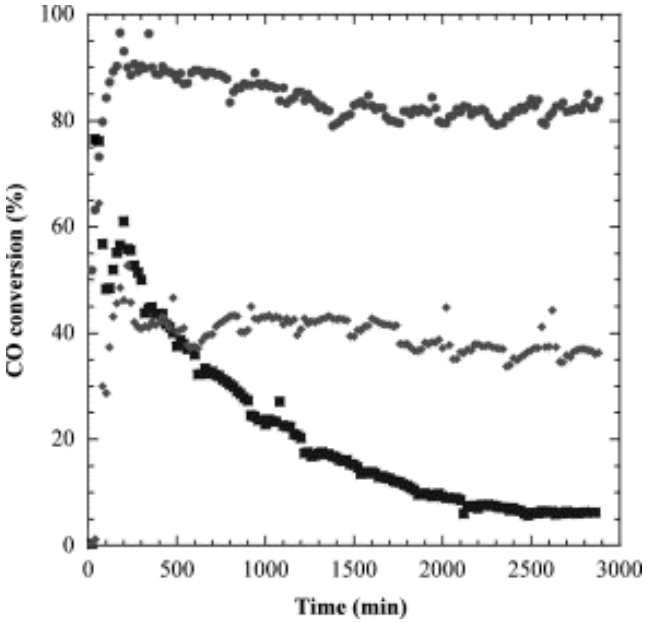

Fig. 2.25 Deactivation test of the Pt/CeO_2 sol–gel, Au/CeO_2 co-precipitation, and Au/Fe_2O_3 deposition–precipitation catalysts; (●) Pt/CeO_2; (□) Au/CeO_2; (□) Au/Fe_2O_3 (***135***).

REFERENCES

1. Twigg, M. V. *Catalyst Handbook,* 2nd ed.; Wolfe: London (UK), 1996.
2. Mazaud, J. P. In *Technique de l'Ingénieur, Traité Génie des Procédés;*, 1996; Vol. J 5 480, p 10.
3. Chinchen, G. C.; Denny, P. J.; Jennings, J. R.; Spencer, M. S.; Waugh, K. C. *Appl. Catal.* **1988,** *36,* 1.
4. Moe, J. M. *Chem. Eng. Prog.* **1962,** *58,* 33.
5. de Molliens, P. In *Technique de l'Ingénieur, Traité Génie des Procédés;* Vol. J 4 080, p 1.
6. Pasel, J.; Samsun, R. C.; Schmitt, D.; Peters, R.; Stolten, D. *J. Power Source* **2005,** *152,* 189.
7. Millar, G. J.; Rochester, C. H.; Waugh, K. C. *J. Catal.* **1993,** *142,* 263.
8. Zhorov, Y. M. *Thermodynamics of Chemical Processes;* Mir Publishers: Moscow [RUS], 1987.
9. Rhodes, C.; Hutchings, G. J.; Waugh, A. M. *Catal. Today* **1995,** *23,* 43.
10. Germani, G.; Schuurman, Y. *AIChE J.* **2006,** *52,* 1806.
11. Ovesen, C. V.; Stolze, P.; Norskovand, J. K.; Campbell, C. T. A. *J. Catal.* **1992,** *134,* 445.
12. Jakdetchai, O.; Nakajima, T. *J. Mol. Struct. (Theor.)* **2002,** *619,* 51.
13. van Herwijnen, T.; de Jong, W. A. *J. Catal.* **1980,** *63,* 83.
14. Ovesen, C. V.; Clausen, B. S.; Hammershøi, B. S.; Steffensen, G.; Askgaard, T.; Chorkendorff, I.; Nørskov, J. K.; Rasmussen, P. B.; Stoltze, P.; Taylor, P. *J.Catal.* **1996,** *158,* 170.
15. Salmi, T.; Hakkarainen, R. *Appl. Catal.* **1989,** *49,* 285.
16. Gokhale, A. A.; Dumesic, J. A.; Mavrikakis, M. M. *J. Amer. Chem. Soc.* **2008,** *130,* 1402.
17. Grabow, L. C.; Gokhale, A. A.; Evans, S. T.; Dumesic, A.; Mavrikakis, M. *J. Phys. Chem.* **2008,** *112,* 4608.
18. Campbell, J. M.; Nakamura, J.; Campbell, C. T. *J. Catal.* **1992,** *136,* 24.
19. Jacobs, G.; Davis, B. H. *J. Catal.* **2007,** *20,* 122.
20. Jacobs, G.; Patterson, P. M.; Graham, U. M.; Sparks, D. E.; Davis, B. H. *Appl. Catal.* **2004,** *269,* 63.
21. Jacobs, G.; Graham, U. M.; Chenu, E.; Patterson, M.; Dozier, A.; Davis, B. H. *J. Catal.* **2005,** *229,* 499.
22. Pigos, J. M.; Brooks, C. J.; Jacobs, G.; Davis, B. H. *Appl. Catal. A* **2007,** *328,* 14.
23. Pigos, J. M.; Brooks, C. J.; Jacobs, G.; Davis, B. H. *Appl. Catal. A* **2007,** *319,* 47.
24. Shido, T.; Yamaguchi, A.; Asakura, K.; Iawasawa, Y. *J. Mol. Catal.* **2000,** *163,* 67.
25. Shido, T.; Iwasawa, Y. *J. Catal.* **1991,** *129,* 343.
26. Koryabkina, N. A.; Phatak, A. A.; Ruettinger, W. F.; Farrauto, R. J.; Rebeiro, F. H. *J. Catal.* **2003,** *217,* 233.
27. Shido, T.; Iwasawa, Y. *J. Catal.* **1992,** *136,* 493.
28. Shido, T.; Iwasawa, Y. *J. Catal.* **1993,** *141,* 71.
29. Mhadeshwar, A. B.; Vlachos, D. G. *Catal. Today* **2005,** *105,* 162.
30. Mhadeshwar, A. B.; Vlachos, D. G. *J.Catal.* **2005,** *234* (1), 48.

31. Tibiletti, D.; Meunier, F. C.; Goguet, A.; Reid, D.; Burch, R.; Boaro, M.; Vicario, M.; Trovarelli, A. *J. Catal.* **2006,** *244,* 183.
32. Nishimura, H.; Yatsu, T.; Fujitami, T.; Uchijima, T.; Nakamura, J. *J. Mol. Catal. A* **2000,** *155,* 3.
33. Klier, K. *Catal. Today* **1992,** *15,* 361.
34. Callaghan, C.; Fishtik, I.; Datta, R.; Carpenter, M.; Chmielewski, M.; Lugo, A. *Surface Sci.* **2003,** *541,* 21.
35. Ratnasamy, C.; Wagner, J. P. *Catal. Rev.* **2009,** *51* (3), 325.
36. Taylor, H. S. *J. Phys. Chem.* **1926,** *30,* 145.
37. Tibiletti, D.; Goguet, A.; Reid, D.; Meunier, F. C.; Burch, R. *Catal. Today* **2006,** *113,* 94.
38. Burch, R. *Phys. Chem.* **2006,** *8,* 5483.
39. Choi, Y.; Stenger, H. G. *J. Power Source* **2003,** *124,* 432.
40. Newsome, D. *Catal. Rev. Sci. Eng.* **1980,** *21,* 275.
41. Fiolitakis, E.; Hofmann, H. *J. Catal.* **1983,** *80,* 328.
42. Froment, G. F.; Bischoff, K. B. *Chemical Reactor: Analysis and Design,* 2nd ed.; Wiley: New York [US].
43. Campbell, J. S. *I.E.&C. Proc. Res. Dev.* **1970,** *9,* 588.
44. Amadeo, N.; Laborde, M. *Int. J. Hydrogen Energy* **1995,** *20,* 949.
45. Lin, S. T.; Chen, Y. H.; Yu, C. C.; Liu, Y. C.; Lee, C. H. *J. Power Source* **2005,** *148,* 43.
46. Lin, S. T.; Chen, Y. H.; Yu, C. C.; Liu, Y. C.; Lee, C. H. *Int. J. Hydrogen Energy* **2006,** *31,* 413.
47. Sun, J.; DesJardins, J.; Buglass, J.; Liu, K. *Int. J. Hydrogen Energy* **2005,** *30,* 1259.
48. Keiski, R. L.; Salmi, T.; Niemisti, P.; Ainassaari, J.; Pohjola, V. J. *Appl. Catal.* **1996,** *137,* 349.
49. Ayastuy, J. L.; Guiterrez-Ortiz, M. A.; Gonzales-Marcos, J. A.; Aranzabal, A.; Gonzales-Velasco, J. R. *I.E.&C. Res.* **2005,** *44,* 41.
50. Boudart, M.; Meais, D. E.; Vannice, M. A. *Ind. Chim. Belg.* **1967,** *32,* 281.
51. Vannice, M. A.; Hyun, S. H.; Kalpakci, B.; Liauh, W. C. *J. Catal.* **1979,** *56,* 358.
52. Podolsky, W. F.; Kim, Y. G. *I.E.&C., Proc. Des. Dev.* **1974,** *13,* 415.
53. Rase, H. F. *Reactors Design for Process Plants;* Wiley: New York [US], 1977; Vol. 2.
54. Grenoble, D. C.; Estadt, M. M.; Ollis, D. F. *J. Catal.* **1981,** *67,* 90.
55. Ward, A. M.; Axon, S. A.; Murray, P. J. to Johnson Matthey PLC. WO Patent 2003,022,427, 2003.
56. O'Brein, R.; Hu, X. D.; Tuell, R.; Cai, Y. to Sud-Chemie Inc. WO Patent 2005,019,099, 2005.
57. Topsoe, H.; Boudart, M. *J. Catal.* **1973,** *31,* 364.
58. Rangel, M. C.; Sassaki, R. M.; Galembeck, F. *Catal. Lett.* **1995,** *33,* 237.
59. Tinkle, M.; Dumesic, J. A. *J. Catal.* **1987,** *103,* 65.
60. Robbins, M.; Wertheim, K. G.; Sherwood, R. C.; Buchanan, D. N. E. *J. Phys. Chem. Solids* **1971,** *32,* 717.
61. Edwards, M. A.; Whittle, D. M.; Rhodes, C.; Rohan, D.; Shannon, M. D.; Hutchings, G. J.; Kiely, C. J. *Phys. Chem. Chem. Phys.* **2002,** *4,* 3902.
62. Domka, F.; Basinska, A.; Fielderow, R. *Surf. Technol.* **1983,** *18,* 275.
63. Wei, K.; Zheng, Q.; Xu, J.; Ling, X. US Patent 6,569,804, 2003.
64. Quadro, E. B.; Dias, M. R.; Amorim, A. M. M.; Rangel, M. C. *J. Braz. Chem. Soc.* **1999,** *10,* 51.
65. Batista, M. S.; Assaf, E. M.; Assaf, J. M.; Ticianelli, E. A. *Inter. J. Hydrogen Energy* **2006,** *31,* 1204.
66. Sidhu, P. S.; Gilkes, R. J.; Posner, A. M. *J. Inorg. Nucl. Chem.* **1978,** *40,* 429.
67. Hawker, P. N. *Hydrocarbon Processing* **1982,** *61,* 183.

68. Borgas, D. J.; Bridger, G. W. *Chem. Ind.* **1960,** 1426.
69. Emmett, P. H.; Schultz, J. F. *J. Am. Chem. Soc.* **1933,** *55,* 1376.
70. Eastman, E. D. *J. Am. Chem. Soc.* **1922,** *44,* 975.
71. Keiski, R. L.; Salmi, T. *Appl. Catal.* **1992,** *87,* 61.
72. Chinchen, G. C.; Logan, R. H.; Spencer, M. S. *Appl. Catal.* **1984,** *12,* 69.
73. Chinchen, G. C.; Spencer, M. S. *Catal Today* **1991,** *10,* 293.
74. Figueiredo, R. T.; Ramos, A. L. D.; Andrade, H. M. C.; Fierro, J. L. G. *Catal. Today* **2005,** *107-108,* 671.
75. Kalchev, M. G.; Andreev, A. A.; Zotov, N. S. *Kinet. Catal.* **1995,** *36,* 821.
76. Sekizawa, K.; Yano, S.; Eguchi, K.; Arai, H. *Appl. Catal.* **1998,** *169,* 291.
77. Ginés, M. J. L.; Amadeo, N.; Laborde, M.; Apesteguía, C. R. *Appl. Catal.* **1995,** *131,* 283.
78. Lima, A. A. G.; Nele, M.; Moreno, E. L.; Andrade, H. M. C. *Appl. Catal.* **1998,** *171,* 31.
79. Figueiredo, R. T.; Andrade, H. M. C.; Fierro, J. L. G. *Braz. J. Chem. Eng.* **1998,** *15,* 168.
80. Panagiotopoulou, P.; Kondarides, D. I. *Catal. Today* **2006,** *112,* 49.
81. Yurieva, T. M.; Minyukova, T. P. *React. Kinet. Catal. Lett.* **1985,** *29,* 55.
82. Fujitani, T.; Saito, M.; Kanai, Y.; Watanabe, T.; Nakamura, J.; Uchijima, T. *Chem. Lett.* **1994,** *24,* 1877.
83. Young, P. W.; Clark, C. B. *Chem. Eng. Prog.* **1973,** *69,* 69.
84. Pepe, F.; Polini, R.; Stoppa, L. *Catal. Lett.* **1992,** *14,* 15.
85. Tanaka, Y.; Utaka, T.; Kikuchi, R.; Sasaki, K.; Eguchi, K. *Appl. Catal.* **2003,** *238,* 11.
86. Saito, M.; Murata, K. *Catal. Surv. Asia* **2004,** *8,* 285.
87. Wu, J.; Saito, M. *J. Catal.* **2000,** *195,* 420.
88. Ray, J. A.; Huang, D. C.; Dienes, E. K. to Catalyst & Chemicals Europe S.A. (BE). EP Patent 0,371,526, 1990.
89. Shishido, T.; Yamamoto, M.; Atake, I.; Li, D.; Tian, Y.; Morioka, H.; Honda, M.; Sano, T.; Takehira, K. *J. Mol. Catal. A* **2006,** *253,* 270.
90. Shishido, T.; Yamamoto, M.; Li, D.; Tian, Y.; Morioka, H.; Honda, M.; Sano, T.; Takehira, K. *Appl. Chem. A* **2006,** *303,* 62.
91. Tanaka, Y.; Utaka, T.; Kikuchi, R.; Sasaki, K.; Eguchi, K. *Appl. Catal. A* **2003,** *242,* 287.
92. Tanaka, Y.; Utaka, T.; Kikuchi, R.; Takeguchi, T.; Sasaki, K.; Eguchi, K. *J. Catal.* **2003,** *215,* 271.
93. Tanaka, Y.; Takeguchi, T.; Kikuchi, R.; Eguchi, K. *Appl. Catal.A.* **2005,** *279,* 59.
94. Li, Y.; Fu, Q.; Stephanopoulos, M. F. *Appl. Catal.* **2000,** *27,* 179.
95. Patt, J.; Moon, D. J.; Phillips, C.; Thompson, L. *Catal. Lett.* **2000,** *65,* 193.
96. Fujita, S.; Usui, M.; Ohara, E.; Takezawa, N. *Catal. Lett.* **1992,** *13,* 394.
97. Burch, R.; Golunski, S. E.; Spencer, M. S. *Catal. Lett.* **1990,** *5,* 55.
98. Burch, R.; Golunski, S. E.; Spencer, M. S. *J. Chem. Soc. Faraday Trans.* **1990,** *86,* 2683.
99. Fierro, G.; Jacono, M. L.; Invers, M.; Porta, P.; Cioci, F.; Lavecchia, R. *Appl. Catal.* **1996,** *137,* 327.
100. Fleisch, T. H.; Mieville, R. L. *J. Catal.* **1984,** *90,* 165.
101. Ratan, S.; Vales, C. F. *Hydrocarb. Process.* **2002,** 57.
102. Ghenciu, A. F. *Curr. Opin. Solid State Mater.* **2002,** *6,* 389.
103. Hilaire, S.; Wang, X.; Luo, T.; Gorte, R. J.; Wagner, J. *Appl. Catal. A* **2004,** *258,* 271.
104. Wheeler, C.; Jhalani, A.; Klein, E. J.; Tummala, S.; Schmidt, L. D. *J. Catal.* **2004,** *223,* 191.
105. Panagiotopoulou, P.; Kondarides, D. I. *J. Catal.* **2004,** *225,* 327.

106. Bunluesin, T.; Gorte, R. J.; Graham, G. W. *Appl. Catal.* **1998,** *15,* 107.
107. Kolb, G.; Pennemann, H.; Zapf, R. *Catal. Today* **2005,** *110,* 121.
108. Gorte, R. J.; Zhao, S. *Catal. Today* **2005,** *104,* 18.
109. Basinska, A.; Kepinski, L.; Domka, F. *Appl. Catal.* **1999,** *183,* 143.
110. Shen, W. J.; Kobayashi, A.; Ichihashi, Y.; Matsumura, Y.; Haruta, M. *Catal. Lett.* **2001,** *73,* 161.
111. Niwa, Y.; Aika, K. *J. Catal.* **1996,** *162,* 138.
112. Murata, S.; Aika, K. *J. Catal.* **1992,** *136,* 118.
113. Murata, S.; Aika, K. *Appl. Catal.* **1992,** *82,* 1.
114. Lu, K.; Tatarchuk, B. L. *J. Catal.* **1987,** *106,* 166.
115. Zalc, J. M.; Sokolovskii, V.; Löffler, D. G. *J. Catal.* **2002,** *206,* 169.
116. Wang, X.; Gorte, R. J.; Wagner, J. P. *J. Catal.* **2002,** *212,* 225.
117. Mendelovici, L.; Steinberg, M. *J. Catal.* **1985,** *96,* 353.
118. Tabakova, T.; Idakiev, V.; Andreeva, D.; Mitov, I. *Appl. Catal. A* **2000,** *202,* 91.
119. Andreeva, D.; Idakiev, V.; Tabakova, T.; Andreev, A. *J. Catal.* **1996,** *158,* 354.
120. Andreeva, D.; Idakiev, V.; Tabakova, T.; Andreev, A.; Giovanoli, R. *Appl. Catal. A* **1996,** *134,* 275.
121. Andreeva, D.; Idakiev, V.; Tabakova, T.; Giovanoli., R. *Bulg. Chem. Comm.* **1998,** *30,* 64.
122. Andreeva, D.; Tabakova, T.; Idakiev, V.; Christov, P.; Giovanoli, R. *Appl. Catal. A* **1998,** *169,* 9.
123. Andreeva, D.; Idakiev, V.; Tabakova, T.; Ilieva, L.; Falaras, P.; Bourlinos, A.; Travlos, A. *Catal. Today* **2002,** *72,* 51.
124. Sakurai, H.; Ueda, A.; Kobayashi, T.; Haruta, M. *Chem. Comm.* **1997,** 271.
125. Haruta, M.; Tsubota, S.; Kobayashi, T.; Kageyama, H.; Genet, M. J.; Delmon, B. *J. Catal* **1993,** *144,* 175.
126. Haruta, M.; Daté, M. *Appl. Catal.* **2001,** *222,* 427.
127. Choudhary, T. V.; Goodman, D. W. *Topics Catal.* **2002,** *21,* 25.
128. Haruta, M. *Catal. Today* **1997,** *36,* 153.
129. Hua, J.; Wei, K.; Zheng, Q.; Lin, X. *Appl. Catal. A* **2004,** *259,* 121.
130. Tabakova, T.; Boccuzzi, F.; Manzoli, M.; Sobczak, J. W.; Idakiev, V.; Andreeva, D. *Appl. Catal. B* **2004,** *49,* 73.
131. Ilieva, L. I.; Andreeva, D. H.; Andreev, A. A. *Thermochim. Acta* **1997,** *292,* 169.
132. Hodge, N. A.; Kiely, C. J.; Whyman, R.; Siddiqui, M. R. H.; Hutchings, G. J.; Pankhurst, Q. A.; Wagner, F. E.; Rajaram, R. R.; Golunski, S. E. *Catal. Today* **2002,** *72,* 133.
133. Schubert, M. M.; Plzak, V.; Garche, J.; Behm, R. J. *Catal. Lett.* **2001,** *76,* 143.
134. Wolf, A.; Schuth, F. *Appl. Catal.* **2002,** *226,* 1.
135. Luengnaruemitchai, A.; Osuwan, S.; Gulari, E. *Catal. Comm.* **2003,** *4,* 215.
136. Hao, Z. P.; An, L. D.; Wang, H. L. *React. Kinet. Catal. Lett.* **2000,** *70,* 153.
137. Horváth, D.; Tóth, L.; Guczi, L. *Catal. Lett.* **2000,** *67,* 117.
138. Lee, S. J.; Gavriilidis, A.; Pankhurst, Q. A.; Kyek, A.; Wagner, F. E.; Wong, P. C. L.; Yeung, K. L. *J. Catal.* **2001,** *186,* 1.
139. Park, E. D.; Lee, S. J. *J. Catal.* **1999,** *186,* 1.
140. Haruta, M.; Yamada, N.; Kobayashi, T.; Iijima, S. *J. Catal.* **1989,** *115,* 301.
141. Taha, R.; Duprez, D.; Mouaddib-Moral, N.; Gauthier, C. *Stud. Surf. Sci.Catal.* **1998,** *116,* 549.
142. Harrison, B.; Diwell, A. F.; Hallett, C. *Plat. Met. Rev.* **1988,** *32,* 73.
143. Venugopal, A.; Scurrell, M. S. *Appl. Catal.* **2004,** *258,* 241.

144. Andreev, A.; Idakiev, V.; Mihajlova, D.; Shopov, D. *Appl. Catal.* **1986,** *22,* 385.
145. Fu, Q.; Weber, A.; Flytzani-Stephanopoulos, M. *Catal. Lett.* **2001,** *77,* 87.
146. Kim, C. H.; Thompson, L. T. *J. Catal.* **2005,** *230,* 66.

3 EXPERIMENTAL SESSION

3.1. MATERIALS

3.1.1 PEROVSKITE (PVK)

Due to their high activity and thermal stability, much attention has been paid to perovskite-type oxides, of general formula ABO_3 (where A and B are usually rare earth and transition metal cations, respectively) (***1***,***2***,***3***). Many metals are stable in the ABO_3 perovskite structure provided that the A (usually a rare-earth metal) and B (usually a transition metal) cations have dimension (r_A > 0.90Å, r_B > 0.51Å) in agreement with the limits of the so-called "tolerance factor" t ($0.8 < t < 1.0$) defined by Goldschmidt (***4***), as $t = (r_A + r_O)/\sqrt{2}(r_B + r_O)$, where r_A, r_B, and r_O are the ionic radii for A, B, and O, respectively. In the perovskite-type oxide, represented by the general formula ABO_3, the B cations have octahedral coordination with oxygen and the A cations are located in the dodecahedral sites of this structure (**Errore. L'origine riferimento non è stata trovata.**).

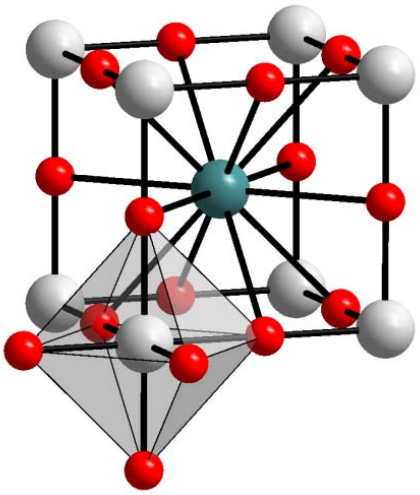

Fig. 3.1 PVK-type structure: A: green; B: grey; O: red. (A: La, Sr, Ba, Ca, etc. B: Ti, V, Cr, Mn, Fe, Co, Ni, Cu, Zr, Nb, Ru, etc.).

In the ABO_3 perovskites the A ions are in general catalytically inactive, and the active transition metal ions at the B position are placed at relatively large distances (ca. 0.4nm) from each other that a gas molecule interacts only with a single site. Even for a single A or B center, there is still the possibility to partially substitute these centers of the ABO_3 composition yielding a great variety of possibilities, e.g. $A_{1-x}A'_xB_{1-y}B'_yO_3$, as well as the possibility of having ordered systems with general formula $A_2BB'O_6$ (***5***).

One of the more successful applications is their use as combustion catalysts in exhaust gas cleaning utilizing low temperature burners. Furthermore, the perovskite materials can found important application in O^{2-} active membrane applications. The reason for the catalytic intent of perovskite oxides lies mainly in the high mobility of oxygen and the stabilization of unusual cations oxidation states in this structure, together with their stability at high temperature.

Modulation of these characteristics could be done by appropriate partial substitution of cations in A and B positions. The substitution in B position has the additional advantage that the cations in these sites are transition cations that usually have an important role in the catalytic processes (***3***). Provendier *et al.* (***6***) reported that $LaFeO_3$ was relatively stable and the substitution of a part of Fe with Ni resulted in an increase in the activity in partial oxidation of methane, in which Ni alone was reduced to form the highly dispersed metal particles without collapsing the $LaFeO_3$ perovskite structure.

3.1.2 HYDROTALCITE (HT)

Anionic clays or layered double hydroxides (LDHs) are lamellar mixed hydroxides with interlayer spaces containing exchangeable anions with general formula:

$$[M^{2+}_{(1-x)}M^{3+}_{x}(OH)_2]^{b+} \cdot (A^{n}_{b/n}) \cdot m\ H_2O$$

This class of compounds, also called hydrotalcite like compounds (HT), are relatively inexpensive to prepare in the laboratory scale (***7***). The most interesting properties are the homogeneous cation distribution and the ion exchange capacity in the precipitates. In addition, other important properties of the oxides obtained by calcination are (***3***):

1) high surface area,
2) basic properties,
3) formation of homogeneous mixture of oxides with very small crystal size, stable to thermal treatments, which by reduction form small and thermally stable metal crystallites,
4) ''memory effect'', which allows the reconstruction, under mild conditions, of the original hydrotalcite structure when contacting the product of the thermal treatment with water solutions containing various anions.

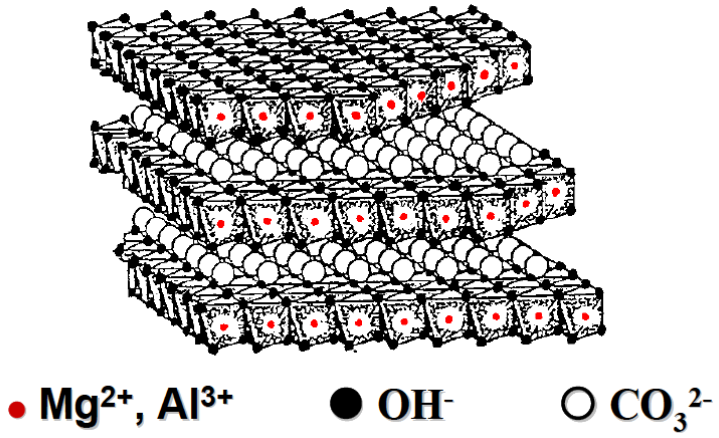

Fig. 3.2 Crystal structure of hydrotalcite-like precursor.

To understand the structure of these compounds, it is necessary to start from the structure of brucite [$Mg(OH)_2$], where octahedral of Mg^{2+} (6-fold coordinated to OH^-) share edges to form infinite sheets. These sheets are stacked on top of each other and are held together by hydrogen bonding (Fig. 3.3). When Mg^{2+} ions are substituted by a trivalent ion having a suitable ionic radius (such as Al^{3+} for hydrotalcite compounds), a positive charge is generated in the hydroxyl sheet.

This net positive charge is compensated by $(CO_3)^{2-}$ anions, which lie in the interlayer region between the two brucite-like sheets, In the free space of this interlayer the water of crystallization also finds a place.

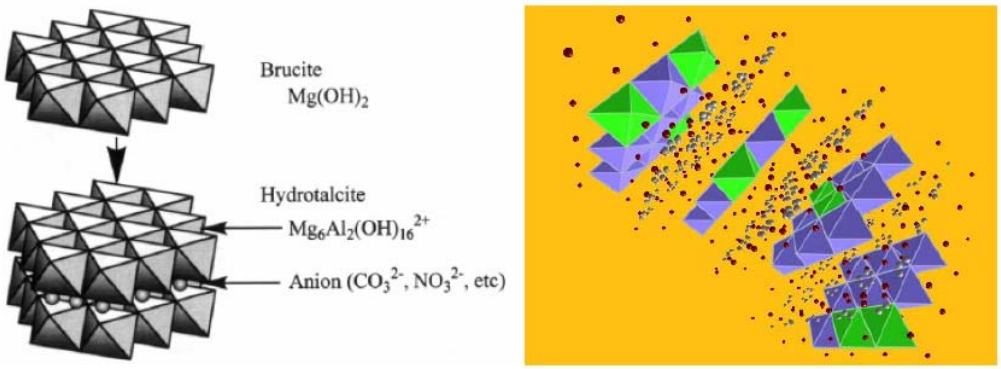

Fig. 3.3 Crystal structure of hydrotalcite-like precursor.

The hydrotalcite-derived catalysts (ex-HT), containing carbonates as interlayer anions, have already been reported as effective catalysts in the production of synthesis gas, using as active phase Ni, Rh and Ni/Rh. Active metal species is homogeneously distributed from the surface to the bulk of the catalyst particles and therefore a large part of the metal species is still located inside of the particles and cannot work as the active species. A general property of the ex- HT is that the amount and the nature of M(II) and M(III) modified the ratio between MgO and spinel phases. The reducibility and stability of the Ni catalysts (in which Ni is preferentially present in a solid solution with Mg), are strongly affected by the Mg/Al/Ni ratio due to three main effects (***8***,***9***).

3.2. CATALYST PREPARATION

3.2.1 PEROVSKITE-TYPE (PVK) SAMPLES

The perovskite-type (PVK) catalysts of the general formula:

$$La_{1-x}A'_xFe_{1-y}B'_yO_3$$

$$(La_{1-x}A'_x)_2CuO_4$$

were synthesized by a sol-gel method (Fig. 3.4), using the nitrates of the selected elements as starting materials and citric acid as complexing agent, known as citrate method (***10***):

1) The metal nitrates (1 M) are dissolved in deionized water, according to the nominal compositions reported in Table 3.1.
2) The calculated minimum amount of citric acid to bind the metals (1 M) is dissolved in de-ionized water, acting both as cation chelating of and reducing agent.
3) The cation solution is added drop by drop (0.67 drop/sec) into the citric acid solution, under vigorous magnetic stirring (rpm = 400) at room temperature (r.t.).
4) The final solution is placed in an electric oven and treated at 90 °C for 4 h (evaporation to dryness), then at 180 °C for 16 h (gel decomposition with NOx and COx evolution) forming a cake with homogeneous flakes of very small particle size.
5) After grinding of the obtained precursor, the powder is calcined at 650 °C (10 °C/min) in a muffle furnace for 12 h.

The most important parameters in the synthesis are the pH and the molar ratio of citric acid to total metal nitrates (C/M). Usually, it is selected a ratio C/M > 1 to ensure the complete chelating of the cations and avoid oxide or hydroxide precipitation. However, C/M ratio must be lower than 2 to avoid the crystallization and subsequent precipitation of citric acid excess during solvent evaporation (***10***,***11***). In the present work, the citric acid solution was prepared by dissolving $C_6H_8O_7$ (1 M) in distilled water to obtain a C/M molar ratio equal to 1.30. The pH was selected to avoid the precipitation before sol formation, in the present case pH = 1-2.

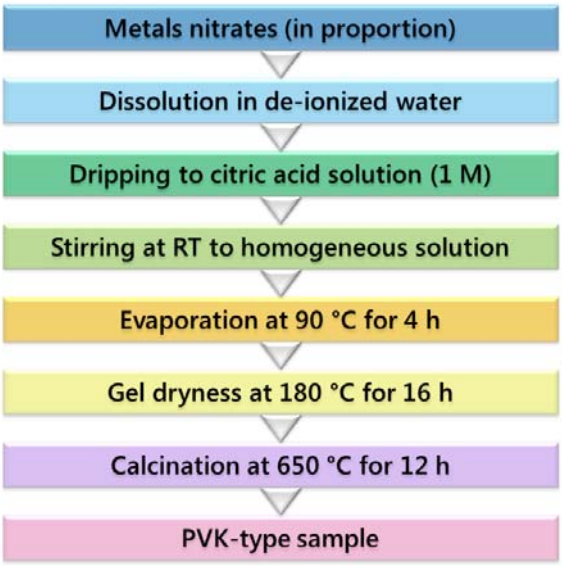

Fig. 3.4 Schematic diagram of the preparation of PVK-type sample (citrate method).

Sample	La	Ce	Fe	Cr	Cu	Formula
LaFe	1		1			*LaFeO3*
LaFeCr-Ce	0.9	0.1	0.9	0.1		*La0.9Ce0.1Fe0.9Cr0.1O3*
LaFeCr-Cu	1		0.9	0.08	0.02	*LaFe0.9Cr0.08Cu0.02O3*
LaCeCu	1.9	0.1		0.1		*La1.9Ce0.1CuO4*
CeFe		1	1			*CeFeO3*
CeFe-Cu		1	0.6		0.6	*CeFe0.6Cu0.6O3*

Table 3.1 Nominal composition of the investigated PVK samples.

3.2.2 HYDROTALCITE-TYPE (HT) PRECURSORS

The hydrotalcite-type precursors (HT) of general formula:

$$\mathbf{Cu_xZn_{6-x}Al_2(OH)_{16}(An)\cdot 4H_2O}$$

were synthesized in the laboratory using the co-precipitation method (Fig. 3.2):

1) The wished metal nitrates (1 M) are dissolved in deionized water, according to the nominal composition reported in Table 3.2.
2) The calculated amount (minimum one necessary to form HT precursors) of aqueous carbonate anions is dissolved in deionized water (2 M).
3) The cation solution is dropwise added, under energetic magnetic stirring, in the aqueous anion solution, at 60 °C, maintaining the pH constant (10.5 ± 0.1) by addition of NaOH (3 M). At the end, the obtained precipitate is maintained well dispersed in the same conditions (at 60 °C and pH = 10.5) under energetic magnetic stirring for 45 min.

4) The precipitate is then separated from the mother liquor by filtration under vacuum, washed with abundant hot water (60 °C) (400 mL/g_{SAMPLE}) and dried overnight at 60 °C.
5) After grinding of the obtained precursor, the powder is calcined at 500 °C (10 °C/min) in a muffle furnace for 2 h (***12***).
   a) Where required, after cooling to room temperature, the calcined sample is doped with 2 wt.% K by using the incipient wetness impregnation method. The water evaporation is carried out at 120 °C for 2 h and, then, the powder is calcined at 550 °C (10 °C/min) in a muffle furnace for 2 h.

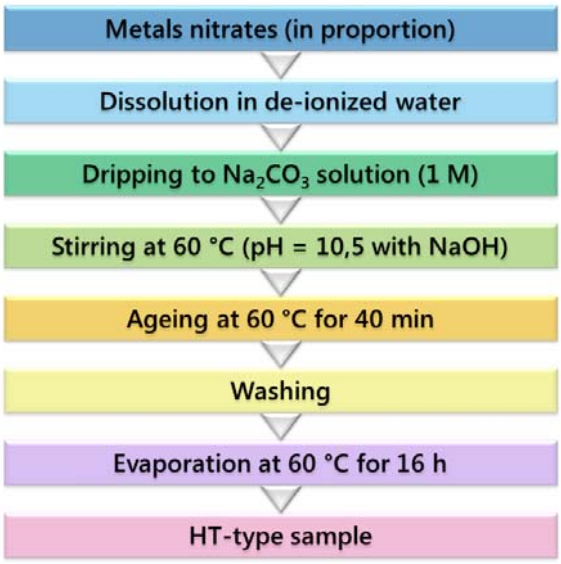

Fig. 3.5 Schematic diagram of the preparation of HT-type sample.

Sample	M^{2+}/M^{3+}	Cu (wt.%)	An	Formula
ZA3K (BO86-3)	3	-	carbonate	$Zn_6Al_2(OH)_{16}(CO_3)\cdot 4H_2O$
ZAC1c	3	≤ 20	carbonate	$Cu_xZn_{6-x}Al_2(OH)_{16}(CO_3)\cdot 4H_2O$
ZAC20c	3	≤ 20	carbonate	$Cu_{2x}Zn_{6-2x}Al_2(OH)_{16}(CO_3)\cdot 4H_2O$

Table 3.2 Nominal composition of the HT precursors.

3.3. CHARACTHERIZATION METHODS

3.3.1 X-RAY DIFFRACTION ANALYSIS (XRD)

The XRD powder analyses have been carried out using a Philips PW1050/81 diffractometer equipped with a graphite monochromator in the diffracted beam and controlled by a PW1710

unit (Cu Kα, λ = 0.15418 nm) (Fig. 3.6). A °2θ range from 10° to 80° has been investigated, by using a step size of 0.1° and a time per step of 2 sec.

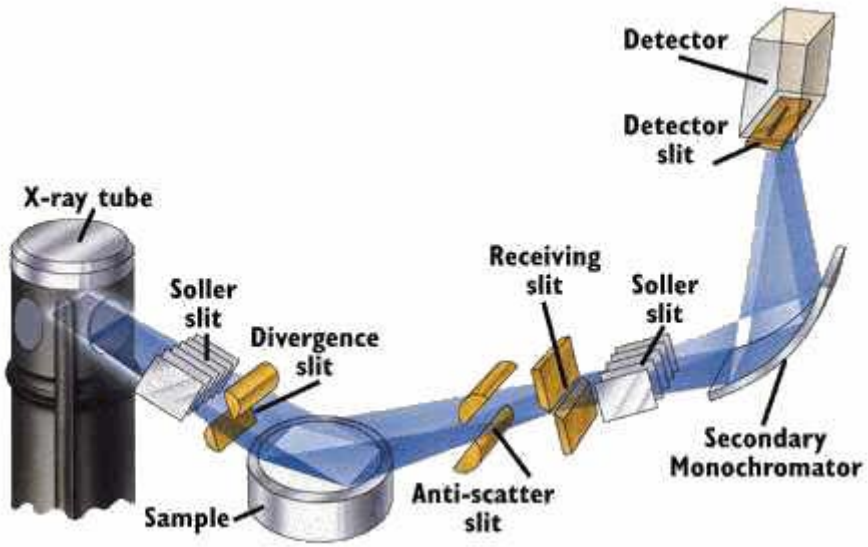

Fig. 3.6 Scheme of the instrument for the X-ray diffraction analysis

The phases present in the pattern have been analysed by using the Bragg's Law (Eq. 3.1 and Fig. 3.7), in order to calculate the *d* values to compare with those reported in the literature (***13***,***14***) and collected in a database of X'Pert Highscore software.

$$n\lambda = 2d \sin\theta \qquad \textbf{Eq. 3.1}$$

where:

- n = the order of the reflection (an integer);
- λ = the wavelength of the X-ray beam incident on a crystal with lattice planes;
- d = the distance between atomic layers in a crystal;
- θ = the diffraction angle.

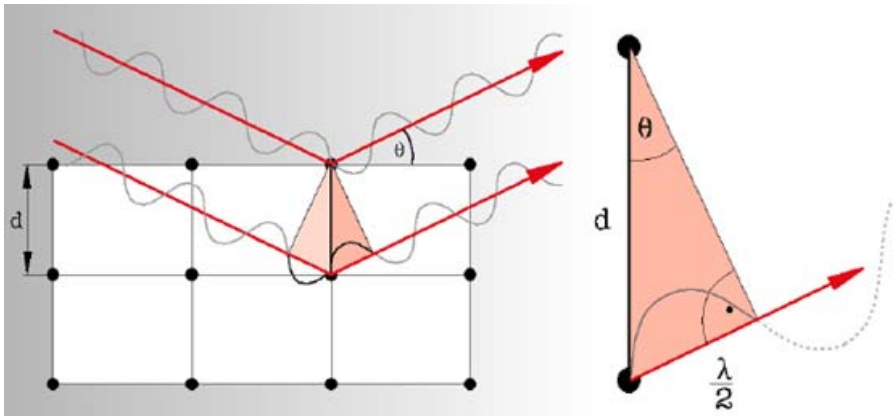

Fig. 3.7 Scheme of X-ray diffraction phenomenon.

The particle size (*D*) has been calculated by using the Debye-Scherrer's formula (Eq. 3.2).

$$D = \frac{k\lambda}{\beta \cos\theta} \qquad \textbf{Eq. 3.2}$$

where:

- k = a dimensionless constant that may range from 0.89 to 1.39 depending on the specific geometry of the scattering objects, but assumed ≈ 1 because its exact calculation required a fitting between the obtained diffractograms and the one of the perfect crystalline sample;
- λ = the wavelength of the X-ray beam incident;
- β = *B-b*, the integral breadth of a reflection (in radians 2θ) located at °2θ; B is the FWHM, while b is the instrumental distortion (FWHM in the same conditions of a material with crystallite size > 1000 Å);
- θ = the diffraction angle.

3.3.2 TEMPERATURE PROGRAMMED ANALYSES (TPR/O)

The reduction or oxidation profiles have been measured by using a ThermoQuest Instrument TPD/R/O 1100 Catalytic Surface Analyser, equipped by a TCD detector (Fig. 3.8). The analyses were carried out loading 0.05 g of sample, by using the following procedure:

- *Pre-treatment*: the sample was pre-treated under N_2 (20 mL/min) from r.t. to 150 °C (20 °C/min) and hold for 30 min at 150 °C.
- *Reduction*: after cooling until 60 °C, the reduction analysis was carried out using a 5 % H_2/Ar gas mixture (20 mL/min) up to 550 °C (10 °C/min) and hold for 60 min.
- *Oxidation*: after cooling until 60 °C, the oxidation analysis was carried out using a 5 % O_2/He gas mixture (20 mL/min) up to 550 °C (10 °C/min) and hold for 60 min.

TPO/R/O cycles are carried out on the spent sample to evaluate the redox of the active metals, while TPO/Mass Spectrometer Quadrupole analyses, heating the used sample from 60 to 950 °C (10 °C/min) in 5% O_2/He flow (20 mL/min), after the pre-treatment, allow to evaluate possible tar deposits on the catalyst surface by evolution of CO_x, monitored by the mass spectrometer.

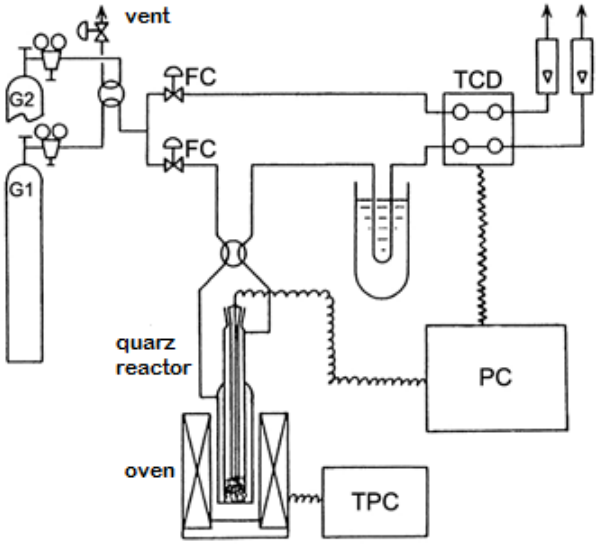

Fig. 3.8 Scheme of TPR/O instrument.

3.3.3 SURFACE AREA AND POROSIMETRY ANALYSES

The surface area values of the catalysts were determined by N_2-physisorption at – 196 °C by using the one point Brunauer-Emmet-Teller (BET) method (3.1) (***15***), using a Carlo Erba Sorpty model 1750. The sample (1 g) is pre-treated at 200 °C under vacuum to eliminate impurities and water superficial adsorbed; subsequently, it is analysed in a liquid nitrogen bath.

$$\frac{P}{V(P_0 - P)} = \frac{1}{V_m C} + \frac{C-1}{V_m C} \cdot \frac{P}{P_0} \qquad \textbf{3.1}$$

where:

- P = the equilibrium pressure;
- P_0 = the saturation pressure of adsorbate at the temperature of adsorption;
- V = the adsorbed gas quantity (i.e. volume of adsorbed gas per gram of solid at P);
- V_m = the monolayer adsorbed gas quantity (adsorbed N_2 volume per gram);
- $C = (E_1\text{-}E_L/RT)$, the BET constant; E_1 is the heat of adsorption for the first layer, and E_L is that for the second (and higher) layers, assumed equal to the heat of liquefaction.

This equation is linear in the range $0.05 < P/P_0 < 0.35$ of relative pressure; V_m and C are calculated from the slope value ($(C\text{-}1/V_mC)$) and from the y-intercept ($1/V_mC$). The specific surface (S_{BET}, m^2/g) is calculated by the following equation:

$$S_{BET} = \frac{V_m}{V_0} \cdot N_A \cdot \frac{k}{g_{CAT}} \qquad \textbf{3.2}$$

where:

- V_m = the monolayer adsorbed gas quantity (adsorbed N_2 volume per gram);
- V_0 = the molar adsorbed gas volume;
- N_A = 6.0221418×10^{23} mol^{-1}, Avogadro number;
- k = the conversion factor, takes into account also density and molar weight of adsorbed gas;
- g_{CAT} = the sample weight.

The porosimetry analysis has been carried out with a Micromeritics ASAP 2020 (Accelerated Surface Area and Porosimetry System). All samples (300 mg) were previously degassed under vacuum at 150 °C until a pressure of 30 µm Hg was reached and maintained for 30 min. Finally, they were heated up to 250 °C and maintained for 30 min. After pre-treatment, the sample holder was moved to analysis section. The N_2 adsorption/desorption analysis at -196 °C followed a protocol that consisted an establishing a listing of target pressure at which data were collected. This instrument, as the previous one, uses the BET equation but, measuring the adsorption and desorption isothermal curves by the volume of adsorbed/desorbed N_2, as a function of relative pressure, can also calculate,, in addition to the BET surface area value, the volume and the pore size distribution of the sample through the BJH equation (***15***).

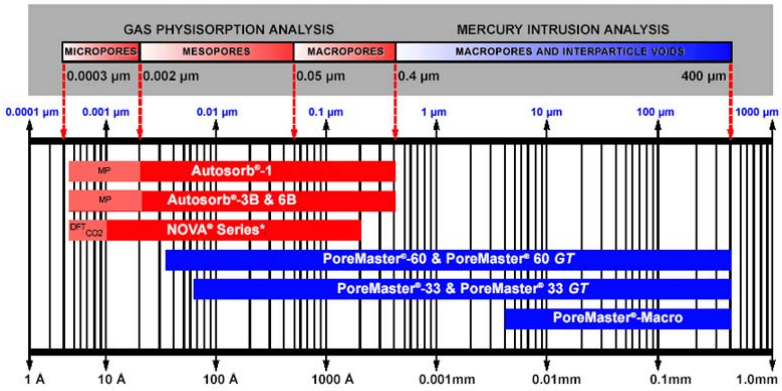

Fig. 3.9 Classification of pore size distribution and appropriate methods of analysis.

3.4. PLANT SPECIFICATIONS

3.4.1 CATALYST SHAPE

The prepared catalyst powders (PVK or ex-HT) are pressed, in form of round plate pellet (diameter ≈ 20 mm and thickness ≈ 4 mm) in a stainless steel mould under a homogeneous pressure of 3.2 t/cm^2. After 90 min (PVK) or 15 min (ex-HT), the pressure is released and the disk removed is milled and sieved to obtain pellets of desired size. The commercial catalysts, being

already in tablet or monolithic form, are directly crushed and sieved. The wanted size of the sample loaded in the reactor is 30-40 mesh, to optimize the radial gradient of temperature and concentration, avoiding diffusion phenomena ($d_{REACT}/d_{CAT} \geq 5$). On the other hand, the minimum length of the catalytic bed is selected to avoid any preferential by-pass, which may change the contact time in real conditions ($d_{REACT}/d_{CAT} \geq 10$) (***16***).

3.4.2 REDUCTION STEP

Before the catalytic tests, all the investigates samples are reduced *in situ*, in order to generate the active phases, using the right procedure for each catalyst type.

3.4.2.1 TYPICAL REDUCTION OF HTS CATALYSTS

3.4.2.1.1 REDUCTION OF PVK-TYPE SAMPLES

The reduction of PVK-type samples are carried out using a typical HTS reduction process, considering the Fe-containing active phase (Fig. 3.10). It is always carried out with process gas and conditions have to be chosen in order to allow the required reactions, avoiding any further reduction to metallic iron.

1) The reactor is initially purged free from air using N_2, reaching a pressure of 0.5 MPa.
2) The converter is heated at 120 °C/h for the first hour and then using a 70 °C/h ramp up to 500 °C. Reduction usually commences at about 150 °C and, during this step, the process gas stream is characterized by a S/H_2 ratio of 3.
3) When the temperature of 500 °C is reached on the top of the bed and is stabilized, it is possible to increase the pressure and decrease the S/H_2 ratio.

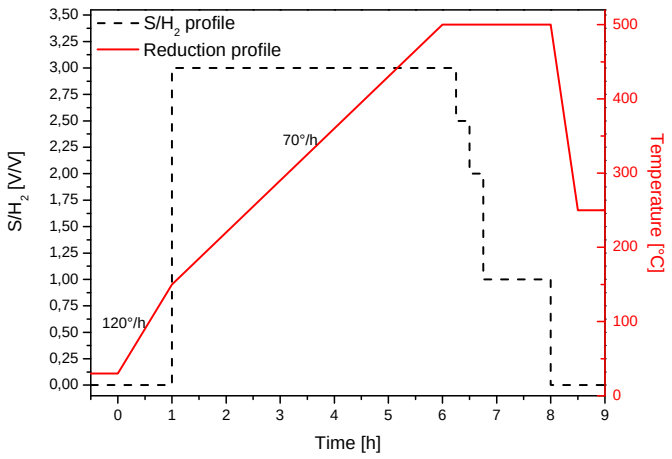

Fig. 3.10 Reduction procedure of the PVK-type samples.

3.4.2.1.2 REDUCTION OF PRECIOUS-METAL SAMPLES

The precious-metal (PM) based catalyst is reduced with the process gas, using a typical industrial procedure for these types of catalyst (Fig. 3.11), consisting to the following tasks:

1) the reactor is purged with N_2 to remove O_2 eventually present and heated up to 350 °C (180 °C/h).
2) The reduction starts at 150 °C and the process gas used has a S/DG ratio of 0.33.
3) The inlet temperature at 350 °C is kept constant for 1 h and, in the middle of this step, the pressure is increased from 0.5 to 1.0 MPa.

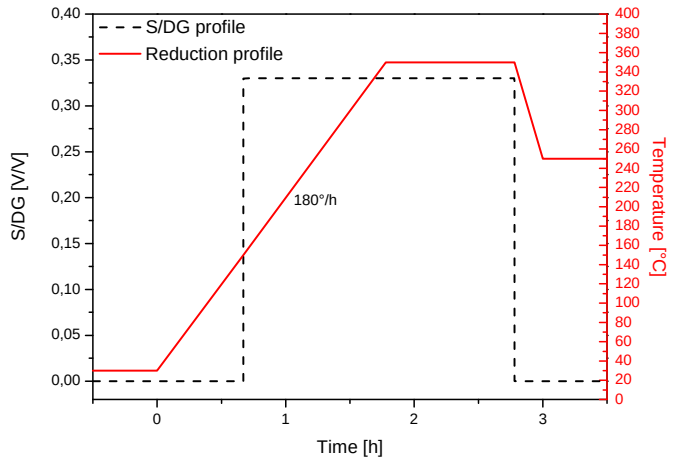

Fig. 3.11 Reduction procedure of the PM-based samples.

3.4.2.2 TYPICAL REDUCTION OF M/LTS CATALYSTS

The temperature rise during the reduction is controlled by adjusting the H_2 flow in the carrier gas. During the reduction step, the hot spot temperature is controlled at 220 °C and never should be allowed to exceed 250 °C.

The N_2 pressure is 1.0 MPa with a gas hourly space velocity between 300 and 400 h^{-1}. Typical industrial procedure is (Fig. 3.12):

1) The first task is to remove O_2 by purging N_2 in the reactor and, after that, to heat the catalyst to 175 °C (50 °C/h).
2) When 175 °C is reached and kept constant, a flow of 0.8 % of H_2 is added, maintaining the inlet temperature of 175 °C.
3) The H_2 concentration is increased with step of 0.2 v/v % without to exceed 1.2 v/v % at this stage for 18 h.
4) The temperature is increased up to 220°C (15 °C/h), avoiding to exceed 1.5 % of H_2 in N_2.
5) When 220 °C is reached and stabilized, the H_2 concentration may slowly be increased up to 4 v/v %, with step of 0.5 v/v %, observing that the catalyst hot spot temperature does not exceed 230 °C. If the catalyst hot spot exceeds 250 °C, the protocol must be

interrupted (injection of H_2/N_2 stopped, depressurization of the reactor, sweeping by fresh N_2).

6) The reduction is considered completed when a H_2 consumption of less than 0.2v/v % is verified consecutively for 2 h.

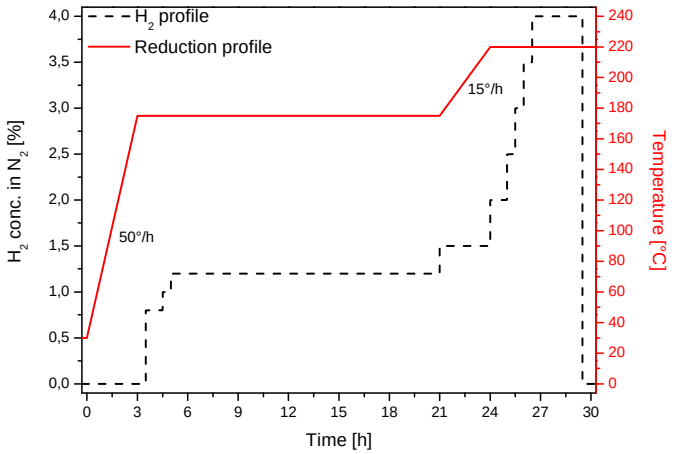

Fig. 3.12 Reduction procedure of the M/LTS samples.

3.4.3 LAB-SCALE PILOT PLANT

The activity tests have been carried out in a lab-scale pilot plant, schematically reported in figure 3.10, consisting of the following sections:

I. Feed section.
II. Reaction section.
III. Separation section.
IV. Analysis section.

The feed section consists of a three independent gas lines [dry gas (DG), N_2,H_2] and a H_2O line. Gas flow rates are controlled by using thermal mass flow controllers (MFC's), whereas an HPLC pump is utilized to feed the distilled water, pre-heated to allow its vaporization before the mixing with DG. A by-pass line allows to the inlet gas to flow without to cross on the catalyst bed, in order to determine a right and accurate analysis of the inlet DG composition.

The reaction section consists of a tubular (fixed bed) reactor with an internal diameter of 1.0 cm, placed vertically inside a furnace. A thermocouple (cromel/alumel, d = 0.8 mm) is inserted inside the reactor to accurately measure the axial thermal profile (Fig. 3.14); in fact, the catalyst is loaded in the isothermal zone of the oven between two region filled by inert material. To avoid any damage in the operating conditions, the reactor is in a special alloy material (INCOLOY 800HT) constituted by chromium (19-23 wt. %), nickel (30-35 wt.%) and iron (>39.5 wt.%), with a

carbon content of 0.06-0.10 wt.%. The pressure is controlled by a pneumatic relief valve, known as grove valve, placed at the exit of the reactor.

After the reaction section, the outlet stream goes in a cooled gas-liquid separator (0 °C) to separate the amount of non-reacted water and, subsequently, the wet gas flow is measured by a drum-type meter. Finally, it is dried through a trap containing a dehydrator agent (drierite, CaSO4) with a Co-salt indicator, 8 mesh) in order to remove any residual traces of water from the syngas. A needle valve may be used to adjust inlet gas pressure to GC, analysing only a fraction of it.

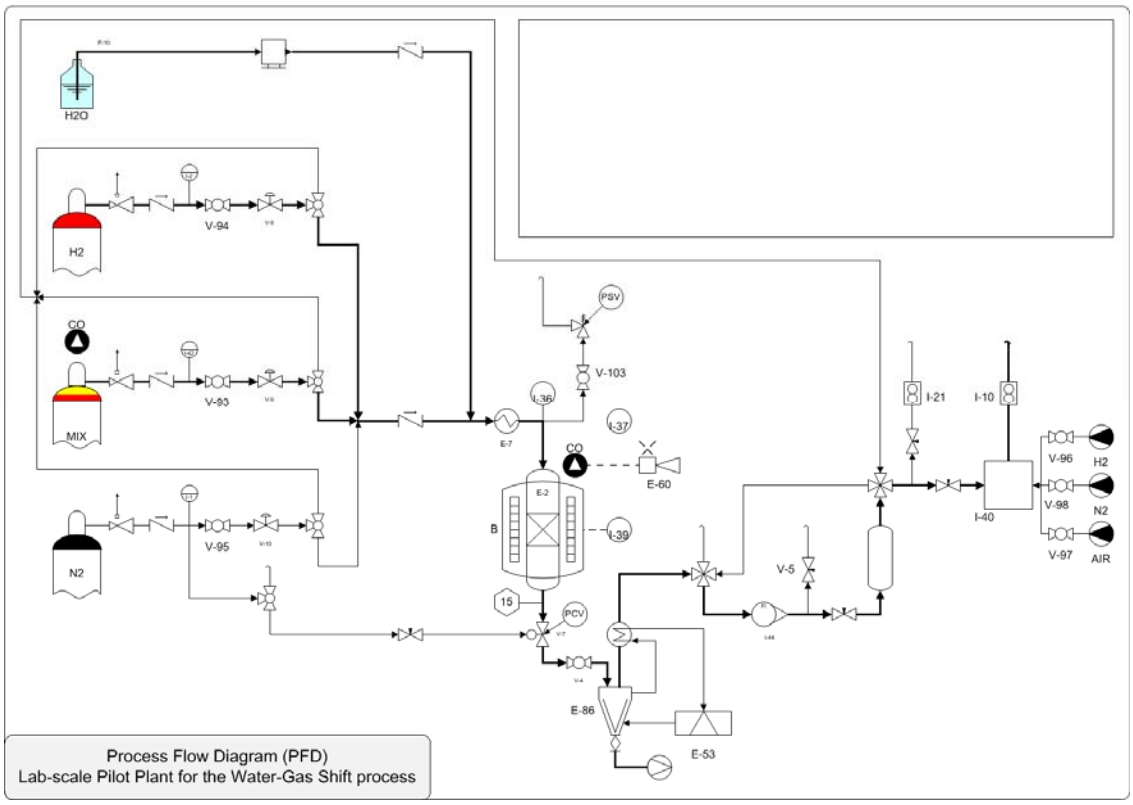

Fig. 3.13 Process flow diagram (PFD) of the lab-scale pilot plant.

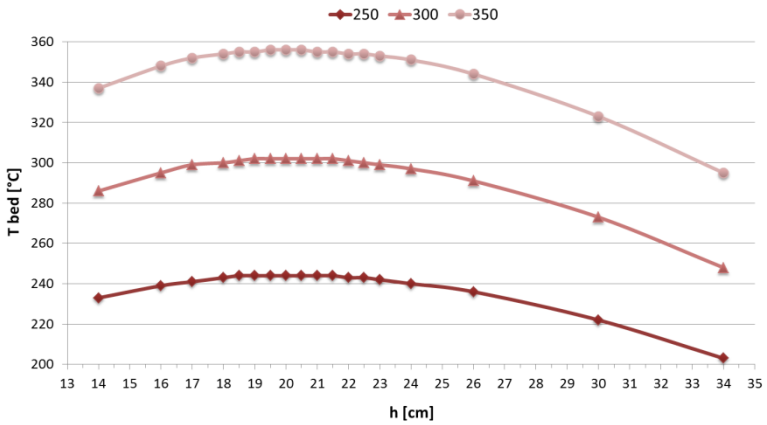

Fig. 3.14 Thermal profile of the oven for three different imposed temperatures.

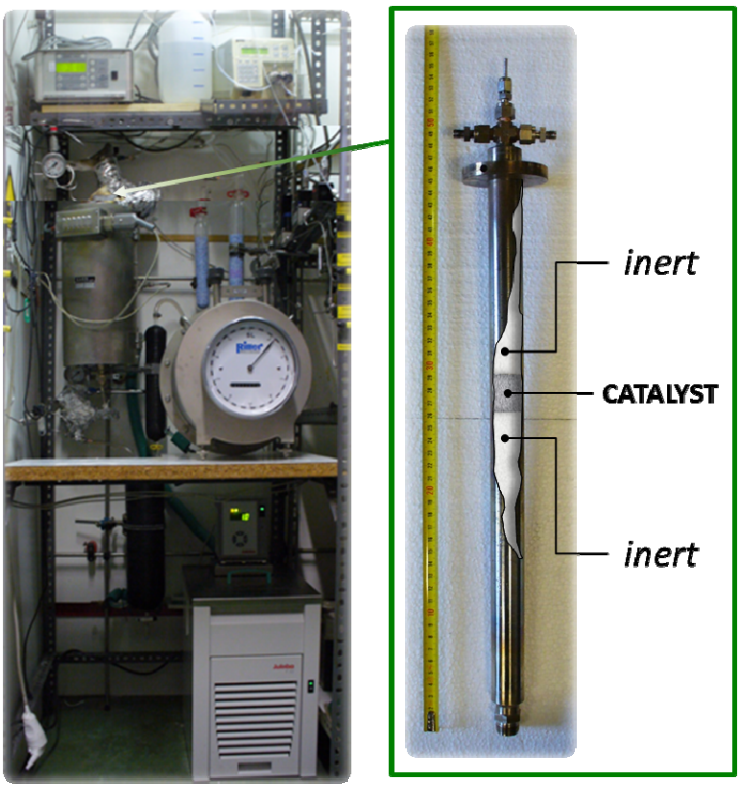

Fig. 3.15 Pictures of the lab-scale pilot plant and tubular reactor.

3.4.4 INERT MATERIAL

Before the catalytic tests, it has been necessary to define the right inert for the reactor loading. The blank tests (6 h) have been carried out at different temperatures (250-480 °C), with a S/DG ratio of 0.72 and a contact time of 1.0 sec, to favour the WGS reaction, testing three different materials, chosen between those potentially more interesting:

i. steatite ($Mg_3Si_4O_{10}(OH)_2$);
ii. corundum (α-Al_2O_3);
iii. quartz (SiO_2).

As shown in figure 3.13, the outlet DG composition is practically the same for all the investigated inert materials, in comparison to the inlet one. For analogy with the industrial R&D group, *corundum* (20 mesh) has been selected.

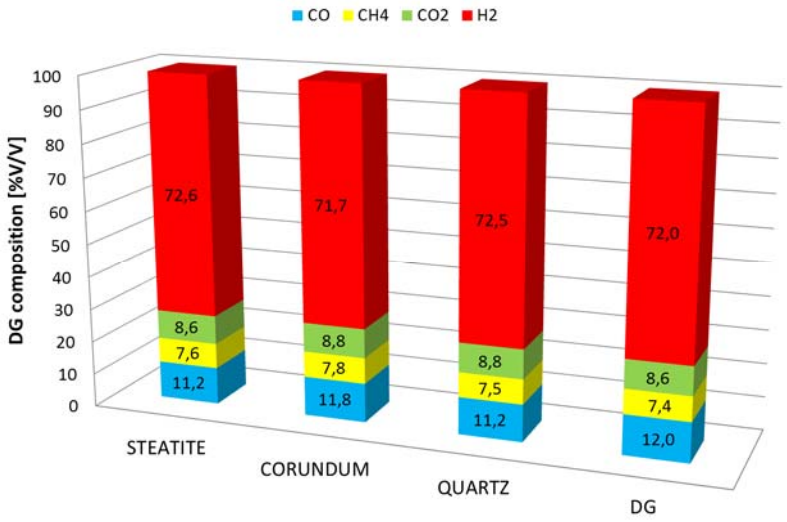

Fig. 3.16 Reactivity of the inert materials in term of the outlet percentage of DG (DG_{INLET} = H_2 72 v/v %, CO 12 v/v %, CH_4 7.4 v/v %, CO_2 8.6 v/v %).

3.4.5 ACTIVITY TESTS

The activity of the catalysts has been studied as a function of different parameters, approaching the possible industrial conditions (Table 3.1): pressure (P), temperature measured at the outlet of the catalytic bed (T), steam to dry gas ratio (S/DG) and contact time (τ). The study was focused not only to check the catalytic activity at middle temperature, but also to define the operating conditions for a good conversion with low S/DG ratio and contact time values, thus ensuring a lower overhead of the plant.

To evaluate the stability with time-of-stream, some catalysts have been subjected to stability for 100 h at 300 °C, τ =f 1.0 sec and the lower S/DG ratio (0.25).

SAMPLE	OPERATING CONDITIONS		WET GAS		FLOW CONDITIONS	
Name	T_{exp} °C	P_{exp} bar	S/DG	S/C	τ s	GHSV h^{-1}
L 5 H	**250**	15	**0,55**	1,96	**1,00**	3600
L 2 H	**250**	15	**0,25**	0,89	**1,00**	3600
L 5 M	**250**	15	**0,55**	1,96	**0,50**	7200
L 2 M	**250**	15	**0,25**	0,89	**0,50**	7200
L 5 L	**250**	15	**0,55**	1,96	**0,25**	14400
L 2 L	**250**	15	**0,25**	0,89	**0,25**	14400
M 5 H	**300**	15	**0,55**	1,96	**1,00**	3600
M 2 H	**300**	15	**0,25**	0,89	**1,00**	3600
M 5 M	**300**	15	**0,55**	1,96	**0,50**	7200
M 2 M	**300**	15	**0,25**	0,89	**0,50**	7200
M 5 L	**300**	15	**0,55**	1,96	**0,25**	14400
M 2 L	**300**	15	**0,25**	0,89	**0,25**	14400
H 5 H	**350**	15	**0,55**	1,96	**1,00**	3600
H 2 H	**350**	15	**0,25**	0,89	**1,00**	3600
H 5 M	**350**	15	**0,55**	1,96	**0,50**	7200
H 2 M	**350**	15	**0,25**	0,89	**0,50**	7200
H 5 L	**350**	15	**0,55**	1,96	**0,25**	14400
H 2 L	**350**	15	**0,25**	0,89	**0,25**	14400

Table 3.1 List of the tests carried out for the WGS process.

3.5. QUALI-QUANTITATIVE ANALYSIS

3.5.1 GAS CHROMATOGRAPHY

The product syngas is analysed using an online GC (PERKIN ELMER Auto System XL), equipped with a Carbosphere 80/100 packed column (6 ft × 1/8 in. outer diameter), able to separate H_2, CO, CO_2 and CH_4 at an oven temperature of 120 °C.

A thermal conductivity detector (TCD, carrier gas = N_2) is used to detect the H_2 amount, whereas CO, CO_2 and CH_4 are detected by a flame ionisation detector (FID) with a methanator before it (Fig. 3.17). A six-port valve is used to inject a constant volume of charge into the column, using a sampling loop of 1.0 mL (Fig. 3.18).

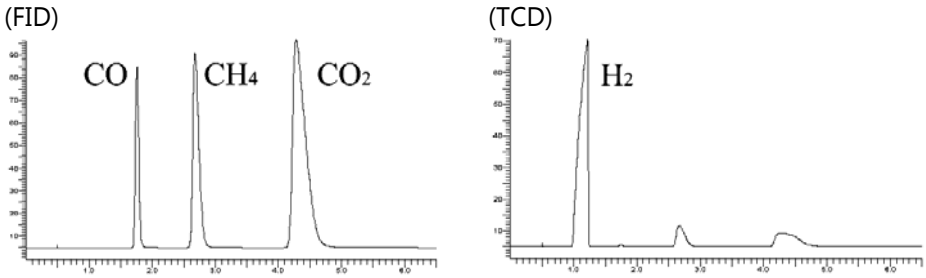

Fig. 3.17 Examples of typical FID and TCD chromatograms of outlet synthesis gas.

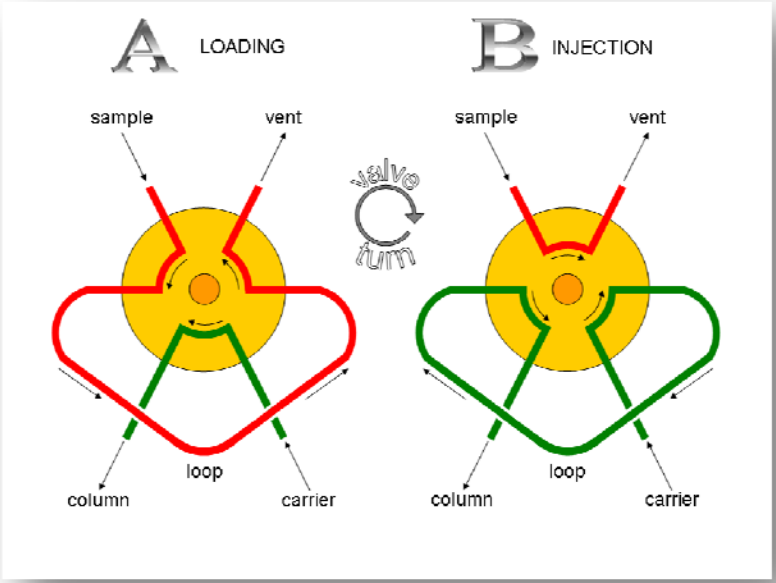

Fig. 3.18 6-ports valve to inject flow non-stop: (A) LOAD position; (B) INJECT position

3.5.2 DATA ELABORATION

The data obtained from the GC analyses show the DG composition after reaction, that, together with the total condensed water, permits to calculate the conversion (χ), selectivity (*S*), yield (γ) and mass balance ($C_{OUT/IN}$) values, by using the following formula:

$$\chi_{CO} = \frac{[CO]^{IN} - [CO]^{OUT}}{[CO]^{IN}} \cdot 100 = 1 - \frac{[CO]^{OUT}}{[CO]^{IN}} \cdot 100 = \left(1 - \frac{\%CO^{OUT} \cdot F_{DG}^{OUT}}{\%CO^{IN} \cdot F_{DG}^{IN}}\right) \cdot 100$$

$$\chi_{H_2O} = \frac{[H_2O]^{IN} - [H_2O]^{OUT}}{[H_2O]^{IN}} \cdot 100 = 1 - \frac{[H_2O]^{OUT}}{[H_2O]^{IN}} \cdot 100 = \left(1 - \frac{V_{H_2O}^{OUT} \cdot 1{,}006}{F_{H_2O}^{IN} \cdot t_{STREAM}}\right) \cdot 100$$

$$S_j = \frac{[j]}{[CO]^{IN} - [CO]^{OUT}} \cdot 100 = \frac{[j]^{OUT} - [j]^{IN}}{[CO]^{IN} - [CO]^{OUT}} \cdot 100 = \left(\frac{\%j^{OUT} \cdot F_{DG}^{OUT} - \%j^{IN} \cdot F_{DG}^{IN}}{\%CO^{IN} \cdot F_{DG}^{IN} - \%CO^{OUT} \cdot F_{DG}^{OUT}}\right) \cdot 100$$

j = CH_4, CO_2, H_2

$$\gamma_{H_2} = \frac{[H_2]}{[CO]^{IN}} \cdot 100 = \frac{[H_2]^{OUT} - [H_2]^{IN}}{[CO]^{IN}} \cdot 100 = \left(\frac{\%H_2^{OUT} \cdot F_{DG}^{OUT} - \%H_2^{IN} \cdot F_{DG}^{IN}}{\%CO^{IN} \cdot F_{DG}^{IN}}\right) \cdot 100$$

$$\gamma_{H_2} = \frac{[H_2]}{[CO]^{IN}} \cdot 100 = \frac{[H_2]}{[CO]^{IN} - [CO]^{OUT}} \cdot \frac{[CO]^{OUT} - [CO]^{IN}}{[CO]^{IN}} \cdot 100 = \frac{\chi_{CO} \cdot S_{H_2}}{100}$$

$$\%C_{OUT/IN} = \frac{[CO]^{OUT} + [CH_4]^{OUT} + [CO_2]^{OUT}}{[CO]^{IN} + [CH_4]^{IN} + [CO_2]^{IN}} \cdot 100 = \left(\frac{\%CO^{OUT} + \%CH_4^{OUT} + \%CO_2^{OUT}}{\%CO^{IN} + \%CH_4^{IN} + \%CO_2^{IN}} \cdot \frac{F_{DG}^{OUT}}{F_{DG}^{IN}}\right) \cdot 100$$

Legend:

$\%CO^{IN}$	Inlet percentage of CO	$\%CO^{OUT}$	Outlet percentage of CO
$\%CO_2^{IN}$	Inlet percentage of CO_2	$\%CO_2^{OUT}$	Outlet percentage of CO_2
$\%CH_4^{IN}$	Inlet percentage of CH_4	$\%CH_4^{OUT}$	Outlet percentage of CH_4
$\%H_2^{IN}$	Inlet percentage of H_2	$\%H_2^{OUT}$	Outlet percentage of H_2
F_{DG}^{IN}	Inlet flow of Dry Gas	F_{DG}^{OUT}	Outlet flow of Dry Gas
$F_{H_2O}^{IN}$	Inlet flow of H_2O	$V_{H_2O}^{OUT}$	Outlet Volume of H_2O
t_{STREAM}	Time of stream		

REFERENCES

1. Ciambelli, P.; Cimino, S.; Rossi, S. D.; Lisi, L.; Minelli, G.; Porta, P.; Russo, G. *Appl. Catal. B* **2001,** *29,* 239.
2. Porta, P.; Cimino, S.; Rossi, S. D.; Faticanti, M.; Minelli, G.; Pettiti, I. *Mater. Chem. Phys.* **2001,** *71,* 165.
3. Takehira, K. *Catal. Surv. Japan* **2002,** *6,* 19.
4. Goldschmidt, V. M. *Akad. Oslo. J. Mat. Natur.* **1926,** *2,* 7.
5. Fierro, J. L. G. *Catal. Today* **1990,** *8,* 153.
6. Provendier, H.; Petit, C.; Estournes, C.; Libs, S.; Kiennemann, A. *Appl. Catal. A* **1999,** *180,* 163.
7. Trifirò, F.; Vaccari, A. Chapter 8. In *Comprehensive Supramolecular Chemistry;* Atwood, J. L., Davies, J. E. D., MacNicol, D. D., Vögtle, F., Eds.; Pergamon: Oxford (UK), 1996; Vol. 7, p 251.
8. Basile, F.; Basini, L.; D'Amore, M.; Fornasari, G.; Guarinoni, A.; Matteuzzi, D.; del Piero, G.; Trifirò, F.; Vaccari, A. *J. Catal.* **1998,** *173,* 247.
9. Basile, F.; Fornasari, G.; Poluzzi, E.; Vaccari, A. *Appl. Clay Sci.* **1998,** *13,* 329.
10. Xu, Q.; Huang, D.; Chen, W.; Lee, J.; Wang, H.; Yuan, R. *Scripta Materialia* **2004,** *50,* 165.
11. Patil, M. M.; Deshpande, V. V.; Ravi, V. *Ceram. Inter.* **2006,** *32,* 345.
12. Schiødt, N. C. to Haldor Topsoe A/S (DK). EP Patent 2,141,118, 2010.
13. *Powder Diffraction File, Inorganic Phases;* International Centre for Diffraction Data: Swarthmore PA (US), 1991.
14. Klug, H. P.; Alexander, L. E. *X-Ray Diffraction Procedures;* Wiley: New York (US), 1974.
15. Gregg, J. S.; Sing, K. S. W. *Adsorption, Surface Area and Porosity,* 2nd ed.; New York (US), 1982.
16. Sanfilippo, D. *Catal. Today* **2004,** *34,* 259.

4 RESULTS AND DISCUSSION

4.1. AIM OF THE WORK

The current PhD thesis refers to the water-gas shift (WGS) reaction and the requirements for a further develop of the industrial processes. Most ammonia plants convert CO to CO_2 by high-temperature CO conversion, followed by low-temperature process. For special process designs, it may be advantageous to combine these two steps to form only one step, called "medium temperature shift" (MTS), carried out in an isothermal or adiabatic reactors, with an exit temperature of about 300°C.

Initially, the study has been focused on the investigation of commercial catalysts, examining their deactivation in industrial conditions. The catalytic activity of the commercial catalysts has been studied as a function of different parameters: pressure, temperature, steam to dry gas ratio (S/DG) and contact time (τ). The aim was not only to check the catalytic activity at middle temperature, but also to define the operating conditions for a good conversion operating at low S/DG ratio and contact time values, thus ensuring a lower overhead of the plant.

Successively, innovative materials, as bulk (PVK and ex-HT) catalysts, have been studied in view of the preparation of structured reactor (i.e. membrane reactor), that may enhance the H_2 production by the WGS process.

4.2. COMMERCIAL CATALYSTS

4.2.1 CU/ZN-BASED CATALYST

Cat A, Cat B and Cat C are three conventional medium/low-temperature shift (M/LTS) catalysts, supplied as tablets and after grinded and sieved to 30-40 mesh size, before to be loaded in the reactor. Before the tests, the catalysts are reduced with a defined protocol, as previously reported in § 3.3.2.2.

The chemical compositions of the commercial Cu-based catalysts are summarized in Table 4.1. All the fresh catalysts have CuO as active phase, reduced to Cu^0 in the operating conditions, supported on ZnO, as guard compound. The first sample (Cat A) contains the highest amount of CuO, about three times that of the other two samples.

The Cat A sample contains alumina, that enhances the strength and the mechanical properties of the catalyst, so it is a classic LTS catalyst. The Cat B sample is a typical MTS catalyst and contains chromia, that acts as support providing the thermal stability and a high poisoning resistance. Differently, the Cat C sample may be considered a "hybrid" between the previously cited samples: it contains both chromium and aluminium oxides, this latter in the same amount of the Cat A, and a ZnO content, two times higher than the other formulations.

SAMPLE	Cat A	Cat B	Cat C
CuO [wt.%]	64	15-20 (Cu = 16.1*)	18-22
ZnO [wt.%]	24	25-35 (Zn = 22.8*)	53-63
Cr_2O_3 [wt.%]	-	35-50 (Cr = 51.2*)	9-12
Al_2O_3 [wt.%]	10.5	-	10-13
other [wt.%]	*Promoter* = 1.5	*$ZnCrO_4$* = 5-10	*Graphite* = 1-5 *Cr(VI)* = 2-3
form	*tablet*	*tablet*	*tablet*
size [mm]	5.3×3.0	4.5×4.5	4.8×4.8
S_{BET} [m^2/g]	89	78	62
Volume [mL]	2.0	3.5	2.0
Weight [g]	1.94	3.09	2.86
(*): ICP analysis of element (wt.%) carried out by external lab (Neotron)			

Table 4.1 Chemical composition of the three M/LTS commercial catalysts investigated.

X-ray powder diffraction (XRPD) patterns of the fresh Cat A and Cat C catalysts (Fig. 4.1) show the presence of CuO and ZnO, whereas, alumina is detected as spinel ($CuAl_2O_4$ and/or $ZnAl_2O_4$) only in the latter sample. Fresh Cat B sample presents only broad peaks of spinels ($CuCr_2O_4$ and/or $ZnCr_2O_4$), showing a good dispersion. Cr(VI)-containing phases, ascribed to Cat B and Cat C samples were not detected, suggesting that they are amorphous present in amount too low to be detectable.

The sharp peak at 26.5°, present in all the samples, is due to the graphite used as solid lubricant. As shown in Table 4.2, the C-presence was confirmed in the Cat B sample by CHNS/O analysis carried out in an external laboratory. It is mainly due to the graphite that may be removed operating in oxidizing conditions at T > 700 °C. It is usually included in the formulations to increase the shear rate of the catalyst particles or, also, to the residual carbonates used in the preparation.

Sample	C (wt.%)	H (wt.%)	N (wt.%)	S (wt.%)
LK-811 fresh	3.37	0.44	0.00	0.00

Table 4.2 CHNS/O analysis of the fresh Cat B sample.

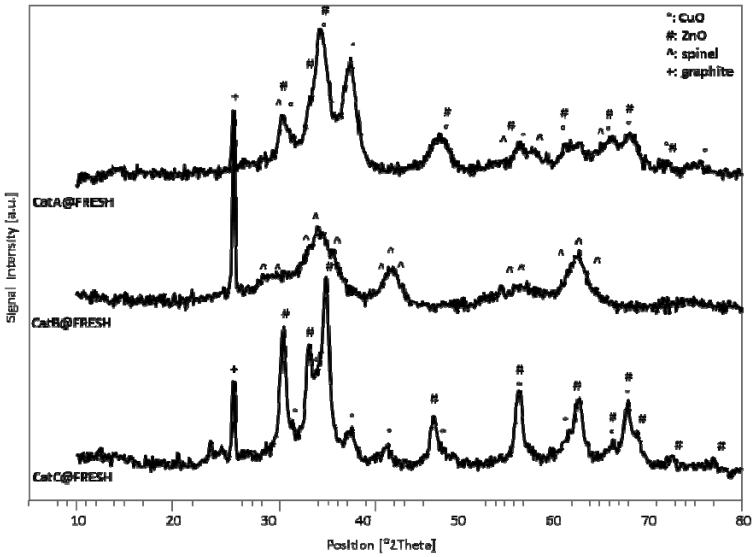

Fig. 4.1 XRPD patterns of the three commercial Cu-based catalysts before the catalytic tests.

Mass spectrometry (MS) analysis during TPO analysis of the Cat B sample, before and after reaction, shows that the CO_2 evolution is due mainly to the burning of graphite burning, with a maximum at 700 °C, and of an amorphous carbon, with a signal in the range 220-300 °C (Fig. 4.2). Similar behaviours was showed by the other samples, before and after reaction, and thus they are not reported. MS analysis of the fresh Cat B catalyst shows an O_2-evolution at 470 °C, attributable to the reduction of Cr^{VI} to Cr^{III} ($ZnCrO_4 \rightarrow ZnCr_2O_4$) (***1***,***2***), and a further peak at 950 °C. This latter is not an artefact of the instrument, but it is related to specific reactions in the samples; in fact, $CuCr_2O_4$ may decompose (equation 1) (***3***) or reacts with CuO excess (equation 2) (***4***) forming $Cu_2Cr_2O_4$ with an isothermal O_2 loss at high temperature. Above 900 °C, these reactions may be ready driven to completeness (***3***,***5***).

$$2\ CuCr_2O_4 \rightarrow Cu_2Cr_2O_4 + Cr_2O_3 + \tfrac{1}{2}O_2\ (T > 900\ °C) \quad [1]$$

$$CuCr_2O_4 + CuO \rightarrow Cu_2Cr_2O_4 + \tfrac{1}{2}O_2\ (T > 900\ °C) \quad [2]$$

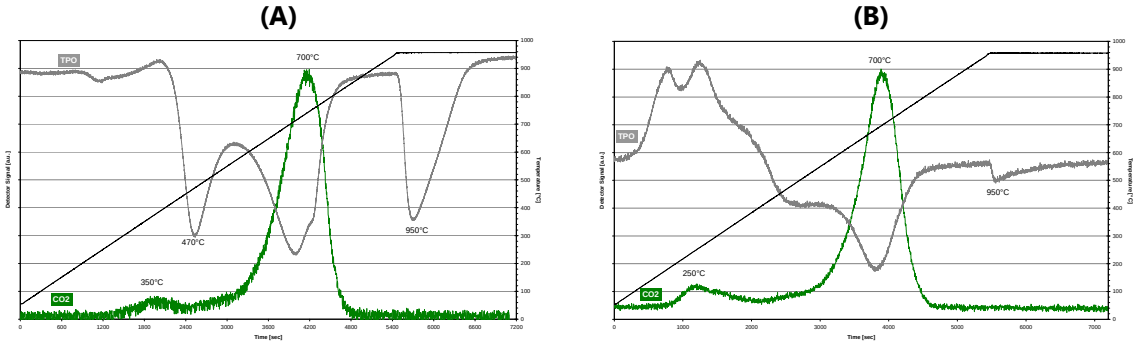

Fig. 4.2 Mass spectrometry (MS) analysis of the Cat B catalyst: before (A) and (B) after the catalytic tests.

It is possible to detect different Cu-containing species on the basis of the literature data, as summarized in Table 4.3. Strong oxide-oxide interactions may be present, with formation of different surface Cu-containing species (***6***).

Species	T [°C]	Description	Reduction step
"Free" CuO	160-250	*Small particles highly dispersed*	$Cu^{2+} \rightarrow Cu^{+}$ Cu^{2+} or $Cu^{+} \rightarrow Cu^{0}$
CuO	250-330	*CuO strongly bounded with ZnO* *Bulky CuO*	Cu^{2+} or $Cu^{+} \rightarrow Cu^{0}$
Cu-spinel	400-600	*Cu(II) in the matrix*	$Cu^{2+} \rightarrow Cu^{0}$

Table 4.3 Cu-species in the different temperature ranges.

All the fresh catalysts are completely reduced at temperatures below 350 °C, with a peak related to the CuO reduction to Cu^0 (Fig. 4.3). Several authors (***7***,***8***) attributed the broad peak to the reduction of "free" CuO and "bulky" CuO in the CuO/ZnO phase, suggesting that CuO interacts with the support. The reduction profile may involve to reduction of Cu^{II} via Cu^{I} ($Cu^{2+} \rightarrow Cu^{+} \rightarrow Cu^{0}$) (***9***,***10***). The rate of Cu^{+} reduction to metallic copper is only slightly slower than that of the Cu^{II} reduction to Cu^{I} and this may explain the appearance of only one peak in the TPR profile, with only a small shoulder at lower temperature.

The first peak in the reduction profile of the Cat B sample is probably due to the Cr^{VI} reduction: in fact, in the case of Fe/Cr catalysts, Khan *et al.* (***11***) showed that the reduction peak at 225 °C corresponded to the reduction of Cr^{VI} to Cr^{III}. Pure ZnO does not reduce under the same experimental conditions, according to Okamoto *et al.* (***6***); therefore, the small peak at 500 °C may be attributed to the reduction of Cu^{II} in a mixed Cu/Zn spinel-type phase.

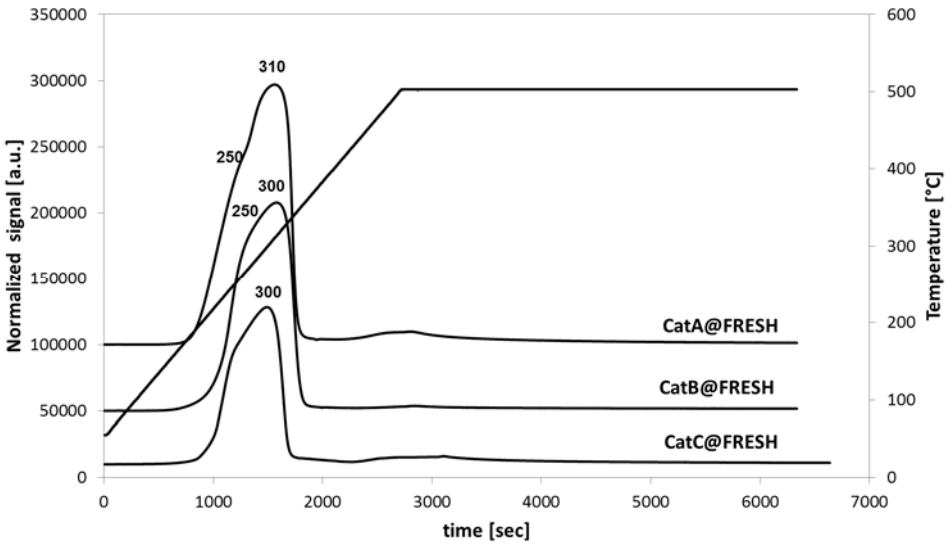

Fig. 4.3 TPR profiles of the three commercial Cu-based samples before the catalytic tests.

A first approach is to understand the dependence on the pressure, in order to evaluate optimum conditions to obtain the same performance with a lower consumption of dry gas (DG). Practically, the performances of the catalysts do not change decreasing the pressure from 2.0 to 1.5 MPa, with small differences attributable to the accuracy in the measure (Fig. 4.4). Therefore, a lower pressure is the best choice to reduce the consumption of inlet DG.

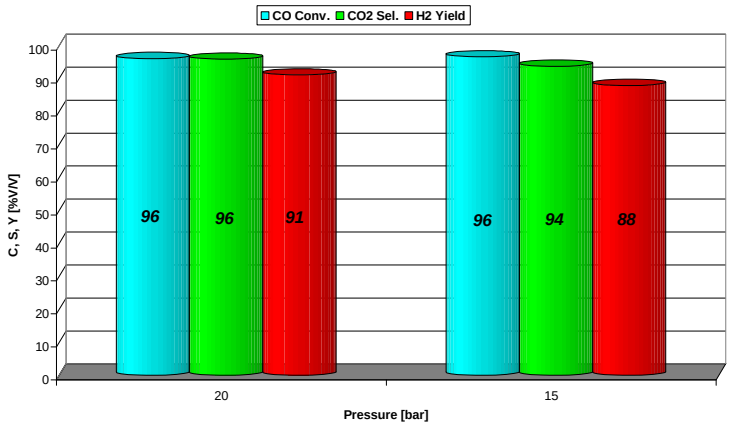

Fig. 4.4 Performances of Cat B as a function of the pressure (T = 250 °C, S/DG = 0.75, τ = 1.0 sec).

The Cat A sample is a classic LTS catalyst, optimised to have good CO conversion and thermal stability below 300 °C (Fig.s 4.6 and 4.7). The decrease of the S/DG ratio from 0.55 to 0.25 strongly affects the performances, in particular at 250 °C where the activity of the catalyst shows a high decrease in conversion and yield (from 95 to 58 %). This decrease is smaller at 300 °C (from 92 to 81 %) and become again important, from 83 to 68 %, increasing the temperature. At the lower temperature (250 °C), the role of the kinetic factors is more evident, giving rise to significant changes, while the performances of this catalyst remain practically constant at the two higher temperatures. However, the changes in CO conversion and H_2 yield values are not pronounced as those related to changes in S/DG ratio values. Therefore, the WGS reaction for the Cat A sample is more affected by a steam excess, that promotes thermodynamically the product formation, than by the kinetics parameter τ.

It may be observed not only the effect of the S/DG ratio and contact time, but also the restrictions on the conversion due to the equilibrium of the WGS reaction. Therefore, while contact time has a small effect on the activity of the Cat A sample, the S/DG decrease changes drastically the performances of the sample in particular at 250 °C. Thus, it is necessary an increase of the temperature to enhance the CO conversion and, consequently, the H_2 yield. However, as shown in the both figures 4.6 and 4.7, the CO_2 selectivity is always higher than 98 %, allowing to exclude side reactions at all the temperatures investigated.

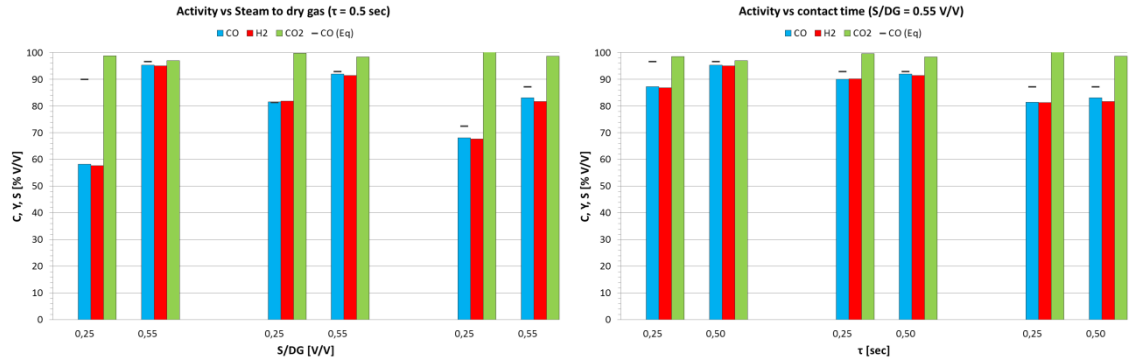

Fig. 4.5 Activity of the Cat A sample as a function of S/DG ratio and contact time values.

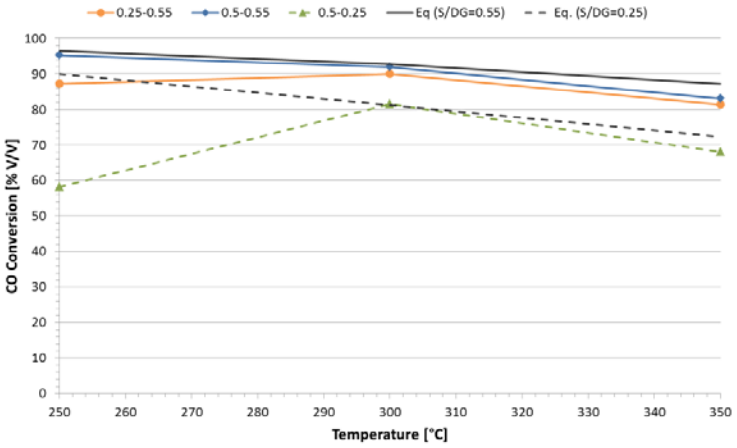

Fig. 4.6 CO conversion for the Cat A sample as a function of the temperature, for different τ and S/DG values.

The Cat B sample is a MTS catalyst, with best performances at temperatures higher than those typical for LTS catalysts. In fact, it shows the best results, in terms of CO conversion, at 300-350 °C (Fig.s 4.8 and 4.9). The decrease of the S/DG ratio has a negative effect at all the temperatures investigated, decreasing CO conversion and H_2 yield values. At 250 °C the CO conversion decreases from 71 to 41 %, while at higher temperatures (300 and 350 °C) the decrease is respectively of 22 and 13 %. In this case, it must be considered also the side reactions, for example the methanol synthesis from CO_2, evidenced by a significant decrease of the selectivity in CO_2. In fact, CO_2 selectivity and H_2 yield values may be justified only considering further reactions besides the WGS reaction, as confirmed by the HPLC analysis of the condensate water, that shows the presence of small amounts of oxygenated compounds, mainly methanol.

The WGS reaction for the Cat B sample is also affected by the contact time and not only by thermodynamic parameter S/DG ratio. At 250 °C, the CO conversion decreases from 71 to 55 % as effect of the contact time decrease, with an effect less evident at 300 °C, showing the good performance of this catalyst. The CO conversion remains constant with a decrease in H_2 yield and CO_2 selectivity values, probably due to the presence of side reactions. Moreover, it is evident that the amounts obtained are near to the equilibrium values. To evidence the possible deactivation of the samples, the first test was repeated at the end of the catalytic tests (≈ 42 h), observing the

same CO conversion, CO_2 selectivity and H_2 yield values of the initial test, indicating a good stability of the sample.

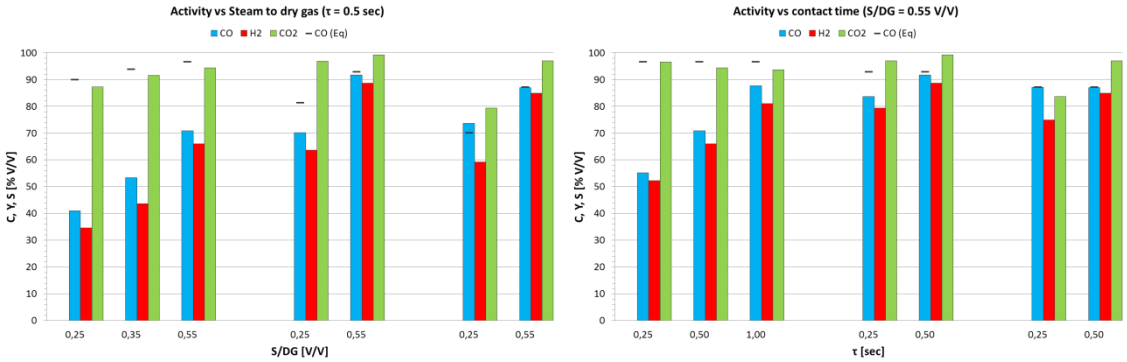

Fig. 4.7 Activity of the Cat B sample as a function of S/DG ratio and contact time values.

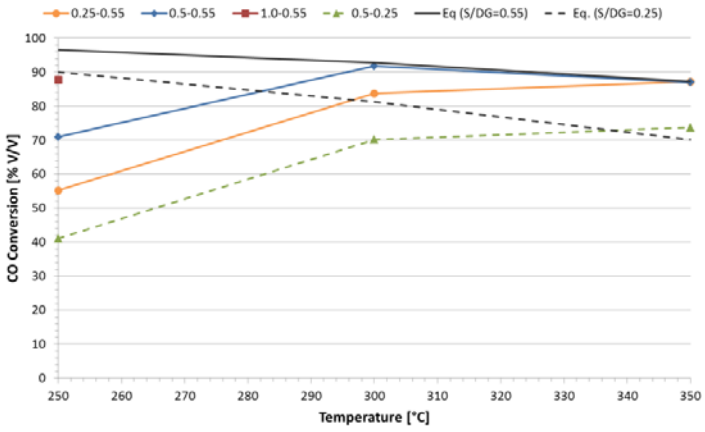

Fig. 4.8 CO conversion for the Cat B sample as a function of the temperature, for different τ and S/DG values.

The Cat C sample has a formulation between those of the first two catalysts and requires, to obtain the best results, temperature in the 250-300 °C range (Fig.s 4.10 and 4.11). The catalytic performances in the WGS process are strongly affected by the decrease of the S/DG ratio from 0.55 to 0.25, in particular at low and high temperature. The activity exhibits a decrease of CO conversion from 72 to 40 % at 250 °C and from 37 to 20 % at 350 °C, showing a high decrease also in terms of selectivity and yield. Therefore, these values do not allow to exclude side reactions mainly at 350 C. At 300 °C, it may be observed a smaller increase in CO conversion and H_2 yield values (from 59 to 64 %); to understand if it may be an instrumental trouble, the following day this test was repeated at the same operating conditions, observing the same results.

At 300 °C, also the effect of the contact time is less pronounced than at 250 °C (at 350 °C, a pump trouble did not allow to perform the test). The performances of the Cat C sample remain practically constant at 300 °C, decreasing of about 20% with the contact time at 250 °C. However, the contact time effect is not so pronounced as that due to the S/DG ratio. Therefore, the activity for this sample is more affected by the thermodynamic factor (steam excess) than by the kinetic one (τ). The S/DG value decrease from 0.55 to 0.25 changes drastically the performances, with the

exception of the test at 300 °C. Together with the effect of the S/DG ratio and contact time values, it may be observed also the restrictions on the conversion due to the equilibrium of the WGS reaction.

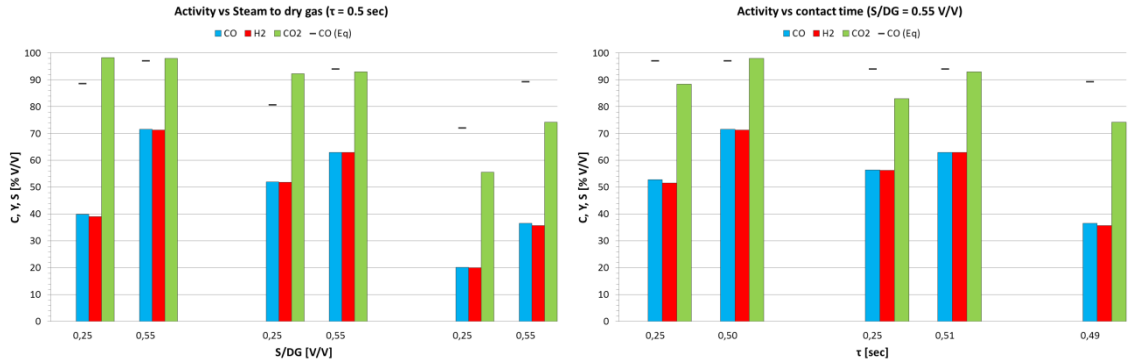

Fig. 4.9 Activity of the Cat C sample as a function of S/DG ratio and contact time values.

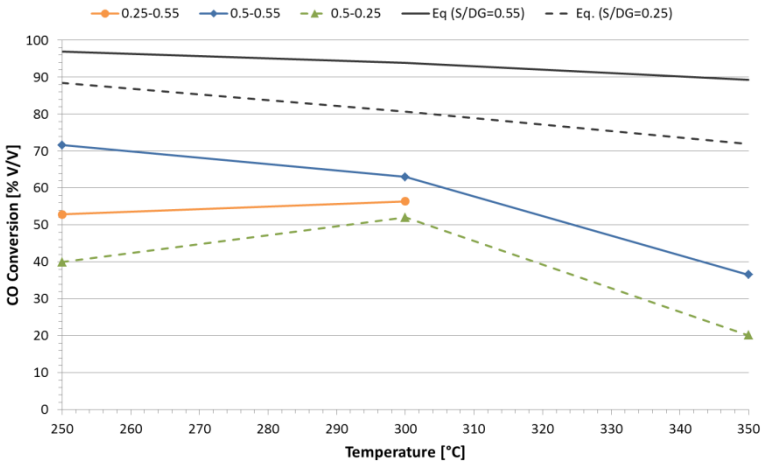

Fig. 4.10 CO conversion for the Cat C sample as a function of the temperature, for different τ and S/DG values.

4.2.1.2 CHARACTERIZATION AFTER REACTION

A summary of the chemical-physical properties before and after reaction is reported in Table 4.4. After reaction, the characteristic reflections of metallic copper at 43.4, 50.5 and 74.1° are observed in all the samples, confirming the catalyst reduction (Fig.s 4.12-4.14). In the Cat C sample are present also the reflections attributable to the Cu^{I} oxide, showing a not complete reduction during reaction or, more probably, a partial re-oxidation after discharge. The reduction effect is very evident in the Cat A sample after reaction, which shows a higher crystallinity than the other catalysts, evidence of a particle sintering. The sintering phenomena and the agglomeration of Cu^{0} crystallites is the most evident drawback for the Cu-based catalysts, reducing the range of operating temperature. This effect is also confirmed by the surface area values, that drastically decreased for the Cat A sample, while it is less pronounced in the Cat C sample, probably due to

the chromia content, that increases the thermal stability. The Cat B sample shows a different behaviour in terms of surface area, that practically does not change after reaction., evidencing the stabilization effect related to the presence of a spinel phase. Moreover, the combustion of graphite during reaction or, more probably, the reduction of an amorphous $ZnCrO_4$ may balance the loss of surface area expected after reaction.

Crystal size of the Cu-containing phases and zinc oxide, before and after reaction, were calculated by the Debey-Scherrer formula (***12***) by using the best resolved reflections at 43.3° for Cu^0. In the Cat A sample, the crystallite size of Cu^0 is more than two times that in the Cat B sample, as expected on the basis of the catalyst characteristics and already observed in the XRD patterns. Unfortunately, this parameter cannot be exactly determined in the Cat C sample, because of the overlapping of the different peaks. Despite it, the XRD pattern does not evidence a dramatic sintering in this sample after reaction (Fig. 4.14).

Sample		Phases	S_{BET} [m^2/g]	$d_{Cu(0)}$ [nm]
Cat A	*fresh*	CuO, ZnO, Spinel, graphite	89	
	used	Cu^0, ZnO, spinel, graphite	45	18
Cat B	*fresh*	spinel, graphite	78	
	used	Cu^0, spinel, graphite	80	8
Cat C	*fresh*	CuO, ZnO, graphite	62	
	used	Cu^0, Cu_2O, CuO, ZnO, graphite	52	n.d.

Table 4.4. Chemical-physical properties of the investigated commercial Cu-based catalysts.

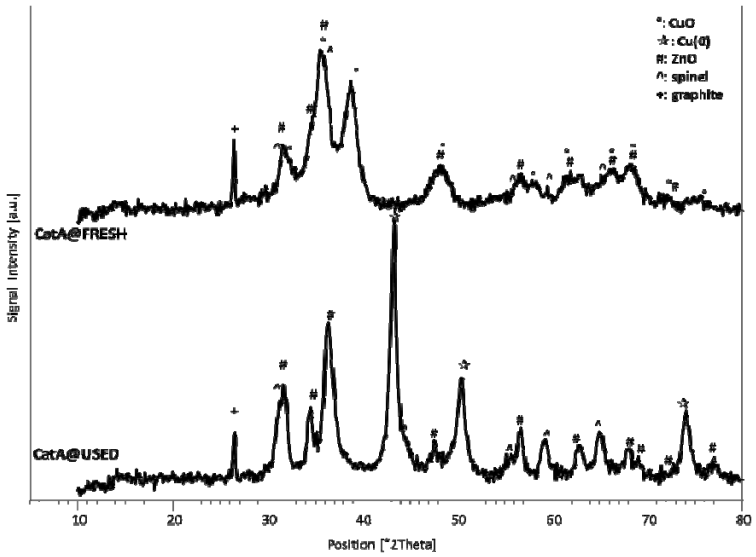

Fig. 4.11 XRD patterns Cat A sample before and after the catalytic tests.

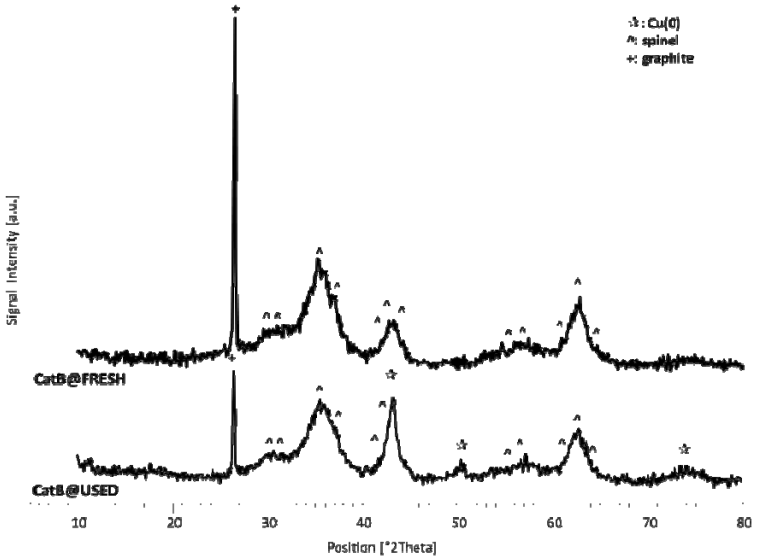

Fig. 4.12 XRD patterns Cat B sample before and after the catalytic tests.

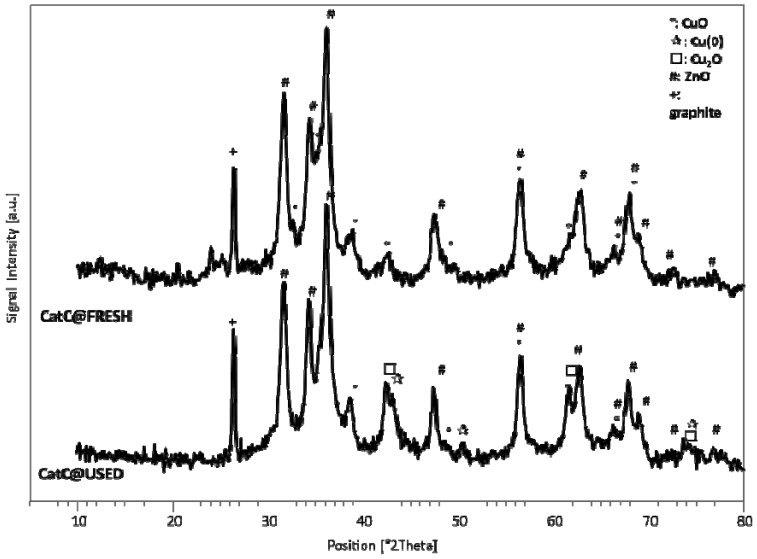

Fig. 4.13 XRD patterns Cat C sample before and after the catalytic tests.

The different reducibility of the phases was determined by Temperature Programmed Reduction (TPR) analysis, after oxidation for the unloaded catalysts. The TPR profiles show that CuO is fully reduced at 350 °C (Fig. 4.15-Fig. 4.16). The TPR profile of the Cat A sample shows the same behaviour before and after oxidation, even if it is slightly broad towards the low temperature. Differently, Cat B and Cat C samples evidence a shift of the reduction peak towards temperatures about 30 °C, showing a decrease of CuO interaction with the support. This effect is confirmed by the presence of a shoulder at 200 °C attributable to free CuO in the Cat A sample. Therefore, these evidence an increase of the amount of more reducible Cu-containing species after reaction (***13***,***14***,***15***), with a re-dispersion effect observed also in the Temperature Programmed Oxidation (TPO) profile before and after reduction.

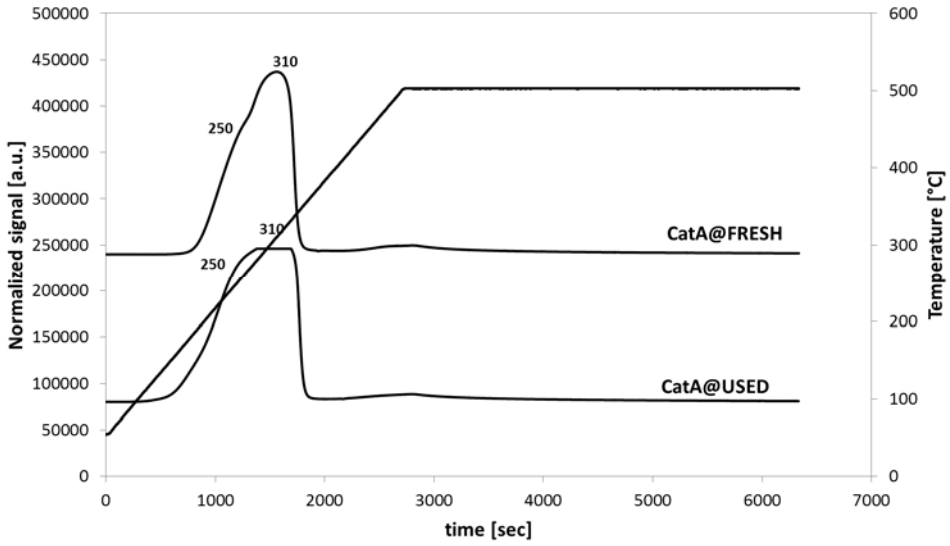

Fig. 4.14 TPR profiles for the Cat A sample before and after the catalytic tests.

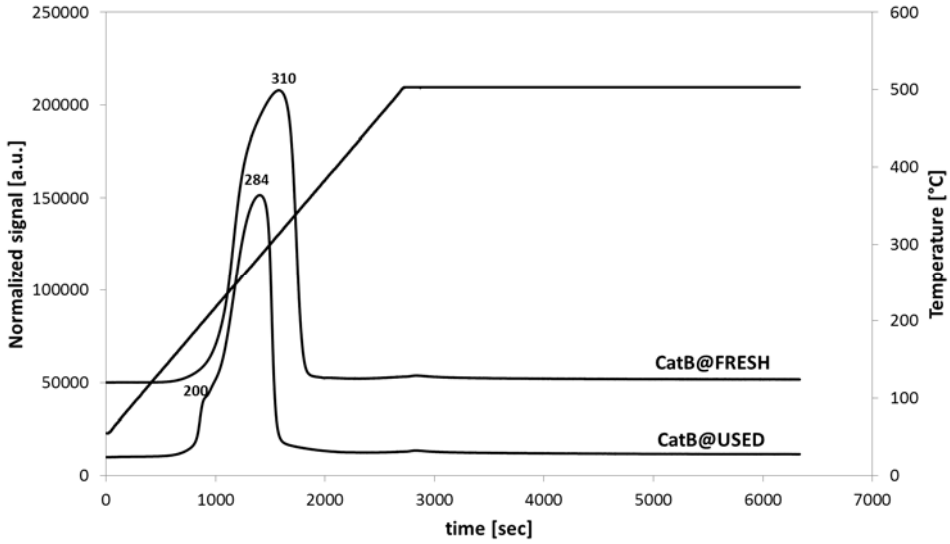

Fig. 4.15 TPR profiles for the Cat B sample before and after the catalytic tests.

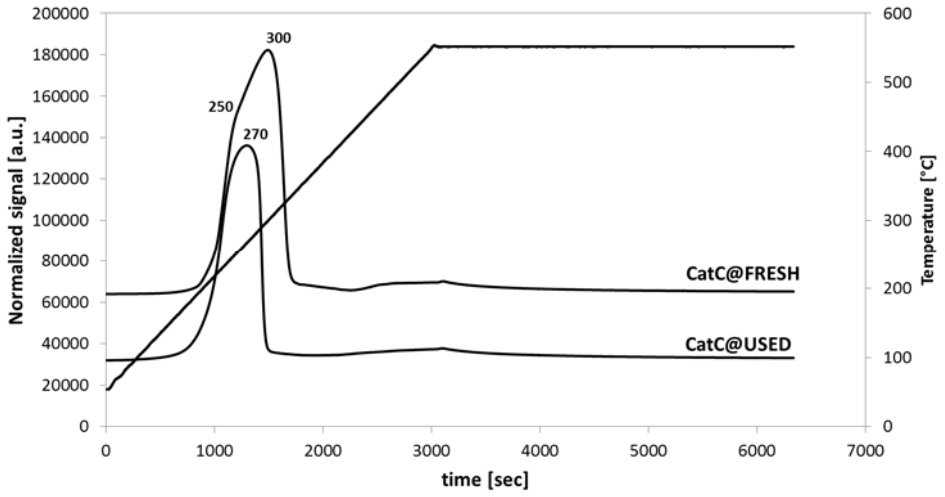

Fig. 4.16 TPR profiles for the Cat C sample before and after the catalytic tests.

Table 4.5 shows the values of surface area (S_{BET}), cumulative pore volume of mesopores (17-3000 Å diameter, V_{PORES}) and average pore diameter (d_{PORE}). As previously reported, the Cat B sample has practically the same surface area values, before and after the catalytic tests; while the other catalysts show a decrease of the surface area after reaction, mainly for the catalyst with the higher Cu-content (Cat A). In this sample, pore volume remains unaffected, while the surface area halves, with an increase in pore size, suggesting a possible breakage of the pores.

The pore size distribution of the Cat A sample is before reaction bi-modal (Fig. 4.17), whereas after reaction, the pores between 3 and 4 nm almost disappear and those centered at 9 nm strongly decrease, confirming a possible pore breakage. The Cat B sample show a different behaviour (Fig. 4.18), with almost the same pore size distribution before and after reaction, centered between 3 and 7 nm. Furthermore, the microporosity increases in the unloaded Cat B sample, due to coke deposition or, more probably, to graphite combustion, that generates a further porosity. The Cat C sample shows a pore size distribution (Fig. 4.20) similar to that reported for the Cat A sample (Fig. 4.19); after reaction, the pore size distribution of the sample before reaction at 3-6 nm almost disappears and that at diameter higher than 10 nm decreases, with an increase of volume due to pore with an intermediate diameter range (4-9 nm). It may be related to a structural sintering with a reorganization of porosity.

Sample		S_{BET} [m^2/g]	V_{PORES} (BJH des.) [cm^3/g]	D_{PORE} (BJH des.) [nm]
Cat A	*fresh*	89	0.28	10
	used	45	0.27	18
Cat B	*fresh*	78	0.36	15
	used	80	0.28	12
Cat C	*fresh*	62	0.28	15
	used	52	0.28	17

Table 4.5 Morphological data of all the commercial Cu-based catalysts.

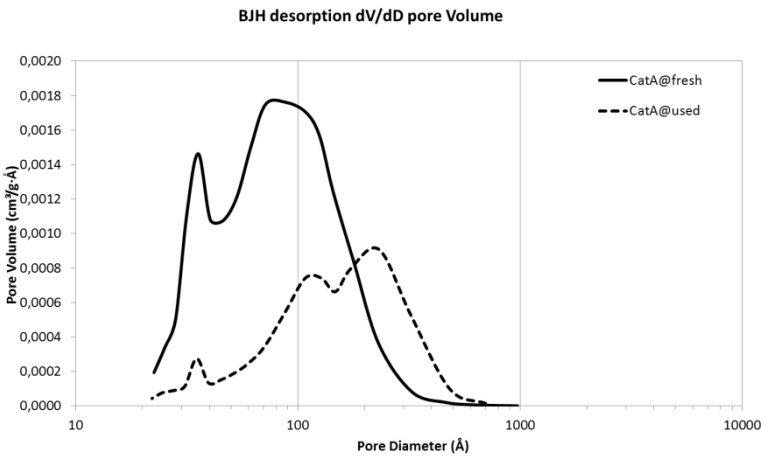

Fig. 4.17 BJH pore distribution for the Cat A sample before and after reaction.

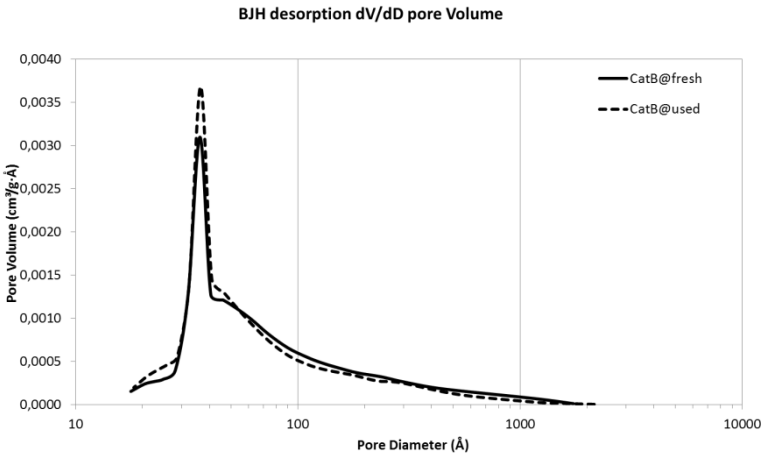

Fig. 4.18 BJH pore distribution for the Cat B sample before and after reaction.

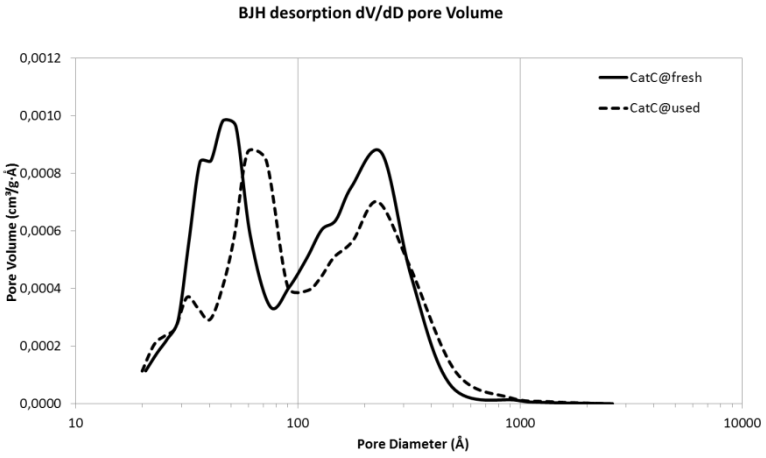

Fig. 4.19 BJH pore distribution for the Cat C sample before and after reaction.

The isotherms of all commercial Cu-based catalysts may be identified as **TYPE IV** of the IUPAC classification, while the hysteresis loop is **TYPE H4** (***16***) (Fig. 4.20). Therefore, the pore size distributions and the isotherms indicated that the commercial M/LTS catalysts contain mainly mesopores (2-50 nm).

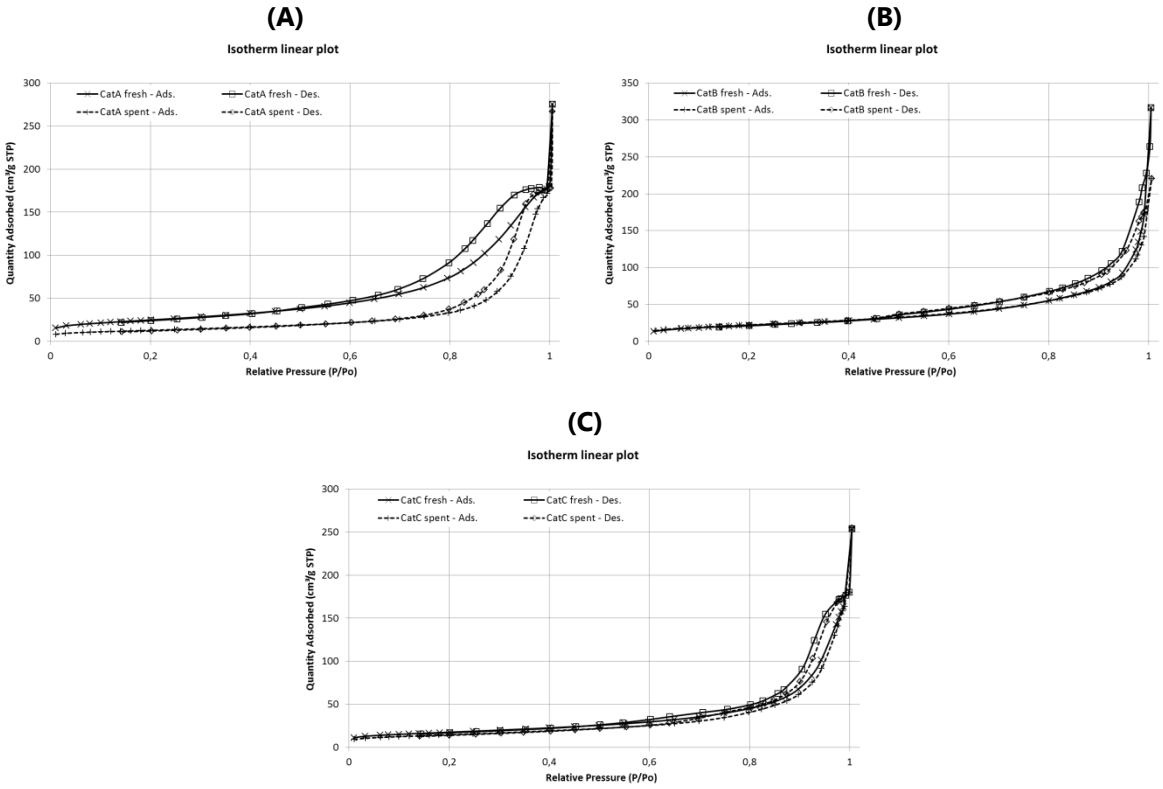

Fig. 4.20. Isotherms of the commercial Cu-based catalysts before and after reaction: (A) Cat A, (B) Cat B, (C) Cat C.

4.2.2 PT/RE-BASED CATALYST

The Cat D sample is a new generation high-temperature shift (HTS) catalyst, optimized to operate at about 425 °C and with a space velocity (GHSV) between 9,000 and 250,000 h^{-1}, in which the precious metals (PM) are washcoated on a monolith. Before to be loaded into the reactor, the sample was grinded and sieved to 30-40 mesh, reducing the PM before the reaction.

The fresh sample contains Pt/Re and zirconia (probably doped with La and Gd) supported on a monolith of cordierite ($Mg_2Al_4Si_5O_{18}$). Pt is the primary active phase, while Re was introduced as a structural promoter, allowing to operate above 400 °C, without any significant metal sintering. The amounts of the elements (in terms of atomic and weight %) was determined by SEM-EDX analysis (Fig. 4.21) and corresponded to optimum reported in literature (Pt = 1-2 wt.%; Pt:Re = 2:1). The fresh sample is a cordierite (monolith) and zirconia (support) with the phase PtO_2. The Re-containing phase is not detected, indicating a good dispersion or, more probably, an amount too low.

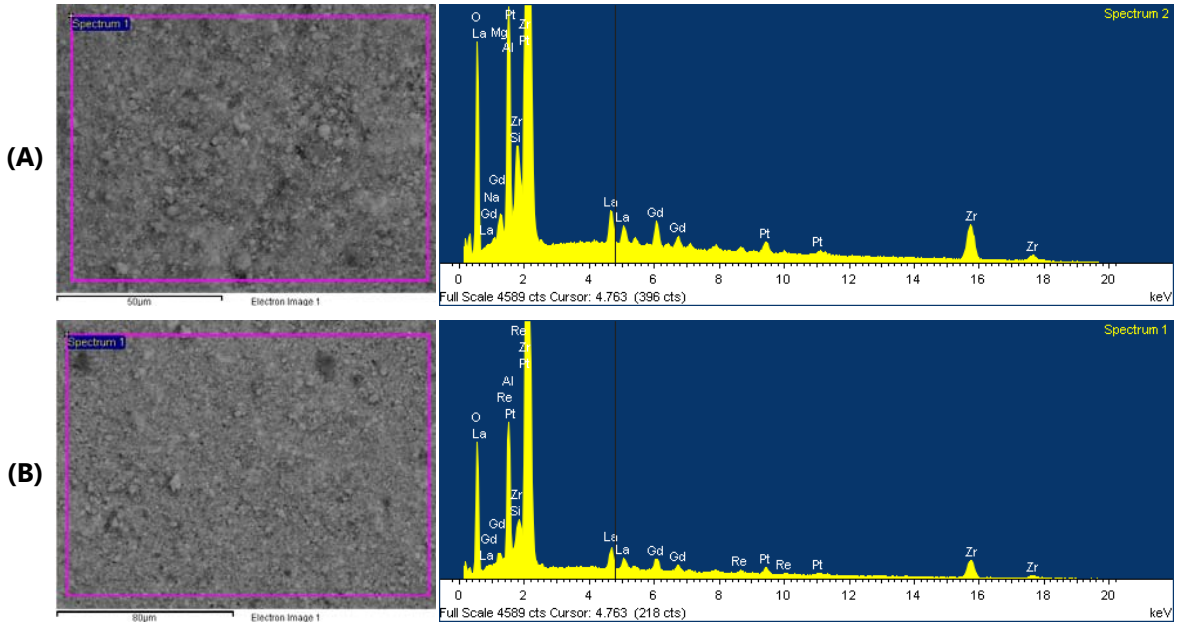

Fig. 4.21 SEM replica and EDX spectra of the Cat D sample, before (A) and after reaction (B).

Sample	FRESH		SPENT	
Element	**Weight%**	**Atomic%**	**Weight%**	**Atomic%**
O K	34.2	71.3	34.0	72.6
Mg K	0.7	0.9	-	-
Al K	5.1	6.3	4.8	6.1
Si K	1.4	1.6	0.4	0.4
Zr L	48.3	17.7	49.9	18.7
La L	3.9	0.9	3.4	0.8
Gd L	3.6	0.8	2.8	0.6
Re L	0.8	0.1	1.5	0.3
Pt L	2.2	0.4	3.4	0.6
Totals	*100*	*100*	*100*	*100*

Table 4.6 Chemical composition of the Cat D sample carried out by SEM-EDX analysis.

On the basis of the literature data, it is possible to summarize the possible species present in this type of catalyst (Table 4.3). PtO_x are reduced at lower temperature than Re_2O_7 and there are more reduction peaks attributable to Pt and Re differently interacting with the support (***17***). PtO_2 is reduced to Pt^0, that catalysed the reduction of rhenium oxide closeness located at about 500 °C (***18***). However, other fractions of rhenium oxide may be segregated and reduce only at higher temperature (***17***). However, the structure and role of Re in the Pt/Re-based catalysts are not fully defined: it has been proposed that Re^0 provides sites for hydrogenolysis of coke deposits (***19***) and that acts independently of Pt, being able to convert coke precursors into harmless products (***20***), or anchoring Pt to the support and, thereby, stabilising its dispersion (***21***). The TPR profile of the fresh sample is reported in the comparison with the used one in the following paragraph 4.2.2.2: it is fully reduced below 550 °C, evidencing specific Pt-Re interactions, where the first peak corresponds to the reduction of platinum oxide, while the further ones at 380 and 450 °C may be

attributed to the reduction of rhenium oxide particles closeness to Pt^0 crystallites or far from them, respectively (***24***).

Phase	T [°C]	Description	Reference
Free PtO_x	80-150°C	*Small particles highly dispersed*	(***18***,***22***)
PtO_x **Re_2O_7**	150-250°C	*PtO_x strongly bounded with support* *Partial reduction of rhenium oxide*	(***18***,***22***,***23***,***24***,***25***)
Re_2O_7	250-400	*Re_2O_7 near to Pt crystals*	(***18***,***22***,***23***,***24***,***25***,***17***)
Re_2O_7	400-500°C	*Re_2O_7 far from Pt^0*	(***17***,***18***,***22***,***24***)
Re_2O_7	550-600°C	*Bulky rhenium oxide*	(***18***,***24***,***25***)

Table 4.7 Detected species in a typical Pt/Re-based catalyst for different temperature ranges.

4.2.2.1 ACTIVITY

The Cat D catalyst is a HTS catalyst, with a formulation optimized to operate at temperature above 300 °C (Fig.s 4.25 and 4.26).

The catalytic performances of this sample in the WGS reaction are affected by the decrease of both S/DG ratio (from 0.55 to 0.25) and contact time (from 0.5 to 0.25 sec) values. At all the reaction temperatures, the activity halves with a decrease of CO conversion values. The activity of the catalyst shows a maximum in CO conversion and H_2 yield values at 350 °C (both about 54 %). The effect of the contact time is the same at all the temperatures investigated and the performances, related to the S/DG ratio value, show practically the same trend. On the other hand, it is important to note that the CO_2 selectivity reaches values of about 90 % only at 350 °C., evidencing the presence of side reactions.

Although it is evident the limited activity of this sample in the WGS reaction; the trends of the CO conversion and H_2 yield values are the same, regardless of the conditions, showing best performances by increasing the temperature.

To evidence if a deactivation occurred in this catalysts, the test at 250 °C (S/DG = 0.55 V/V and τ = 0.5 sec) was repeated (Fig. 4.24), observing an evident deactivation with a time-on-stream of about 10 h, with a decrease in the CO conversion decreased from 16 to 9 %, with a value of 6 % at the end of the catalytic tests (27 h).

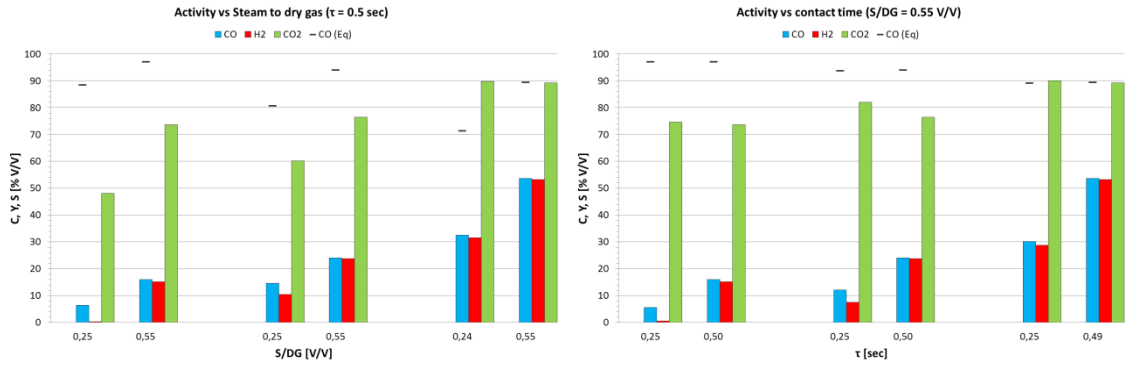

Fig. 4.22 Activity of the Cat D sample as a function of S/DG ratio and contact time values.

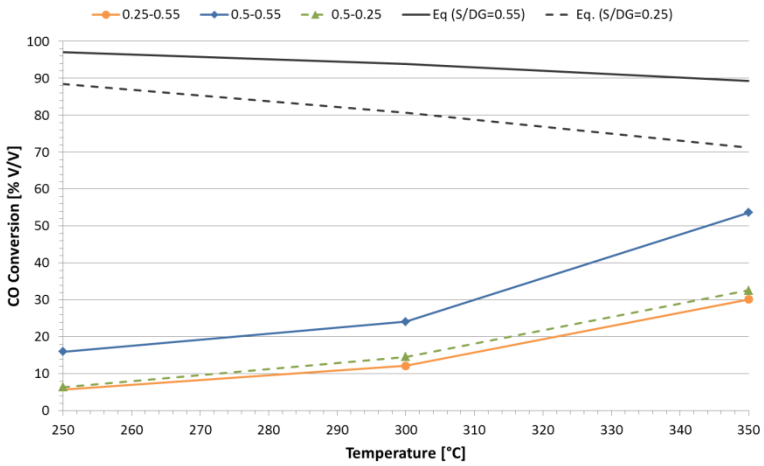

Fig. 4.23 CO conversion for the Cat D sample as a function of the temperature, for different τ and S/DG values.

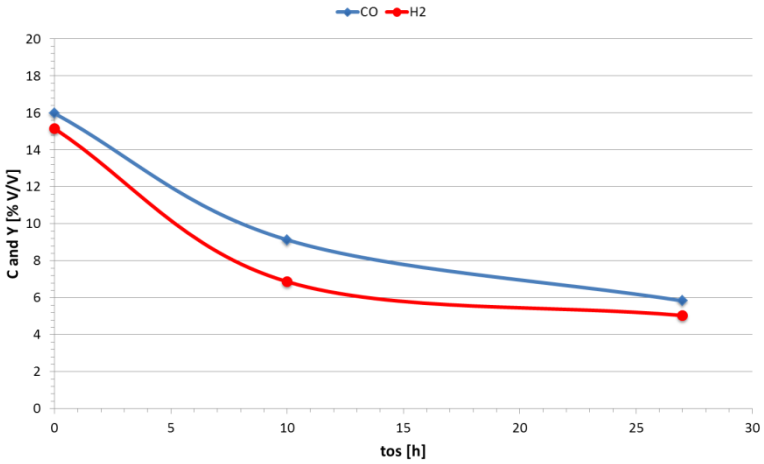

Fig. 4.24. Deactivation of the Cat D sample with time-on-stream (T = 250 °C, S/DG = 0.55 V/V, τ = 0.25 sec).

4.2.2.2 CHARACTERIZATION AFTER REACTION

After reaction, the XRD patterns (Fig. 4.28) show the characteristic reflections of Pt^0 and PtO in the unloaded sample, confirming the partial reduction of the catalyst, with, furthermore, the presence also corundum (inert used in the reactor). However, Cat D does not show any increase of crystallinity after reaction, such as confirmed by the surface area values (Table 8). After the catalytic tests, the Cat D sample show very stable values of surface area (very low) and pore size.

The TPR analysis after oxidation of the unloaded catalyst after reaction (Fig. 4.29) shows a profile attributable to the same phases observed in the fresh sample: the first peak may be attributed to free PtO_x, occurring at the same temperature; the second peak is shifted at lower temperature (300 °C), probably due to a partial reduction of the Pt, with an increase of the amount of more reducible rhenium oxide closeness to Pt^0 particles. The peak at high temperature

(520 °C) may be related to the rhenium oxide segregated after the catalytic tests, showing a decrease of the Re-support interaction.

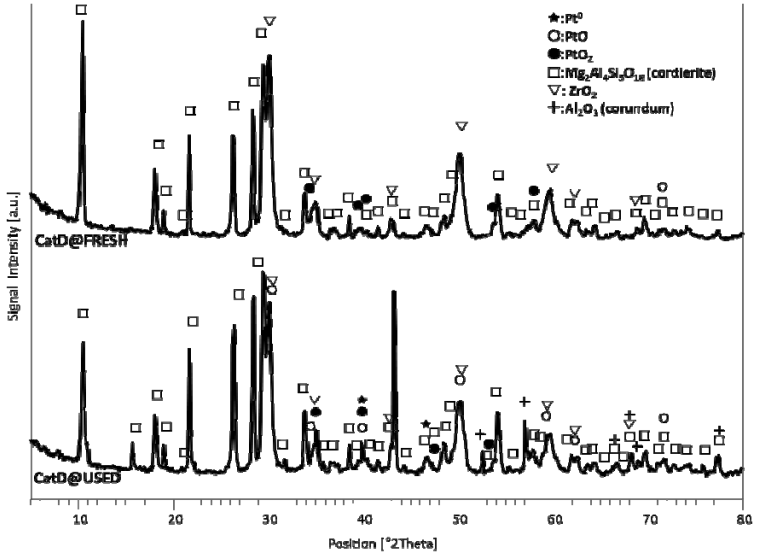

Fig. 4.25 XRPD patterns of the Cat D sample before and after reaction.

Samples		S_{BET} [m^2/g]	V_{PORES} (BJH des.) [cm^3/g]	d_{PORE} (BJH des.) [nm]
Cat D	*fresh*	11	0.037	12
	used	11	0.042	12

Table 4.8 Morphological data for the Cat D sample.

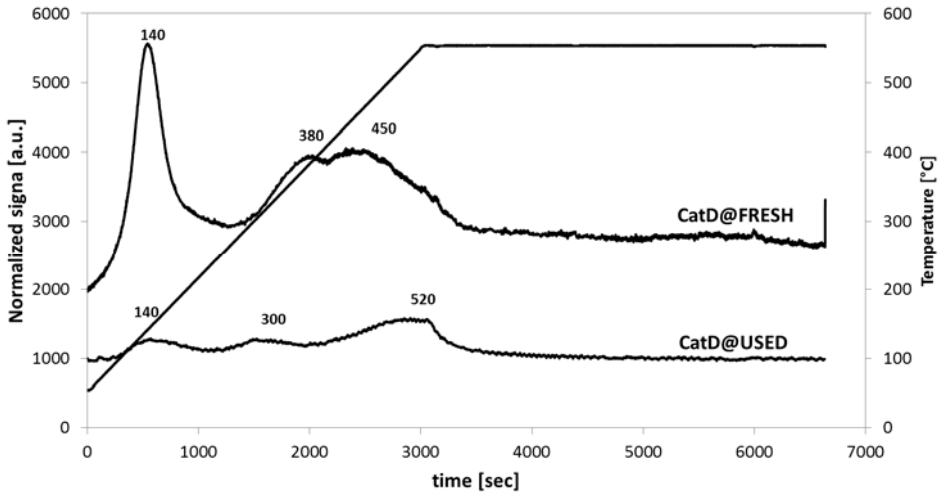

Fig. 4.26 TPR of the Cat D sample before and after oxidation.

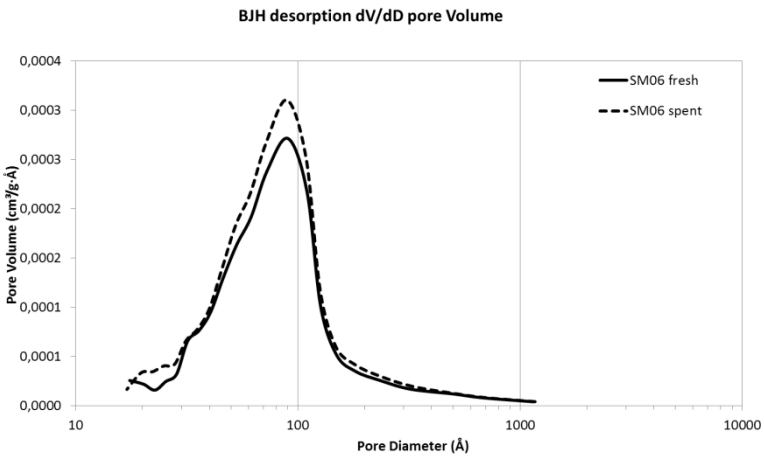

Fig. 4.27 BJH pore distribution for the Cat D sample before and after reaction.

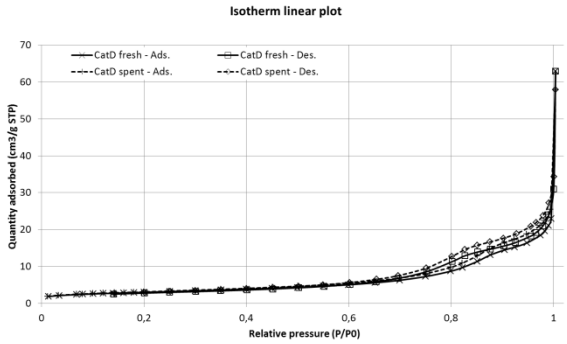

Fig. 4.28 Isotherms of the Cat D sample before and after reaction.

After reaction, the microporosity practically does not change; in fact, the pore size distribution of the Cat D catalyst shows the same profile before and after the catalytic tests, centered at about 9 nm (Fig. 4.27). In the IUPAC classification (***16***), the isotherm (**TYPE IV**) (Fig. 4.31) and the hysteresis loop (**TYPE H4**) indicate that the Cat D sample is mesoporous (2-50 nm).

4.2.3 COMPARISON AMONG THE COMMERCIAL CATALYSTS

The three commercial Cu-based catalysts belong to different classes for formulation and reaction conditions. The Cat A sample is a classic LTS catalyst containing an Al-based spinel as support, whereas the Cat B sample is an MTS catalyst containing a Cr-based spinel as support and thermal stabilizer. On the other hand, the Cat C catalyst is intermediate between the previous formulations. Fully different is the Cat D sample, a Pt/Re-based catalyst, with a high thermally stable monolith support.

All Cu-based catalysts show a significant sensibility to the operating conditions (T, S/DG, τ). The Cat A sample shows clearly higher performances at 250 °C, regardless of S/DG ratio and contact time values (Fig. 4.29). This sample presents always the best activity in all the operating conditions, with CO conversion values close to equilibrium values also at low S/DG ratio when

temperature is higher than 250 °C. At 250 °C, Cat B and Cat C samples show the same trend in comparison to both thermodynamic and kinetic parameters. However, while Cat B reaches the equilibrium values of CO conversion increasing the temperature, Cat C gives only moderate results at temperature below 300 °C (Fig. 4.30). The Cat B sample is the most active catalyst at 350 °C (Fig. 4.31).

The Cat D sample shows a very low activity in the WGS reaction, but reaches a CO conversion value higher than that of the Cat C sample at the highest temperature investigated. However, it is noteworthy that its activity is not sufficient to schedule a possible application in the medium temperature range.

The Cr-spinel has a protection role, evidenced by a very low decrease of surface area value for the Cat B sample after reaction, with also a low sintering of Cu^0 crystallites (8 nm - Cat B - instead of 18 nm - Cat A). Considering the behaviour for long time-on-stream, it is possible to hypothesize that the deactivation of the Cat A sample may occur more quickly than for the other Cu-based catalysts. In the Cat D sample, Re acted as a structural promoter, stabilizing the Pt and avoiding any metal sintering.

In conclusion, the Cat A sample (LTS) shows an optimization focused to the use at about 250 °C, in particular at very low contact time values, although its formulation is not thermally stable. The Cat B sample may be consider as a possible MTS catalyst to be used at conventional values of S/DG ratio and contact time, showing an interesting activity at 300 °C associated with a good thermal stability. The Cat C sample shows a lower activity than the other commercial Cu-based samples. Finally, the Cat D sample is a new type of HTS catalyst, with a sufficient activity only at high temperature, although its performances are not suitable for the MTS conditions.

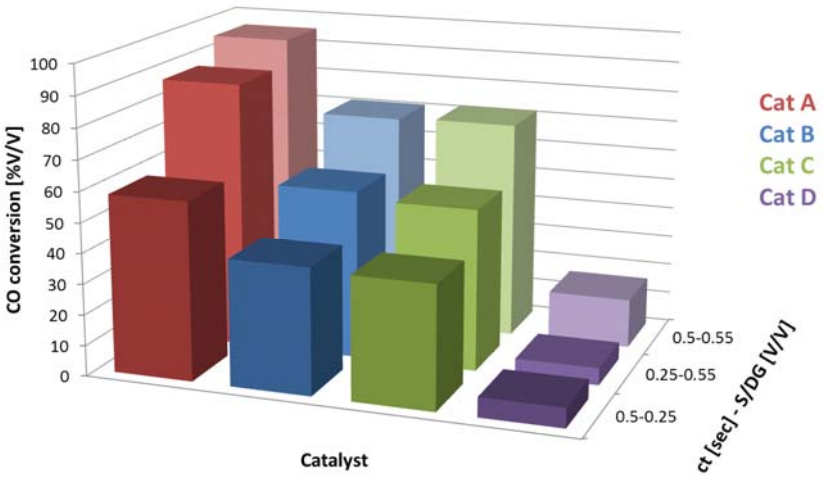

Fig. 4.29 Activity at 250 °C of the commercial catalysts investigated.

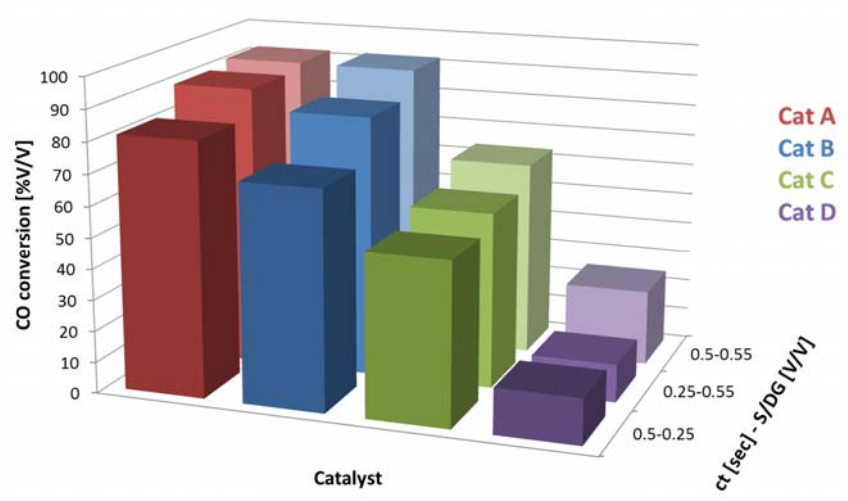

Fig. 4.30 Activity at 300°C of the commercial catalysts investigated.

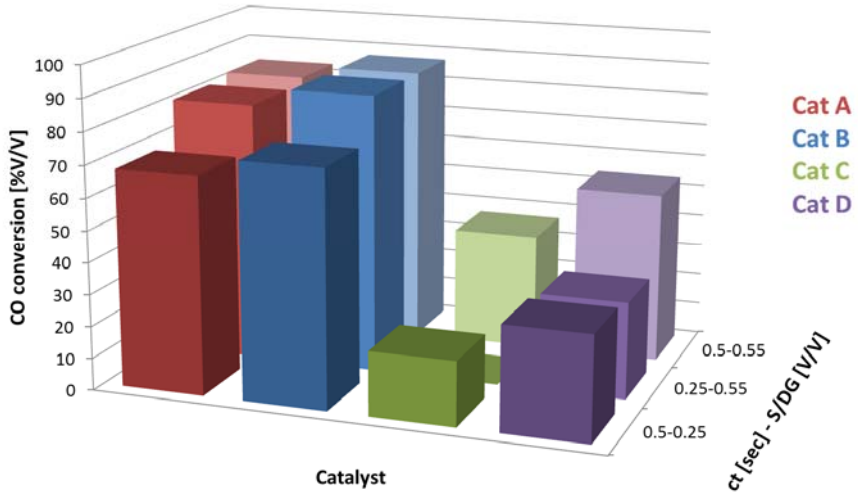

Fig. 4.31 Activity at 350 °C of the commercial catalysts investigated.

4.3. PEROVSKITE-TYPE CATALYSTS

Due to their high activity and thermal stability, high attention has been devoted to perovskite PVK) mixed oxides, with general formula ABO_3 (where A and B are usually rare earth and transition metal cations, respectively) (***26***,***27***). Even for a single A or B cation, there is still the possibility to partially substitute these centres in the ABO_3 composition, yielding a wide variety of possible compositions, e.g. $A_{1-x}A'_xB_{1-y}B'_yO_3$, as well as the possibility to have ordered systems with general formula $A_2BB'O_6$ (***28***).

ABO_3 perovskite-type catalysts were prepared by citrate method (***29***), which allows a very homogeneous dispersion of the precursor salts and decrease the calcination temperature in

comparison to the typical values for crystalline PVK formation (900-1100°C), preserving highest surface area values.

4.3.1 PVK-TYPE SAMPLES

The $LaFeO_3$ phase has a PVK-type structure, with high thermal stability, metal dispersion and good redox activity (***30***). Hence, PVK structure may disperse the Fe^{III} species, preventing their sintering and over-reduction at high temperatures, both of which decreasing the catalytic activity. The study of the perovskite $LaFeO_3$ (LaFe, one of the most investigated PVK in literature) and the perovskite La_2CuO_4 is linked to the use of iron and copper as typical active phases in the HTS and LTS reaction. Furthermore, the activity could be promoted by introducing Cr, Ce and Cu in the PVK-structure (Table 4.9):

- Cr: as structure stabilizer;
- Ce: to favour a non-stoichiometric PVK-type structure and, therefore, the redox mechanism of the WGS reaction;
- Cu: to promote the catalytic activity of iron.

In particular, CeO_2 could participate in the WGS reaction enhancing the catalyst activity under HTS conditions, as a function of its high oxygen storage capacity (OSC), high oxygen mobility and easy reducibility (***31***,***32***,***33***).

Sample	La	Ce	Fe	Cr	Cu	Formula
LaFe	1		1			$LaFeO_3$
LaFeCr-Ce	0.9	0.1	0.9	0.1		$La_{0.9}Ce_{0.1}Fe_{0.9}Cr_{0.1}O_3$
LaFeCr-Cu	1		0.9	0.08	0.02	$LaFe_{0.9}Cr_{0.08}Cu_{0.02}O_3$
LaCeCu	1.9	0.1		0.1		$La_{1.9}Ce_{0.1}CuO_4$

Table 4.9 The PVK-type samples synthesized by citrate method in this PhD thesis work.

Preliminary, a study of the calcination temperature has been performed to obtain the PVK phase with a right compromise between crystallinity and surface area of the sample. In the XRD pattern of the LaFe sample, (Fig. 4.35) a further amorphous phase is present at 500 °C, that disappears completely at about 650 °C, without any further change in the sample calcined at 900 °C. Considering the instrumental error, the surface area values of the samples calcined at 550, 600 and 650 °C are the same, whereas the sample at 500 °C has a value slightly lower. Therefore, the temperature of 650 °C seems to be the right choice to obtain a crystalline PVK phase, with a sufficiently high surface area value.

The PVK phase $LaFeO_3$ is the only phase observed also in the samples partially substituted with Cr, Ce and Cu (LaFeCr-Cu and LaFeCr-Ce) and calcined at 650 °C (Fig. 4.36). On the other hand, the LaCeCu sample after calcination at different temperatures (Fig. 4.34) shows at 650 °C the formation of some PVK phases ($(La_{0.935}Ce_{0.065})_2CuO_4$ and La_2CuO_4) and CuO, with the same behaviour reported in literature (***34***). On the other hand, the calcination at 450 °C for 2 h is not able to form the PVK phase, showing mainly La_2CO_5.

For this reason, all PVK-type catalysts were calcined at 650 °C for 12 h; the calcined powders were grinded and sieved to obtain pellets of 30-40 mesh, that were reduced before the catalytic tests.

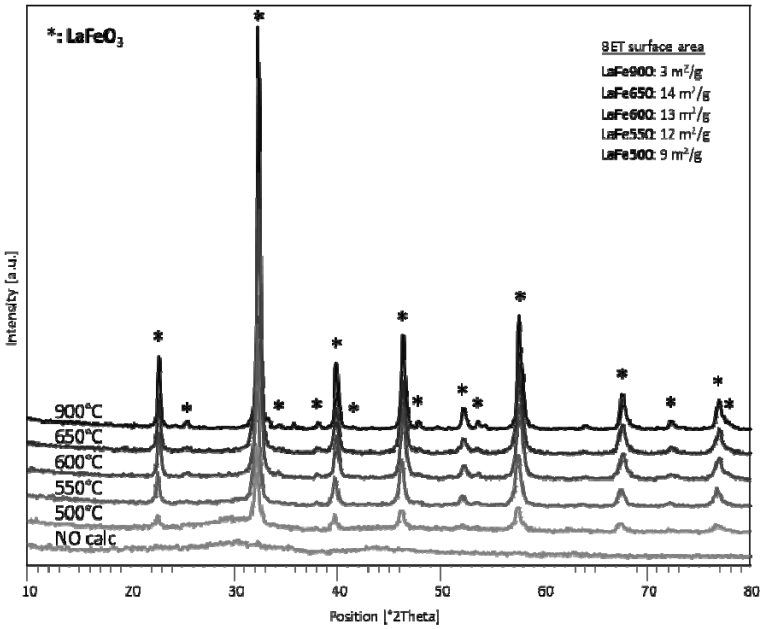

Fig. 4.32 XRD patterns of the LaFe sample calcined at different temperatures.

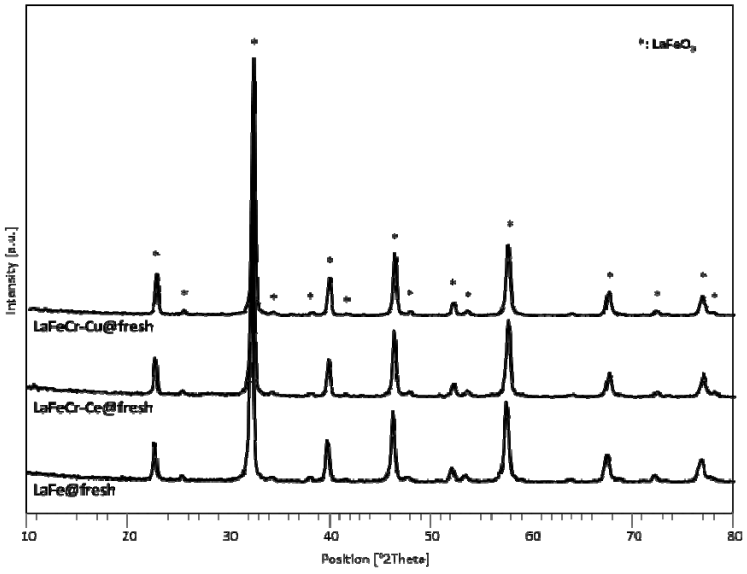

Fig. 4.33 XRD patterns of the LaFe, LaFeCr-Ce and LaFeCr-Cu samples calcined at 650°C.

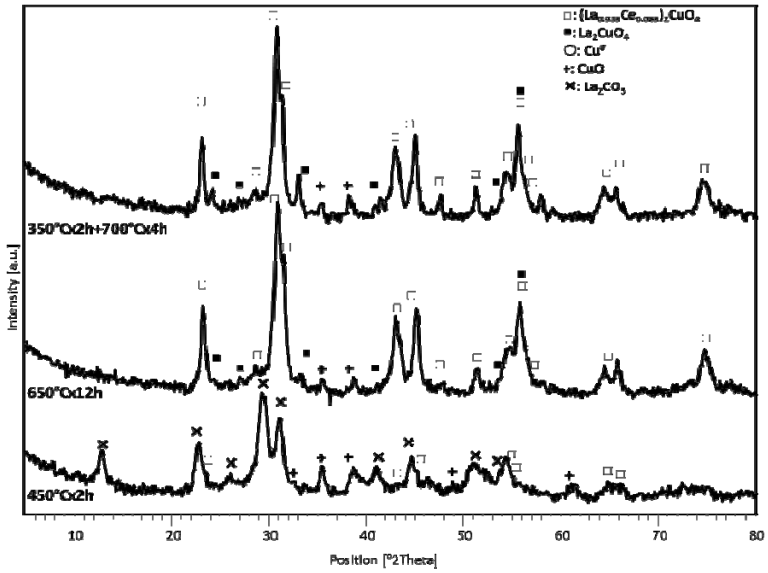

Fig. 4.34 XRD pattern of the LaCeCu sample calcined at different temperatures.

4.3.1.1 ACTIVITY

A summary of all the catalytic results is not reported because the Fe-containing samples are inactive in the shift reaction regardless the operating conditions employed. Practically, the LaFe sample is the only PVK-type sample that shows a low CO conversion value (about 30 %), obtained when the temperature is pushed until 400 °C. To evaluate a possible further reduction eventually occurred after the test at this latter temperature, the test at 300 °C was repeated, without to observe a change in the activity, with the outlet DG composition almost the same of the inlet one, with small differences mainly attributable to the accuracy in the measures.

The addition of Cr, Ce and Cu in the formulation (LaFeCr-Cu and LaFeCr-Ce) has a negative effect and these samples are practically no active in all the investigated conditions, with only a CO conversion of 5-7 % at 400 °C. After this test, for the Cu-containing sample a new reduction step was performed to evidence if the first reduction has been sufficient to activate the sample. The temperature has been increased until 500 °C (60 °C/h) and hold for 3 h under a flow with a S/DG ratio of 0.72, like the last value in the first reduction. The outlet and inlet DG have practically the same composition, evidencing that the CO conversion remains unchanged.

Differently, the LaCeCu sample (without Fe) is active although it shows a very low activity at 350 °C and with a contact time of 1.2 sec, regardless the S/DG ratio (Fig. 4.35). At 350 °C, the CO conversion and H_2 yield values increase to 29 and 24 %, respectively, when the S/DG ratio is increased from 0.25 to 0.55. An activity improvement of 10 % is observed also at 400 °C, by increasing the S/DG value from 0.25 to 0.43.

This catalyst was tested using operating conditions different from those employed for the previously investigated PVK-type samples (S/DG = 0.43 v/v, τ = 2.5, 3.5, 4.7 sec), to verify if the results previously reported in the literature were reproducible (***34***). Being moderately active in HTS conditions above 300 °C (Fig. 4.36), the effect of the contact time was studied at 350 °C and with a S/DG ratio of 0.55 (Fig. 4.35). An increase of the contact time from 0.5 to 3.5 sec gives rise to a consequent increase of the activity, reaching CO conversion and H_2 yield values respectively of

about 50 and 40 % at the highest contact time value. Unfortunately, a further increase of the contact time (4.7 sec) shows an improving of CO conversion, but with a corresponding decrease of the H_2 yield, probably due to side-reactions giving rise to H_2 consumption, such as confirmed . by the decrease in the CO_2 selectivity.

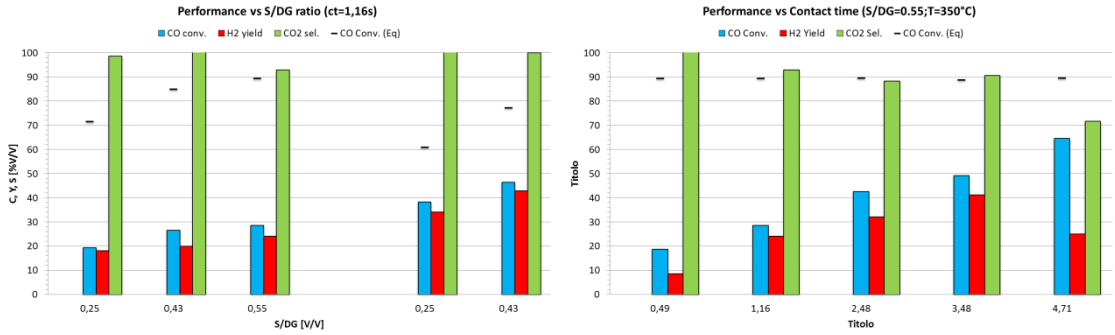

Fig. 4.35 Activity of the LaCeCu sample as a function of S/DG ratio and contact time values.

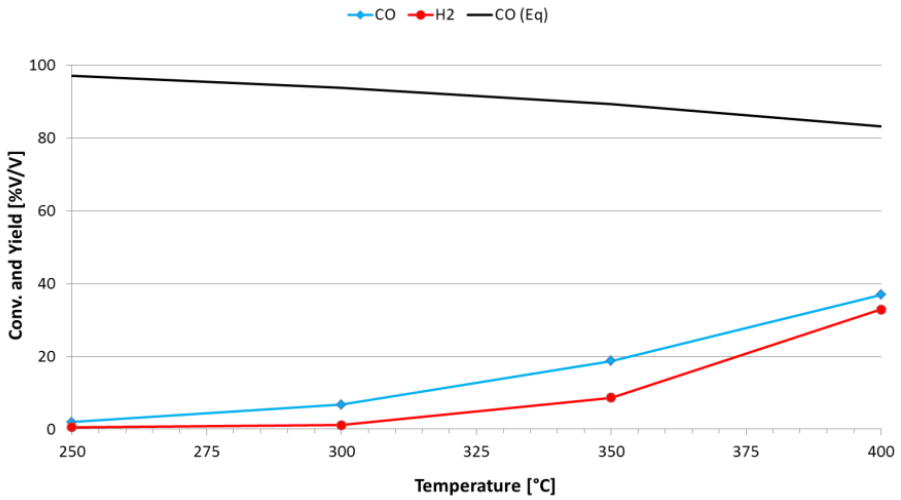

Fig. 4.36 CO conversion for the LaCeCu sample as a function of the temperature (τ = 0.5 sec and S/DG = 0.55 V/V).

4.3.1.2 CHARACTERIZATION AFTER REACTION

As described in Table 4.10, all the Fe-containing samples before and after the catalytic tests show the characteristic peaks of a PVK-type phase ($LaFeO_3$), while those of segregated Cu- or Ce-containing phases are not present, although it cannot be excluded their presence as amorphous phases or in not detectable amounts. The PVK-type phases present in the LaCeCu sample before reaction ($(La_{0,935}Ce_{0,065})_2CuO_4$ and La_2CuO_4), disappear after reaction with formation of carbonates (La_2CO_5) (Fig. 4.37); probably, this latter phase may be attributed to deactivation processes due to the CO_2 formed in the WGS reaction. A reduction of CuO occurs during the catalyst activation.

The crystallite size calculated by the Debey-Scherrer formula (***12***), using the reflection at ≈ 32.3° corresponding to the crystallographic plane (121), indicates a high crystallinity in agreement with the low values of the surface area. In particular, the spent LaFeCr-Ce sample presents a crystal size value three times higher than that of the sample before reaction, confirmed also by the value of the surface area. In the case of the LaCeCu sample after the catalytic tests, the crystal size of the metallic copper at 50.4° is about 17 nm. However, this latter value is not critical one because there is an out-and-out change of phase.

Sample		XRD phase	S_{BET} (m^2/g)	d_{PVK} (nm)
LaFe	fresh	$LaFeO_3$	14	42
	used	$LaFeO_3$	17	52
LaFeCr-Cu	fresh	$LaFeO_3$	11	54
	used	$LaFeO_3$	8	56
LaFeCr-Ce	fresh	$LaFeO_3$	12	49
	used	$LaFeO_3$	2	165
LaCeCu	fresh	$(La_{0,935}Ce_{0,065})_2CuO_4$, La_2CuO_4, CuO	9	-
	used	CuO, Cu, La_2CO_5	8	$d_{Cu(0)}$ = 17

Table 4.10 Chemical-physical properties of the PVK-type samples investigated, before and after the catalytic tests.

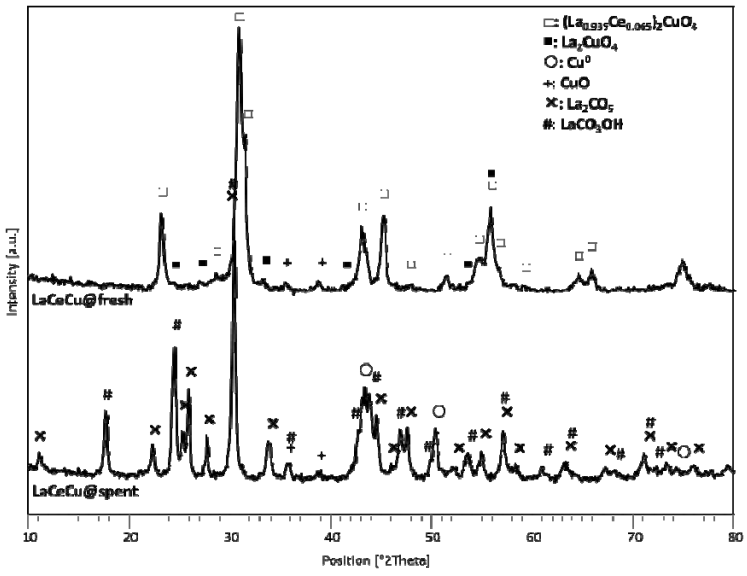

Fig. 4.37 XRD patterns of the LaCeCu sample before and after the catalytic tests

As shown in Fig. 4.38, the temperature programmed oxidation (TPO) after a further reduction of the LaCeCu sample after the catalytic test shows mainly a negative peak at 500 °C, that may be due to carbonate oxidation with evolution of CO_x, confirming the formation of carbonates during the catalytic tests, as already shown in the XRD pattern (Fig. 4.41).

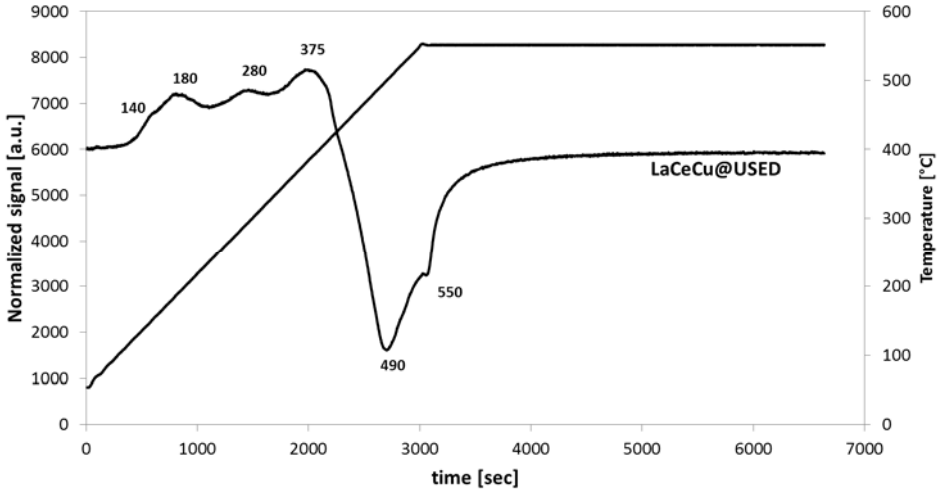

Fig. 4.38 TPO of fresh and spent LaCeCu samples, previously reduced.

The redox properties of the PVK-type samples were investigated by some reduction/oxidation/reduction cycles in temperature programmed (TPR/O/R). The first TPR profile of the $LaFeO_3$ sample shows two overlapped H_2 consumption peaks at 360 and 540 °C (Fig. 4.39). Since La^{3+} is not reducible under these conditions, these H_2 consumptions are due to the reduction of Fe^{3+} ions in the PVK-type structure: the first peak to the reduction of Fe^{III} species on the surface, while that at 540 °C to those in the bulk (***35***). The change in the reduction profile after the oxidation cycle, indicates that some structural changes took place in the PVK structure: the first shoulder at 320 °C may be attributed to the reduction of Fe^{4+} formed during the oxidation cycle (***36***), whereas the second one at 390 °C is attributable to the reduction of surface Fe^{III} to Fe^{III}. The reduction of "bulky" Fe^{III} is observed at 480 °C, i.e. at a temperature lower than that observed in the first TPR run.

$$LaFeO_3 + 1/2\ H_2 \rightarrow LaFeO_{2.5} + 1/2\ H_2O$$

The partial substitution of iron by copper and chromium (LaFeCr-Cu) changes the redox properties of the PVK-type phase: the first H_2 consumption peak ranging from 200 to 350 °C may be attributed to the reduction of Cu^{II} (from Cu^{2+} to Cu^{+} and from Cu^{+} to Cu^{0}) (Fig. 4.40). The reduction peaks of the Fe^{III} species shift towards lower temperatures (340 and 510 °C) than those observed in the LaFe sample, suggesting an Fe-reducibility promoted by Cu^0 ions. Cr^{III} species are not reduced under these conditions, because the reduction of well dispersed chromates (La_2CrO_6) to La_2O_3 and stable $LaCrO_3$ species occurs at temperatures higher than 650 °C (***37***,***38***). However, it is not possible to fully exclude the oxidation of segregated Cr-containing phases during the oxidation step.

The Ce-containing sample (LaFeCr-Ce) shows the reduction of the Fe^{III} ions at 350-390 °C, whereas the peak at 450 °C may be related to the reduction of Ce^{IV} to Ce^{III} (Fig. 4.41). At higher temperature (610 °C), Fe^{III} species in the matrix and chromates (amorphous La_2CrO_6) reduction occurs. After the TPO step, all the reduction peaks are shifted towards lower temperatures.

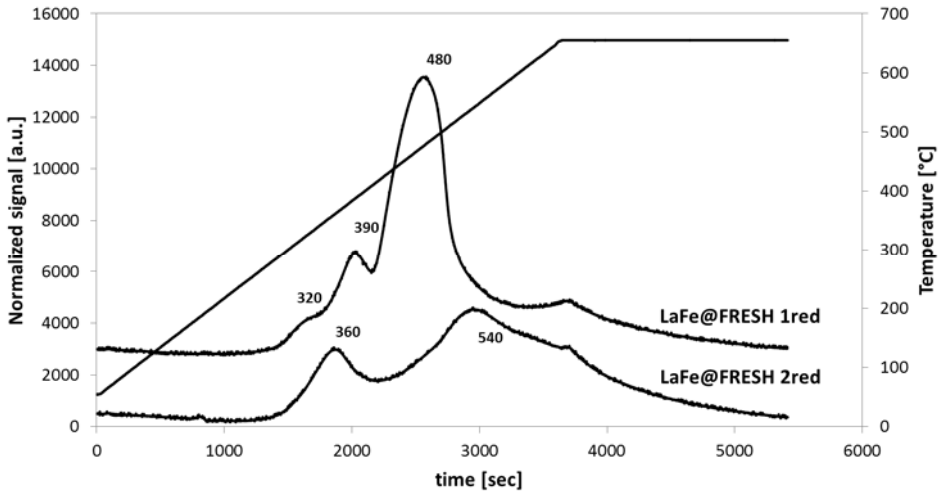

Fig. 4.39 TPR of the LaFe sample before and after the oxidation cycle.

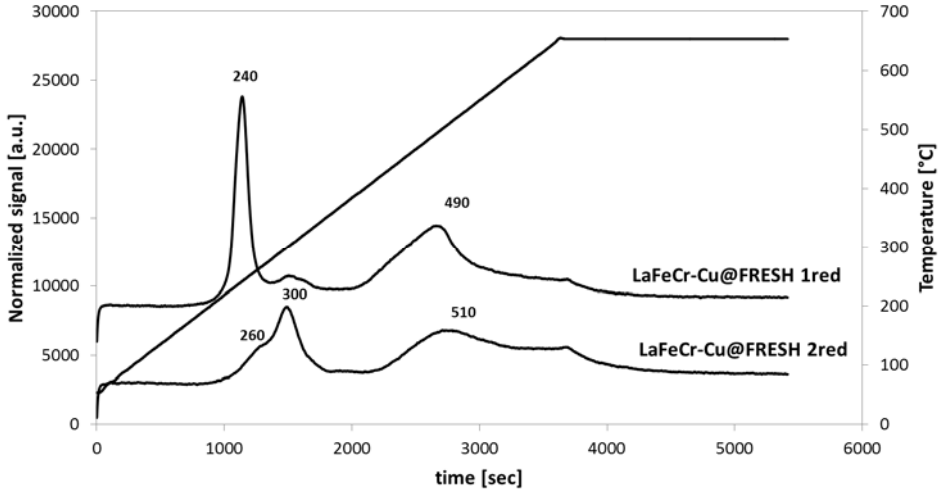

Fig. 4.40 TPR of the LaFeCr-Cu sample before and after the oxidation cycle.

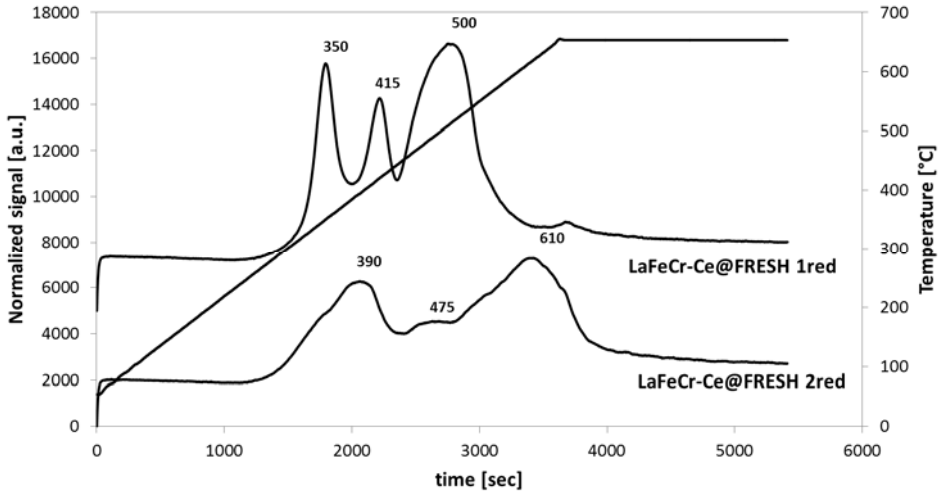

Fig. 4.41 TPR of the LaFeCr-Ce sample before and after the oxidation cycle.

In the LaCeCu sample (Fig. 4.42), the CuO reduction occurs between 265 e 300 °C (reactions 4.1 and 4.2), whereas the broad peak at higher temperature (490 °C) may be due to the reduction of Ce^{4+} to Ce^{3+}. Differently, the TPR after oxidation shows a superposition of three peaks between 190 and 380 °C, due to a segregation of Cu-containing phases on the surface, thus becoming more reducible. The replacement of La^{3+} by Ce^{4+} ions produces an excess of positive charges in the PVK-type structure, which is balanced by the reduction of the Cu^{2+} to Cu^{+} ions (***39***). Also the Ce^{4+} species may be reduced in the same temperature range (***40***,***41***,***42***,***33***,***43***).

$$2\ La_2CuO_4 + H_2 \rightarrow Cu_2O + La_2O_3 + H_2O \qquad \text{reaction 4.1}$$

$$Cu_2O + H_2 \rightarrow Cu^0 + H_2O \qquad \text{reaction4.2}$$

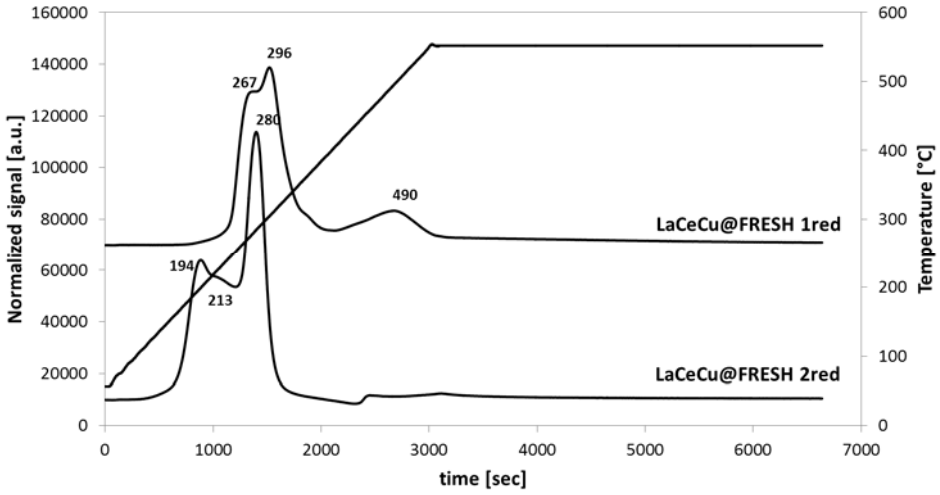

Fig. 4.42 TPR of the LaCeCu sample before and after the oxidation cycle.

The pore size distribution of the LaFe sample before reaction is bi-modal, with pores of 3 and 15 nm diameter (Fig. 4.43). After reaction, the pores with smaller size disappears with a shift of the distribution towards bigger diameters (30 nm). The LaFeCr-Cu sample shows the presence of pores with diameter between 20 and 30 nm, which strongly decreases after reaction, such as previously reported for the LaFe sample (Fig. 4.44). Instead, the LaFeCr-Ce sample shows a homogeneous distribution of the pores, with diameters between 3 and 50 nm (Fig. 4.45). After reaction, this sample does not show any pore-size distribution, probably related to the deactivation phenomena occurred during the catalytic tests, giving rise to a dramatic decrease of the surface area value (Table 4.11), in agreement with the results previously shown in the XRD pattern.

Differently, the LaCeCu sample presents before and after reaction, pores with diameter at 2, 3-4 and 40 nm (Fig. 4.46). After reaction, it is possible to observe a change in terms of pore volume due to a decrease of the porosity attributable to the pores with highest diameter. This is probably a consequence of the sintering occurred during the reaction. Moreover, this result may also contribute to decrease of the surface area, that is, however, less affected by deactivation phenomena being balanced by an increase of the pores with diameter between 3 and 4 nm. As shown in Table 4.11, the average pore diameter of the Fe-containing samples shows an increase during reaction, being also marked by the increase of the pellet brittleness.

Samples		S_{BET} [m^2/g]	V_{PORES} (BJH des.) [cm^3/g]	d_{PORE} (BJH des.) [nm]
LaFe	*fresh*	14	0.12	26
	used	9	0.13	49
LaFeCr-Cu	*fresh*	9	0.12	42
	used	7	0.07	32
LaFeCr-Ce	*fresh*	12	0.07	16
	used	3	0.02	36
LaCeCu	*fresh*	10	0.09	29
	used	9	0.06	26

Table 4.11. Physical properties of the PVK-type samples before and after reaction.

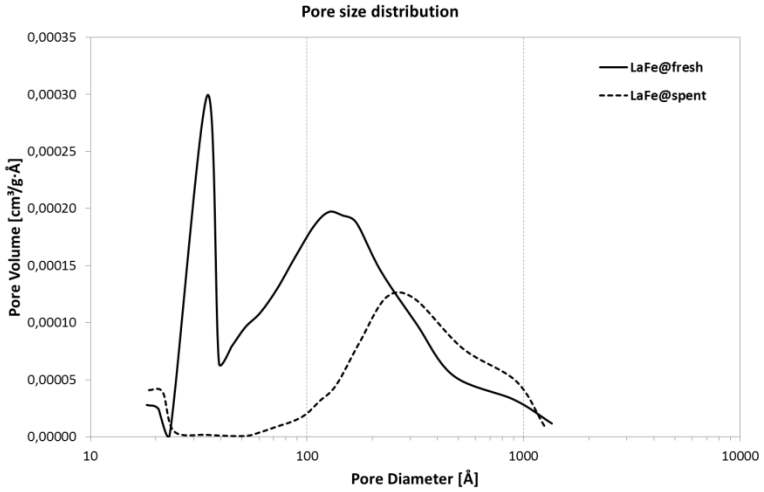

Fig. 4.43 BJH pore distribution for the LaFe sample before and after reaction.

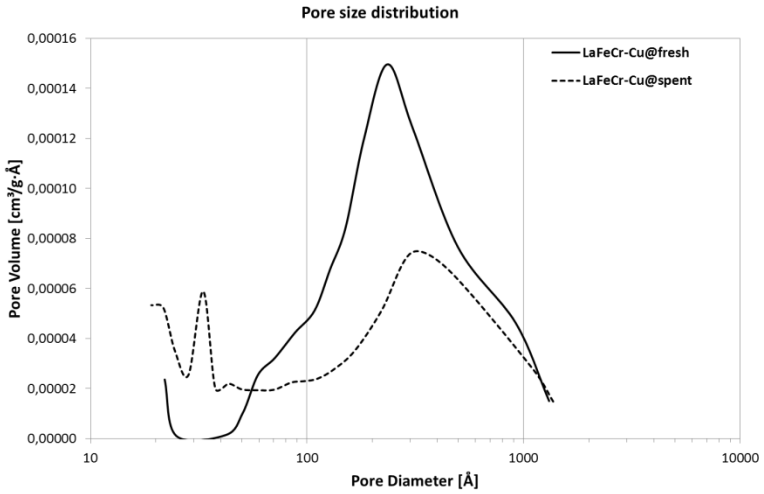

Fig. 4.44 BJH pore distribution for LaFeCr-Cu sample before and after reaction.

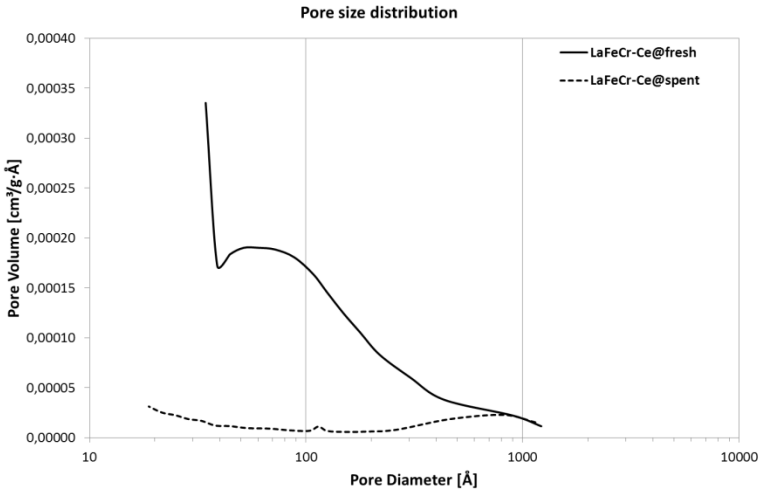

Fig. 4.45 BJH pore distribution for LaFeCr-Ce sample before and after reaction.

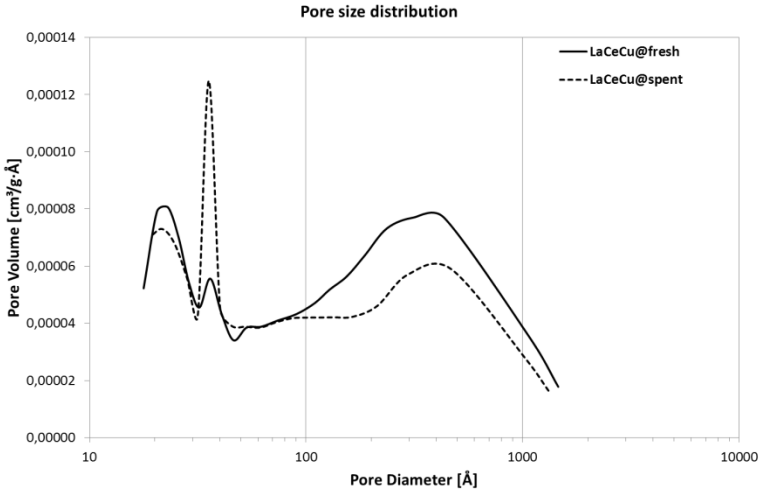

Fig. 4.46 BJH pore distribution for LaCeCu sample before and after reaction.

The isotherms and the hysteresis loops are the same for all samples, before and after reaction, and, respectively, of **TYPE IV** and **TYPE H4** of the IUPAC classification (***16***) (Fig. 4.47). Therefore, the pore analysis shows that all the PVK-type samples contain mainly mesopores (2-50 nm).

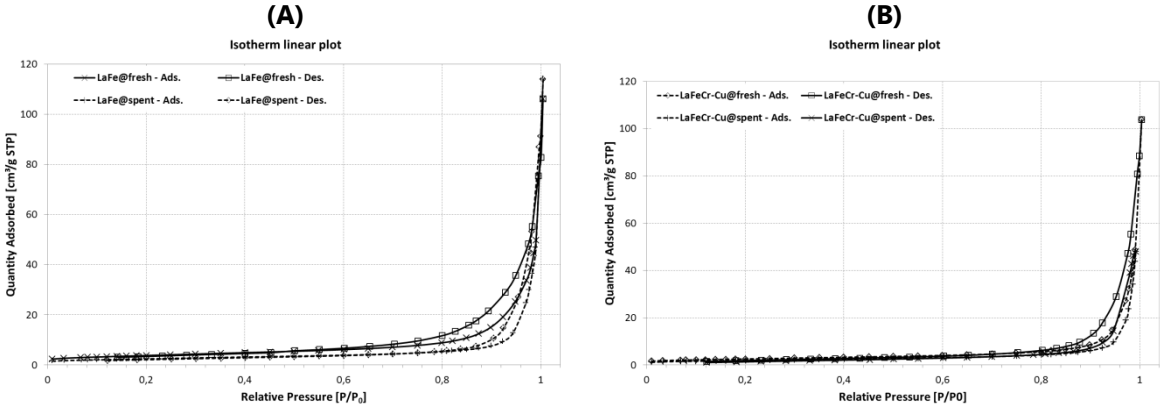

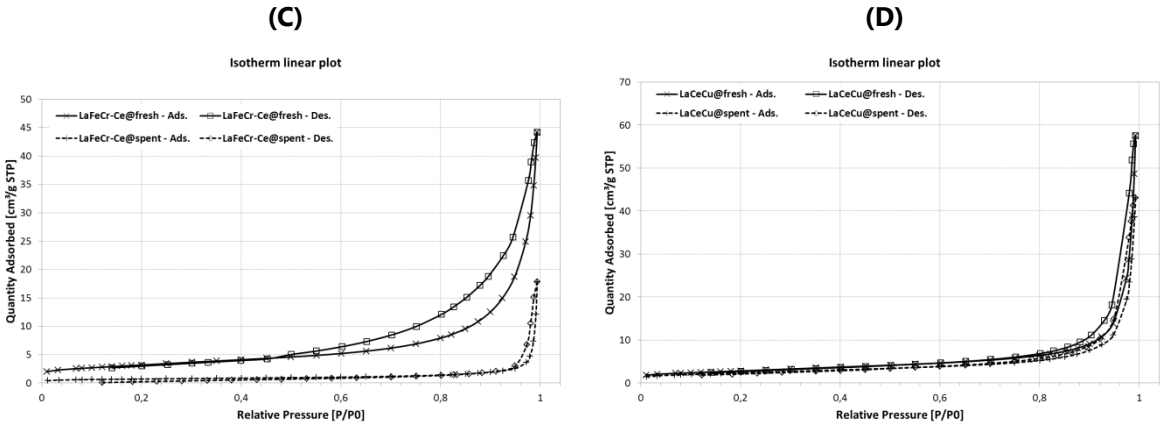

Fig. 4.47 Isotherms of the PVK-type samples: (A) LaFe, (B) LaFeCr-Cu, (C) LaFeCr-Ce, (D) LaCeCu.

4.3.2 Ce-containing SAMPLES

The PVK-type Ce-containing ternary oxides have formula $A^{II}Ce^{IV}O_3$, with unusual ionic conductivity behaviours at moderate and high temperatures (***45***). Some researchers (***46***,***47***) indicated the presence mainly of Fe^{II} ions in $CeFeO_3$. Ce/Fe-based samples, promoted or unpromoted by copper, have been prepared by citrate method, according to the synthesis employed in the preparation of the previous La/Fe-containing samples. The molar M^{4+}/M^{2+} ratio was about 1, with a small excess of M^{2+} ions when copper was present (Table 4.12).

Sample	Ce	Fe	Cu	Formula
CeFe	1	1		$CeFeO_3$
CeFe-Cu	1	0.6	0.6	$CeFe_{0.6}Cu_{0.6}O_3$

Table 4.12 Composition of the Ce/Fe-based samples synthesized..

Properly, these samples are mixed oxides of iron and cerium, while PVK phases are not present. The difficulty to obtain the $CeFeO_3$ PVK-type phase are in agreement with the data of literature (***37***,***48***), where it is reported that $CeFeO_3$ forms only after 10 redox cycles occurring on Ce/Fe mixed oxides. This formation after 10 redox cycles is possible because continuous redox processes may contribute to a grain refining of complex oxides and change the physicochemical properties of the sample surface, which may promote the inter-dispersion between the two single oxides and produce $CeFeO_3$ phase (***48***). For these reasons, the Ce/Fe-based catalysts prepared in this PhD thesis may be considered anyway as PVK-like samples.

The XRD patterns the Ce/Fe-based samples (Fig. 4.48), with (CeFe-Cu) or without (CeFe) copper, show mainly the presence of CeO_2. In the CeFe sample, also haematite (Fe_2O_3) phase is observed, that disappears after the partial substitution of iron with copper. In fact, the XRD pattern of the CeFe-Cu sample shows the reflections of copper oxide, without any evidence of Fe-containing phases. Diffraction peaks corresponding to iron oxides were observed only in samples

with high Fe-contents (***49***). The absence of iron oxides may indicate a substitution of iron ions in the ceria lattice, with the formation of a solid Ce-Fe oxide solution (***48***).

The Ce/Fe samples exhibit an increase of the ceria reducibility, with a shift of the reduction peak to lower temperatures (***48***). Moreover, the position on the temperature maximum depends on the particles size and preparation parameters (***11***). The addition of Cu to Fe_2O_3 enhances considerably the reduction of the haematite to magnetite (Fe_3O_4), that occurs below 300 °C, as compared to that observed in the pristine Fe_2O_3 sample (***11***).

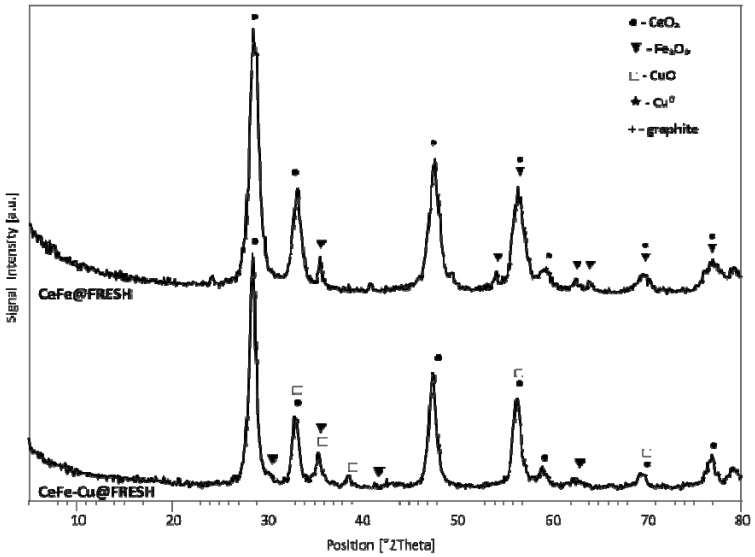

Fig. 4.48 XRD pattern of the CeFe and CeFe-Cu samples before reaction.

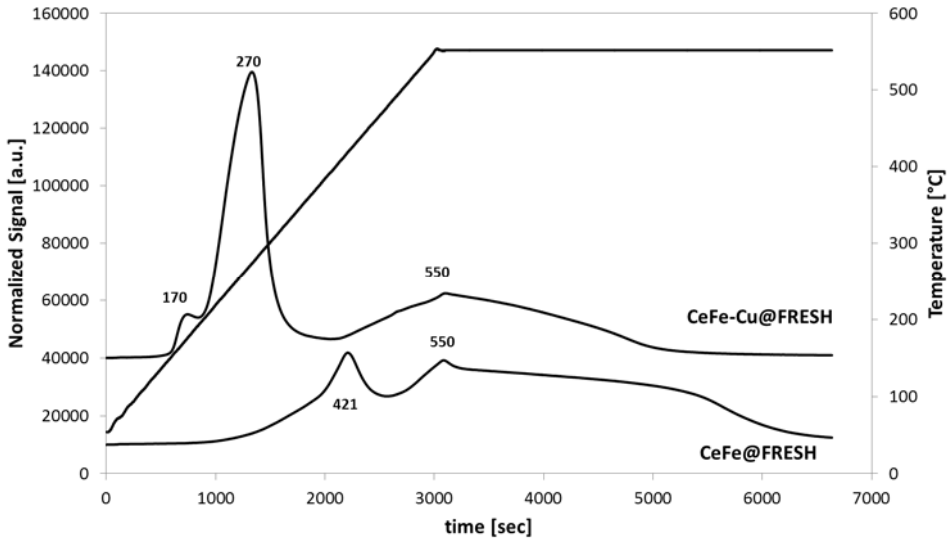

Fig. 4.49 TPR of the fresh Ce/Fe-based catalysts.

4.3.2.1 ACTIVITY: EFFECT OF COPPER PROMOTING

As for the PVK-type catalysts, the CeFe-based catalysts were tested using contact time values higher than the standard ones. At 400 °C, The CeFe sample reaches a CO conversion of only 18 %, with a S/DG ratio of 0.55 and contact time value higher than 2 sec. Hence, it may be considered inactive in the typical WGS reaction conditions. Thus, it was promoted adding copper in the preparation, in order to verify its role on the catalytic activity.

The CeFe-Cu sample shows good performances in HTS conditions (350 °C), reaching CO conversion and H_2 yield values of about 40 % with a contact time of 0.5 sec and higher excess of steam (Fig. 4.50). Since the thermodynamic parameter (S/DG ratio) has a moderate effect on the activity, the CeFe-Cu was tested in the HTS conditions by changing the contact time. The CO conversion already reaches a value of 27 % at the lowest contact time (0.25 sec). CO conversion and H_2 yield values show a gradual and constant increase (up to 76 and 70 %, respectively) by increasing the contact time from 0.25 to 2.6 sec. The trend of CO conversion results in a good activity only above 350 °C (Fig. 4.51); in fact, it reaches a value of 60 % ca. at 400 °C, by using a short contact time (0.5 sec). Despite it, the result is far from the equilibrium one. The CO_2 selectivity is always higher than 94 %, evidencing that the change of the different parameters does not favour the side-reactions.

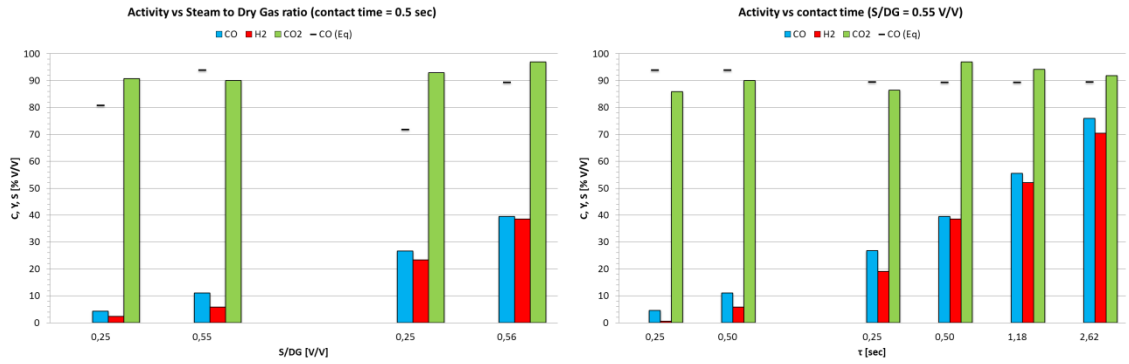

Fig. 4.50 Activity of the CeFe-Cu sample as a function of S/DG ratio and contact time values.

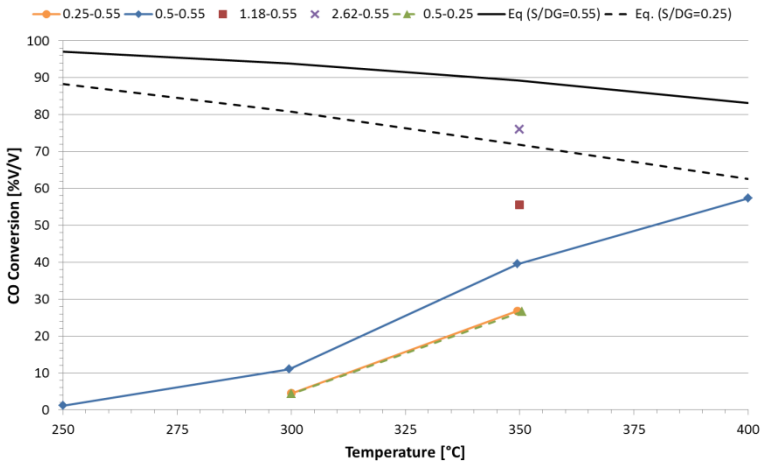

Fig. 4.51 CO conversion for the CeFe-Cu sample as a function of the temperature, for different τ and S/DG values.

4.3.2.2 CHARACTERIZATION AFTER REACTION

A summary of the chemical-physical properties is reported in the Table 4.13. Before and after reaction, CeO_2 is the main phase, showing a reduction temperature lower than that typical for the cerium oxide. In the CeFe sample after the catalytic tests, the typical reflections of magnetite (Fe_3O_4) are present, confirming the catalyst reduction during the activation (Fig. 4.52).

Differently, in the Cu-promoted sample (CeFe-Cu) are present also the reflections attributable to metallic copper (Fig. 4.53). As expected, the reduction effect is more evident in this sample, being the sintering of copper particles more favoured than that of Fe-containing species. Probably, the magnetite phase is re-oxidized during the catalyst unloading, thus not present in the XRD pattern. The sintering is also confirmed by the surface area value, that decreases in the CeFe-Cu sample, whereas it remains practically constant in the CeFe sample. CeO_2 has been reported to be able to suppress the aggregation of the main active component, such as Fe, during the redox reaction (***49***).

Sample		XRD phase	S_{BET} (m^2/g)	Cu^0 crystal size (nm)
CeFe	fresh	CeO_2, Fe_2O_3	18	-
	used	CeO_2, Fe_3O_4	17	-
CeFe-Cu	fresh	CeO_2, Fe_2O_3, CuO	11	
	used	CeO_2, Fe_2O_3, Cu	8	34

Table 4.13 Chemical-physical properties of the Ce/Fe-based samples.

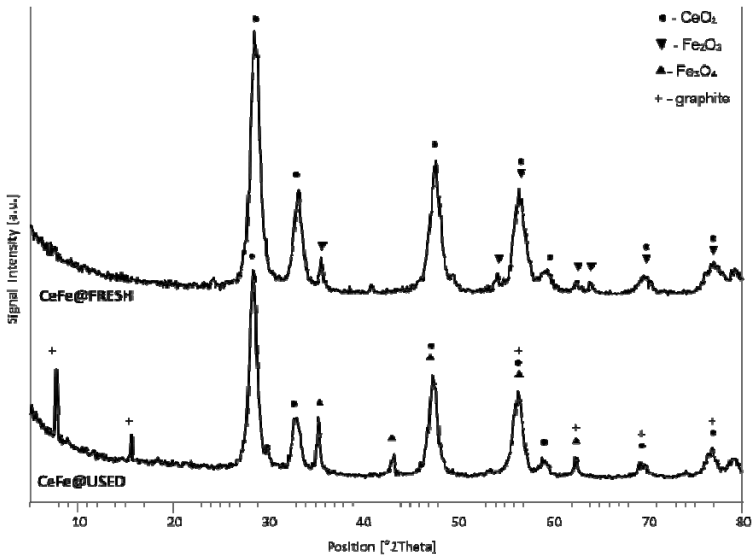

Fig. 4.52 XRD patterns of the CeFe sample before and after reaction.

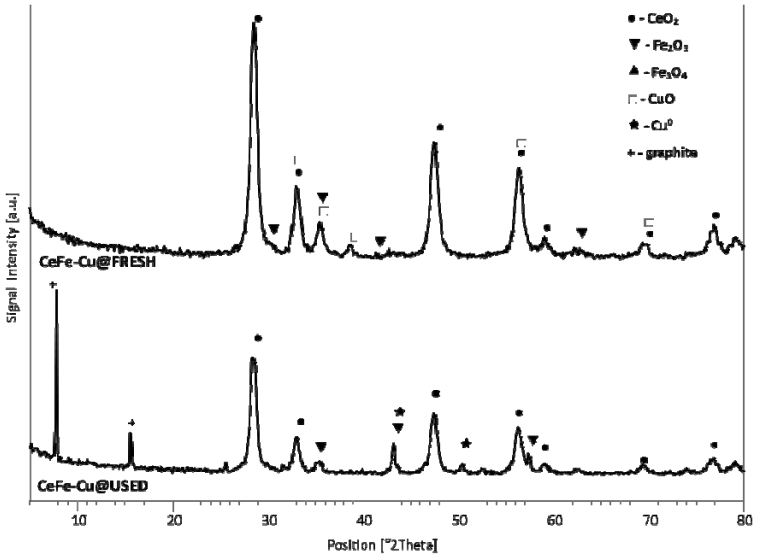

Fig. 4.53 XRD patterns of the CeFe-Cu sample before and after reaction.

The TPR analysis of the CeFe sample after reaction shows a single peak at 420 °C, broad at lower temperature, due to the reduction of haematite ($Fe_2O_3 \rightarrow Fe_3O_4$) and CeO_2 to CeO_{2-x} (Fig. 4.54). In the reduction after a further oxidation of the sample unloaded after the catalytic tests, two peaks, at 330 and 410 °C, are observed and attributed to the reduction of surface particles of Fe_2O_3 and CeO_2, respectively. At temperature higher than 550 °C, it is possible to observe an increase in the profile, attributable to a not complete reduction of both bulk Fe_3O_4 and CeO_2.

On the other hand, the CeFe-Cu sample after reaction presents the same reduction profile of the fresh one (Fig. 4.55). Again, both peaks at 170 and 270 °C are due to copper oxides reduction: the first peak is attributable to CuO-particles finely dispersed on the CeO_2 surface, whereas the second one is due to bulk CuO. As in the case of the Ce/Fe sample, the broad peak at high temperature may be related to an incomplete reduction of Fe- and Ce-containing species, that occurs at temperatures above 600 and 800 °C, respectively.

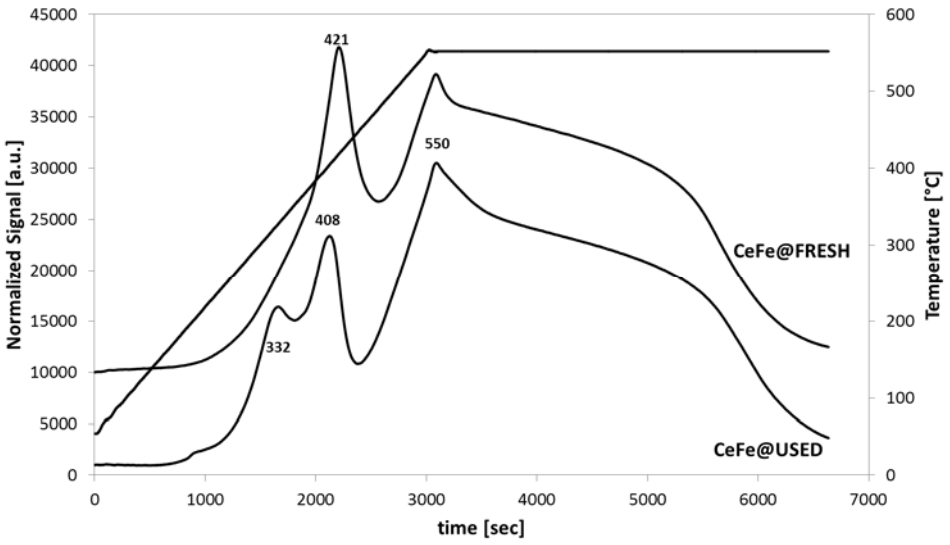

Fig. 4.54 TPR of the CeFe sample before and after oxidation.

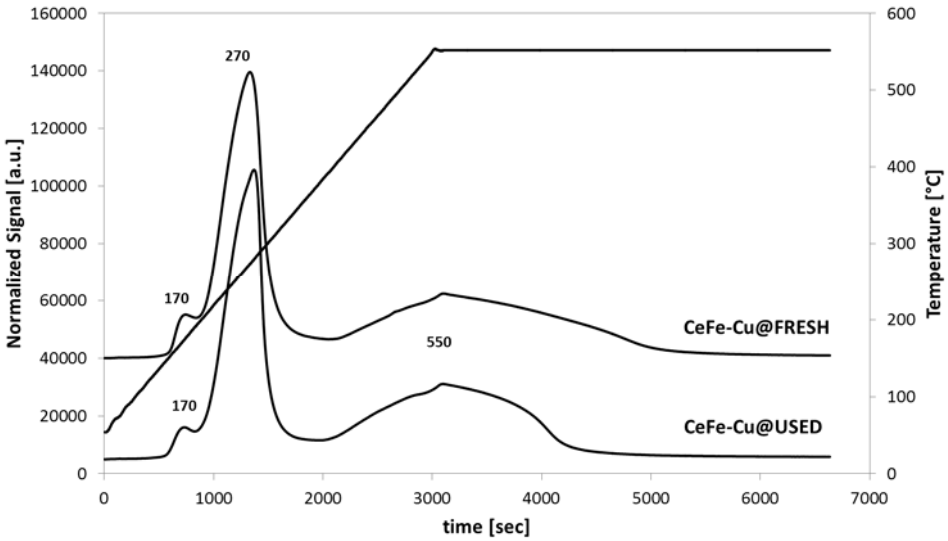

Fig. 4.55 TPR of the CeFe-Cu sample before and after oxidation.

The two Ce/Fe-based catalysts show similar pore size distributions, both before and after reaction (Fig. 4.56 Fig. 4.57). In both the samples before reaction, the distribution is mono-modal with a maximum between 3 and 4 nm. After reaction, the porosity strongly decreases and this may be linked to an increase of volume due to pores with larger size (10 nm) in the CeFe sample. In the CeFe sample, a breakage of pores may describe the increase of the pore volume, although the surface area remains practically constant (Table 4.14). On the other hand, it completely disappears in the Cu-promoted sample (CeFe-Cu), in which a structural sintering occurs, evidenced also by the surface area value in the CeFe-Cu sample after reaction. The pore sizes are always lower than 30 nm and, related to isotherms of **TYPE IV**, with hysteresis loops of **TYPE H4**, confirming the presence of mesopores in both catalysts (***16***) (Fig. 4.58).

Samples		S_{BET} [m^2/g]	V_{PORES} (BJH des.) [cm^3/g]	d_{PORE} (BJH des.) [nm]
CeFe	*fresh*	18	0.061	7
	used	17	0.069	12
CeFe-Cu	*fresh*	11	0.059	14
	used	8	0.053	19

Table 4.14 Chemical-physical properties of the PVK-like samples.

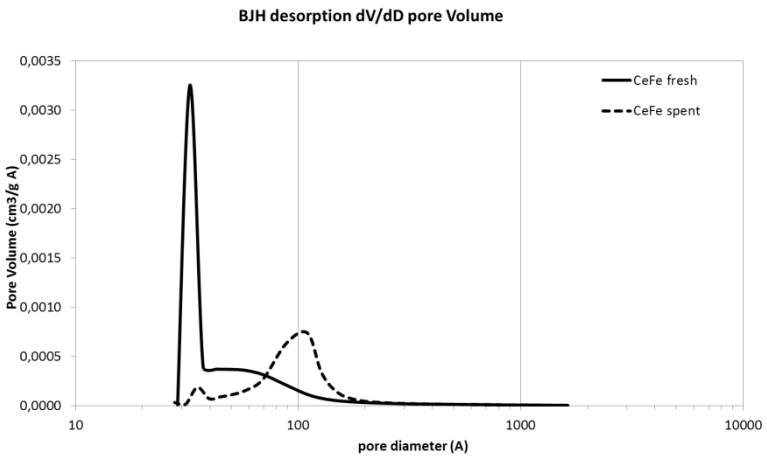

Fig. 4.56 BJH pore distribution for the CeFe sample before and after reaction.

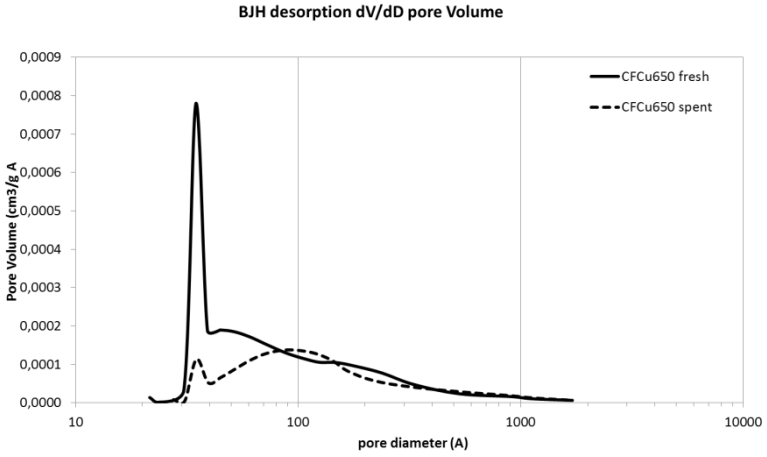

Fig. 4.57 BJH pore distribution for the CeFe-Cu sample before and after reaction.

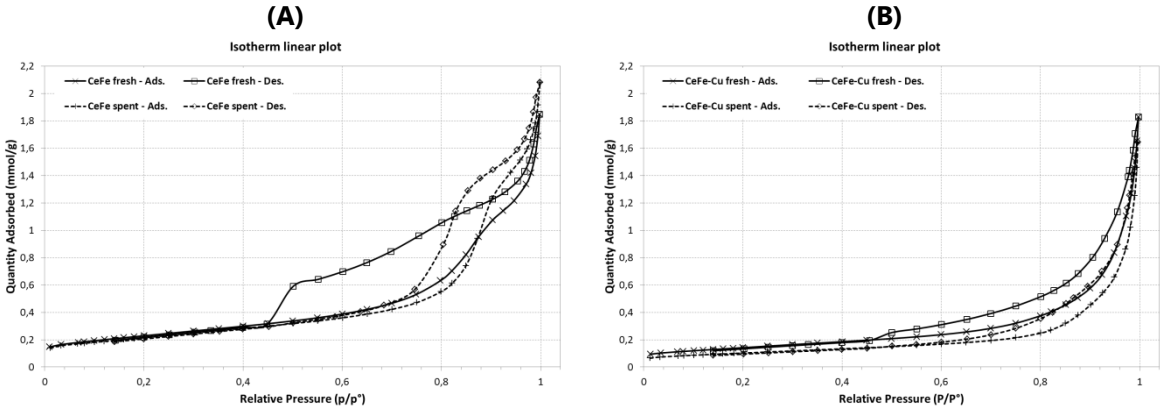

Fig. 4.58 Isotherms of the CeFe and CeFe-Cu catalysts before and after reactions.

4.3.3 COMPARISON AMONG THE PEROVSKITE SAMPLES

Some PVK-type catalysts have been studied to be used in MTS conditions, choosing the perovskite structure to avoid dishomogeneity or phase segregations. The samples were prepared using the citrate method to obtain the PVK-type phase at 650°C, preserving good surface area values. The reducibility and stability of all species are significantly affected by the composition and different thermal treatments. Ce/Fe-based samples are more really mixed oxides, but they were considered PVK-type catalysts because of preparation method used (citrate method).

The samples were submitted to a catalytic study to evidence the promoting effect of Cu or the stabilization effects of Ce or Cr, as shown in the chemical-physical characterizations. All these samples show a negligible activity in the WGS process and after reaction samples low surface area values and high crystallite sizes. On the other hand, the LaCeCu sample shows the best activity in the WGS reaction, with a CO conversion of about 50 % at 350 °C and with a contact time of 3.5 sec. Increasing the contact time, the CO conversion increases up to 65 % but H_2 yield decreases, probably due to side-reactions giving rise to a H_2 consumption.

On the other hand, the Ce/Fe-based sample is active only if promoted by copper, with the best performances observed for the CeFe-Cu sample above 350 °C. The CO conversion reaches aa value of 76 % by increasing the contact time up to 2.6 sec.

Considering this behaviours, it is not possible to hypothesize the use of the PVK-type samples in the WGS process, with the exception of the LaCeCu sample. However, it must be noted that this sample reaches an activity (as CO conversion) that is 50% lower than that observed for the CeFe-Cu sample. In this case, it could be possible to improve the activity at middle temperature, optimizing the composition and using the catalyst in more favourable operating conditions (high S/DG ratio and contact time).

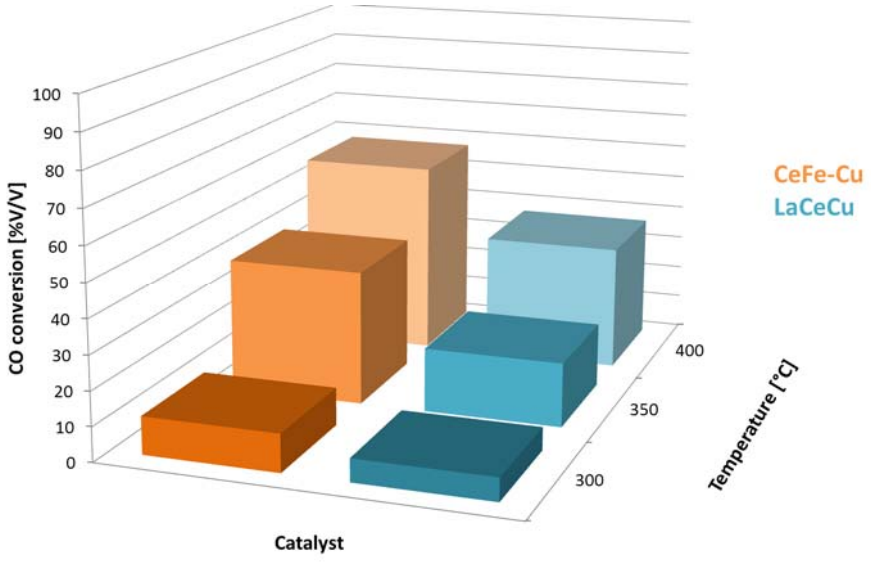

Fig. 4.59 Activity as a function of the temperature for the CeFe-Cu and LaCeCu catalysts investigated (S/DG = 0.55 V/V and τ = 0.5 sec).

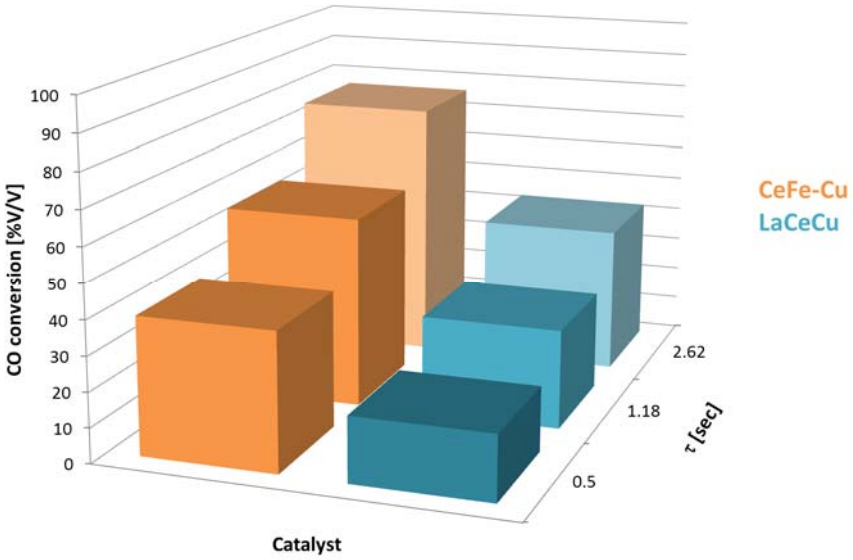

Fig. 4.60 Activity as a function of the contact time for the CeFe-Cu and LaCeCu catalysts investigated T = 350 °C and S/DG = 0.55 V/V).

4.4.EX-HT SAMPLES

New layered materials, anionic clays or hydrotalcite-type (HT), have been used as precursors to obtain new catalysts, with unusual properties due to the presence of all active elements inside the brucite-type layers of the precursors. HT-type samples, having general formula e $M^{II}M^{III}(OH)_{16}(A^{2-})\cdot 4H_2O$, are very interesting because they have a flexible structure allowing the partial substitution of the cations with active ones and, therefore, to obtain final product with a great variety of formulations. HT-type phases form by controlled mixed oxides with high thermal stability, surface area and active-phase dispersion, factors directly affecting the catalytic activity.

HT precursors are prepared by a co-precipitation method with a simultaneous precipitation of all the elements to obtain a homogeneous product. The final calcined samples (ex-HT), used as catalyst, were grinded and sieved to 30-40 mesh size before to the reactor loading. Before the tests, the ex-HT catalysts were reduced with a defined protocol, as previously reported in § 3.3.2.2.

4.4.1 EX-HT CATALYSTS

Initially, the study has been focused on a stable formulation that not only may act as support with good physico-chemical properties in the MTS conditions, but also as promoter of the main active phase during the WGS reaction. Actually, zinc and aluminium oxides are the most suitable phases, used as support in the industrial WGS units. A recent patent (***50***) claimed Zn/Al ex-HT samples as good catalysts in the HTS conditions, after relevant doping by K_2O; therefore, it has

been chosen as starting sample and obtained by calcination of a HT precursor with a M^{II}/M^{III} molar ratio equal to 3. It was also impregnated with K by incipient wetness impregnation method, to reproduce the formulation reported in the patent.

Further development of this formulation has been the introduction of copper as active metal to enhance the activity at lower temperatures; copper is highly active element in the WGS reaction, but require to be stabilized to operate in MTS conditions, avoiding methanation reaction. Two ex-HT samples have been prepared, both containing a Cu-content lower than 20 wt.%, , with a Cu-amount in ZAC2c two times higher than in ZAC1c. Therefore, the inclusion of Cu^{2+} ions (and, after reduction, of Cu^0 particles) in a stable matrix, such as ex-HT Zn/Al mixed oxides, may allow to stabilize Cu^{II} species and, consequently, to avoid side reactions (mainly methanation) and a quick deactivation by sintering.

As shown in Table 4.16 and figure 4.65, all the precursors present the characteristic reflections of HT phases with the same size, together with small amounts of ZnO. After calcination (Fig. 4.66), the HT structure evolve topotactically and the XRD patterns shows the presence of only ZnO, regardless of the composition, without any segregation of Cu-containing species, thus in amount not detectable or well dispersed in the mixed oxide matrix. It is noteworthy that the study on these samples is in progress and all data (such as the compositions) have been not reported due to confidentiality restrictions.

Sample		Phases	S_{BET} [m^2/g]	d_{HT} [nm]
ZA3K	*precursor*	$Zn_6Al_2(OH)_{16}(CO_3)\cdot 4H_2O$	-	n.d.
	fresh	ZnO	60	-
ZAC1c	*precursor*	$(Cu,Zn)_6Al_2(OH)_{16}(CO_3)\cdot 4H_2O$	26	31
	fresh	ZnO	62	-
ZAC2c	*precursor*	$(Cu,Zn)_6Al_2(OH)_{16}(CO_3)\cdot 4H_2O$	32	33
	fresh	ZnO	48	-

Table 4.156. Physico-chemical properties of the ex-HT catalysts and their precursors.

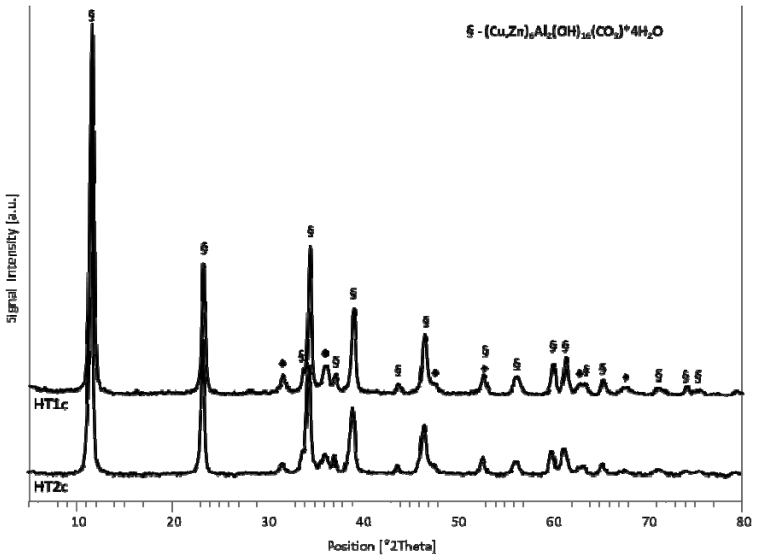

Fig. 4.65 XRD pattern of the HT precursors.

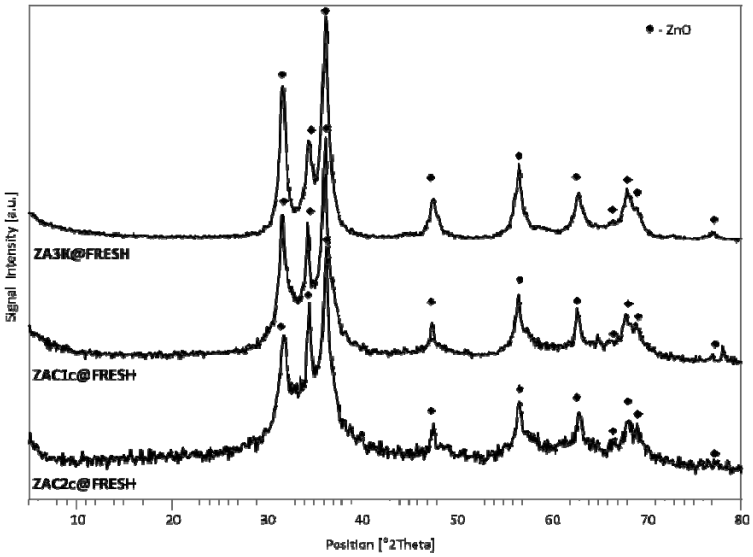

Fig. 4.66 XRD pattern of the calcined ex-HT samples before reaction.

For the Cu-containing samples (ZAC1c and ZAC2c), it is possible to hypothesize the presence of different Cu-containing species on the basis of the literature data, with different oxide-oxide surface interactions [3] (Table 4.3. The TPR profiles of both ex-HT Cu-containing catalysts show that, before reaction, thay are completely reduced at temperatures below 300 °C with a peak related to reduction of the highly dispersed Cu species to metallic copper (***7***,***8***,***9***,***10***). ZnO does not reduce under the experimental conditions, as reported in literature (***6***) and observed for the , ZA3K sample .

Species	T [°C]	Description	Reduction step
"Free" CuO	160-250	*Small particles highly dispersed*	$Cu^{2+} \rightarrow Cu^{+}$ Cu^{2+} or $Cu^{+} \rightarrow Cu^{0}$
CuO	250-330	*CuO strongly bounded with ZnO* *Bulky CuO*	Cu^{2+} or $Cu^{+} \rightarrow Cu^{0}$
Cu-spinel	400-600	*Cu(II) in the matrix*	$Cu^{2+} \rightarrow Cu^{0}$

Table 4.16 Possible Cu-species as a function of the temperature range.

4.4.1.1 EFFECT OF CU-CONTENT ON THE ACTIVITY

The first approach has been to understand if the Zn/Al-based catalyst, claimed in the patent (***50***), is really able to show a significant activity in the WGS reaction. Different conditions have been employed, also reproducing those already reported in the original patent. Furthermore, it is noteworthy that an analogous r Mg/Al sample (replacing zinc with magnesium, i.e. an hydrogenating element with a basic one) to evidence the role of zinc and the potassium added as doping.

For the ZA3K sample, the decrease of the S/DG ratio from 0.55 to 0.25 strongly affects the performances (Fig. 4.67); in particular at 400 °C, where the catalyst shows a sufficient activity, the

CO conversion decreases from 40 to 10 % decreasing the S/DG ratio. The role of the kinetic factors is more evident above 375 °C, being necessary an increase of the temperature to enhance the CO conversion. Despite it, the variations in CO conversion values are more pronounced than those in H_2 yield. Although the operating conditions are favourable, these latter are always lower than the CO conversion values and reaches the highest value at 400 °C (Fig. 4.68). This may be justified hypothesizing the presence of side-reactions with H_2 consumption, favoured by the high surface basicity, with formation of oxygenated product, as reported by Anderson *et al.* (***51***,***52***,***53***). This was confirmed by the HPLC analyses on the liquid condensates, that show a significant presence of oxygenated products, mainly methanol.

The ZAC1c sample shows the best performance in all the temperature range investigated (Fig. 4.69), reaching the equilibrium values of CO conversion already at 300 °C. The decrease of the S/DG ratio has a negative effect at all the temperatures, although is significant only at 250 °C; in fact, the CO conversion is only lower of 5 % than the equilibrium value at 300 °C. Differently, the ZAC1c sample shows best performances using the typical S/DG ratio of industrial conditions (0.55 v/v) (Fig. 4.70). The WGS reaction for this sample is slightly affected by the contact time: at 300 °C, the CO conversion decreases only if using the lower contact time value (0.25 sec), whereas at 250 °C reaches a value of 90 % with a contact time of 1.0 sec. However, ZAC1c sample reaches at 250 °C the equilibrium value of CO conversion using the industrial contact time values. The H_2 yield has practically the same trend of CO conversion: this result together with the H_2 yield and CO_2 selectivity values (always higher than 97 %) evidences the absence of significant side-reactions.

Finally, the equilibrium values reached in more soft conditions, suggests a good performance of this catalyst in the MTS conditions. For this reason, the possible deactivation of the ZAC1c sample has been studied at 300°C for 100 h, by using a most favourable contact time (1.0 sec), but hard conditions in term of S/DG value (0.25 v/v) (Fig. 4.71). The outlet DG composition is close to equilibrium one and remains stable during the long test. The CO amount increases only of 0.7 % after 100 h of tos (time-of-stream), evidencing a very stable behaviour of this sample also under pushed shift conditions. The same behaviour is observed for the ZAC2c sample, thus not reported.

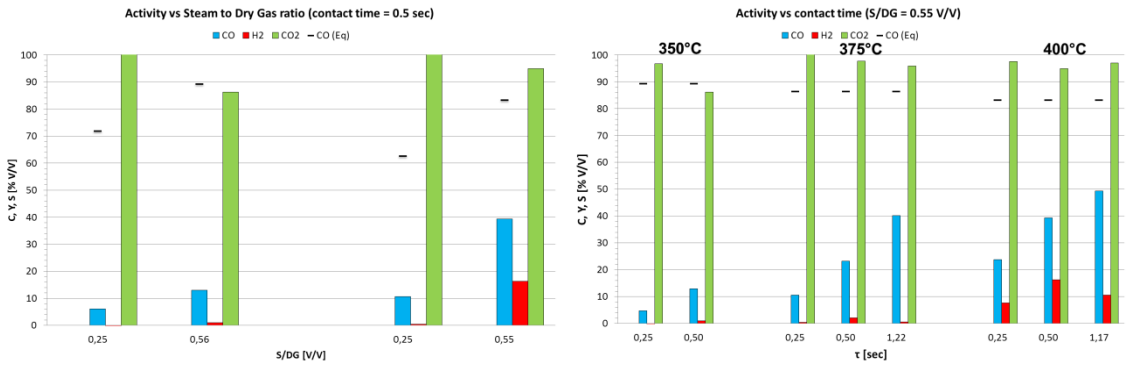

Fig. 4.67 ZA3K activity as a function of S/DG ratio and contact time values.

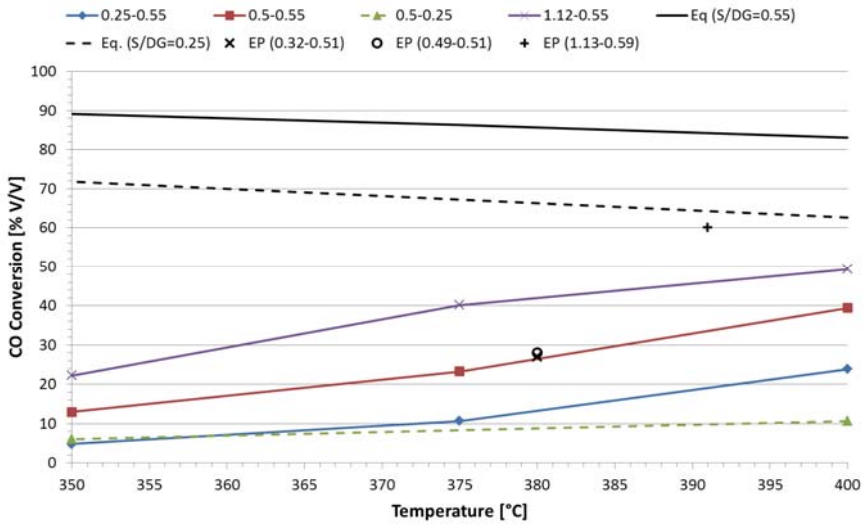

Fig. 4.68 CO conversion of the ZA3K sample as a function of the temperatures (for different τ and S/DG values).

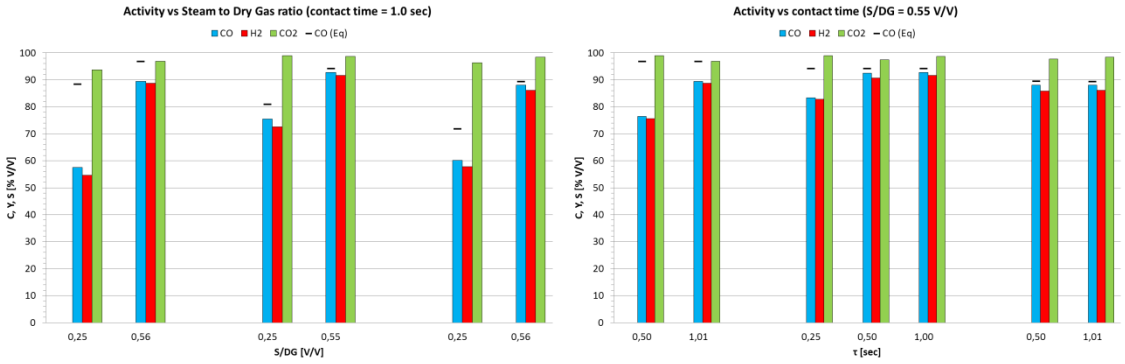

Fig. 4.619 ZAC1c activity asa function of S/DG ratio and contact time values.

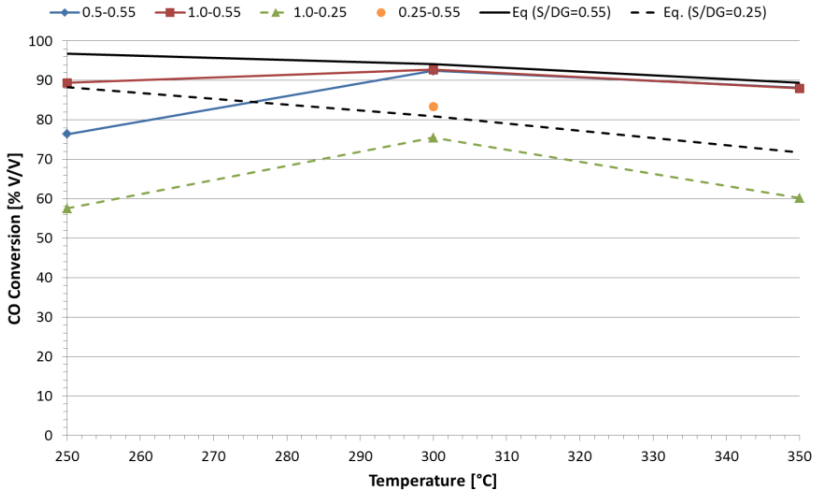

Fig. 4.620 CO conversion of the ZAC1c sample as a function of the temperatures: (for different τ and S/DG values).

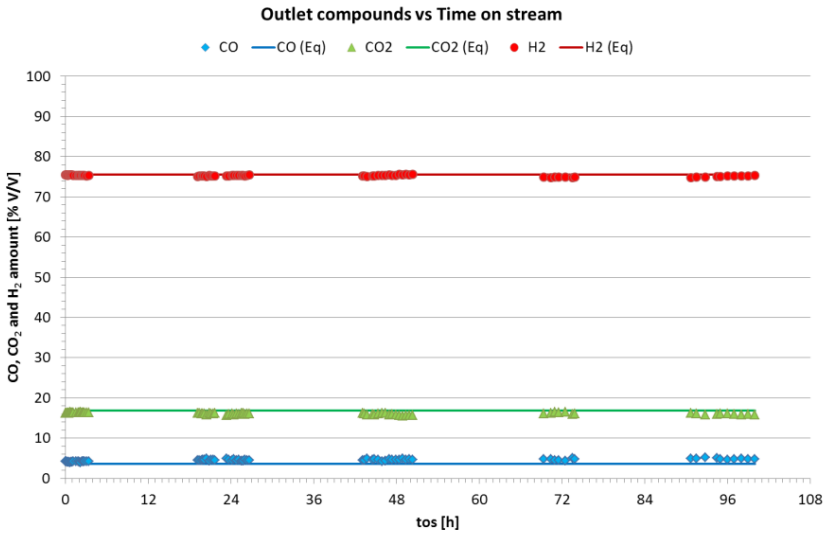

Fig. 4.71 Stability of the ZAC1c catalysts with time-of-stream.

The ZAC2c sample has a Cu-content two times higher that ZAC1c (but remaining lower than 20 wt.%), trying to observe improved results at temperature between 250 and 300 °C. The catalytic performances in the WGS reaction are strongly affected by the S/DG ratio only at 250 °C (Fig. 4.72), where the CO conversion decreases from 92 to 68 % by decreasing the S/DG value from 0.55 to 0.25. At temperatures ≥ 300 °C, the S/DG ratio effect is negligible, being CO conversion and H_2 yield values always close to the equilibrium values.

The contact time effect is not so evident at 250 °C as well as that related to the S/DG ratio (Fig. 4.73); in fact, the activity of the ZAC2c sample remains always very close to equilibrium values. At 300 °C, only a drastic decrease of contact time causes a decrease in both CO conversion and H_2 yield values. The results, considering both the H_2 yield and CO_2 selectivity values, allow to exclude the presence of side-reactions. Therefore, the activity for this sample seems to be slightly affected by the thermodynamic (steam excess) and kinetics (τ) parameters, in particular at temperatures ≥ 300 °C, where the ZAC2c sample shows the best performances.

Finally, this sample tested under long time-on-stream (100 h), such as previously do for the ZAC1c sample, shows a good stability , although the deactivation seems to be more pronounced than in the sample with lower Cu-content (ZAC1c).

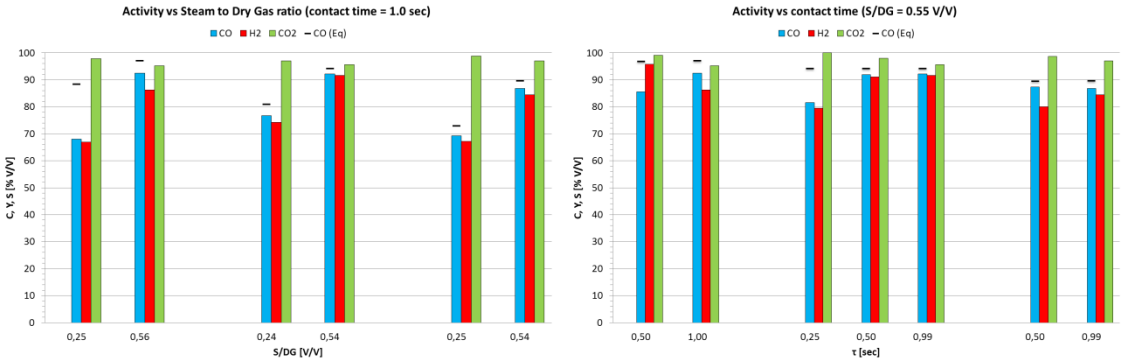

Fig. 4.72 ZAC2c activity of as a function of S/DG ratio and contact time values .

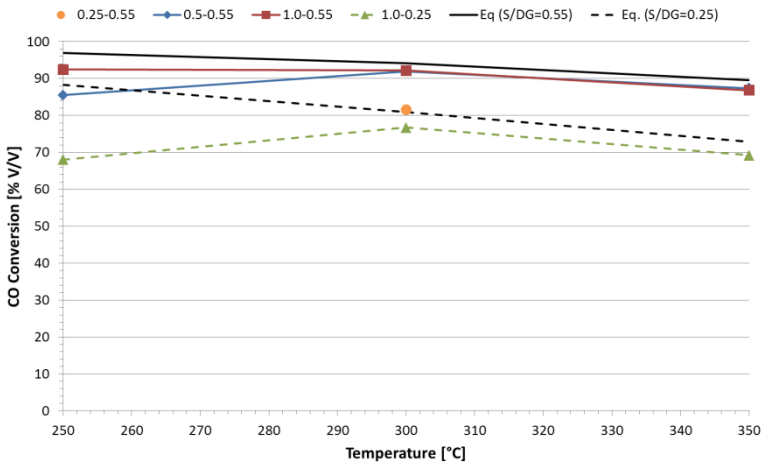

Fig. 4.73 CO conversion of ZAC2c as a function of the temperature, for different τ and S/DG values.

4.4.1.2 CHARACTERIZATION AFTER REACTION

A summary of the chemical-physical properties, before and after reaction, is reported in Table 4.4. After reaction, the ZA3K sample shows practically the same XRD pattern of the fresh one, evidencing only the ZnO phase (Fig. 4.11). The characteristic reflections of Cu^0 at 43.3, 50.5 and 74.1° are observed in the Cu-containing samples, confirming the catalyst activation (Fig. 4.12urthermore, they show also the spinel phases that sinterises during the reaction. The sintering effects are evident in the Cu-containing samples after reaction; in particular, a higher crystallinity is observed in the ZAC2c sample. The sintering and the agglomeration of Cu^0 crystallites are the main problem for the Cu-based catalysts; this effect is also confirmed by the surface area values, that decreased for all samples, but particularly for the ZAC1c catalyst..

The crystal size of the Cu-containing samples, before and after reaction, are calculated by the Debey-Scherrer formula (***12***) by using the best resolved reflections: at 43.3° for Cu^0 and at 36.2° for ZnO. The samples shows an increase of ZnO crystal size before and after reaction, evidencing a slight structural sintering of support, while the crystallite size of metallic copper can be solved only for the sample with higher amount of Cu, reaching a value of 13 nm. It is in agreement with the XRD pattern that shows a higher crystallinity of this sample, but it is not the result of a drastic sintering phenomena.

Sample		Phases	S_{BET} [m^2/g]	$d_{Cu(0)}$ [nm]	d_{ZnO} [nm]
ZAC1c	*fresh*	ZnO	62	-	10
	used	Cu^0, ZnO, spinel	34	n.d.	16
ZAC2c	*fresh*	ZnO	48	-	10
	used	Cu^0, ZnO, spinel	34	13	14

Table 4.18 Chemical-physical properties of the ex-HT catalysts.

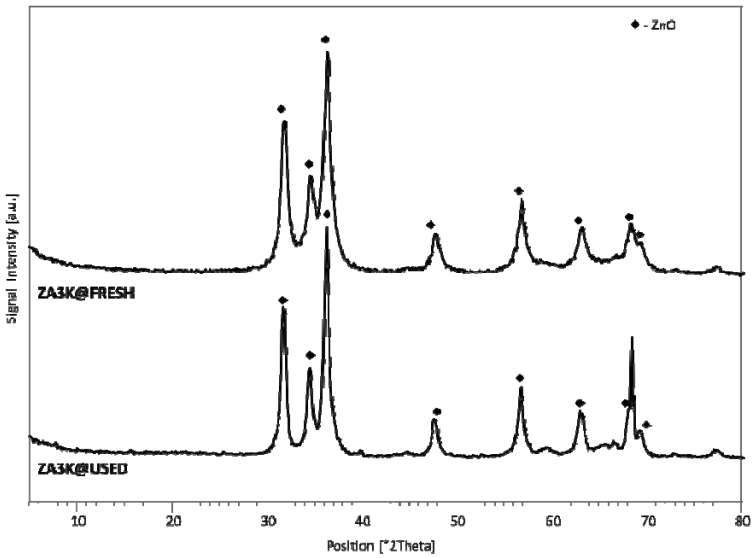

Fig. 4.74 XRD patterns of the ZA3 sample before and after reaction.

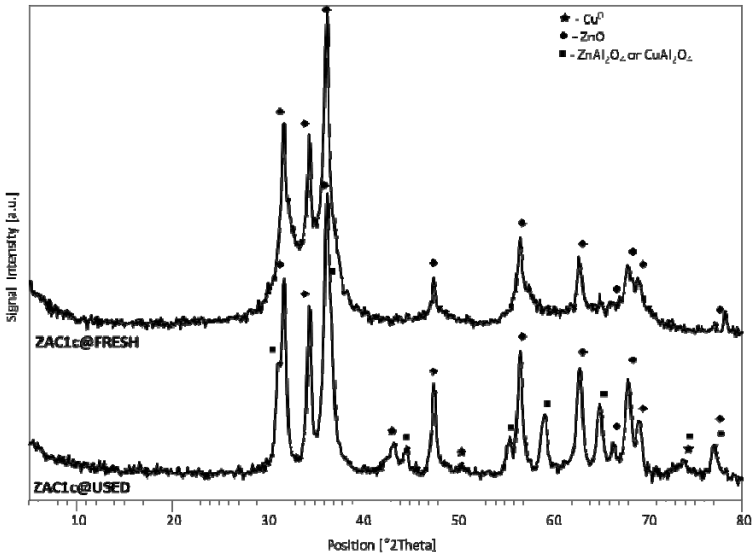

Fig. 4.75 XRD pattern of the ZAC1c sample before and after reaction .

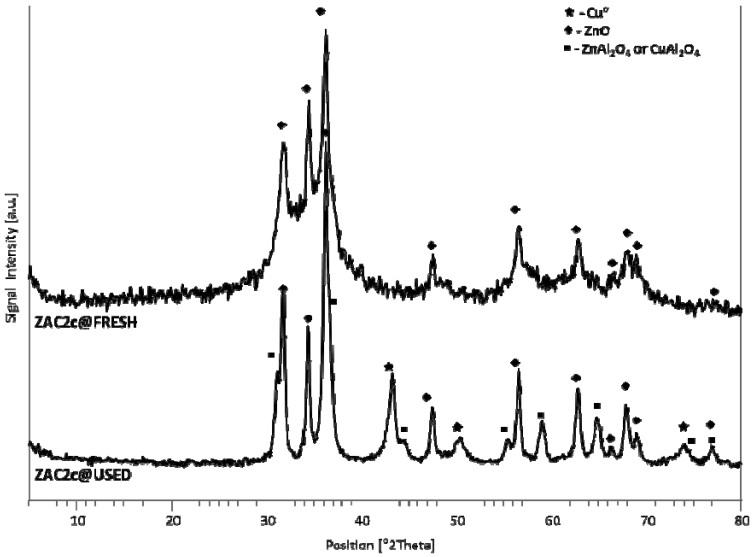

Fig. 4.76 XRD pattern of the ZAC2c sample before and after reaction.

The different reducibility of the phases was analysed by TPR analysis after oxidation for the unloaded catalysts. The ZA3K sample is not reduced under the analysis conditions, whereas the reduction after oxidation of the Cu-containing samples shows the presence of CuO fully reduced below 300 °C (Fig. 4.14). The TPR profile of the ZAC1c sample is typical of of Cu-free phases before and after oxidation; this samples evidences a shift of the reduction peak towards lower temperatures of about 60 °C, showing a decrease in the CuO interaction with the support. Hence, there is an increase after reaction of the amount of the most reducible Cu-containing species (***13***,***14***,***15***), although a re-dispersion occurs also during the TPO before and after reduction. The ZAC2c shows a single reduction peak of Cu species, with practically the same behaviour of the ZAC1c sample, thus has not been reported.

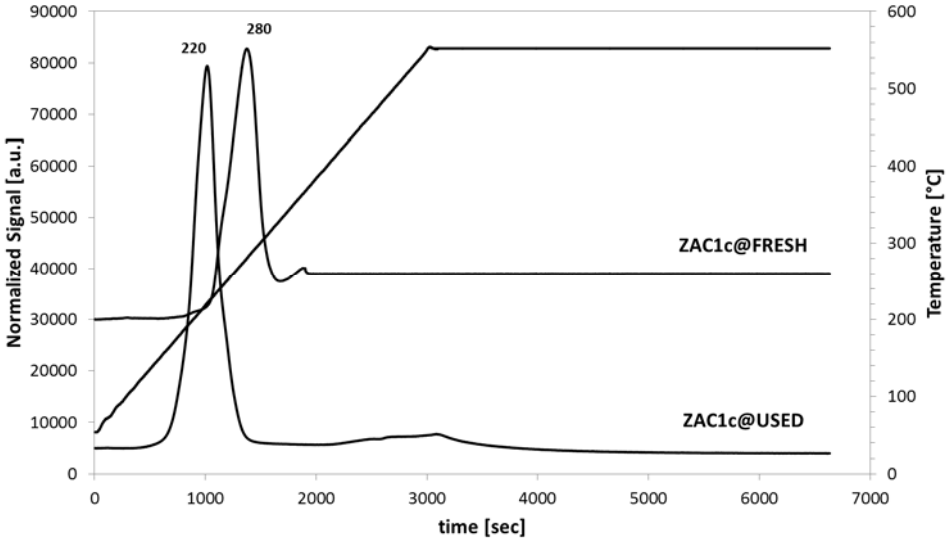

Fig. 4.77 TPR of the ZAC1c sample before and after reaction.

Table 4.5 shows the values of surface area (S_{BET}), cumulative pore volume between 17 and 3000 Å diameter (V_{PORES}) and average pore diameter (d_{PORE}). As previously depicted, the ZA3K sample

has practically the same surface area values, before and after the catalytic tests; on the contrary, the Cu-containing catalysts shows a decrease of the surface area after reaction. In these latter sample, the pore volume remains almost unaffected, but the pore size increases, showing that a structural sintering coupled with a possible breakage may occur. The pore size distribution of all the fresh ex-HT samples is bi-modal (Fig. 4.17): the pores between 3 and 4 nm disappears after reaction and those with higher diameter (10-40 nm) decrease, with an increase of the volume due to larger pores.

Sample		S_{BET} [m^2/g]	V_{PORES} (BJH des.) [cm^3/g]	D_{PORE} (BJH des.) [nm]
ZA3K	*fresh*	60	0.27	16
	used	-	-	-
ZAC1c	*fresh*	62	0.34	20
	used	34	0.33	31
ZAC2c	*fresh*	48	0.35	28
	used	34	0.35	34

Table 4.19 Morphological data of all the ex-HT catalysts.

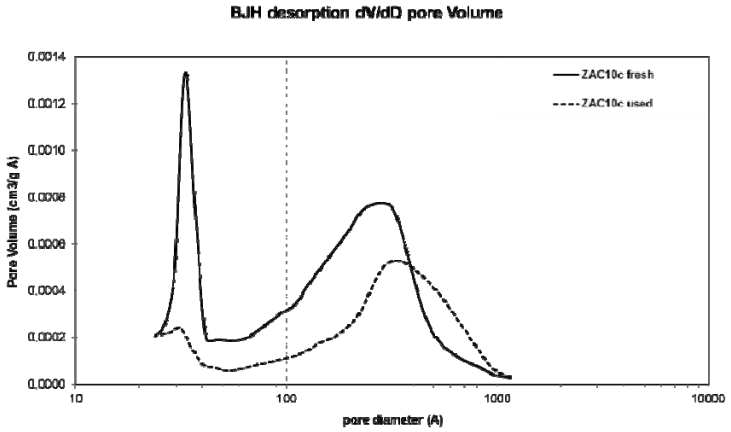

Fig. 4.79 BJH pore distribution for the ZAC1c sample.

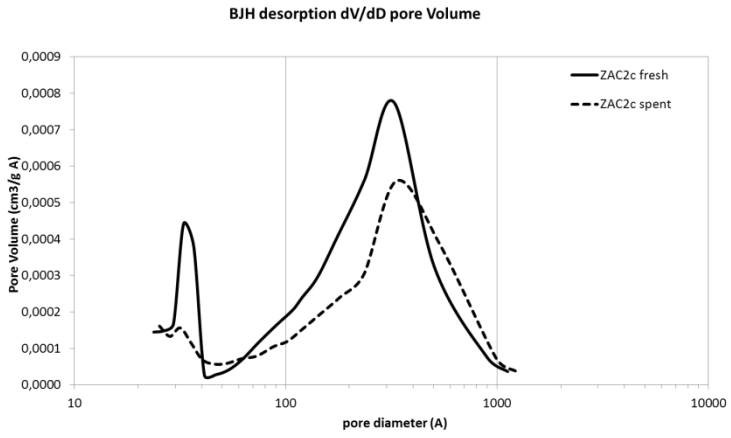

Fig. 4.80 BJH pore distribution for the ZAC2c sample.

The isotherms of all these catalysts can be grouped into **TYPE IV** of the IUPAC classification, while the hysteresis loops are **TYPE H4** (***16***) (Fig. 4.20); therefore, the pore size distributions and the isotherms indicate that the ex-HT catalysts contains mainly mesopores (2-50 nm).

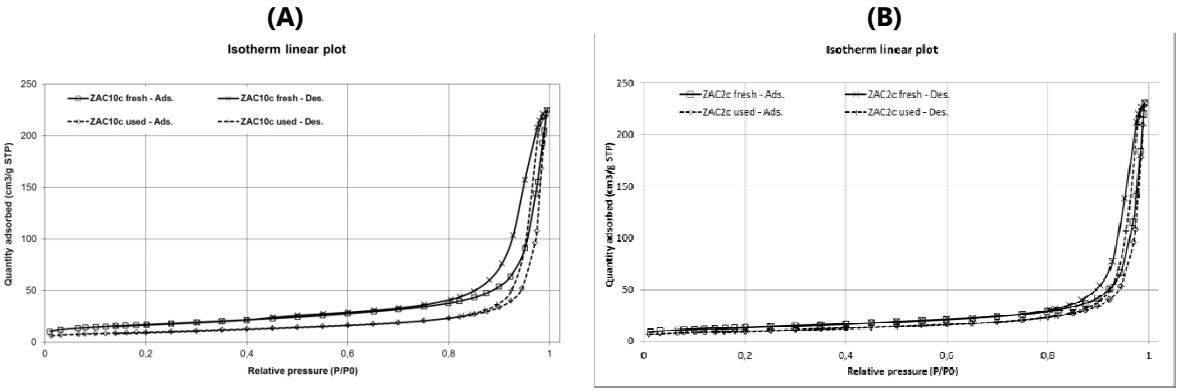

Fig. 4.81 Isotherms of the catalysts before and after reaction : (A) ZAC1c, (B) ZAC2c.

4.4.2 COMPARISON AMONG THE EX-HT CATALYSTS

The three ex-HT catalysts are mixed oxides obtained by calcination of HT precursors. The ZA3K sample is a K-doped Zn/Al-based catalyst, whereas the ZAC1c and ZAC2c samples are two Cu-containing samples, where the second one contains an amount of copper (as wt.%) two times that in the first one. In both cases, copper is introduced by partial substitution of zinc in the HT precursors by co-precipitation. The sample without copper shows a relatively good activity at high temperature, but the CO conversion is associated to a H_2 consumption, due to the significant presence of side reactions with formation of oxygenated products (mainly methanol), attributable to its high basicity. Therefore, it seems not actually suitable as catalyst for the WGS processes, but mostly an interesting matrix to be optimized by inclusion of a more active phases, such as, for example, copper.

Both Cu-based catalysts shows very good performances in all the operating conditions, regardless of S/DG ratio and contact time values adopted. At 250 °C (Fig. 4.29), a significant dependence on the operating conditions (S/DG and τ values) is observed for both the samples (ZAC1c and ZAC2c), mainly related to the S/DG ratio. However, the ZAC2c sample reaches an activity, in terms of CO conversion value, higher than that of the sample with the lower Cu-content (ZAC1c). On the contrary, both samples presents the best activity, with values of CO conversion close to equilibrium ones, regardless of the S/DG ratio, when temperature is $\geq$ 300 °C (Fig. 4.30), with the same trend for both ZAC1c and ZAC2c as a function of the thermodynamic and kinetic parameters. The ZAC2c sample shows a better performance than ZAC1c sample, operating at 350 °C and with a lower amount of steam (0.25 v/v) (Fig. 4.31).

Both samples show the same decrease of surface area values after reaction, although the sample with the lower Cu-content shows a lower sintering of Cu^0 crystallites, with a very stable behaviour with time-on-stream and a deactivation occurring slowly after 100 h.

In conclusion, the ZA3K sample is able to partially convert CO but with a significant H_2 consumption due to side-reactions. The ZAC1c sample shows significantly better performances, due to the promoting effect of cupper. The ZAC2c sample may be consider the best catalyst, suitable also for non-conventional values of the S/DG ratio. The very good performances in the MTS conditions, associated with a good thermal stability, justify a further optimization focused on the use of promoted ex-HT catalyst catalysts in the WGS processes, in order to minimize sintering phenomena and side-reactions with H_2 consumption.

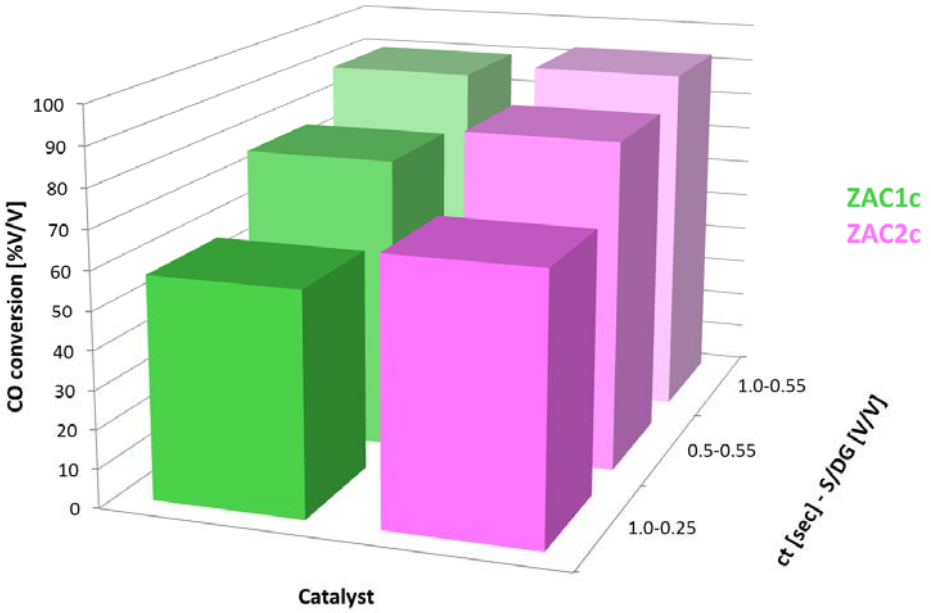

Fig. 4.82 Activity of the two Cu-containing ex-HT catalysts at 250 °C.

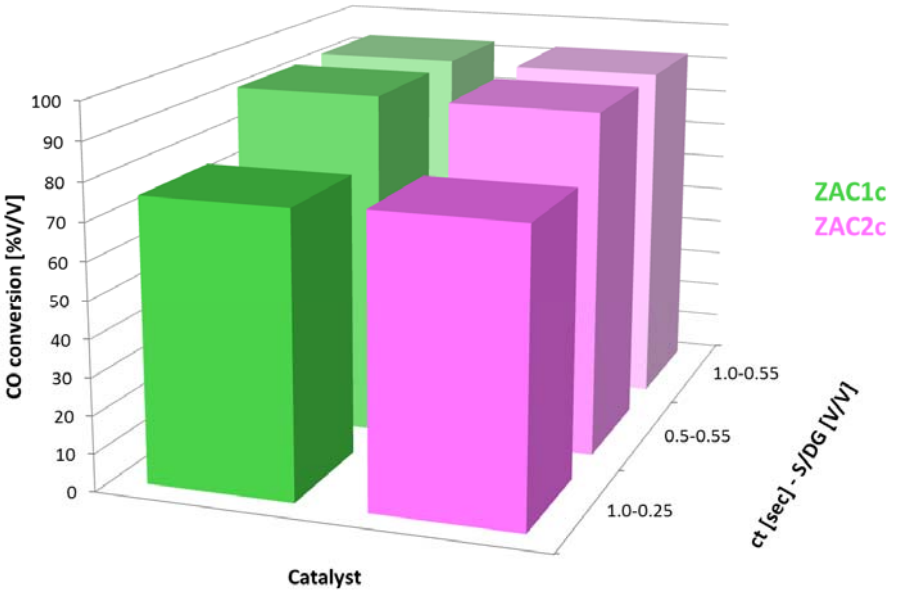

Fig. 4.83 Activity of the two Cu-containing ex-HT catalysts at 300 °C.

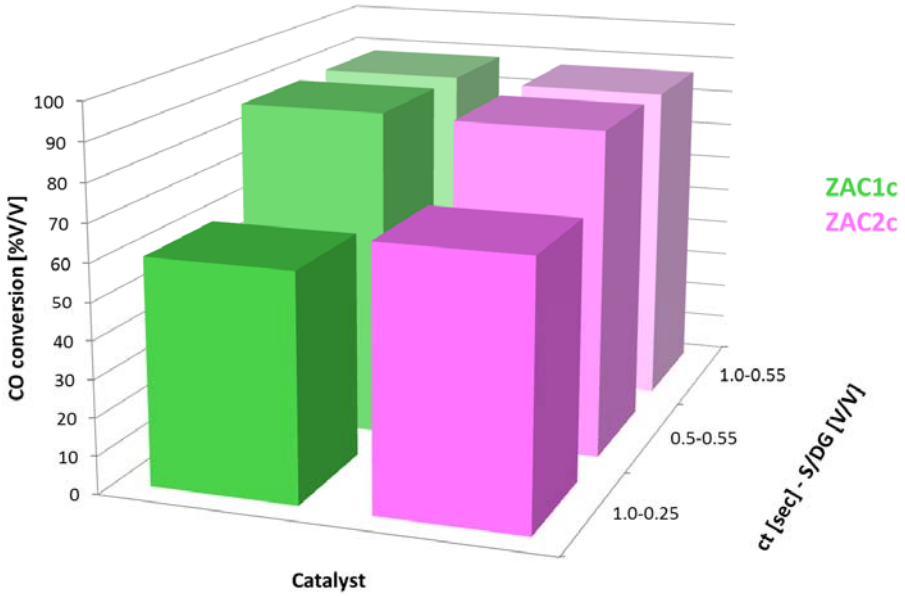

Fig. 4.84 Activity of the two Cu-containing ex-HT catalysts at 350 °C.

4.5. STUDY OF THE DEACTIVATION PHENOMENA

This study has been carried out during a stage of three months performed at the CRCD of Air Liquide (Jouy-en-Josas F), in the frame of the Marco Polo program.

The temperature profile along the MTS reactor gives precious information on the catalyst activity and may be measured by the thermocouples (temperature rise = temperature measured – inlet temperature) placed along an MTS unit. The thermocouples position is indicated in the legend and corresponds to the proportion of the total bed height (as percentage). It is possible to observe that the top of the catalytic bed is initially active, but successively deactivates (Fig. 4.85). This rapid deactivation occurs in the two first layers of the catalytic bed, that may be supposed to act as a guard layer, in which poisons are preferentially adsorbed. The temperature measured by the thermocouple below the first part of the bed presents a slow and gradual decrease. If the desired equilibrium is not reached, the inlet temperature is increased to enhance the kinetics, such as usually performed in these situations. Usually, when the catalyst works well, the inlet temperature is kept as low as possible, although with some margin above the dew point to avoid condensation.

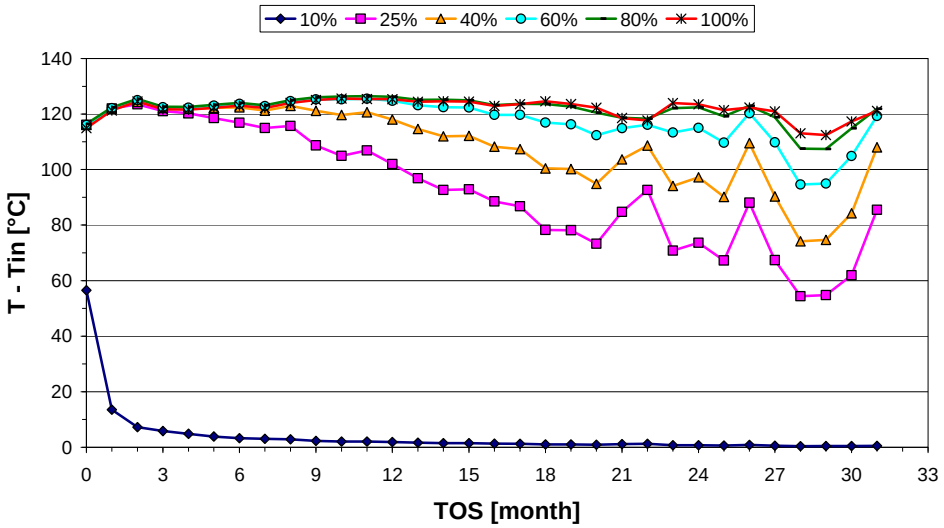

Fig. 4.85 Catalyst deactivation in a MTS plant.

4.5.1 MODEL OF THE WGS REACTOR

The model and the corresponding tool developed enable to simulate the WGS reactor. The tool has been programmed with Visual Basic for Applications (VBA) and can be used with Microsoft Excel. The reactor is modelled like a PFR and supposed to be adiabatic. Wet gas is treated like an ideal gas and the pressure is assumed to be almost constant along the reactor. Furthermore, it is assumed that only the WGS reaction occurs, so that the changes in the CO, H_2O, CO_2 and H_2 contents correspond to the stoichiometry of the shift reaction. In this model, it is not separated the bulk (gas phase where species are transported) and the catalyst surface (solid phase where the reaction occurs).

The literature indicates that under the MTS operating conditions, the reaction probably follows a Langmuir-Hinshelwood (L-H) mechanism, while the impact of the pressure on the kinetics is not well quantified. Catalyst composition affects the behaviour of the catalyst, which should have an influence on the design of the catalytic guard.

The main active phase is Cu, although other elements (ZnO) may act not only as supports. Catalyst deactivation is caused by a sintering accelerated by poisoning. Indeed, in the presence of sulphur and chlorine, low-melting-point compounds are formed on the surface of the catalyst; being both WGS and poisoning reactions diffusion limited, the pellet size becomes an important parameter that may affect the spreading of the poisons along the reactor. The inlet concentration of different components in the feed gas may have an impact on the catalytic guard.

The tool gives a predicted volume following the same logic of Haldor Topsoe A/S design and it is satisfactory to obtain good results, although it does not prove that the assumptions are fully true (L-H kinetics and decay law by sintering).

The main limit of this tool is that it is not possible to extrapolate to cases different from those presented in this work or with different specification.

4.5.1.1 PROCEDURE

The input data are the inlet flow rate, composition, temperature, pressure and density of the fixed-bed catalyst; in addition, thermodynamic and kinetic parameters are already included in the model (rate expression, equilibrium constant, heat capacities, heat of reaction). In order to consider a right equilibrium constant expression, it has been performed a comparison between the most popular expressions of K_{eq}. All the expressions give rise to similar trends in the temperature range, in particular in the WGS range (200-350 °C). The tool actually solves the following system of eight ordinary differential equations along the reactor ("V" is the volume of catalyst) using the 4th order of the Runge-Kutta method.

Different rate expressions may lead to different shapes of the temperature profiles; typically, the power laws and those based on the redox mechanism give sigmoid profiles, with an inflexion like the red curve, as shown in Fig. 4.86. The Langmuir-Hinshelwood rate expressions have this small inflexion, that it is not visible, like the green curve, after the initial horizontal segment. However, it is very difficult to know what really happens in the yellow area.

The profiles obtained using the kinetics found in the literature do not fit well the measured profiles, due to many phenomena, such as diffusion limitations and pressure effects. Therefore, a correction factor (f) has to be included to fit well the real profiles (Fig. 4.87).

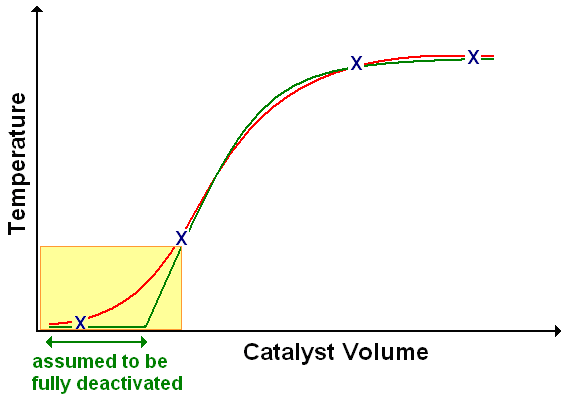

Fig. 4.86 Typical shape of the temperature profile.

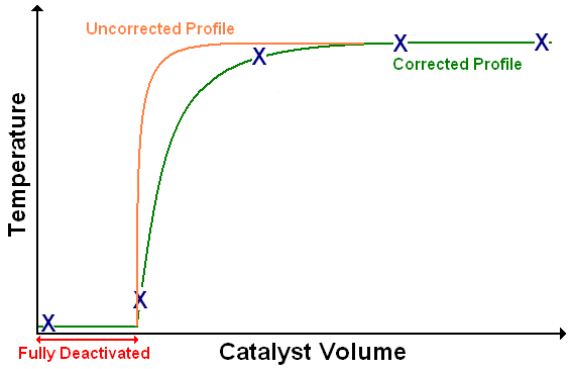

Fig. 4.87 Determination of the correction factor "*f*".

Catalyst deactivation induces a decrease in the apparent reaction rate.; in the case of sintering, the most commonly used decay law takes the following expression (***54***,***55***):

$$r_d = -\frac{\partial a}{\partial t} = k_d\left(a - a_\infty\right)^n$$

Activity superscript is usually of the second order (n = 2) with the different mechanism of thermal deactivation reported in the literature, although its value is normally 1 or 2 (***54***). Sintering is a temperature-activated process and the decay constant follows the Arrhenius equation (***55***). According to the literature, typical values for the activation energy (E_d) range between 30 and 60 kJ/mol. It is important to note that r_d is temperature-dependent and, therefore, the catalyst deactivation is not an uniform process along the reactor.

Catalyst deactivation is probably caused by sintering accelerated by poisoning; this is the reason for our fitting of an activity-decay-law with the form previously described. Since the deactivation rate constant is temperature dependent, the catalyst deactivation will depend on the temperature profile, which in his turn depends on the inlet conditions. The main source of error comes from the fact that it is not possible to know exactly the inlet composition of the reactor, but only the typical one.

The fitting of temperature profiles regarding the first load of a MTS plant is very good in all the ranges of time-on-stream below 3 years of aging (Fig. 4.88).

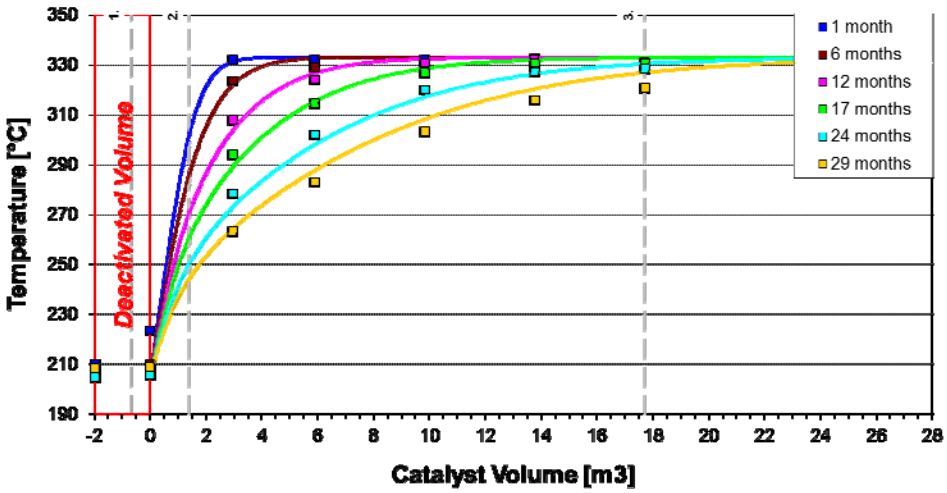

Fig. 4.88 Temperature profiles for a MTS industrial plant.

4.5.1.2 Results

Using the simulation tool with the deactivation law determined from plant data, it is possible to link the volume of active catalyst (not including the catalytic guard, because it has been assumed completely deactivated) to the approach at the equilibrium obtained at the outlet. The predicted catalyst volume is calculated to achieve 90 % of maximum conversion after 3 years of operation (time-on-stream), being a reasonable criterion to determine the catalyst volume.

The design tool gives volumes very similar to those recommended (Table 4.20); however, these calculated volumes should be considered with precaution. Indeed, it is important to remember that they have been calculated on the basis of a deactivation law, the accuracy of which is limited. Furthermore, it is difficult to design the catalytic guard, because it is probably the result of complex poisoning models. It is fundamental to keep in mind that the results depend on deactivation laws based on the profiles measured along the MTS reactor.

Volume	MTS unit
Calculated	16.9
Recommended	16.4

Table 4.20 Calculated and recommended catalyst volume for the main bed.

REFERENCES

1. Del Piero, G.; Di Conca, M.; Trifirò, F.; Vaccari, A. In *Reactivity of Solids;* Barret, P., Dufour, L. C., Eds.; Elsevier: Amsterdam (NL), 1985; p 1029.
2. Charcosset, H.; Turlier, P.; Trambouze, Y. *J. Chem. Phys.* **1974,** *61,* 1257.
3. Stroupe, J. D. *J. Am. Chem. Soc.* **1949,** *71,* 569.
4. Gadalla, A. M. *Ind. Eng. Chem. Fundamen.* **1984,** *23* (4), 436.
5. Harrison, P. G.; Lloyd, N. C.; Daniell, W.; Ball, I. K.; Bailey, C.; Azelee, W. *Chem. Mater.* **2000,** *12,* 3113.
6. Okamoto, Y.; Fukino, K.; Imanaka, T.; Teranishi, S. *J. Phys. Chem.* **1983,** *87,* 3740.
7. Robinson, W. R. A. M.; Mol, J. C. *Appl. Catal.* **1990,** *60,* 61.
8. Castiglioni, G. L.; Vaccari, A.; Fierro, G.; Inversi, M.; Lo Jacono, M.; Minelli, G.; Pettiti, I.; Porta, P.; Gazzano, M. *Appl. Catal.* **1995,** *123,* 123.
9. Als-Nielsen, J.; Grübel, G.; Clausen, B. S. *Nucl. Instrum. Methods Phys. Res. B* **1995,** *97,* 522.
10. Reitz, T. L.; Lee, P. L.; Czaplewski, K. F.; Lang, J. C.; Popp, K. E.; Kung, H. H. *J. Catal.* **2001,** *199,* 193.
11. Khan, A.; Chen, P.; Boolchand, P.; Smirniotis, P. G. *J. Catal.* **2008,** *253,* 91.
12. Klug, H. P.; Alexander, L. E. *X-Ray Diffraction Procedures;* Wiley: New York (US), 1974.
13. Ruggeri, O.; Trifirò, F.; Vaccari, A. *J. Solid State Chem.* **1982,** *42,* 120.
14. Gusi, F.; Trifirò, F.; Vaccari, A. *React. Solids* **1986,** *2,* 59.
15. Delmon, B. *Introduction à la cinetique hétérogène;* Technip: Paris (F), 1969.
16. IUPAC. *Pure Appl. Chem.* **1985,** *57* (4), 603.
17. Pieck, C. L.; Vera, C. R.; Parera, J. M.; G.N. Giménez, L. R. S.; Carvalho, L. S.; Rangel, M. C. *Catal. Today* **2005,** *107-108,* 637.
18. Pieck, C. L.; González, M. B.; Parera, J. M. *Appl. Catal. A* **2001,** *205,* 305.
19. Parera, J. M.; Beltramini, J. N. *J. Catal.* **1988,** *112,* 357.
20. Bertolacini, R. J.; Pellet, R. J. In *Catalyst deactivation ;* Delmon, B., Froment, G. F., Eds.; Elsevier: Amsterdam (NL), 1980; p 73.
21. Yermakov, Y. U.; Kuznetsor, B. N. *J. Mol. Catal.* **1980,** *9,* 13.
22. Guryev, Y. V.; Ivanova, I. I.; Lunin, V. V.; Grünert, W.; Van Den Berg, M. W. E. *Appl. Catal. A* **2007,** *329,* 16.
23. Jacobs, G.; Graham, U. M.; Chenu, E.; Patterson, P. M.; Dozier, A.; Davis, B. H. *J. Catal.* **2005,** *229,* 499.
24. Carvalho, L. S.; Pieck, C. L.; Rangel, M. C.; Fígoli, N. S.; Grau, J. M.; Reyes, P.; Parera, J. M. *Appl. Catal. A* **2004,** *269,* 91.
25. Du, X.; Gao, D.; Yuan, Z.; Liu, N.; Zhang, C.; Wang, S. *Intern. J. Hydr. Energy* **2008,** *33,* 3710.
26. Ciambelli, P.; Cimino, S.; de Rossi, S.; Lisi, L.; Minelli, G.; Porta, P.; Russo, G. *Appl. Catal. B* **2001,** *29,* 239.
27. Porta, P.; Cimino, S.; de Rossi, S.; Faticanti, M.; Minelli, G.; Pettiti, I. *Mater. Chem. Phys.* **2001,** *71,* 165.
28. Fierro, J. L. G. *Catal. Today* **1990,** *8,* 153.

29. Xu, Q.; Huang, D.; Chen, W.; Lee, J.; Wang, H.; Yuan, R. *Scr. Mater.* **2004,** *50,* 165.
30. Pena, M. A.; Fierro, J. L. G. *Chem. Rev.* **2001,** *101,* 1981.
31. Sun, Y.; Hla, S. S.; Duffy, G. J.; Cousins, A. J.; French, D.; Morpeth, L. D.; Edwards, J. H.; Roberts, D. G. *Int. J. Hydrog. Energy* **2011,** *36,* 79.
32. Fy, Q.; Weber, A.; Flytzani-Stephanopoulos, M. *Catal. Lett.* **2001,** *77,* 87.
33. Ricote, S.; Jacobs, G.; Milling, M.; Ji, Y.; Patterson, P. M.; Davis, B. H. *Appl. Catal. A* **2006,** *303,* 35.
34. Maluf, S. S.; Assaf, E. M. *J. Nat. Gas Chem.* **2009,** *18,* 131.
35. Zhang, R.; Alamdari, H.; Kaliaguine, S. *J. Catal.* **2006,** *242,* 241.
36. Ciambelli, P.; Cimino, S.; Lisi, L.; Faticanti, M.; Minelli, G.; Pettiti, I.; Porta, P. *Appl. Catal. B* **2001,** *33,* 193.
37. Teraoka, Y.; Yoshimatsu, M.; Yamazoe, N.; Seyama, T. *Chem. Lett.* **1984,** 893.
38. Ifrah, S.; Kaddouri, A.; Gelin, P.; Bergeret, G. *Catal. Commun.* **2007,** *8,* 2257.
39. Mizuno, N.; Yamato, M.; Tanaka, M.; Mizuno, M. M. *Chem. Mater.* **1989,** *1,* 232.
40. Rønning, M.; Huber, F.; Meland, H.; Venvik, H.; Chen, D.; Holmen, A. *Catal. Today* **2005,** *100,* 249.
41. Tabakova, T.; Boccuzzi, F.; Manzoli, M.; Sobczak, J. W.; Idakiev, V.; Andreeva, D. *Appl. Catal. A* **2006,** *298,* 127.
42. Nishida, K.; Atake, I.; Li, D.; Shishido, T.; Oumi, Y.; Sano, T.; Takehira, K. *Appl. Catal. A* **2008,** *337,* 48.
43. Nagai, M.; Zahidul, A. M.; Matsuda, K. *Appl. Catal. A* **2006,** *313,* 137.
44. *Cerium: a guide to its role in chemical technology;* Molycorp Inc.: Mountain Pass CA (US), 1992.
45. Buscail, H.; Larpin, J. P. *Solid State Ion.* **1996,** *92,* 243.
46. Ma, H. Q.; Tan, X.; Zhu, H. M.; Zhang, J. Y. *J. Chin. Rare Earth Soc.* **2003,** *21* (4), 445.
47. Kongzhai, L.; Wang, H.; Wei, Y.; Liu, M. *J. Rare Earths* **2008,** *26* (5), 705.
48. Reddy, A. S.; Chen, C. Y.; Chen, C. C.; Chien, S. H.; Lin, C. J.; Lin, K. H.; Chen, C. L.; Chang, S. C. *J. Mol. Catal. A* **2010,** *318,* 60.
49. Lee, J. B.; Park, C. S.; Choi, S. I.; Song, Y. W.; Kim, Y. H.; Yang, H. S. *J. Ind. Eng. Chem.* **2005,** *11* (1), 96.
50. Schiødt, N. C. to Haldor Topsoe A/S (DK). EP Patent 2,141,118, 2010.
51. Smith, K. J.; Anserson, R. B. *J. Chem. Eng.* **1983,** *61,* 40.
52. Hofstadt, C. E.; Scneider, M.; Bock, O.; Kochloefl, K. In *Preparation of catalysis III;* Poncelet, G., Grange, P., Jacobs, P. A., Eds.; Elsevier: Amsterdam (NL), 1983.
53. Vedage, G. A.; Himelfarb, P. B.; Simmons, J. W.; Klier, K.; Grasselli, R.; Brazdil, J. F. *Solid state chemistry in catalysis;* ACS: Washington DC (US), 1985.
54. Fuentes, G. A. *Appl. Catal.* **1985,** *15,* 33.
55. Aparacio, M. L.; Laborde, M. A.; Amadeo, N. E. *Inf. Tecnol.* **1996,** *7* (1), 29.

5 CONCLUSIONS

This PhD work has been focused on the H_2 production by means of the WGS reaction, focusing the attention on the development of new formulations for an advantageous single step carried out at 300 °C (Medium Temperature Shift or MTS). The goal was to obtain MTS catalysts able to reach the desired target of conversion values with low S/DG ratio and contact time values, thus allowing a lower overhead of the shift unit.

Initially, the study has been devoted to some commercial catalysts to understand the role of reaction parameters, such as pressure, temperature, S/DG ratio and contact time. values Successively, innovative bulk materials, perovskite-type (PVK) or hydrotalcite-type (HT), have been synthesized also taking into account the possibility to use structured reactors, which may improve the H_2 production by WGS processes.

The three commercial catalysts are M/LTS formulations with copper, as active phase, and ZnO, as support. The first sample (CatA) is a classic LTS catalyst containing Al-based spinel and shows the best performances. However, it contains a very high Cu-amount (three times higher than those of that the other two Cu/Zn-based catalysts). Furthermore, it shows a significant increase of crystallinity after reaction, that suggests a rapid deactivation due to particle sintering.

The CatB sample contains chromia, as thermal stabilizer, that avoids the increase of the crystallite size and the decrease of the surface area after reaction. The morphological behaviour is an important parameter to define a catalyst as optimum solution for long time-on-stream processes. Moreover, it shows a CO conversion comparable to that of the CatA sample in the MTS conditions (300 °C). This behaviour does it as the best candidate for the industrial application at middle temperature.

The CatC sample is supported on both chromia and alumina and reaches CO conversion values comparable to those of CatB sample only at 250 °C. In the other operating conditions, it shows an activity lower than those of other commercial samples. Finally, CatD is is a precious-metal-based catalyst, with Pt/Re, as active phase, supported on a monolith of cordierite, that has to be conidered a new type of high temperature shift (HTS) catalyst.

Differently, all the Fe-containing PVK samples investigated are inactive in the WGS reaction, while the LaCeCu catalyst shows a moderate activity only at high temperature (400 °C) and using high contact time values. Further Ce-containing samples (that not are PVK phases, but really mixed oxides) are more active than the PVK catalysts when promoted by copper (CeFe-Cu). The CeFe-Cu sample shows a good CO conversion at 350 °C byand using a typical S/DG ratio (0.55 v/v) and high contact time values. After reaction, it does not show significant sintering phenomena; thus this catalyst may be a good starting poiny for a further optimization focused on promoting and doping elements, that may enhance the activity and the stability in the shift reaction at middle temperature.

Finally, a Zn/Al-based catalyst produced according to a recent patent by calcination of a hydrotalcite-type (HT) precursor and doped by potassium, is active only at high temperature, with furthermore, significant side reactions forming oxygenated compound and consuming H_2. On the other hand, if relatively small amounts of copper are introduced during the co-precipitation of the HT precursors, the ex-HT Cu-promoted catalysts show significant improvements of the

activity. Two ex-HT samples, with zinc partially substituted by copper, the first one (ZAC1c) with a Cu-content equal to 50% of that in the second sample (ZAC2c), reach CO conversion and H_2 yield values close to the equilibrium data at temperatures ≥ 300 °C. At 250 °C, the ZAC2c sample shows an improvement of the performances at low contact time values, although associated to a high growth of Cu crystallites after reaction. Therefore, a future tuning of the Cu-content and properties may be necessary to achieve the best compromise between catalytic activity and stability with time-on-stream.

ACKNOWLEDGMENTS

Thanks are due to:

- Air Liquide (F) for the financial supports to this work.
- Dr.s D. Gary, P. Del Gallo and all the staff of the CRCD of Air Liquide in Jouy-en-Josas (F) for their scientific support and friendly collaboration.
- The EU Program Marco Polo for a grant obtained.
- The Department of Industrial Chemistry and Materials of ALMA MATER STUDIORUM – University of Bologna for the friendly support and hospitality.
- All the laboratory friends for three years together.